UiT The Arctic University of Norway
University of South-Eastern Norway
Western Norway University of Applied Sciences
NTNU Norwegian University of Science and Technology

Faculty of Science and Technology
Department of Technology and Safety

Local-Scale Advanced Ship Predictor towards Enhanced Maritime Situation Awareness

Yufei Wang

A dissertation for the degree of Philosophiae Doctor

September, 2024

UiT The Arctic University of Norway
Faculty of Science and Technology
Department of Technology and Safety

Norwegian University of Science and Technology
Faculty of Engineering
Department of Ocean Operations and Civil Engineering

University of South-Eastern Norway
Faculty of Technology, Natural Sciences and Maritime Studies
Department of Maritime Operations

Western Norway University of Applied Sciences
Faculty of Business Administration and Social Sciences
Department of Maritime Studies

Local-Scale Advanced Ship Predictor towards Enhanced Maritime Situation Awareness

Yufei Wang

Doctoral thesis in partial fulfillment of the requirements for the degree of Philosophiae Doctor

UiT Norges arktiske universitet

Faculty of Science and Technology
Department of Technology and Safety

September, 2024

Supervised by:
Bjørn-Morten Batalden, UiT
Lokukaluge Prasad Channa Perera, UiT
Runar Ostnes, NTNU
Javad Barabady, UiT

Abstract

With the introduction of autonomous and remotely-controlled ships, close vessel encounter situations can be associated with higher collision risk and near-miss scenarios. To avoid such possible incidents, i.e., collision and near-miss, a higher level of situation awareness is required to support the respective decision-making process in ship navigation. Advanced Ship Predictors (ASPs) are thus proposed to be a solution framework to enhance situation awareness for ship navigation as the main contribution of this thesis. The research presented in this thesis focuses on local-scale predictions conducted by the ASP, with the typical prediction horizons ranging from 10 to 90 seconds.

The workflow of the local-scale ASP is divided into two main parts: vessel navigation state estimation and pivot point (PP)-based trajectory prediction. Kalman filter (KF)-based algorithms, combined with kinematic motion models, are used to estimate vessel navigation states. These estimated states are then employed to determine the PP of the vessel. The predicted trajectory is generated by utilizing the PP's role in navigation. Since the pivot point is widely understood and applied in ship navigation education and training, the local-scale prediction is designed to integrate this understanding to the vessel trajectory prediction.

The evaluation of the designed local-scale ASP begins with simulated maneuvers conducted in the UiT bridge simulator. It is then followed by sea trials on the UiT research vessel, Ymir RV. The performance of the local-scale ASP has been gradually improved through modifications after each evaluation. The evaluation based on simulated maneuvering data shows that the 90-second position prediction yields a median L2-norm error between 10 and 15 meters, while the median heading error at the 90th second ranges from 0 to -5 degrees. During sea trials conducted by the Ymir RV, the predictions are calculated over a 10-second horizon. After the vessel entered a steady state following the execution of a new rudder order, the position prediction revealed a maximum L2-norm error of approximately 8.7 meters, while the maximum heading error was about 13 degrees.

Acknowledgements

When I embarked on my Ph.D. journey, it was during one of the most significant crises humanity has faced in the information age—the COVID-19 pandemic in 2020. Those days were characterized by widespread fear of illness and uncertainty about the future. Now, four years later, humanity has demonstrated its resilience and ingenuity in restoring some order out of the chaos caused by the pandemic. While we have achieved substantial milestones in the battle against the virus, the final chapter of this struggle is yet to be written. In many ways, the work of Ph.D. candidates reflects humanity's fight against this virus.

I am deeply grateful to UiT for providing me with the opportunity to explore the development of autonomous shipping, a field still in its infancy. These four years of my research journey have often felt like navigating through uncharted waters, with only the faint glow of a candle that seemed ready to extinguish at any moment. I take pride in having ventured into the unknown and uncovered new realms of knowledge. Yet, I also recognize that the path ahead remains shrouded in dense fog, possibly leading to more challenges or even dead ends. However, I believe this uncertainty embodies the essence of scientific research. Just as a great work of art requires years of meticulous refinement, the pursuit of truth often demands a lifetime of dedication.

Throughout my Ph.D. journey, I have many individuals to whom I owe my heartfelt gratitude. First and foremost, I would like to express my sincere appreciation to my main supervisor, Bjørn-Morten Batalden. His warm welcome during the pandemic and steady support throughout my research have been invaluable. His advice on survival skills in Tromsø, particularly the essential recommendation to buy a house early and to learn how to ski, has been incredibly helpful. I would also like to extend my deepest thanks to my co-supervisor, Professor Lokukaluge Prasad Channa Perera. I am especially grateful for his rigorous academic guidance and his patience, particularly during the early stages of my research, when I made numerous mistakes. His understanding and concern meant a great deal to me. A special thank you as well to my co-

supervisors, Runar Ostnes (NTNU) and Javad Barabady, for providing valuable research resources and support.

My heartfelt thanks also go to my colleagues in the nautical science group. Special mentions go to Adnan, Brian, Egil, Hadi, Helene-Xue, Hosna, Johan-Fredrik, Khanh, Mahmood, Tae Eun, Tiantian, and Øyvind. Your collaboration, insights, and encouragement have been vital in my progress. It has been an honor to work alongside each of you. I also want to express my gratitude to my friends and colleagues in the same building who provided invaluable support. Special thanks to Amar, Behrooz, Bright, Bryan, Gunn-Helene, Gabriela, Hao, Jibola, Kaori, Kåre, Leikny, Lihong, Magne-Petter, Mao, Minh Tuan, Nikolai, Sahil, and Sushmit. Your camaraderie has significantly enriched my Ph.D. experience. I am also thankful to Ricardo, Clàudio, and André from Portugal, for their support of my research. Thanks to all of you, my life in Tromsø has felt warm and welcoming.

To my beloved parents and wife, I owe my deepest appreciation. Norway is the third country I have lived in during my studies abroad. When I decided to move here from Germany, my parents provided me with tremendous support. To my wife, Xiaoyu—words cannot convey my gratitude. We married in Tromsø, and I am incredibly thankful for her bravery in joining me in a country she had never been before, especially during the pandemic. Her constant care and encouragement have been invaluable, and I am forever grateful for everything you have done behind the scenes.

As this unforgettable journey draws to a close, a new and even more meaningful one begins. My wife and I are overjoyed as we prepare to welcome our child in the spring of 2025. I hope that the next generation will lead lives that are even more fulfilling and vibrant than our own.

Yufei Wang

Tromsø, Norway

22, Sep, 2024

Contents

List of Figures

List of Tables

Abbreviations

ACG	Apparent Center of Gravity
AI	Artificial Intelligence
ARPA	Automatic Radar Plotting Aid
ASP	Advanced Ship Predictor
CAA	Constant Angular Acceleration Model
CG	Center of Gravity
CMM	Curvilinear Motion Model
COLREGs	International Regulations for Preventing Collisions at Sea 1972
CTRA	Constant Turn Rate & Acceleration Model
DCPA	Distance to Closest Point of Approach
DoF	Degree of Freedom
ECDIS	Electronic Chart Display and Information System
EKF	Extended Kalman Filter
GNSS	Global Navigation Satellite System
GPR	Gaussian Process Regression
GRU	Gated Recurrent Unit
IMU	Inertial Measurement Unit
IMO	International Maritime Organization
MASS	Maritime Autonomous Surface Ships
MSC	Maritime Safety Committee
NIS	Normalized Innovation Squared
PP	Pivot Point
RNN	Recurrent Neural Network
RO	Research Objective
SOLAS	International Convention for the Safety of Life at Sea
TCPA	Time to Closest Point of Approach
UiT	University of Tromsø–The Arctic University of Norway
UTM	Universal Transverse Mercator
UKF	Unscented Kalman Filter

Nomenclature

a_n	Acceleration component normal to V
a_t	Acceleration component tangential to V
a_u	Linear acceleration component derived from u
a_v	Linear acceleration component derived from v
a_E	Acceleration component in easting
a_H	Acceleration component in vertical direction of $\{\mathbf{N}\}$ (3D)
a_N	Acceleration component in northing
P_E	Easting in the UTM coordinate system
P_H	Height referenced to the WGS 84 ellipsoid origin (3D)
P_N	Northing in the UTM coordinate system
$\mathbf{Q}$	Covariance matrix of $\mathbf{w_x}$
r	Turn rate of a vessel
$\mathbf{R}$	Covariance matrix of $\mathbf{w_z}$
t	Continuous-time unit used in models
t_k	Discrete-time unit used in models
u	Surge velocity of a vessel at vessel ACG
$\mathbf{u}$	Input state used in KF-based algorithms
v	Sway velocity of a vessel at vessel ACG
v_E	Course-speed vector component in easting
v_H	Course-speed vector component in vertical direction of $\{\mathbf{N}\}$ (3D)
v_N	Course-speed vector component in northing
V	Course-speed vector of a vessel at vessel ACG
$\mathbf{w_x}$	System noise used in KF-based estimation
$\mathbf{w_z}$	Measurement noise used in KF-based estimation
$\mathbf{x}$	System state used in KF-based algorithms
$\mathbf{z}$	Measurement state used in KF-based algorithms
$\{\mathbf{N}\}$	Local navigation frame
$\{\mathbf{XV}\}$	Vessel body-fixed navigation frame
$\{\mathbf{XS}\}$	Sensor reference frame (IMU and Gyroscope)
α	Scale factor used in adaptive tuning

β	Scale factor used in adaptive tuning
γ	Grid convergence in the UTM coordinate system
ϕ	Roll angle of a vessel
θ	Pitch angle of a vessel
χ	Direction of V (counted from grid north)
ψ	Vessel heading counted from geographic true north
ψ_G	Vessel heading counted from grid north

Superscripts

$\dot{}$	First order time derivative
$\ddot{}$	Second order time derivative
$\hat{}$	Symbol for state estimated from KF-based algorithms

Chapter 1

Introduction

An overview of the research study is presented in this chapter. It begins with stating the research background and motivation. This is followed by a description of the research questions and objectives. Subsequently, the contributions of this research are listed. The relevant publications are also included and briefly summarized. This chapter concludes with the thesis outline.

1.1 Background and Motivation

In recent years, the pace of global digitalization has accelerated significantly. The technologies driving this shift are central to Industry 4.0, which is expected to revolutionize the production of goods and the nature of work (Schwab, 2017). To adapt to the trend of digitalization, the maritime industries have shown a strong interest and continuously invest in research and development. This includes integrating applications with the latest technologies, such as big data, communication technology, cloud computing, Internet of Things, and Artificial Intelligence (AI) (Razmjooei et al., 2023; Tijan et al., 2021).

Maritime transportation is playing a crucial role in global economic systems, environmental sustainability, and international relations. Studies indicate that between 80% and 90% of world trade is transported by sea (UNCTAD, 2023). The adaptation of Industry 4.0 for the maritime sector, termed Shipping 4.0 (Aiello et al., 2020), proposes the integration of autonomous ships as innovative elements in the maritime ecosystem (Askari and Hossain, 2022). This devel-

opment is expected to drive significant transformations and advancements in maritime transportation.

Development of Autonomous shipping

Fully autonomous technologies that aim to replace the conventional navigation role of human beings in vehicle operations are considered essential components of Industry 4.0. Currently, the development of autonomous cars is advancing at a rapid pace. Industrialized countries are promoting the development of driverless cars and have established relevant autonomous driving regulatory policies (Yoganandhan et al., 2020; Rico Lee-Ting Cho and Ho, 2021; Fagnant and Kockelman, 2015). For maritime transportation, although progress is slower compared to other transport industries, the International Maritime Organization (IMO) has already prioritized autonomous ships on its agenda. The IMO's Maritime Safety Committee (MSC) has completed the regulatory scoping exercise for safety treaties concerning Maritime Autonomous Surface Ships (MASS) (IMO, 2021). The MSC's next step is to develop a MASS code aimed at further navigation regulations towards the MASS (IMO, 2022).

Currently, numerous institutions and commercial companies are devoted to the development of autonomous ship-related technologies. In Norway, where the maritime industry is a significant part of the national economy, the first research project on this front, Maritime Unmanned Navigation through Intelligence in Networks (MUNIN), was initiated in 2012 (MUNIN, 2012). Additionally, the projects launched by DNV GL and YARA Birkeland are particularly notable (DNV-GL, 2018a; Yara, 2020). The prototypes of autonomous ships emerging from these projects are considered great advancements in maritime logistics.

The potential benefits of autonomous ships can have economical, environmental, and social impacts around the world. For fully autonomous ships, energy-efficient vessel design can be introduced, as accommodations and other life-support facilities for humans can be eliminated (Ang et al., 2017). Comparisons between autonomous and conventional ships reveal that the former can reduce energy consumption by up to 74.5% by omitting some life-support systems (Ait Allal et al., 2018). This substantial decrease in energy consumption directly leads to reduced greenhouse gas emissions, supporting the IMO's objectives for decarbonization (IMO, 2023). From a social perspective, the adoption of autonomous shipping can mitigate the effects of declining birth rates on the shipping industry across various countries (Rødseth et al., 2023). In addition, the application of autonomous ship navigation systems can replace human tasks in many dangerous navigation environments, thereby reducing possible casualties. During COVID-19 type pandemic situations, autonomous

transportation can play a crucial role in addressing several challenges posed by the need for social distancing and minimizing human contact (Kapser et al., 2021). These applications suggest a growing role for autonomous shipping in the future.

Currently, fully autonomous ships are unable to operate completely independently due to a range of technical, regulatory, and safety challenges. The shift from conventional manned vessels to fully autonomous ships will not occur instantly but is expected to progress gradually. Various institutions and companies have their own ways of defining the levels of autonomy for autonomous ships. For example, the IMO uses a four-level definition (IMO, 2021), DNV GL employs a five-level definition (DNV-GL, 2018b), and Lloyd's Register has a seven-level definition (Register, 2017). Despite some variations, the definitions generally specify the degree of human and machine involvement in ship control, as well as the roles of human operators and AI in decision-making for various navigational tasks.

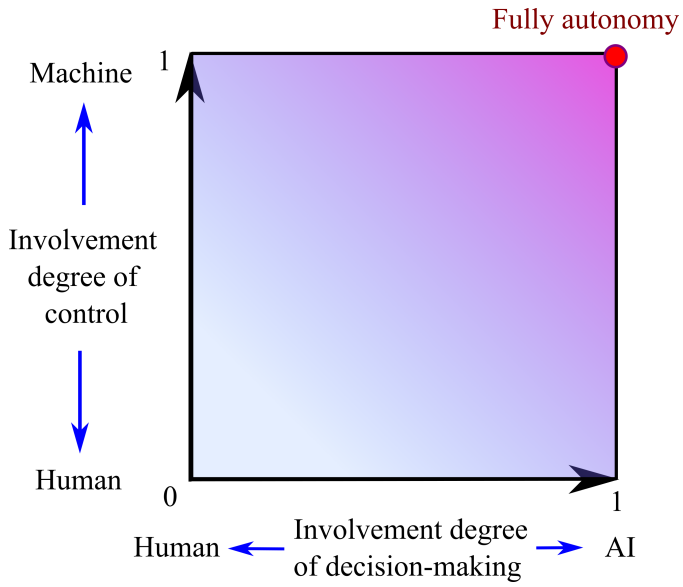

Figure 1.1: Two key factors—the involvement degree of control and the involvement degree of decision-making—are used in describing the progression toward fully autonomous ships.

The summary of control and decision-making involvement levels in the autonomy definitions is illustrated in Fig. 1.1. The level of involvement is measured on a scale from 0 to 1, where 0 represents complete human involvement and 1 signifies full machine or AI involvement. Before achieving the highest level of autonomy, remote-controlled ships can become the general type in which humans and artificial intelligence jointly participate in ship control and decision-making.

The control by machines can be categorized as automation. With advancements in sensor technologies, machine learning, and other related fields, human involvement in control systems is gradually diminishing, as seen in the widespread use of autopilot systems in both aircraft and ships. When discussing autonomous ships, the focus is primarily on the role of AI in decision-making. At present, decision-making on ship navigation still relies heavily on professional training and experience.

Safety of Navigation

Navigational safety is crucial for maritime transportation. Since 2020, the world has repeatedly observed major marine accidents on both severe society and the environment consequences. In July 2020, a bulk carrier ran aground on a coral reef off the coast of Mauritius. The resulting fuel oil spill from the grounding is considered the worst environmental disaster in Mauritius history (JTSB, 2023). In March 2021, the container ship *Ever Given* blocked the Suez Canal for six days. This obstruction significantly slowed trade between Europe, Asia, and the Middle East by disrupting one of the world's busiest maritime routes (PMA, 2021). In March 2024, a container ship collided with a pier of the bridge over the Patapsco River in Baltimore, causing the bridge to collapse and resulting in casualties. The collapse obstructed most shipping routes to and from the port, with the economic impact of this accident estimated at $15 million per day (NTSB, 2024).

The shift toward autonomy in maritime transportation can offer numerous benefits but also introduces critical safety concerns that must be addressed. Because autonomous ships depend heavily on digital technologies, they could be vulnerable to cyberattacks (Kavallieratos et al., 2019; Tusher et al., 2022). Failures in software algorithms, sensor malfunctions, or errors in data interpretation can also result in accidents involving autonomous ships (Rødseth et al., 2021). Furthermore, current maritime regulations are primarily designed for conventional shipping. Although the MASS regulations are currently being developed, an adjustment period may be necessary to ensure that the legal framework for autonomous ships aligns with existing laws and regulations, such as the International Regulations for Preventing Collisions at Sea 1972 (COLREGS) (Hannaford et al., 2022; Rødseth et al., 2023). The trolley dilemma (Foot, 1967) intersects with the development of autonomous ships. This dilemma raises questions about how machines can and should make decisions that traditionally require human moral judgment (Martin Cunneen and Ryan, 2020). It is crucial to resolve these issues promptly to advance the development of autonomous ships.

Collisions at sea are among the most significant safety concerns in maritime

transportation. The European Maritime Safety Agency (EMSA) reported in its 2023 overview of marine casualties and incidents that "collision" accounted for 21.6% of all occurrences involving ships from 2014 to 2022 (EMSA, 2023). With the introduction of autonomous ships with various levels of autonomy, the maritime environment is expected to become more complex due to interactions among different types of ships (Kim et al., 2022). In this complex scenario, it is essential to handle ship encounters with heightened diligence and caution to effectively reduce the risk of collisions. However, complex environments can impair human decision-making by increasing cognitive load (Choi et al., 2014). This heightened cognitive demand can result in poor decision-making due to a reduced capacity to effectively process all relevant information. Therefore, it is essential to develop specific technologies and tools designed to enhance human decision-making and adapt to the complexities of the maritime environment, including harsh weather conditions. These technologies can be supported by AI decision-making systems. By enabling both human navigators and AI-based digital navigators to utilize the same decision-support system, more harmonious interactions among different types of ships can be achieved.

Advanced Ship Predictor

Decision-making is crucial for maritime collision avoidance due to the complex nature of the maritime environment as discussed before. Safe and efficient navigation requires quick, accurate, and informed decisions in some critical situations. This process is systematic and professional, requiring the integration of technologies, human expertise, and adherence to various regulations. To make the correct decisions to avoid collisions, navigators must first ensure that the surrounding navigation information is accurate and up-to-date. They must then filter and utilize the relevant information to evaluate the current situation, focusing on the navigation states of their own ship and other vessels. Additionally, a thorough assessment of potential collision risks should be conducted based on these observations. Finally, certain predictions should be made to determine the possibility of a collision. Navigators need to accurately predict the vessel's trajectory when deciding whether to turn the rudder or slow down. Accurate predictions offer valuable feedback and improve the effectiveness of their decisions.

These three steps are formulated as the three levels of situation awareness (Endsley, 1995b): perception (level 1), comprehension (level 2), and projection (level 3). The authors further argue that to support decision-making, it is situation awareness that needs enhancement, not merely automation (Endsley, 2016). Enhancing automation, such as through the application of autopilot systems, can significantly reduce the physical and mental workload on human operators. This allows human navigators to focus on other critical tasks, such

as monitoring weather conditions, scanning for traffic, or coordinating with control centers. However, excessive reliance on automation can lead to a diminished understanding of ship systems, making operators less effective during emergencies (Vered et al., 2023).

To enhance situation awareness for collision avoidance, current maritime navigation practices have specific requirements. According to International Convention for the Safety of Life at Sea (SOLAS), modern ships must be equipped with various navigation-related equipment. This equipment includes Global Navigation Satellite Systems (GNSSs), Automatic Identification System (AIS) systems, marine radars, Inertial Measurement Units (IMUs), and other related tools. Additionally, marine VHF radios must be properly maintained for effective ship-to-ship and ship-to-shore communication. The aforementioned equipment must function correctly, and the relevant measurement data must be communicated to navigators promptly. Tools such as Electronic Chart Display and Information System (ECDIS) and Automatic Radar Plotting Aid (ARPA) provide navigators with electronic nautical charts that track and continuously update ship positions. These displays, combined with visual observations, enable navigators to better understand their surrounding environment.

However, for trajectory prediction which corresponds to level 3 of situation awareness, even the most advanced devices offer limited support. Most equipment relies on linear extrapolation based on current navigation states of the ships (Perera and Murray, 2019a). Navigators' experience and judgment remain crucial in trajectory prediction. Yet, such predictions can lead to misjudgments in complex marine environments, such as failing to predict potential collision or near-miss points in ship encounter situations. Therefore, ASPs types of supportive systems must be developed to support the highest level of SA for maritime navigation safety in the future. Additionally, for predictions with a relatively short horizon (referred to as local-scale predictions in this thesis), the dimensions of vessels must be carefully considered. The impact of the vessels' under-actuated properties should also be taken into account. This property implies that general sea-going ships have limited maneuverability in the sway direction during normal cruising phases. The limited maneuverability can cause inconsistencies between heading and course-speed vectors when ships are turning. As a result, ships can create swept areas that are larger than their own beam. Any obstacle in this swept path must be factored into collision avoidance.

1.2 Research Questions and Objectives

The main research objective of the Ph.D. project is to develop the local-scale ASP which can enhance level 3 situation awareness in maritime navigation. The process of the local-scale ASP development is divided into two phases: system development and performance evaluation. During the system development phase, the initial task is to ensure the local-scale ASP can accurately generate the required vessel navigation states. Once the states are obtained, the ASP then executes predictions based on these states. In the performance evaluation phase, the utilized methods in the system development will be assessed at two levels. The first level involves the evaluation using simulated maneuvers executed by the University of Tromsø–The Arctic University of Norway (UiT) bridge simulators to make initial improvements. The refined algorithms will then be experimentally evaluated at the second level. Sea-trial experiments will be conducted using the UiT research vessel Ymir RV, which is equipped with an advanced navigation and control platform. The main research objectives can be detailed as follows:

RO1: The implementation of the KF-based algorithms for navigation state estimation and that consists of sub-objectives of:

(i) Identify the kinematic motion models that best describes the ship maneuvering behaviors;
(ii) Apply appropriate KF-based estimation algorithms to estimate the vessel navigation states;

RO2: The development of trajectory prediction considering the ship maneuvering features in the local-scale prediction and that consists of sub-objectives of:

(i) Calculate the location of the PP based on the estimated navigation states;
(ii) Design the trajectory prediction method based on the understanding of the PP;

RO3: The performance evaluation of the methods implemented and that consists of sub-objectives of:

(i) The evaluation through the simulated maneuvering from the UiT bridge simulator;
(ii) The evaluation through the sea-trial experimental maneuvering from the UiT research vessel Ymir RV.

1.3 Research Scope

Enhancing maritime situation awareness is a highly systematic process. The local-scale ASP is designed to specifically contribute to level 3 situation awareness by providing accurate local-scale trajectory predictions to support decision-making for collision avoidance. Currently, the implementation of the local-scale ASP is limited to the own ship, as it directly accesses measured data from its onboard equipment. However, through data communication and sharing, the own ship can also apply the same local-scale predictions to nearby target ships. It is important to note that evaluating collision risk based on these predictions is beyond the scope of this work. Nevertheless, metrics for risk evaluation can be developed by integrating the prediction results.

1.4 Publications

The appended papers included in this thesis are listed below

(**I**) **Wang, Y.**, Perera, L. P. and Batalden, B.-M. (2022). The Comparison of Two Kinematic Motion Models for Autonomous Shipping Maneuvers. *Proceedings of the ASME 2022 41st International Conference on Ocean, Offshore and Arctic Engineering. Volume 5A: Ocean Engineering*. Hamburg, Germany, June 5-12, 2022. V05AT06A031. ASME. https://doi.org/10.1115/omae2022-79583.

(**II**) **Wang, Y.**, Perera, L. P. and Batalden, B.-M. (2023). Kinematic motion models based vessel state estimation to support advanced ship predictors. In *Ocean Engineering*, 286:115503, https://doi.org/10.1016/j.oceaneng.2023.115503

(**III**) **Wang, Y.**, Perera, L. P. and Batalden, B.-M. (2023). Coordinate Conversion and Switching Correction to Reduce Vessel Heading-Related Errors in High-Latitude Navigation. *The 22nd World Congress of the International Federation of Automatic Control (IFAC 2023). 56-2, 11590–11595*. Yokohama, Japan, July 9-14, 2023. https://doi.org/10.1016/j.ifacol.2023.10.477

(**IV**) **Wang, Y.**, Perera, L. P. and Batalden, B.-M. (2024). Adaptive Kalman Filter-Based Estimator with Sea Trail Data to Calculate Ship States in Complex Navigation Conditions. *The 34th International Ocean and Polar Engineering Conference (ISOPE 2024). ISOPE-I-24-536*. Rhodes, Greece, June 9-14, 2024.

(**V**) **Wang, Y.**, Perera, L. P. and Batalden, B.-M. (2024). Localized Advanced Ship Predictor for Maritime Situation Awareness with Ship Close En-

counter. In *Ocean Engineering*, https://doi.org/10.1016/j.oceaneng.2024.117704

(**VI**) **Wang, Y.**, Perera, L. P., and Batalden, B.-M. (2024). Pivot Point Estimation based Advanced Ship Predictor Evaluation with Vessel Maneuvers under Sea Trial Conditions. Submitted in *Ocean Engineering*.

Published Paper but Not Included in thesis

- **Wang, Y.**, Perera, L. P. and Batalden, B.-M. (2021). Particle Filter Based Ship State and Parameter Estimation for Vessel Maneuvers. *The 31st International Ocean and Polar Engineering Conference (ISOPE 2021). ISOPE-I-21-4176*. June 20, 2021.

- Adnan, M., **Wang, Y.**, Perera, L. P. (2024). Role of Onshore Operation Centre and Operator in Remote Controlled Autonomous vessels Operations Accepted in *the Journal of Ocean Technology*. Vol. 19, No. 3, 2024

Brief Summary of Appended Papers

In **Paper I**, two kinematic motion models—the Curvilinear Motion Model (CMM) and Constant Turn Rate & Acceleration Model (CTRA)—are introduced to describe ship maneuvering behaviors. The required ship navigation states are represented in vector form and estimated using KF-based algorithms. The validation of both models and estimation algorithms is carried out through simulated maneuvers using the UiT bridge simulator.

In **Paper II**, these two kinematic motion models are further examined through simulated maneuvers. Enhancements have been made to the acceleration measurements within the models to improve the accuracy of the estimates. Additionally, stability and consistency tests have been performed to validate the application of the KF-based estimation methods.

Paper III addresses projection errors in the Universal Transverse Mercator (UTM) coordinate system, which is used to represent navigation states in high-latitude regions, such as the Tromsø fjord area. This issue is not significant in **Paper I** and **Paper II** because the simulated areas are near the equator, where projection distortion errors are minimal. However, since later sea-trial experiments are conducted in the Tromsø fjord area, the modifications proposed in **Paper III** have been adopted in subsequent papers.

Paper IV utilizes sea-trial experimental data to validate the KF-based estimation with the CMM and CTRA models. A series of sea-trial experiments

were conducted by the UiT research vessel, Ymir RV, in the Tromsø fjord area. Given the complexity of the sea environment, an adaptive tuning mechanism is incorporated into the KF-based algorithms to enhance estimation precision. Additionally, this tuning mechanism has led to modifications in the CMM and CTRA models.

Paper V and **Paper VI** focus on local-scale trajectory prediction while considering the impact of the PP. In **Paper V**, simulated maneuvers are used, leveraging the extensive data from the bridge simulator. The Gated Recurrent Unit (GRU) neural network is employed to process this data. In **Paper VI**, sea-trial maneuvering data from the Ymir RV is utilized. The approaches for local-scale trajectory prediction in **Paper VI** differ from those in **Paper V**, including variations in the kinematic motion models and the calculation methods for the PP. Neural networks are not used in **Paper VI** due to the limited sample size of sea-trial data.

1.5 Thesis Outline

Part I of the thesis covers the methodology and context, consisting of three chapters. Chapter 2 discusses enhancements to maritime situation awareness supported by the developed local-scale ASP. Chapter 3 explores the relevant kinematic motion models and KF-based algorithms. Chapter 4 outlines the calculation approaches for ship PP and the PP-based trajectory prediction algorithm.

The research outcomes are presented in **Part II**. Chapter 5 provides a summary of the appended papers. Chapter 6 discusses the results, while Chapter 7 includes conclusive remarks and future proposals. All the appended papers are presented in **Part III**.

Part I

Methodology and Context

Chapter 2

Maritime Situation Awareness Enhancement

The maritime environment is inherently complex and constantly changing. The introduction of remotely operated and fully autonomous ships can increase navigation complexity interactions among different types of vessels. Consequently, navigators must maintain a high level of situation awareness to make effective conflict avoidance decisions. This chapter explores the critical role of maritime situation awareness and the development of supportive systems to enhance it in the future maritime industry. The first section provides an overview of situation awareness. The second section examines its application in ship navigation. The final section discusses the ASP for improving situation awareness in ship navigation.

2.1 Overview of Situation Awareness

Situation awareness refers to perceiving one's surroundings and understanding the significance of the perceived information in both the present and future. It is essential in human-operated environments that demand a keen sense of safety and efficiency, such as traffic management, critical care, and vehicle operations. The concept of situation awareness originated primarily in aviation psychology and was formally developed and popularized in the 1980s (Endsley, 1988). It was introduced to enhance understanding of pilot performance and decision-making in complex, dynamic environments. This concept has gradually evolved into a substantial theoretical framework and is now applied across

various sectors, including aviation, industrial production, security, networking, and maritime. In recent years, the emergence of autonomous vehicles has driven extensive research into situation awareness to address the navigation challenges posed by these new types of transportation.

2.1.1 Endsley Model for Situation Awareness

With reference to the concept of situation awareness, a three-level model known as the Endsley Model is proposed (Endsley, 1995a). The three levels in this model include the perception of situational elements, understanding of the situation, and prediction of future states. This model has become the most widely adopted framework for situation awareness in numerous research studies.

Figure 2.1 illustrates each level of situation awareness and the influence of both internal and external factors on the decision-making process. Along the information processing chain, the first level involves perceiving different elements within the environment (information input), the second level encompasses a thorough understanding of the current situation (information processing), and the third level involves predicting and planning for future scenarios (information output).

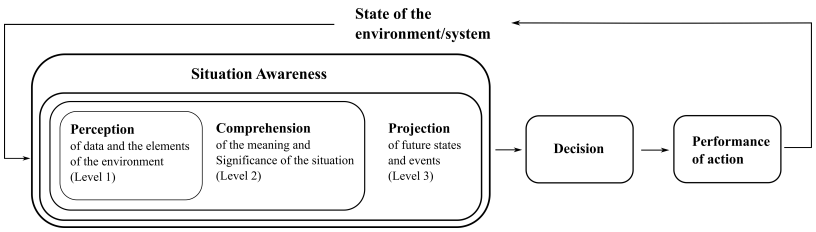

Figure 2.1: Endsley model of situation awareness (Endsley, 1995a)

In Endsley (2015), the authors clarify a common misconception about the three levels of the situation awareness model. The relationship among these levels is progressive rather than strictly linear. The model is emphasized as cyclical and dynamic. As illustrated in Fig. 2.1, it incorporates a dynamic feedback loop that facilitates continuous information collection and response. This adaptability is crucial, as situation awareness must evolve to remain accurate and relevant in a changing environment. Therefore, tools and systems designed to support Level 3 situation awareness must also ensure robust capabilities at the first and second levels. Additionally, effectively updating the relevant information on the situation awareness in complex working environments should be included.

2.1.2 System Design to Support Situation Awareness

The Endsley model for situation awareness emphasizes the significance of tasks and goals, as well as the challenges involved in maintaining situation awareness. It acknowledges that human factors such as workload, fatigue, and data overload can complicate this task (Endsley, 2011). Given the physiological and psychological limitations of humans, as well as cognitive bottlenecks in information processing, achieving and sustaining high levels of situation awareness in complex environments can be difficult. Consequently, in the operation and control of modern complex systems, supportive technologies and systems are often required to assist human operators for various navigation tasks.

Insufficient of Automation

Automation significantly enhances human interaction with complex systems by improving efficiency, reducing errors, and supporting more effective decision-making. For example, autopilot systems are extensively used in both aviation and maritime navigation. Such systems automates some monotonous and routine tasks in vehicle operations allowing pilots and drivers to focus on monitoring system performance and making strategic decisions rather than being tied to constant manual control. When the autopilot is engaged, operators can concentrate on other essential tasks, such as system checks, navigation planning, and communication. This multitasking capability is essential, particularly in complex navigation environments.

However, relying exclusively on automation to support situation awareness can introduce new challenges and increase the risk of erroneous decisions (Endsley, 2011). Instead, the authors suggest that support systems should prioritize situation awareness, especially in environments where human oversight is crucial and decisions have significant consequences. With the advent of autonomous ships, the maritime environment is likely to become such a setting—one that is too complex to be fully managed by automation-support systems alone. Furthermore, human intervention remains critical in unusual or unforeseen circumstances, even though automation can handle some routine tasks (Haight and Kecojevic, 2005; Veitch and Andreas Alsos, 2022). Decision support systems designed with a focus on situation awareness could ensure that operators are thoroughly informed and adequately prepared to intervene and make critical decisions.

Compatibility with AI

In rapidly changing and highly dynamic work environments, situation awareness must continuously evolve to remain accurate and up-to-date. Systems designed to support situation awareness can provide operators with constant

updates, which are crucial for human learning and continuous improvement in operational performance. It is important to note that these update mechanisms are also beneficial for training AI, which is considered the digital navigators for operating autonomous ships (Thombre et al., 2022). Compared to traditional methods, AI has demonstrated remarkable superiority in learning capabilities in some applications, including driverless vehicles. Its ability to rapidly process and analyze vast amounts of data allows AI to identify patterns and insights that might be imperceptible to humans.

In the development of autonomy within the transportation industry, human supervision is expected to remain necessary until fully autonomous driving is achieved. Therefore, systems that can support both humans and AI offer significant economic and practical benefits. These types of systems not only integrate human expertise with AI but also ensure that both entities evolve together. Hybrid intelligence, which evolves from the interaction between human intelligence and AI, is expected to be a major research topic in the future (Jarrahi et al., 2022).

2.2 Situation Awareness in Ship Navigation

Situation awareness is crucial for the safety of ship navigation. In a complex maritime environment, navigators must continuously monitor various factors, including weather conditions, nearby vessels, navigational hazards, and the performance of the own vessel. Constant vigilance is essential for maintaining effective maritime situation awareness in such situations.

Avoiding collisions during ship navigation is a systematic task that requires rigorous education, training, and experience. Navigators must undergo comprehensive and detailed training programs to effectively interpret and respond to various navigational challenges and potential dangers. In a typical scenario where two ships encounter each other in open waters and are visible to each other, the collision avoidance process is summarized in Fig. 2.2.

Ship navigators must continuously verify the presence of approaching ships through visual observations with the use of radar and other equipment. Once a target is detected, the navigator should gather data on the target ship movements and analyze the respective information. A decision is then made based on this comprehensive analysis.

If it is determined that both the own and target ships can pass safely, no action is required. However, if a risk of collision is identified, collision avoidance actions must be promptly implemented. The COLREGS provides specific rules

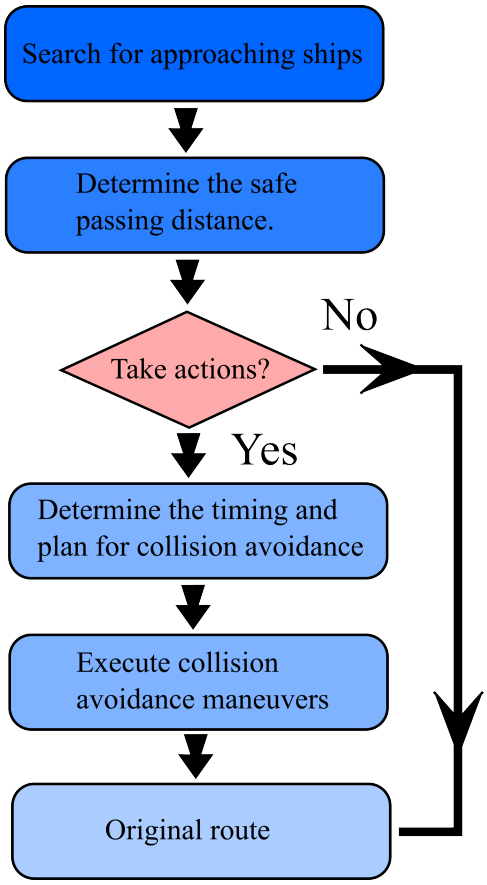

Figure 2.2: Ship collision avoidance process

for collision avoidance between two ships. In general, collision avoidance plans should be adhere to these regulations. If the own ship is identified as the give-way vessel according to the COLREGS, it must execute the necessary maneuvers to comply with the give-way requirements until it safely returns to its original course. Once this process is successfully completed, the collision avoidance process is considered finished.

In the collision avoidance process depicted in Fig. 2.2, searching for approaching ships, understanding the safe passing distance, and determining the timing and plan for collision avoidance correspond to the situation awareness. Modern technologies have significantly improved situation awareness for collision avoidance in ship navigation. A variety of onboard equipment, such as GNSS, IMU, AIS, and radar systems, provides navigators with essential information about both their own and target ships. Additionally, this measured data is usually managed and displayed by systems such as ARPA and ECDIS. These systems are typically mounted on the bridge to provide the navigators with convenient

platforms for a comprehensive understanding of their surroundings.

2.2.1 Decision-making in Collision Avoidance

Decision-making in maritime collision avoidance is a critical process that requires careful evaluation of multiple factors to ensure safety at sea. Navigators must synthesize data from various onboard systems, account for environmental conditions, and apply their expertise to make well-informed decisions. The complexity of this process underscores the critical role of maritime situation awareness, where real-time information and predictive tools work together to guide effective and timely actions. This integration is essential for preventing accidents and ensuring safe navigation, specially in varying ocean environments with wind, wave, and tides.

COLREGS

The COLREGS provide standardized navigational practices and procedures that all navigators must adhere to. This legal framework ensures that the collision avoidance actions taken by ocean going vessels are predictable and consistent. For example, the same regulations specify the responsibilities of both parties to avoid collisions in common encounter scenarios, such as overtaking (Rule 13), head-on (Rule 14), crossing (Rule 15), and stand-on (Rule 17), By clearly defining the required actions for each situation, the COLREGS facilitate informed decision-making and enhance the safe navigation of vessels.

However, the current version of COLREGS also has certain limitations. Firstly, although the risk of collision is mentioned in many encounter scenarios, the COLREGS do not provide a clear definition or quantification of collision risk (García Maza and Argüelles, 2022). Although it is common practice to use Distance to Closest Point of Approach (DCPA) and Time to Closest Point of Approach (TCPA) as metrics for assessing this risk, the specific values used are still subject to individual judgment (Huang and van Gelder, 2020).

Secondly, the responsibilities and other provisions outlined in the COLREGS are specifically designed for situations where two ships encounter each other. However, applying these rules can be problematic in highly congested areas. Furthermore, as larger ships are increasingly deployed, their restricted maneuverability can pose challenges to full compliance with these regulations.

Finally, with autonomous ship navigation, there have been numerous calls to amend the current COLREGS established in 1972. For instance, the COLREGS have established specific guidelines for situations when ships are not visible to each other, known as the "Rules of Conduct for Vessels in Restricted Visibility"

(Rule 19). Consequently, there are two distinct sets of rules based on whether or not ships have visual contact with one another. This distinction arose because, due to the technological limitations of the time, obtaining timely information about other ships was often possible only through direct visual observation. However, modern onboard ship systems cannot only provide the position and speed of nearby vessels under limited visibility, but also identify the type of these approaching vessels. The widespread adoption of advanced AI technologies can simplify the current approach of applying different sets of rules based on visibility (Maritime and Coastguard Agency, 2024). The emergence of cutting-edge technologies, especially autonomous ships, could further drive the maritime industry to re-evaluate the COLREGS in the future. Numerous research studies indicate that traditional collision avoidance rules formulated by the COLREGS may pose challenges for the tactics employed by AI-driven autonomous ships (Perera, 2019; Zhou et al., 2019; Hu et al., 2022).

Proactive Approach for Collision Avoidance

Proactive collision avoidance encompasses the strategies and actions implemented to prevent near-encounter situations before the collision risk arises. This approach emphasizes anticipating potential collision risks and taking proactive measures well in advance, rather than simply reacting to situations as they arise. This collision avoidance strategy is also supported by the COLREGS, as Rule 8(i) states: "Any action taken to avoid collision shall be taken in accordance with the Rules of this Part and shall, if the circumstances of the case permit, be positive, made in ample time, and with due regard to the observance of good seamanship."

Maintaining the highest level of situation awareness is crucial for implementing proactive collision avoidance. Accurate and reliable predictions of nearby vessels enable navigators to detect potential collision risks in advance, providing them with more time to respond to any emerging threats. Effectively maintaining the highest level of situation awareness relies heavily on modern equipment, supplemented by the crew's experience. However, it is important to note that current shipboard equipment may not be fully adequate to support level 3 situation awareness (Perera and Murray, 2019b; Murray, 2021). Additionally, it remains uncertain whether the crew's experience will be sufficient to navigate the increasingly complex maritime environment in the future.

2.2.2 Insufficient Support

The ability to maintain level 3 situation awareness is critical for maritime safety. However, the reality is that the systems and equipment commonly used on the bridge today have limited support for achieving this level of awareness.

Inadequate Motion Model

The widely used indicators for assessing collision risk are the DCPA and TCPA. However, these metrics assume that both vessels will maintain their current courses and speeds until the closest point of approach. In other words, the calculation of DCPA and TCPA relies on linear motion models of vessel maneuvering. Relying exclusively on a linear motion model to predict ship trajectories may be potentially dangerous, as vessels can follow curvilinear paths influenced by navigational adjustments or various sea conditions. Consequently, using a model that assumes linear motion may fail to accurately predict future ship positions and orientations (heading), as illustrated in Fig. 2.3.

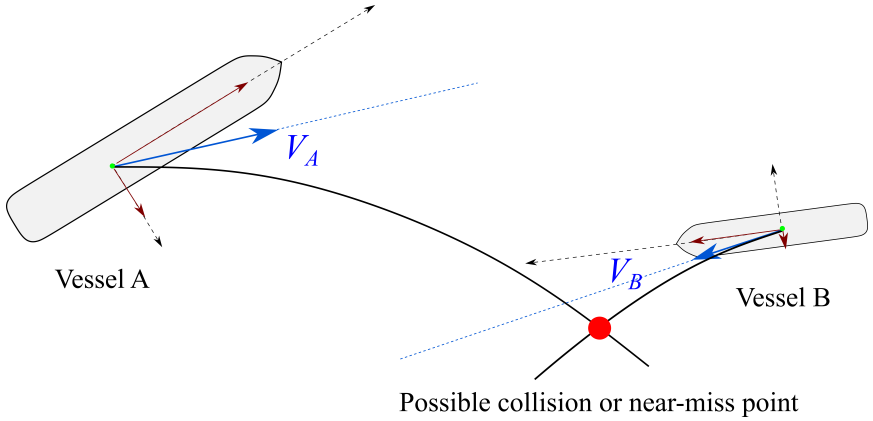

Figure 2.3: The overlook of the potential risk of a collision or near-miss by linear motion prediction.

Additionally, DCPA and TCPA do not account for the differences in vessel types and sizes, which can pose significant challenges in making accurate local-scale predictions. This oversight is particularly problematic during short prediction horizons, where a precise and detailed understanding of ship maneuvering behavior is crucial. For example, a large tanker and a small fishing boat might have identical DCPA and TCPA in a given scenario, yet their ability to respond to close encounters will vary significantly due to differences in size, heading, and maneuverability. Therefore, more suitable models capable of making curvilinear predictions should be developed and integrated with the decision support systems on situation awareness.

Ship Underactuation

Underactuated systems are defined as systems that have more degrees of freedom than available actuators. Such systems may not be directly controlled in all motion dimensions due to lack of comprehensive control inputs (Dixon et al., 2003). This characteristic necessitates the use of more sophisticated

control strategies and actuators, as the control inputs do not directly correspond to all of the system's movements.

Generally, seagoing vessels are equipped with a limited number of actuators, typically the rudder and propeller systems. When the ship's motion is simplified to three degrees of freedom—surge, sway, and heading—these actuators are primarily responsible for controlling the vessel's heading and surge. There is no dedicated actuator for controlling sway during normal cruising. While some modern ships are equipped with azimuth thrusters or bow thrusters, these are primarily designed to enhance maneuverability during docking, undocking, and navigating through narrow passages.

The underactuation nature of vessels further complicates collision avoidance maneuvers. Limited control options due to underactuated vessels can pose significant problems in emergency situations where avoiding a collision might require intricate maneuvers. Meanwhile, the inherent limitations in control or vessel speed lead to slower response times to navigational commands, and this delay can be critical when timing is essential. This emphasizes the importance of maintaining the highest level of situation awareness once again. Accurate predictions enable the early identification of potential collision courses, thereby providing more time to implement necessary corrective collision avoidance actions.

Impact of Pivot Point

As depicted in Fig. 2.3, the ship's heading and course speed do not always align during ship maneuvers. This discrepancy becomes especially evident during turning and circular maneuvers that require rudder adjustments. Specifically, when a ship turns its rudder while moving forward, the bow moves inward while the stern swings outward, as shown in Fig. 2.4.

The location of the PP is critical for local-scale predictions. As illustrated in Fig. 2.4a and Fig. 2.4b, the ship exhibits different behaviors, i.e., different heading, depending on the PP's location. When the PP is closer to the bow, it results in a larger area being swept during circular motion. For navigational safety, it is essential to account for all obstacles within this swept area. These obstacles pose potential collision risks to both the port and starboard sides of the ship. Such collisions could increase the risk of capsizing. Consequently, in scenarios such as local-scale predictions with short prediction horizons, the impact of the PP should be carefully evaluated.

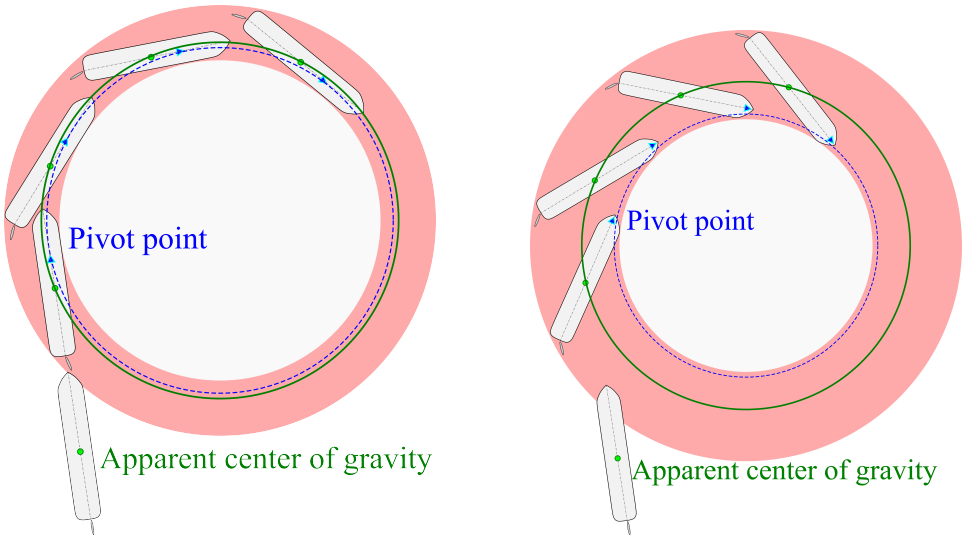

(a) (b)

Figure 2.4: Vessel turning with different location of the pivot point.

2.3 Advanced Ship Predictor

ASPs type techniques are proposed in this thesis to offer significant support for situation awareness in ship navigation within mixed environments where remote-controlled, autonomous, and manned vessels interact. These techniques are essential for improving the accuracy of collision risk assessments by predicting ships' trajectories, thus allowing for timely and effective collision avoidance maneuvers. Various maritime datasets can be effectively integrated using ASPs type techniques. The ASP outlined in (Perera and Murray, 2019b) leverages onboard sensors and AIS data to predict the future positions and orientations of vessels on both local and global scales. This predictive capability facilitates the early detection of potential collision situations, significantly extending the time available for corrective actions.

ASPs can also be incorporated into collision risk assessments to quantify collision risks using predicted ship maneuvers. This ensures that the predictive capabilities of ASPs directly contribute to more precise and dynamic risk assessments. Additionally, the prediction results can be synchronized with existing systems, such as ECDIS and ARPA, to enhance decision support. By predicting potential close encounter scenarios and evaluating collision risks, ASPs could assist navigators in ensuring that navigation actions comply with the COLREGS. Adherence to these regulations is essential for maintaining legal and safe navigation practices. Furthermore, ASPs provide crucial support for both human and AI navigators. This dual support is critical in ocean environments where human supervision is needed.

2.3.1 Predictions in Local-Scale

When making predictions, it is essential to differentiate between global-scale and local-scale predictions due to the different factors that influence ship maneuvers. Global-scale predictions focus on longer-term outcomes with relatively large prediction horizons (Murray, 2021). Details such as the size of vessels or specific maneuvering characteristics can be omitted in this type of prediction, as these factors are less critical over long prediction horizons. In contrast, local-scale predictions, with their shorter horizons, require careful consideration of detailed factors like ship size and maneuvering characteristics. This distinction is crucial for accurately assessing and responding to navigational challenges at the local scales.

Given the distinct requirements of each prediction scale, it is crucial to select data sources that align with the necessary specificity and context. AIS navigation data is highly suitable for global predictions due to its extensive historical volume, which supports big data analysis methods such as machine learning algorithms. However, using AIS data for local-scale predictions involves specific challenges that require careful consideration. One challenge is that AIS transmit navigational data at varying frequencies depending on the ship's status and maneuvering conditions. For example, a vessel moving at a lower speed transmits data less frequently than one traveling at a higher speed (Artikis and Zissis, 2021). This variability can result in data gaps, complicating the maintenance of a continuous and accurate prediction of a ship's trajectory. Additionally, AIS data can exhibit anomalies (Wolsing et al., 2022), such as inaccuracies in reported position, speed, or heading, which further challenge the reliability of AIS data for precise local-scale predictions.

In this thesis, measurements from various onboard equipment are utilized for the local-scale prediction. Since these measurements often contain errors, KF-based algorithms will be employed to generate the required ship navigation states. These estimated states will then be used to calculate the PP and to further support trajectory prediction.

Chapter 3

Vessel Navigation State Estimation

This chapter and the next will explore the methods used to develop the local-scale ASP. In this chapter, the focus is on methods for vessel navigation state estimation, with particular emphasis on kinematic motion models associated with KF-based algorithms.

3.1 Kinematic Motion Models

In mechanics, kinematics studies the motion of objects without considering the forces and moments causing that motion, while dynamics examines how external forces and moments influence it. Both kinematic and dynamic motion models can describe ship maneuvering behaviors. However, using dynamic motion models in applications based on KF-based algorithms can be challenging. For ship maneuvering, dynamic motion models involve parameters such as nonlinear hydrodynamic forces and moments. These parameters are difficult to measure directly with onboard sensors. The lack of these measurements can cause instability and divergence in KF-based applications. To mitigate this issue, this thesis employs kinematic motion models to represent vessel maneuvering behaviors.

3.1.1 Reference Frames for Navigation State Representation

Accurate representation of a vessel's state, i.e., its position, velocity, and orientation relative to its surroundings, requires a clear and consistent frame of reference. In maritime navigation, the local tangent plane is commonly used as the inertial frame, also referred to as the navigation reference frame. These reference systems are based on a tangent plane defined by the local vertical direction and the Earth's axis of rotation.

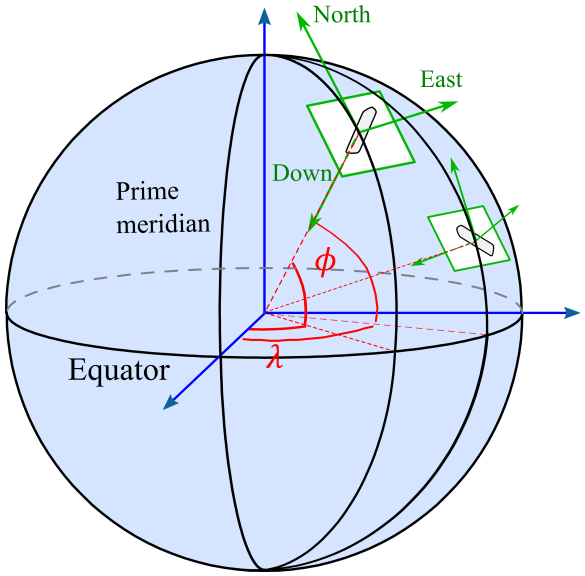

Figure 3.1: The NED local tangent plane coordinate.

The Local North-East-Down (NED) coordinate frame is a specific type of local tangent plane coordinate system (see Fig. 3.1). In this system, the north axis points toward geographic north and the east axis points toward geographic east. The down axis is the direction perpendicular to the oblate spheroid used to model Earth's ellipsoid and points downward. Utilizing the NED coordinate system in maritime navigation offers significant advantages, particularly due to its alignment with traditional navigation practices and its simplification of understanding heading, position, and depth. However, when managing multiple ship maneuvering, it is important to closely monitor the NED coordinate values. This is especially true for the north and east components, which require careful monitoring to ensure accuracy and avoid potential errors.

3.1.2 The UTM Coordinate System

The UTM coordinate system is widely used in mapping, surveying, and positioning applications, known for its optimal balance between local accuracy and global coverage. By utilizing the transverse Mercator projection, the Earth's curved surface can be represented on a flat map with minimal loss of precision. In local-scale predictions, the designated sea area is often approximated as a flat plane. Vertical movements perpendicular to the horizontal plane are typically ignored during various maneuvers. Therefore, the UTM coordinate system offers an effective platform for local-scale predictions, allowing clear illustration of the results. Furthermore, this coordinate system uses meters as its standard unit of measurement. Units of length, such as meters, are universally recognized and offer a practical way to measure distances, making them more intuitive and actionable than degrees of latitude and longitude.

Characteristics of the UTM Coordinate System

The UTM coordinate system is a global spatial referencing framework that divides the world into 60 longitudinal zones, each spanning six degrees of longitude (see Fig. 3.2). These zones are mapped using the transverse Mercator projection, with coordinates expressed as "northing" and "easting" values in meters. In the Northern Hemisphere, northing values start at 0 at the equator and increase northward. In the Southern Hemisphere, a false northing value of 10,000,000 meters is used to prevent negative values. Easting values represent the horizontal position within each zone. To avoid negative coordinates, a false easting of 500,000 meters is assigned to the central meridian of each zone. Each UTM zone is further divided into latitude bands, labeled with letters ranging from 'C' to 'X'. These bands each cover 8 degrees of latitude. These latitude bands help further define a location within a UTM zone and provide a more precise spatial reference.

Each of the 60 UTM zones has a reference central meridian located at its center. This meridian bisects the zone and serves as the baseline for measuring easting values. Centering the transverse Mercator projection on this meridian allows the UTM system to effectively minimize distortions that occur when projecting a three-dimensional surface onto a two-dimensional plane. This approach, which uses a fixed reference meridian for each zone, ensures consistent data interpretation and integration across various regions and mapping systems. For local-scale predictions, it is generally assumed that multiple vessels are within the same UTM zone and latitude band.

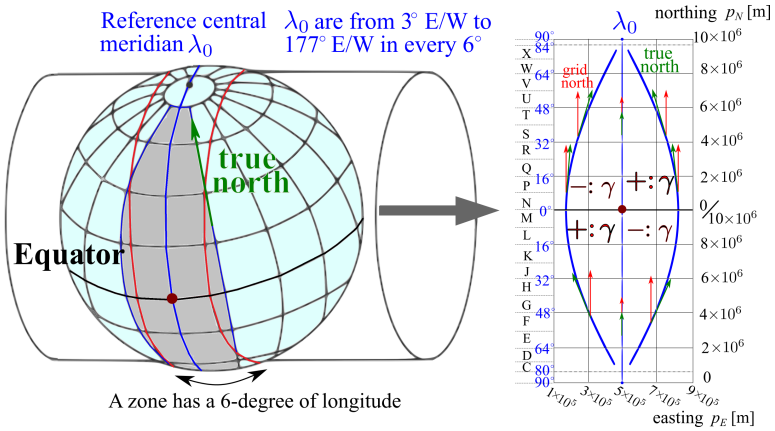

Figure 3.2: The schema of the UTM projection and coordinate system. There are 60 divided zones in total. (Figure from Paper III)

Projection Distortion Errors of UTM

Projecting the Earth's curved surface onto a flat plane inevitably introduces projection errors due to the geometric differences between a spherical surface and a two-dimensional plane. These errors cause distortions in distance, direction, scale, and area, with the extent varying depending on the projection method used. The UTM coordinate system is designed to minimize these distortions within each zone. However, to ensure reliable predictions, it is important to address the impact of residual projection distortion errors.

UTM Scale Factor

The UTM scale factor corrects distortions that occur when projecting the Earth's surface onto the UTM grid. In each UTM zone, the scale factor is set to 0.9996 along the central meridian to minimize distortion across the zone (see Fig. 3.3). This means that the map distance along the central meridian is 0.04% smaller than the true ground distance. The scale factor varies as one moves away from the central meridian due to the cylindrical nature of the UTM projection.

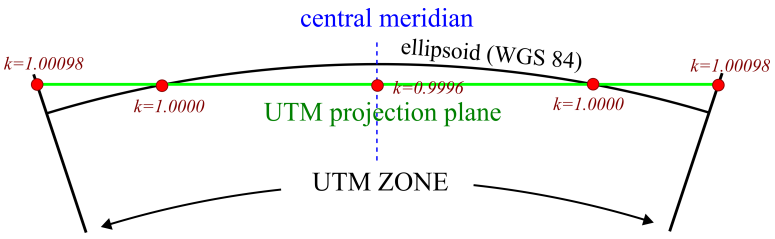

Figure 3.3: Variation in the scale factor (k) across the cross-section of a UTM grid zone.

The UTM scale factor reaches its maximum at the edges of each UTM zone and increases with latitude. This factor is essential for converting map measurements into actual ground distances. However, in maritime navigation, where vessels generally travel at low speeds and predictions are made over short durations, the impact of projection distortion errors is minimal. Consequently, while these errors can be calculated using relevant formulas, they are considered negligible for the purposes of this thesis.

Grid Convergence

Grid convergence in the UTM coordinate system refers to the angle between true north (toward the geographic North Pole) and grid north (indicated by the north-south lines on the UTM grid) (Fig. 3.4). This phenomenon results from the transverse Mercator projection. While each zone is aligned with its central meridian, the longitudinal lines on the globe converge toward the poles but appear as curved lines converging toward the central meridian on the map. This curvature causes the grid lines to deviate from true north. Understanding grid convergence is crucial for applications that use the UTM coordinate system. Its effects become more pronounced in polar and near-polar regions, where meridians converge more sharply toward the poles.

Special attention is needed to measure vessel headings that does not align with grid north in the UTM coordinate system. For example, magnetic compasses measure headings relative to the magnetic north pole, while fiber-optic gyroscopes are calibrated to geographic north. These discrepancies must be accounted for in navigation applications using the UTM coordinates. The Tromsø fjord area, where the sea trial experiments are conducted, is situated at a high latitude of 69 degrees north and falls within the UTM zone 33W. The maximum grid convergence angle in this region can exceed 3 degrees. Therefore, adjustments for grid convergence must be considered.

Calculation of the UTM Coordinates

Latitude and longitude are the primary global positioning metrics obtained directly from GNSS systems. The UTM coordinate system discussed in this thesis is calculated based on these measured latitude and longitude values. The latitude and longitude data sets used in this research are based on the current version of the World Geodetic System (WGS 84). This version defines the Earth's size and shape using a mathematical model that approximates it as an oblate spheroid with flattened poles and a bulging equator. Several parameters of the WGS 84 system are detailed in Tab. 3.1.

The parameters a and $1/f$ are used in the calculation. Given a set of measured

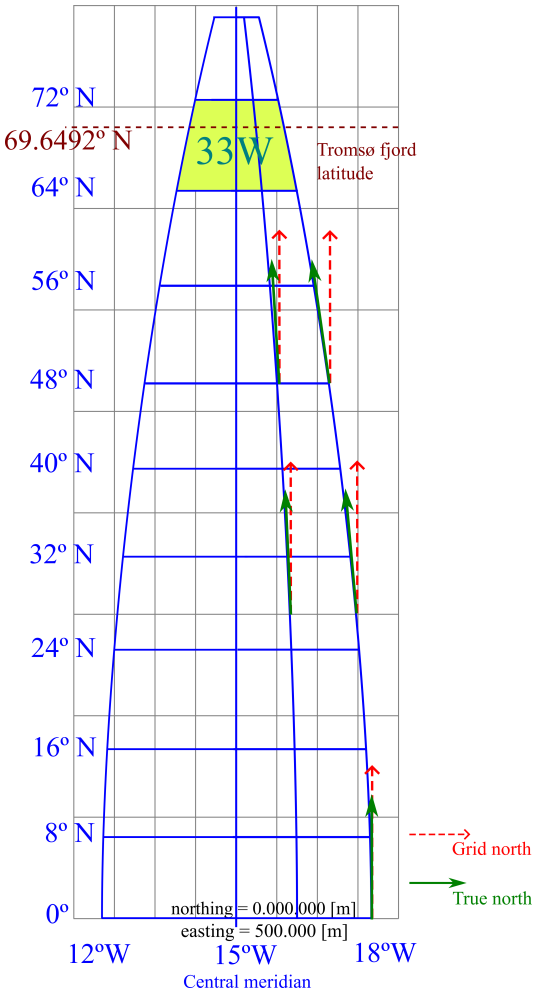

Figure 3.4: The grid convergence in the UTM coordinate system with the central meridian $15°W$

latitude and longitude (ϕ, λ), the corresponding northing and easting (p_N, p_E) are calculated as the formulas shown below (Kawase, 2013).

1) Calculate preliminary constant parameters based on a and $1/f$:

$$n = \frac{f}{2-f} \; ; \; A = \frac{a}{1+n}\left(1 + \frac{n^2}{4} + \frac{n^4}{64} + \ldots\right) \tag{3.1}$$

$$\alpha_1 = \frac{1}{2} - \frac{2}{3}n^2 + \frac{5}{16}n^3 \; ; \; \alpha_2 = \frac{13}{48}n^2 - \frac{3}{5}n^3 \; ; \; \alpha_3 = \frac{61}{240}n^3 \tag{3.2}$$

Parameter	Notation	Value
semi-major axis	a	6378137.0 $[m]$
inverse flattening	$1/f$	298.257223563
geocentric gravitational constant	GM	3.986005×10^{14} $\left[\mathrm{m}^3/\mathrm{s}^2\right]$
angular velocity of the Earth	ω	7.292115×10^{-5} $\left[\mathrm{s}^{-1}\right]$

Table 3.1: Parameters defined in WGS 84

2) Calculate northing and easting (p_N, p_E)

$$p_N = N_0 + k_0 A(\xi^{'} + \sum_{j=1}^{3} \alpha_j \, sin(2j\xi^{'}) \, cosh(2j\eta^{'})) \tag{3.3}$$

$$p_E = E_0 + k_0 A(\eta^{'} + \sum_{j=1}^{3} \alpha_j \, cos(2j\xi^{'}) \, sinh(2j\eta^{'})) \tag{3.4}$$

3) Calculate grid convergence γ and local point scale k

$$\gamma = tan^{-1}\left(\frac{\tau\sqrt{1+t^2} + \sigma \, t \, tan\,(\lambda - \lambda_0)}{\sigma\sqrt{1+t^2} - \tau \, t \, tan\,(\lambda - \lambda_0)}\right) \tag{3.5}$$

$$k = \frac{k_0 A}{a}\sqrt{\left(1 + \left(\frac{1-n}{1+n} tan\phi\right)^2\right)\frac{\sigma^2 + \tau^2}{t^2 + cos^2\,(\lambda - \lambda_0)}} \tag{3.6}$$

where:

$N_0 = 0$ in northern hemisphere ; $N_0 = 10,000[km]$ in southern hemisphere

$$E_0 = 500[km] \; ; \; k_0 = 0.9996$$

λ_0 : central meridian (15° in Tromsø area)

$$t = sinh\left(tanh^{-1}\,(sin\phi) - \frac{2\sqrt{n}}{1+n} tanh^{-1}\left(\frac{2\sqrt{n}}{1+n} sin\phi\right)\right)$$

$$\xi^{'} = tan^{-1}\left(\frac{t}{cos(\lambda - \lambda_0)}\right); \eta^{'} = tanh^{-1}\left(\frac{sin\,(\lambda - \lambda_0)}{\sqrt{1+t^2}}\right)$$

$$\sigma = 1 + \sum_{j=1}^{3} 2j\alpha_j \, cos\left(2j\xi^{'}\right) cosh\left(2j\eta^{'}\right)$$

$$\tau = \sum_{j=1}^{3} 2j\alpha_j \, sin\left(2j\xi^{'}\right) sinh\left(2j\eta^{'}\right)$$

In this thesis, the vessel's heading in the mathematical models is measured relative to grid north and is denoted as ψ_G. The relationship between ψ_G and the heading measured from true north ψ is expressed as:

$$\psi = \psi_G + \gamma \tag{3.7}$$

3.1.3 Mathematical Models for Ship Maneuvering

The mathematical models used for vessel maneuvering are based on kinematic motion models, as discussed previously. The vessel is considered as a rigid body. The rigid body motions can be decomposed into translational and rotational components. Translational motion refers to the movement in which all points of a body move uniformly in the same direction. The relative positions of different points on the object remain unchanged, meaning the body maintains the same orientation throughout its motion. In translational motion, all points on the object share the same motion properties, such as velocity and acceleration. To simplify the mathematical modeling, a single representative point—typically the rigid body's Center of Gravity (CG)—is commonly chosen. For waterborne vessels, the added mass effect is significant and generally cannot be ignored. In this thesis, the combination of the vessel's own mass and the added mass is referred to as the apparent mass. The center of this apparent mass, represented by the vessel's Apparent Center of Gravity (ACG), is chosen as the reference point for the mathematical representation of its translational motion. For rotational motion, the primary focus is on heading, though pitch and roll can also impact the vessel. The details of these mathematical models are discussed below.

Curvilinear Motion Model

The CMM offers a more comprehensive approach to modeling ship maneuvers in the horizontal plane compared to the linear motion model. The ship's navigation states within this model are illustrated in Fig. 3.5. The vertical and horizontal axes in Fig. 3.5 represent northing and easting in the UTM coordinate system. The ship is considered a rigid body within the horizontal plane. Consequently, the vessel's maneuvering involves three DOF: surge, sway, and heading.

The states V (with components v_N and v_E), a_t, and a_n denote the course-speed vector, tangential acceleration, and normal acceleration at the vessel ACG, respectively. These states are related by the following equation:

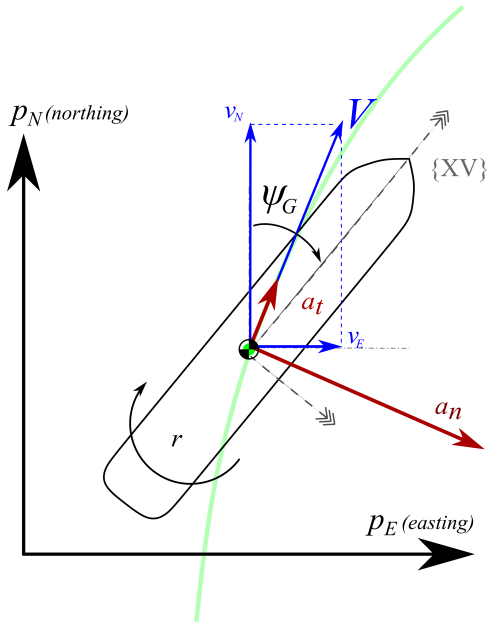

Figure 3.5: Vessel states used in the CMM. (Figure from Paper I)

$$\dot{p_N} = V cos(\chi) = v_N \tag{3.8}$$

$$\dot{p_E} = V sin(\chi) = v_E \tag{3.9}$$

$$\ddot{p_N} = a_t \, cos(\chi) - a_n \, sin(\chi) \tag{3.10}$$

$$\ddot{p_E} = a_t \, sin(\chi) + a_n \, cos(\chi) \tag{3.11}$$

$$\dot{\psi}_G = r \tag{3.12}$$

where:

$$a_t = Const; \;\; a_n = Const; \;\; r = Const; \tag{3.13}$$

In Eqs. 3.8 to 3.11, the angle χ represents the direction of the course-speed vector V, while ψ_G denotes the vessel's grid heading. These two angles generally differ during circular or turning maneuvers.

The CMM provides the flexibility in modeling various types of motion. While the equations accommodate general curvilinear motion, the values of a_t and a_n enable the model to be simplified to either linear or circular motion. When a_n is zero, the model represents linear motion, and when a_t is zero, it represents circular motion.

Constant Turn Rate & Acceleration Model

The CTRA is formulated using the vessel's body-fixed reference frame, denoted as {**XV**}. While the position is expressed in the UTM coordinate system, the velocity and acceleration are represented within the {**XV**} frame. The navigation states used in the CTRA model are illustrated in Fig. 3.6.

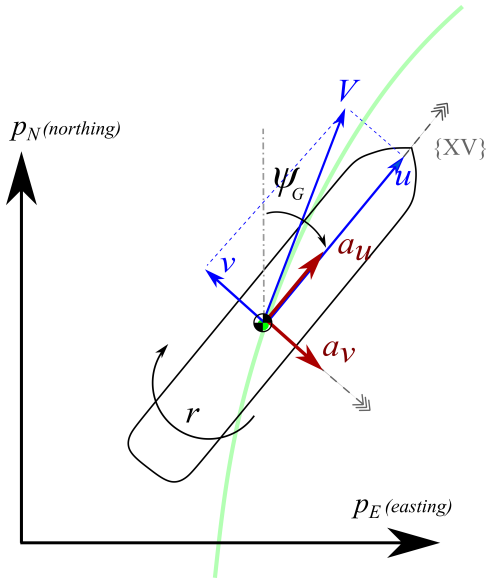

Figure 3.6: Vessel states used in the CTRA. (Figure from Paper I)

The origin of {**XV**} is assumed to be located at the vessel ACG. The navigation states shown conform to the following relationship:

$$\dot{p_N} = u\ cos(\psi_G) - v\ sin(\psi_G) \tag{3.14}$$

$$\dot{p_E} = u\ sin(\psi_G) + v\ cos(\psi_G) \tag{3.15}$$

$$\dot{u} = a_u \quad \text{(acceleration with respect to \{XV\});} \tag{3.16}$$

$$\dot{v} = a_v \quad \text{(acceleration with respect to \{XV\});} \tag{3.17}$$

$$\dot{\psi_G} = r \tag{3.18}$$

where:

$$a_u = Const;\ a_v = Const;\ r = Const; \tag{3.19}$$

It should be noted that u and v are defined in {**XV**}. The time derivatives of these components should account not only for translational accelerations but also for additional terms arising from the rotational motion of {**XV**}. However, in Eq. 3.16 and 3.17, the time derivatives of u and v are assumed to represent only the translational accelerations.

Model in Three-dimensional Space

The two models described above are defined on a two-dimensional plane and are primarily used when surge, sway, and heading are sufficient to simulate vessel maneuvering. Vessel heave motions generally have a minor impact on overall maneuvers compared to surge and sway moments Additionally, under calm weather conditions, the vessel's roll and pitch have minimal effects, particularly for large-tonnage vessels.

However, the Ymir RV used in the sea trials is relatively small and has a low weight. It exhibited sensitive seakeeping characteristics in the respective sea trials. Furthermore, the sea conditions in Tromsø Fjord where the sea trials were executed are highly complex. Located in a relatively enclosed marine environment, the fjord is dominated by strong and intricate ocean currents (Fig. 3.7). The velocity distribution of these currents adds to the complexity. The confined nature of the fjord also causes Kelvin waves generated by passing ships to dissipate more slowly.

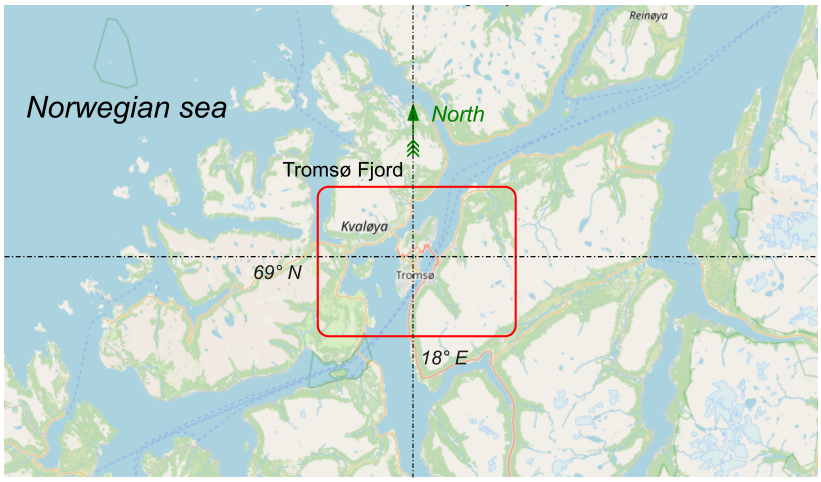

Figure 3.7: The area map around Tromsø Fjord. (The map is from the OpenStreetMap)

For a small vessel operating in these complex sea conditions, modeling the vessel maneuvering behaviors in a two-dimensional plane is insufficient. The vessel maneuvers of the Ymir RV involve significant roll and pitch motions. These attitude angles can substantially impact onbroad sensor data, particularly from the IMU. Therefore, a three-dimensional model is considered more appropriate for this situation.

Figure 3.8 illustrates the reference frames used in a three-dimensional space. The frame $\{\mathbf{N}\}$ is the local navigation frame, where the plane is defined by the N and E axes correspond to the UTM projected plane. A downward vertical

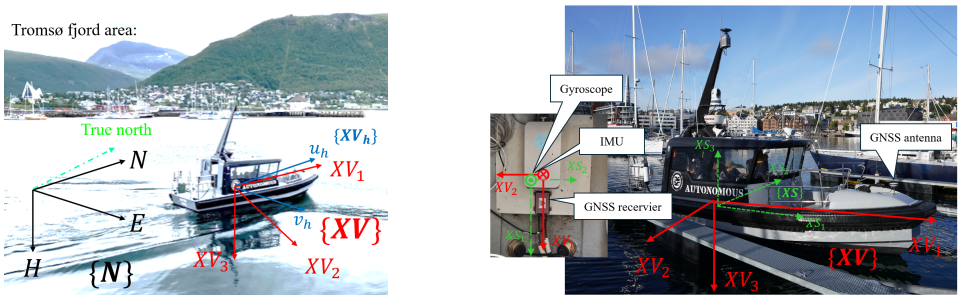

(a) **(b)**

Figure 3.8: Utilized reference frames in the Ymir RV. (Figure from Paper VI)

axis H is added to {**N**}. The origin of the vertical axis H is at the surface of the WGS 84 reference ellipsoid. The frame {**XV**} is the vessel body-fixed reference frame. An additional axis XV_3 is introduced in {**XV**}. The vessel's attitude is determined by the transformation between the {**N**} and {**XV**}, which includes the heading, pitch, and roll (ψ_G, θ, ϕ).

Given a random vector (x_1, x_2, x_3) represented in {**XV**}, the related component in {**N**}—$(x_1^{'}, x_2^{'}, x_3^{'})$ can be thus represented as:

$$\begin{bmatrix} x_1^{'} \\ x_2^{'} \\ x_3^{'} \end{bmatrix} = R_{\psi_G} \cdot R_\theta \cdot R_\phi \begin{bmatrix} x_1 \\ x_2 \\ x_3 \end{bmatrix} \tag{3.20}$$

where:

$$R_{\psi_G} = \begin{bmatrix} cos(\psi_G) & sin(\psi_G) & 0 \\ -sin(\psi_G) & cos(\psi_G) & 0 \\ 0 & 0 & 1 \end{bmatrix} \tag{3.21}$$

$$R_\theta = \begin{bmatrix} cos(\theta) & 0 & sin(\theta) \\ 0 & 1 & 0 \\ -sin(\theta) & 0 & cos(\theta) \end{bmatrix} \tag{3.22}$$

$$R_\theta = \begin{bmatrix} 1 & 0 & 0 \\ 0 & cos(\phi) & -sin(\phi) \\ 0 & sin(\phi) & cos(\phi) \end{bmatrix} \tag{3.23}$$

To represent the navigation state of a vessel assumed to be a rigid body in three-dimensional space, both its position and attitude must be specified.

$$\ddot{p}_N = v_N; \ \ddot{p}_E = v_E \ \ddot{p}_H = V_H; \tag{3.24}$$

$$\ddot{V}_N = a_N; \ \ddot{V}_E = a_E \ \ddot{V}_H = a_H; \tag{3.25}$$

$$\dot{\psi}_G = r;\ \dot{\theta} = p;\ \dot{\phi} = q; \tag{3.26}$$

The reference frame {**XS**} shown in Fig. 3.8b is the IMU sensor reference frame. The acceleration measurements are recorded based on this frame. The reference frame $\{\mathbf{XV}_h\}$ shown in Fig. 3.8a is the vessel horizontal frame. This frame is used for the prediction based on the consideration that the prediction mainly focuses on the horizontal plane. These two reference frames will be introduced in the corresponding chapters later.

3.2 Kalman Filter-based Estimation

The KF-based algorithm is a powerful tool for estimating and predicting the state of systems in the presence of uncertainty, which arises from factors such as noisy measurements, sensor inaccuracies, and unpredictable changes in the systems. It is widely used in applications such as target tracking, navigation, and control applications. In kinematic motion models used for ship navigation, some navigation states can be directly measured by the vessel's onboard equipment. However, these measurements may include measurement errors. Additionally, there are navigation states for which direct observations are not available. Given these challenges, KF-based algorithms offer a robust solution for state estimation.

To apply the KF-based estimation, it is essential first to establish the system model and the measurement model. The system model defines how the state evolves, while the measurement model describes how measurements are related to the system state. Once these models are defined, the appropriate algorithms can be chosen and customized according to the specific system properties and the characteristics of the measurements. The classic KF is designed for linear systems. However, many engineering systems exhibit nonlinear characteristics, leading to the development of extensions such as the EKF, the UKF, and the particle filter. This thesis implements and discusses the classic KF, the EKF, and the UKF.

3.2.1 Establishment of System Models

System models are crucial for defining how the state of a system evolves over time. In this thesis, the system models are built using kinematic motion models.

System Model for CMM:

state vector:

$$\mathbf{x}(t) = [p_N, p_E, v_N, v_E, \psi_G, r, a_t, a_n]^T \tag{3.27}$$

model formula:

$$\dot{\mathbf{x}}(t) = \begin{bmatrix} v_N \\ v_E \\ a_t f^{vx} - a_n f^{vy} \\ a_t f^{vy} + a_n f^{vx} \\ r \\ 0 \\ 0 \\ 0 \end{bmatrix} + \mathbf{w_x} \tag{3.28}$$

where:

$$\mathbf{w_x} \sim \mathcal{N}(\mathbf{o}, \mathbf{Q} \in \mathbb{R}^{8\times 8})$$

$$f^{vx} = \frac{v_N}{\sqrt{v_N^2 + v_E^2}}\ ,\ f^{vy} = \frac{v_E}{\sqrt{v_N^2 + v_E^2}}$$

The system noise $\mathbf{w_x}$ accounts for unpredictable changes in the system state caused by modeling errors and external disturbances. In this thesis, all uncertainties of system models are modeled as white Gaussian noise.

System Model for CTRA:

state vector:

$$\mathbf{x}(t) = [p_N, p_E, u, v, \psi_G, r, a_u, a_v]^T \tag{3.29}$$

model formula:

$$\dot{\mathbf{x}}(t) = \begin{bmatrix} u\cos(\psi_G) - v\sin(\psi_G) \\ v\cos(\psi_G) + u\sin(\psi_G) \\ a_u \\ a_v \\ r \\ 0 \\ 0 \\ 0 \end{bmatrix} + \mathbf{w_x} \tag{3.30}$$

where:

$$\mathbf{w_x} \sim \mathcal{N}(\mathbf{o}, \mathbf{Q} \in \mathbb{R}^{8\times 8})$$

System Model for CAA:

In the vessel navigation states used in CMM and CTRA (Eq. 3.27 and 3.29), ψ_G and r describe the rotational motion, while the remaining states pertain to translational motion. Therefore, it is also advisable to seperate ψ_G and r from the state vector represented by Eq. 3.27 and 3.29 to establish a new model. The new model used in this thesis is analogous to the constant linear acceleration model but is specifically applied to rotational motion.

State vector:

$$\mathbf{x}(t) = [\psi_G, r, \dot{r}]^T \tag{3.31}$$

Model formula:

$$\dot{\mathbf{x}}(t) = \begin{bmatrix} 0 & 1 & 0 \\ 0 & 0 & 1 \\ 0 & 0 & 0 \end{bmatrix} \mathbf{x}(t) + \mathbf{w}_\mathbf{x} \tag{3.32}$$

where:

$$\mathbf{w}_\mathbf{x} \sim \mathcal{N}(\mathbf{o}, \mathbf{Q} \in \mathbb{R}^{3\times3})$$

Compared to Eq. 3.28 and 3.30, which assume a constant turn rate for the vessel, the Constant Angular Acceleration Model (CAA) provides a more realistic depiction of the vessel turning behavior. Since the kinematic motion models do not explicitly account for inputs like rudder angle, the estimated turn rate acceleration $\dot{r}$ from the CAA can serve as an indicator of whether the vessel has executed a new rudder command. Additionally, when ψ_G and r are removed from Eq. 3.29, the system model of CTRA becomes linear. This linearity can enhance the filter's effectiveness and improve its efficiency.

System Model used for Ymir RV

As previously discussed, kinematic motion models based on a two-dimensional plane are not suitable for the Ymir RV. Therefore, the model used for the Ymir RV is constructed in three-dimensional space. Since the Ymir RV is treated as a rigid body, its motion can also be decomposed into translational and rotational components. For the rotational part, the CAA is used to represent the heading. The primary focus here is on modeling the translational motion.

State vector:

$$\mathbf{x}(t) = [p_N, p_E, p_H, v_N, v_E, v_H]^T \tag{3.33}$$

Input vector:

$$\mathbf{u}(t) = [a_N, a_E, a_H]^T \tag{3.34}$$

Model formula:

$$\dot{\mathbf{x}}(t) = \begin{bmatrix} 0 & 0 & 0 & 1 & 0 & 0 \\ 0 & 0 & 0 & 0 & 1 & 0 \\ 0 & 0 & 0 & 0 & 0 & 1 \\ 0 & 0 & 0 & 0 & 0 & 0 \\ 0 & 0 & 0 & 0 & 0 & 0 \\ 0 & 0 & 0 & 0 & 0 & 0 \end{bmatrix} \mathbf{x}(t) + \begin{bmatrix} 0 & 0 & 0 \\ 0 & 0 & 0 \\ 0 & 0 & 0 \\ 1 & 0 & 0 \\ 0 & 1 & 0 \\ 0 & 0 & 1 \end{bmatrix} \mathbf{u}(t) + \mathbf{w}_{\mathbf{x}} \tag{3.35}$$

where:

$$\mathbf{w}_{\mathbf{x}} \sim \mathcal{N}(\mathbf{o}, \mathbf{Q} \in \mathbb{R}^{6\times 6})$$

The system model for the translational motion is shown in Eq. 3.35. Unlike the previous model, the accelerations are treated as the input vector $\mathbf{u}$ in the model. The accelerations in $\mathbf{u}$ are the components expressed in $\{\mathbf{N}\}$. These components cannot be directly obtained from the IMU installed in Ymir RV. The raw acceleration measurements are based on the $\{\mathbf{XS}\}$. The transformation of these acceleration components from $\{\mathbf{XS}\}$ to $\{\mathbf{N}\}$ is explained in the relevant section on the measurement model.

3.2.2 Establishment of Measurement Models

Measurement models in the context of KF-based estimation define the relationship between the measurements and the system states. In this thesis, the measurements are assumed to be obtained from the on-board equipment, which includes the GNSS, IMU, and the gyroscope. The GNSS records position data—latitude, longitude, and height—based on the WGS 84 reference frame. The IMU provides acceleration based on the sensor reference frame. The gyroscope provides the vessel attitude which include heading, pitch, roll, and their respective rates. Notably, the fiber-optic gyroscope installed on the Ymir RV for the sea trial provides measurements of true heading.

Regarding measurements, several key points should be highlighted: First, it is important to note that the measured accelerations and attitude angles from the on-board equipment are referenced to the sensor reference frame. In simulation environments, the sensor frame is typically configured to align with the vessel's body-fixed reference frame. However, in real-world applications, there can be notable misalignments between these frames. Therefore, calibration adjustments are essential when developing measurement models for sea-trial experiments. Second, the latitude and longitude measurements from GNSSs are converted to northing and easting coordinates in the UTM coordinate system. As a result, the positions in the state vectors (Eq. 3.27, 3.29, and 3.33) are expressed in meters, specifically as northing and easting. Third, the heading

measured by the gyroscope is referenced to true north. To obtain the grid north ψ_G used in the state vectors (Eq. 3.27, 3.29, and 3.31), the measured heading must be corrected for grid convergence. The calculations for coordinate conversion and grid convergence are detailed in Eq. 3.3, 3.4, and 3.5. Finally, because the measurements are obtained from digital sensors, the measurement models are defined in discrete time t_k.

Measurement Model for CMM:

measurement vector:

$$\mathbf{z}[t_k] = [z_{p_N}, z_{p_E}, z_\psi, z_r, z_{au}, z_{av}]^T \tag{3.36}$$

$$\mathbf{z}[t_k] = \begin{bmatrix} p_N \\ p_E \\ \psi_G + \gamma \\ r \\ (h_{u1} - v_E\, r)\cos(\psi_G) + (h_{u2} + v_N\, r)\sin(\psi_G) \\ (h_{v1} + v_N\, r)\cos(\psi_G) - (h_{v2} - v_E\, r)\sin(\psi_G) \end{bmatrix} + \mathbf{w_z} \tag{3.37}$$

where:

$$\mathbf{w_z} \sim \mathcal{N}(\mathbf{o}, \mathbf{R} \in \mathbb{R}^{6\times 6})$$

$$h_{u1} = \frac{a_t v_N - a_n v_E}{\sqrt{v_N^2 + v_E^2}} + r v_E \quad ; \quad h_{u2} = \frac{a_t v_E + a_n v_N}{\sqrt{v_N^2 + v_E^2}} - r v_N$$

$$h_{v1} = \frac{a_t v_E + a_n v_N}{\sqrt{v_N^2 + v_E^2}} - r v_N \quad ; \quad h_{v2} = \frac{a_t v_N - a_n v_E}{\sqrt{v_N^2 + v_E^2}} + r v_E$$

Measurement Model for CTRA:

measurement vector:

$$\mathbf{z}[t_k] = [z_{p_N}, z_{p_E}, z_\psi, z_r, z_{au}, z_{av}]^T \tag{3.38}$$

$$\mathbf{z}[t_k] = \begin{bmatrix} p_N \\ p_E \\ \psi_G + \gamma \\ r \\ a_u - v\, r \\ a_v + u\, r \end{bmatrix} + \mathbf{w_z} \tag{3.39}$$

where:

$$\mathbf{w_z} \sim \mathcal{N}(\mathbf{o}, \mathbf{R} \in \mathbb{R}^{6\times 6})$$

Measurement Model for CAA:

measurement vector:

$$\mathbf{z}[t_k] = [z_\psi, z_r]^T \tag{3.40}$$

$$\mathbf{z}[t_k] = \begin{bmatrix} 1 & 0 & 0 \\ 0 & 1 & 0 \end{bmatrix} \begin{bmatrix} \psi_G + \gamma \\ r \\ \dot{r} \end{bmatrix} + \mathbf{w_z} \tag{3.41}$$

where:

$$\mathbf{w_z} \sim \mathcal{N}(\mathbf{o}, \mathbf{R} \in \mathbb{R}^{3\times3})$$

Regarding Eq. 3.37 and 3.39, it is important to clarify that the acceleration measurements obtained from the UiT simulator exclude the gravitational acceleration g. However, the centrifugal force components resulting from the rotation of vessel body-fixed reference frame are included.

Measurement Model in Ymir RV:

Measurement Model for Translational Motion

measurement vector:

$$\mathbf{z}[t_k] = [z_{p_N}, z_{p_E}, z_{p_H}]^T \tag{3.42}$$

$$\begin{bmatrix} z_{p_N} \\ z_{p_E} \\ z_{p_H} \end{bmatrix} = \begin{bmatrix} 1 & 0 & 0 \\ 0 & 1 & 0 \\ 0 & 0 & 1 \end{bmatrix} \begin{bmatrix} p_N \\ p_E \\ p_H \end{bmatrix} + \mathbf{w_z} \tag{3.43}$$

where:

$$\mathbf{w_z} \sim \mathcal{N}(\mathbf{o}, \mathbf{R} \in \mathbb{R}^{3\times3})$$

Measurement Model for Rotational Motion

This model is equivalent to that described in Eq. 3.40 and Eq. 3.41.

Sensor Calibration:

To increase estimation accuracy, certain calibrations must be considered for the sensors installed on the Ymir RV. For clarity, Fig. 3.8b is presented again and relabeled as Fig. 3.9.

- GNSS antenna:

  The GNSS receiver initially processes position measurements from the GNSS antenna (Fig. 3.9). The calibration involves the post-processing the

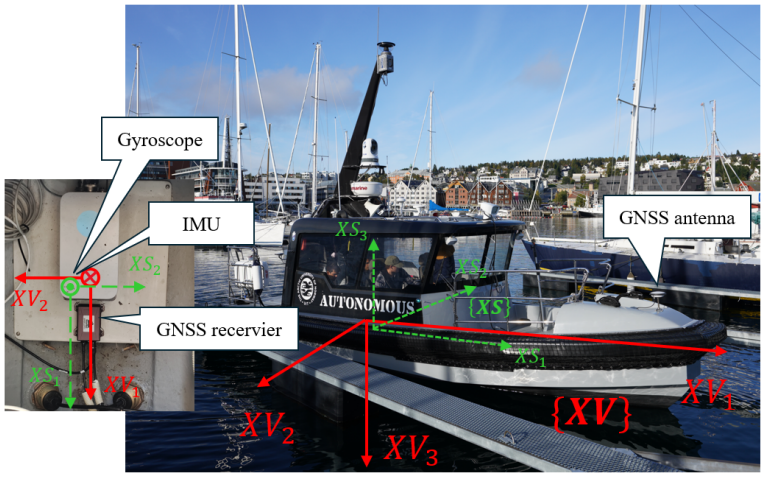

Figure 3.9: Sensor configuration in Ymir RV. {**XV**}: vessel body-fixed reference frame; {**XS**}: sensor reference frame. (Figure from Paper VI)

measured position data to ensure it corresponds to the GNSS receiver's location near the vessel ACG.

- Gyroscope and IMU:

  The calibration of the gyroscope and IMU addresses discrepancies between the reference frames {**XV**} and {**XS**}. This calibration process consists of two stages: coarse calibration and fine calibration. During coarse calibration, aligning {**XS**} with {**XV**} can be accomplished by rotating 180 degrees around the XS_1 axis. This rotation results in a matrix referred to as R_{rough}.

$$\begin{bmatrix} XS_1' \\ XS_2' \\ XS_3' \end{bmatrix} = R_{rough} \begin{bmatrix} XS_1 \\ XS_2 \\ XS_3 \end{bmatrix} = \begin{bmatrix} 1 & 0 & 0 \\ 0 & -1 & 0 \\ 0 & 0 & -1 \end{bmatrix} \begin{bmatrix} XS_1 \\ XS_2 \\ XS_3 \end{bmatrix} \tag{3.44}$$

  Fine calibration involves identifying the small residual angular offsets between {**XS**} and {**XV**}. Once the residual angular offsets (denoted as ϕ_{miss}, θ_{miss}, and ψ_{miss}) have been determined, the following equation can be employed to transform the sensor output into components aligned with {**XV**}.

$$\begin{bmatrix} XV_1 \\ XV_2 \\ XV_3 \end{bmatrix} = R_{\psi_{miss}} \cdot R_{\theta_{miss}} \cdot R_{\phi_{miss}} \begin{bmatrix} XS_1' \\ XS_2' \\ XS_3' \end{bmatrix} \tag{3.45}$$

Acceleration Input:

As shown in Eq. 3.35, the acceleration components in $\{\mathbf{N}\}$, (a_N, a_E, a_H), are treated as inputs to the system model. Given the acceleration measurements in $\{\mathbf{XS}\}$, the corresponding components in $\{\mathbf{N}\}$ can be calculated as:

$$\begin{bmatrix} a_{XV1} \\ a_{XV2} \\ a_{XV3} \end{bmatrix} = -R_{\psi_{miss}} \cdot R_{\theta_{miss}} \cdot R_{\phi_{miss}} \cdot R_{rough} \begin{bmatrix} a_{XS1} \\ a_{XS2} \\ a_{XS3} \end{bmatrix} \tag{3.46}$$

$$\begin{bmatrix} a_N \\ a_E \\ a_H \end{bmatrix} = R_{\psi_G} \cdot R_{\theta} \cdot R_{\phi} \begin{bmatrix} a_{XV1} \\ a_{XV2} \\ a_{XV3} \end{bmatrix} \tag{3.47}$$

Note that the IMU measures inertial forces opposite to the acceleration direction. Therefore, Eq. 3.46 includes a minus sign to account for this.

3.2.3 KF-based Estimation Algorithm

The KF-based estimation algorithm operates through a two-step process: the prediction step and the filtering step. In the prediction step, prior estimates are generated based on system models and their associated uncertainties. Once new measurements become available, the filtering step updates these prior estimates. This update is performed using a weighted average known as the Kalman gain. These steps are executed recursively, enabling real-time implementation of the algorithm.

The classic KF is designed for linear systems. However, many engineering systems exhibit nonlinear characteristics. To address these challenges, extensions of the classic KF have been developed. Notable among these extensions are the EKF and the UKF.

Classic Kalman Filter Algorithm

The classic KF algorithm is designed for linear systems, requiring both system and measurement models to be linear. It also assumes that uncertainties in these models are Gaussian-distributed. Under these conditions, the classic KF provides optimal estimation by minimizing the mean squared error. The algorithm is detailed in Tab. 3.2.

Algorithm: Classic KF algorithm
Given the system model:
$\mathbf{x}[t_k] = \mathbf{A}\mathbf{x}[t_{k-1}] + \mathbf{B}\mathbf{u}[t_{k-1}] + \mathbf{q}, (\mathbf{q} \sim N(\mathbf{o}, \mathbf{Q}))$
$\mathbf{z}[t_k] = \mathbf{C}\mathbf{x}[t_{k-1}] + \mathbf{r}, (\mathbf{r} \sim N(\mathbf{o}, \mathbf{R}))$
Initialization:
initialize state vector $\hat{\mathbf{x}}_{0\|0}$ and covariance $\mathbf{P}_{0\|0}$
Prediction step:
calculate prior state estimate: $\hat{\mathbf{x}}_{t_k\|t_{k-1}} = \mathbf{A}\hat{\mathbf{x}}_{t_{k-1}\|t_{k-1}} + \mathbf{B}\mathbf{u}[t_{k-1}]$
and prior covariance: $\mathbf{P}_{t_k\|t_{k-1}} = \mathbf{A}\mathbf{P}_{t_{k-1}\|t_{k-1}}\mathbf{A}^T + \mathbf{Q}$
Filtering step:
calculate innovation: $\mathbf{e}_z[t_k] = \mathbf{z}[t_k] - \mathbf{C}\hat{\mathbf{x}}_{t_k\|t_{k-1}}$
calculate innovation covariance: $\mathbf{S}[t_k] = \mathbf{C}\mathbf{P}_{t_k\|t_{k-1}}\mathbf{C}^T + \mathbf{R}$
obtain Kalman gain: $\mathbf{K}[t_k] = \mathbf{P}_{t_k\|t_{k-1}}\mathbf{C}^T\mathbf{S}^{-1}[t_k]$
obtain posterior state estimate: $\hat{\mathbf{x}}_{t_k\|t_k} = \hat{\mathbf{x}}_{t_k\|t_{k-1}} + \mathbf{K}[t_k]\,\mathbf{e}_z[t_k]$
obtain posterior estimate covariance: $\mathbf{P}_{t_k\|t_k} = (\mathbf{I} - \mathbf{K}[t_k]\,\mathbf{C})\,\mathbf{P}_{t_k\|t_{k-1}}$

Table 3.2: Classic KF estimation algorithm

Initialization is required before the execution of the algorithm. In the prediction step, system models are used to generate prior estimates of the relevant navigation states, including uncertainties modeled as Gaussian distributions. In the filtering step, the algorithm updates these prior estimates based on new measurements. For real-time applications, both the prediction and filtering steps are performed recursively. This recursive process reduces computational load by incorporating new data into the estimates instead of reprocessing all past data.

Extended Kalman Filter

The EKF is an adaptation of the classic KF designed to handle nonlinear systems. The main feature of this algorithm is that it linearizes the system and measurement models around the current estimate using a Taylor expansion. Typically, this linearization is based on the first-order Taylor expansion. The workflow of the EKF is shown in Tab. 3.3. Note that the nonlinear system model is described in continuous-time, while the measurement model is described in

discrete-time.

Algorithm: EKF algorithm
Given the system model:
$\dot{\mathbf{x}}(t) = \mathbf{f}(\mathbf{x}(t)) + \mathbf{w}_x, (\mathbf{w}_x \sim N(\mathbf{o}, \mathbf{Q}))$
$\mathbf{z}[t_k] = \mathbf{h}(\mathbf{x}[t_k]) + \mathbf{w}_z, (\mathbf{w}_z \sim N(\mathbf{o}, \mathbf{R}))$
Initialization:
initialize state vector $\hat{\mathbf{x}}_{0\|0}$ and covariance $\mathbf{P}_{0\|0}$
Prediction step:
calculate prior state estimate $\hat{\mathbf{x}}_{t_k\|t_{k-1}}$ from the equation:
$\dot{\hat{\mathbf{x}}}(t) = \mathbf{f}(\hat{\mathbf{x}}(t))$
and prior covariance $\mathbf{P}_{t_k\|t_{k-1}}$ from the equation:
$\dot{\mathbf{P}}(t) = \mathbf{F}(t)\mathbf{P}(t) + \mathbf{P}(t)\mathbf{F}^T(t) + \mathbf{Q}$
where $\mathbf{F} = \frac{\partial \mathbf{f}}{\partial \mathbf{x}}$ is the Jacobian matrix of $\mathbf{f}$
Filtering step:
calculate innovation: $\mathbf{e}_z[t_k] = \mathbf{z}[t_k] - \mathbf{h}(\hat{\mathbf{x}}_{t_k\|t_{k-1}})$
calculate innovation covariance: $\mathbf{S}[t_k] = \mathbf{H}[t_k]\mathbf{P}_{t_k\|t_{k-1}}\mathbf{H}^T[t_k] + \mathbf{R}$
where $\mathbf{H} = \frac{\partial \mathbf{h}}{\partial \mathbf{x}}$ is the Jacobian matrix of $\mathbf{h}$.
obtain Kalman gain: $\mathbf{K}[t_k] = \mathbf{P}_{t_k\|t_{k-1}}\mathbf{H}^T[t_k]\mathbf{S}^{-1}[t_k]$
obtain posterior state estimate: $\hat{\mathbf{x}}_{t_k\|t_k} = \hat{\mathbf{x}}_{t_k\|t_{k-1}} + \mathbf{K}[t_k]\mathbf{e}_z[t_k]$
obtain posterior estimate covariance: $\mathbf{P}_{t_k\|t_k} = (\mathbf{I} - \mathbf{K}[t_k]\mathbf{H}[t_k])\mathbf{P}_{t_k\|t_{k-1}}$

Table 3.3: EKF estimation algorithm

Similar to the classic KF, the prediction and filtering steps in the EKF are also executed recursively. The Jacobian matrices play a crucial role in the linearization process of the EKF, as they contain the first partial derivatives of the non-linear states in both the system and measurement models. However, the KF has limitations when applied to highly non-linear systems. The core issue arises from the reliance on the linearization of non-linear models based on Taylor expansion. The relevant linear approximation assumes that the system's non-linearity can be sufficiently represented by the first derivative in the Jacobian matrices at each step. However, in systems with strong non-linearities, this approximation may fail to accurately capture the system's true behavior.

3.2.4 Unscented Kalman Filter

The UKF is another variant of the classic KF designed to handle nonlinear systems. Unlike the EKF which relies on linearization through Jacobian matrices, the UKF utilizes the unscented transformation. This transformation employs a deterministic sampling technique to select a minimal set of sample points, known as sigma points. These sigma points are then propagated through the

nonlinear functions within the system models to capture the prior estimates. The workflow of the UKF is illustrated in Tab. 3.4.

Algorithm: UKF algorithm
Given the system model:
$\dot{\mathbf{x}}(t) = \mathbf{f}(\mathbf{x}(t)) + \mathbf{w}_x, (\mathbf{w}_x \sim N(\mathbf{o}, \mathbf{Q}))$
$\mathbf{z}[t_k] = \mathbf{h}(\mathbf{x}[t_k]) + \mathbf{w}_z, (\mathbf{w}_z \sim N(\mathbf{o}, \mathbf{R}))$
Initialization:
· initialize state vector $\hat{\mathbf{x}}_{0\|0}$ and covariance $\mathbf{P}_{0\|0}$;
· determine parameter λ;
· generate sigma point sets $\boldsymbol{\chi}[t_0]$, sigma point matrix $\mathbf{W}$, and sigma point vector $\mathbf{w}_m$.
Prediction step:
calculate prior state estimate $\hat{\mathbf{x}}_{t_k\|t_{k-1}}$ from the equation:
$\dot{\hat{\mathbf{x}}}(t) = \mathbf{f}(\boldsymbol{\chi}(t))\,\mathbf{W}$
and prior covariance $\mathbf{P}_{t_k\|t_{k-1}}$ from the equation:
$\dot{\mathbf{P}}(t) = \mathbf{f}(\boldsymbol{\chi}(t))\ \mathbf{W}\ \boldsymbol{\chi}^T(t) + \boldsymbol{\chi}(t)\ \mathbf{W}\ \mathbf{f}^T(\boldsymbol{\chi}(t)) + \mathbf{Q}$
Filtering step:
calculate innovation: $\mathbf{e}_z[t_k] = \mathbf{z}[t_k] - \mathbf{h}(\boldsymbol{\chi}[t_k])\ \mathbf{w}_m$
calculate innovation covariance: $\mathbf{S}[t_k] = \mathbf{h}(\boldsymbol{\chi}[t_k])\ \mathbf{W}\ \mathbf{h}^T(\boldsymbol{\chi}[t_k]) + \mathbf{R}$
obtain Kalman gain: $\mathbf{K}[t_k] = \boldsymbol{\chi}[t_k]\ \mathbf{W}\ \mathbf{h}^T(\boldsymbol{\chi}[t_k])\ \mathbf{S}^{-1}[t_k]$
obtain posterior state estimate: $\hat{\mathbf{x}}_{t_k\|t_k} = \hat{\mathbf{x}}_{t_k\|t_{k-1}} + \mathbf{K}[t_k]\,\mathbf{e}_z[t_k]$
obtain posterior estimate covariance: $\mathbf{P}_{t_k\|t_k} = \mathbf{P}_{t_k\|t_{k-1}} - \mathbf{K}[t_k]\ \mathbf{S}[t_k]\ \mathbf{K}^T[t_k]$

Table 3.4: UKF estimation algorithm

3.2.5 Adaptive Tuning Mechanism

The system noise covariance $\mathbf{Q}$ and measurement noise covariance $\mathbf{R}$, as shown in Tab. 3.2 to 3.4, are set to constant by default. However, in real-world applications, these parameters may vary due to the complexity of the environment. When a vessel executes a new rudder command, the assumptions of constant turn rate and acceleration may no longer hold. Consequently, the default constant setting of $\mathbf{Q}$ may be underestimated in this situation. Additionally, real-time GNSSs can be impacted by various external disturbances, such as limited satellite availability or multipath effects. This can lead to sudden, discontinuous outliers in the received measurements. A constant setting for $\mathbf{Q}$ is thus also unsuitable. This presents a challenge in KF-based real-time applications. One solution is to implement adaptive tuning mechanisms which can adjust the values of $\mathbf{Q}$ and $\mathbf{R}$ based on varying conditions. In this thesis, an adaptive tuning mechanism specifically designed for the sea trials conducted with the Ymir RV is proposed (Fig. 3.10).

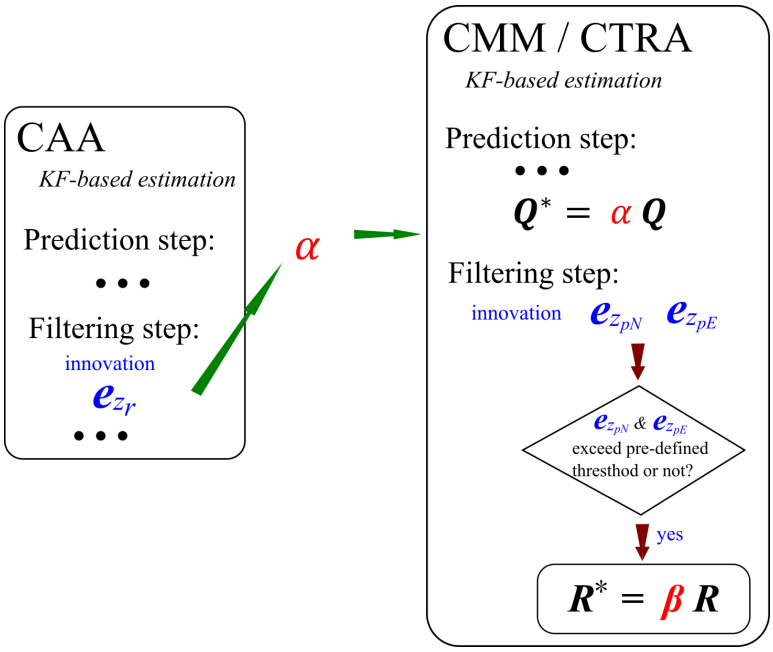

Figure 3.10: The designed adaptive tuning mechanism for the sea trials conducted with the Ymir RV.

The mechanism begins with state estimation using the classic KF algorithm for the CAA. Since the kinematic motion models lack rudder information, the innovation of the estimated turn rate $\mathbf{e}_{z_r}$ serves as an indicator to determine whether the vessel has initiated a new rudder order. This innovation is computed in the filtering step of the KF-based estimation algorithms. It represents the difference between the measured turn rate at a given time step and the optimal estimate of the turn rate based on previously available information. When a relatively large value of $\mathbf{e}_{z_r}$ is detected, a scaling factor α greater than 1 is added to $\mathbf{Q}$ used in the state estimation from the CMM and CTRA. The increase in system noises from the CMM and CTRA suggests that the constant assumptions for acceleration and turn rate are becoming increasingly unrealistic.

The relationship between different values of $\mathbf{e}_{z_r}$ and α can initially be analyzed through multiple simulation trials. Once sufficient reliable data is obtained from these tests, regression methods can then be applied to further analyze the relationship. In this thesis, the GPR type of regression algorithm is implemented. Details of the GPR are provided later, as another calculation utilizes the same method. For abnormal GNSS measurements, the position innovations from the estimation algorithms, denoted as $\mathbf{e}_{z_{pN}}$ and $\mathbf{e}_{z_{pE}}$, are analyzed. Large values of $\mathbf{e}_{z_{pN}}$ and $\mathbf{e}_{z_{pE}}$ suggest a high likelihood of outliers in the position measurements. Once the values of $\mathbf{e}_{z_{pN}}$ and $\mathbf{e}_{z_{pE}}$ exceed the pre-defined thresholds, another

scaling factor β is applied to $\mathbf{R}$. In this study, the scaling factor β is a fixed value. This is because outliers in GNSS measurements during the sea trials were infrequent. When they did occur, they exhibited significant deviations from typical measurements.

Chapter 4

Pivot Point-based Trajectory Prediction

This chapter addresses trajectory prediction, which follows the vessel navigation state estimation process. The first section outlines the method for calculating the PP. The second section describes the trajectory prediction algorithm that uses the PP. The final section covers how trajectory prediction is supported by the GRU.

4.1 The Calculation of the Pivot Point

The vessel PP is a critical concept in ship maneuvering and navigation. Understanding the location of the PP is essential for predicting a vessel's trajectory, especially in confined waters or when precise maneuvers are required. The distance to the PP can be mathematically defined as the ratio of a vessel's sway velocity v to its turn rate r (Tzeng, 1998). This relationship can be expressed by the following equation:

$$L_{PP} = -\frac{v}{r} \tag{4.1}$$

The calculated result L_{PP} is described as the distance from the vessel CG to the PP along the longitudinal axis of the vessel in (Tzeng, 1998). Some references have the same statement (Clark, 2005; Thor, 2011). In this thesis, since the added mass effect on vessel maneuvering is considered, L_{PP} is defined as the

distance from the vessel ACG to the PP.

4.1.1 Pivot Point in Rigid-Body Vessels

Equation 4.1 is straightforward, but its practical implementation presents several challenges. First, since the turn rate appears in the denominator, a small turn rate can cause significant fluctuations in the calculated results. This can lead to results that may lack practical significance. Second, accurately determining the position of the vessel ACG during maneuvering is difficult. In this thesis, the possible location of the ACG is treated as part of the system noises, i.e., a Gaussian distribution with zero mean. As a result, the sway velocities obtained from the model and the KF-based estimation algorithms described in Chapter 3 may show some bias when compared to the actual sway velocities of the ACG. Given these considerations, this thesis proposes two methods to calculate the PP based on the assumption that the vessel behaves as a rigid body.

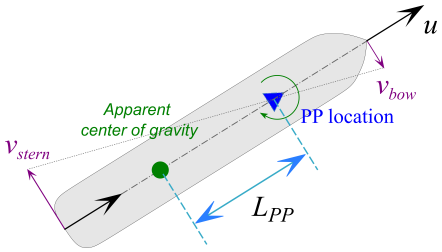

Figure 4.1: Rigid body assumption of a vessel.

Figure 4.1 illustrates the rigid body assumption for a vessel. Since the hull of the vessel does not deform during maneuvering, the velocity components in the surge direction remain uniform across all points, while the velocity components in the sway direction vary linearly. Consequently, if the sway velocities at both the bow and stern are known, the PP can be determined based on this linear distribution.

4.1.2 Gaussian Process Regression

The aforementioned method requires the simultaneous values of sway velocities at both the bow and stern. This necessitates the installation of GNSS antennas at both the bow and stern of the vessel. Furthermore, the measurement positions from the two antennas must be synchronized to ensure that the estimated sway speeds correspond to the same time step. The current performance of the Ymir RV equipment does not yet meet the required data synchronization standards. For Ymir RV, only one reference position's sway velocity can be estimated at the

current stage. Therefore, this study employs an alternative method to calculate the vessel PP, which is based on the GPR.

Summary of the GPR

The GPR is a non-parametric Bayesian method used for regression that excels at modeling complex and nonlinear relationships. Unlike traditional regression techniques that depend on predefined functional forms, the GPR operates by placing a distribution over possible functions that could fit the data. At the core of GPR is the Gaussian process, which assumes that the relationship between inputs and outputs follows this process. This means that for any set of inputs, the joint distribution of the corresponding outputs follows a multivariate Gaussian distribution. This framework enables the modeling of an infinite range of functions that describe the relationship between inputs and outputs. The intuitive nature of the Gaussian Process can be understood as follows: if the inputs are similar to each other, the corresponding outputs will also be similar.

Regarding the multivariate Gaussian distribution of the outputs, the mean is often assumed to be zero. The relationship between two different elements in the covariance matrix is defined by the kernel function. There are many kernel functions that can be used in GPR, such as the radial basis function kernel, exponential kernel, periodic kernel, and the class of Matérn kernels. In GPR applications, the training data are used to calculate the covariance matrix through a selected kernel function. Different kernel functions come with various hyperparameters that influence the model's behavior. These hyperparameters are typically optimized by maximizing the likelihood function based on the training data.

When making a prediction with new input data, the covariance of the multivariate Gaussian distribution of the outputs is updated. New elements are added to the covariance matrix by calculating the relationship between the new input and all the training data. The updated covariance is then used to compute the probabilistic characteristics of the output for the new input, which will also follow a Gaussian distribution. This type of prediction method is particularly advantageous as it allows for an assessment of confidence in predictions, especially in regions with sparse or noisy data.

Generation of Training Data

The generation of the training data for the GPR is also based on the rigid body assumption, which assumes that the hull of vessel does not deform and the sway velocities are linearly distributed along the vessel. Additionally, it assumes that the vessel has limited maneuverability in the sway direction. This indicates

that the maximum possible sway velocities are relatively small compared to the maximum surge velocities. This assumption is supported by factors such as high hydrodynamic resistance, rudder effectiveness, and the design of the propulsion system (Clark, 2005). Due to the limited sway maneuverability, a finite number of sample points can be enumerated to represent all possible bow and stern sway velocities encountered during various maneuvers. Each combination of the enumerated bow and stern sway velocities can then be mapped to the corresponding PP position based on the rigid body assumption (Fig. 4.2).

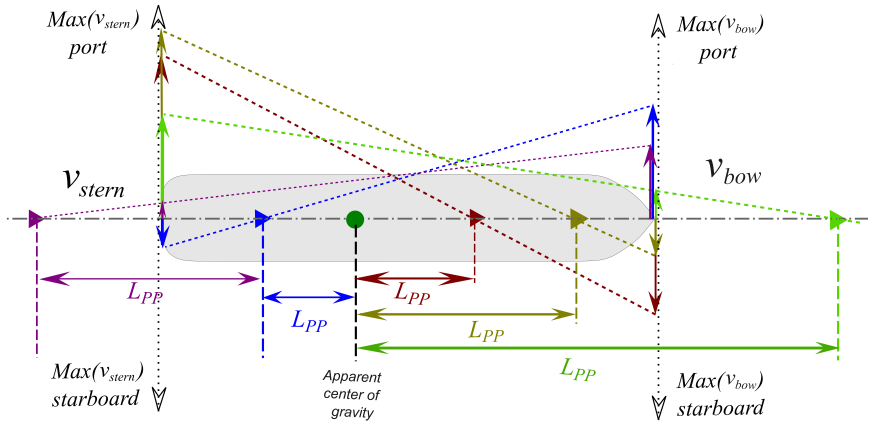

Figure 4.2: The position of the PP is determined by the varying relationships of sway velocities on the bow and stern. The vessel's PP may be located outside the hull or behind the ACG. Cases where v_{bow} and v_{stern} are equal are excluded.

It should be noted that once the bow sway velocity v_{bow} and stern sway velocity v_{stern} of the vessel are determined, the sway velocity at a random point on the vessel v_h and the turn rate r are also uniquely defined. A mapping relation can thus be established (Eq. 4.2).

$$(v_{stern}, v_{bow}) \leftrightarrow (v_h, r \mid L_{PP}) \tag{4.2}$$

By enumerating all possible combinations of v_{bow} and v_{stern}, a database can be created that maps v_h and r to the vessel PP (see Fig. 4.3). During the prediction process, the new input (v_h, r) is supplied by the KF-based algorithm, while the corresponding output L_{PP} are generated by the GPR model.

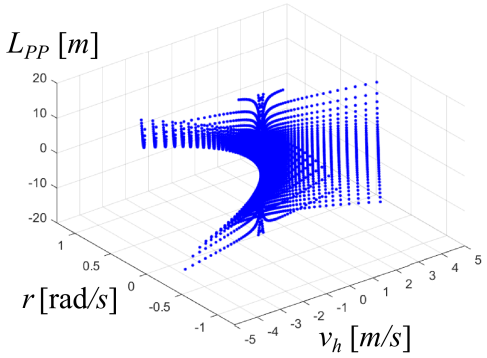

Figure 4.3: The training data from various sets of (v_{stern}, v_{bow}) used in this thesis. There are 10,000 samples in total. The maximum values for both v_{stern} and v_{bow} are set at $5[m/s]$.

4.2 PP-based Trajectory Prediction

Consider a rigid body in a two-dimensional plane. Its general motion can be decomposed into translational and rotational components (Batlle and Condomines, 2020). As illustrated in Fig. 4.4, the prediction of a vessel's position and heading at the next time step involves two distinct parts. The first part relies on translational motion, governed by the surge velocity. The second part focuses on rotational motion, with the PP serving as the center of rotation.

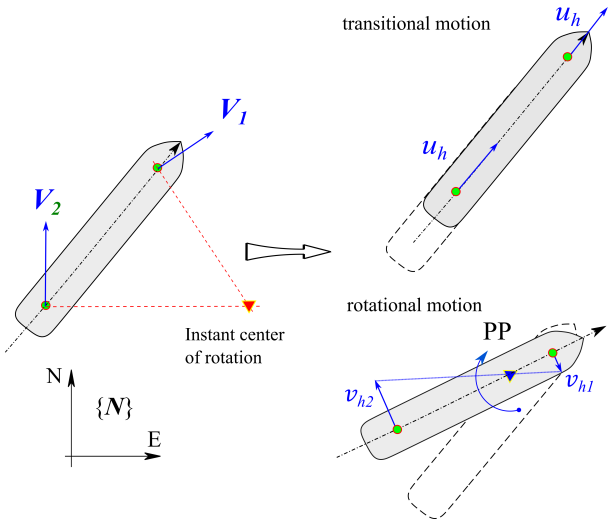

Figure 4.4: The planar motion of a vessel can be decomposed into translational and rotational components under the rigid body assumption. (Figure from Paper VI)

It is important to note that these two steps are not commutative. This means

that calculating the rotational component first may lead to discrepancies in the results. However, these discrepancies are minimal if the time step used in the prediction is sufficiently small. Additionally, while vessel state estimation can utilize models in three-dimensional space, all predictions in this context are based on the horizontal plane. The related algorithm is demonstrated in Tab. 4.1.

Algorithm: PP-based algorithm for ship trajectory prediction

Initialization (prediction starts at time t_k, time step is Δt):

- Given the estimated navigation states:
  P_N, P_E, ψ_G, u, v, and r in t_k
- Determine the PP (L_{PP}) based on the given states

Prediction: (prediction horizon t_{k+1} to t_{k+N}):

for $i = k + 1$ to $k + N$:

$$\Delta L = u \cdot \delta t;$$
$$\Delta\psi_G = r \cdot \delta t;$$

$$P_N^{'} = P_N\left[t_i\right] + \Delta L \cdot cos\left(\psi_G\left[t_i\right]\right);$$
$$P_E^{'} = P_E\left[t_i\right] + \Delta L \cdot sin\left(\psi_G\left[t_i\right]\right);$$

$$PP_N = P_N^{'} + L_{pp} \cdot cos(\psi_G\left[t_i\right])$$
$$PP_E = P_E^{'} + L_{pp} \cdot sin(\psi_G\left[t_i\right])$$

$$P_N\left[t_{i+1}\right] = cos\left(\Delta\psi_G\right)\left(P_N^{'} - PP_N\right) - sin\left(\Delta\psi_G\right)\left(P_E^{'} - PP_E\right) + PP_N$$
$$P_E\left[t_{i+1}\right] = sin\left(\Delta\psi_G\right)\left(P_N^{'} - PP_N\right) + cos\left(\Delta\psi_G\right)\left(P_E^{'} - PP_E\right) + PP_E$$
$$\psi_G\left[t_{i+1}\right] = \psi_G\left[t_i\right] + \Delta\psi_G$$

Table 4.1: PP-based algorithm used in the local-scale ASP

4.3 Prediction supported by the GRU

The prediction algorithm shown in Tab. 4.1 can update the vessel position and heading during the prediction horizon. However, it should be noted that the states u,v, and r are assumed to be constant during the prediction period. Therefore, this prediction algorithm is best suited for use after a transitional period following a rudder order. It works most effectively when the parameters u, v, and r have stabilized and exhibit minimal changes. If the prediction starts immediately after the rudder order is executed, the algorithm may generate significant errors due to the rapid changes in the vessel's motion. For highly maneuverable ships, such as the Ymir RV, the vessel can quickly reach

a steady state—typically within about 2 seconds—after a rudder adjustment. Therefore, the algorithm will primarily exhibit significant errors only during this short adjustment period. However, for large-tonnage vessels, the reaction time following a rudder order is considerably longer, meaning u, v, and r take more time to stabilize. Using this algorithm for immediate predictions after a rudder adjustment in such cases is likely to result in significant errors. However, for large-tonnage vessels, the reaction time following a rudder command is significantly longer. This creates slow state variations, resulting in a long stabilization period. Consequently, applying this algorithm for immediate predictions following a rudder adjustment in these cases is likely to produce large errors.

It is important to note that the kinematic motion models used in this thesis assume constant acceleration and turn rate. As a result, these models, along with the KF-based algorithms, may require longer periods to converge to the actual values of u, v, and r that occur after a new rudder command. To address this challenge, data-driven type of approaches can be employed. These involves leveraging historical maneuvering data from the vessel to improve prediction accuracy. If sufficient historical maneuvering data sets are available for a specific vessel, they can be used as training data for neural networks. Training a neural network on these data sets allows the model to learn and predict how the vessel's velocity will change in response to different rudder orders.

The GRU neural network has been chosen to support the prediction in the local-scale ASP. This selection is based on several reasons. First, because the training data consists of time series, the GRU which is derived from the classic Recurrent Neural Network (RNN), is particularly well-suited for handling this type of data (Sherstinsky, 2020; Hewamalage et al., 2021). Second, the GRU is generally preferred over classical RNN because it more effectively handles long-term dependencies and mitigates the vanishing gradient problem (Levin, 1990). Finally, the GRU features a more streamlined structure compared to the well-known RNN-type neural network Long Short-Term Memory (LSTM), resulting in lower computational costs (Chung et al., 2014). Additionally, numerous studies have found that the GRU often requires fewer training datasets while achieving performance comparable to that of the LSTM (Cahuantzi et al., 2023; Yang et al., 2020).

The GRU consists of the GRU cell, which is the fundamental building block of the network (see Figure). This cell enhances the classical RNN by incorporating two essential gates: the update gate and the reset gate.

- **Update Gate:** The update gate regulates the amount of past information that is retained and passed forward. It determines how much of the gate's parameters should be updated with new information. This mech-

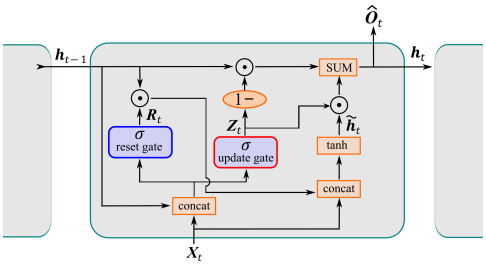

Figure 4.5: GRU cell structure. (Figure from Paper V)

anism allows the GRU to preserve important information across time steps, effectively addressing the challenge of long-term dependencies in sequential data.

- **reset Gate:** The reset gate determines how much of the past information should be forgotten. By managing this reset process, the GRU can selectively forget portions of the previous state, enabling the network to concentrate on newer information when making predictions.

The update and reset gates work together to balance "remembering" and "forgetting" during the training process. This balance enables the GRU to excel in tasks involving sequences, such as time series prediction, language modeling, and speech recognition.

The GRU's predictions of a vessel's surge, sway, and turn rate can be integrated into the PP-based prediction algorithm. During the prediction horizon from t_{k+1} to t_{k+N}, the vessel's navigation states u, v, and r can be replaced with the GRU-based predicted values.

Part II

Research Outcomes

Chapter 5

Summary of Research

This chapter summarizes the attached papers. The research objectives are repeated here to enhance readability.

RO1: The implementation of the KF-based algorithms for navigation state estimation and that consists of sub-objectives of:

(i) Identify the kinematic motion models that best describes the ship maneuvering behaviors;
(ii) Apply appropriate KF-based estimation algorithms to estimate the vessel navigation states;

RO2: The Development of trajectory prediction considering the ship maneuvering features in the local-scale prediction and that consists of sub-objectives of:

(i) Calculate the location of the PP based on the estimated navigation states;
(ii) Design the trajectory prediction method based on the understanding of the PP;

RO3: The performance evaluation of the methods implemented and that consists of sub-objectives of:

(i) The evaluation through the simulated maneuvering from the UiT bridge simulator;

(ii) The evaluation through the sea-trial experimental maneuvering from the UiT research vessel Ymir RV.

In the first section, Papers I through IV detail the application of KF-based algorithms for estimating vessel navigation states . These estimates are crucial for supporting subsequent trajectory predictions. In the second section, Papers V and VI summarize trajectory predictions based on an understanding of the PP. For evaluation purposes, both state estimation and trajectory prediction approaches are initially assessed through the data sets from the simulated maneuvers using the UiT simulator. Subsequently, these methods are validated through sea trials data with the Ymir RV in Tromsø Fjord.

5.1 KF-based Estimation for Vessel Navigation State

In this section, the focus is placed on using the KF-based estimation to estimate relevant vessel navigation states. This process involves selecting appropriate system and measurement models, as well as the corresponding estimation algorithm. The system models are based on the kinematic motion models outlined in Chapter 3. The measurement models are derived from data collected using the UiT bridge simulator. These measurements include the vessel's position, heading, turn rate, and accelerations. For simulated maneuvers, large-tonnage cargo vessels are selected, and the conditions are set to calm weather and tranquil seas. Typically, it is sufficient to model the motion of large-tonnage vessels within a horizontal plane, considering three degrees of freedom: surge, sway, and heading. However, for the sea-trial maneuver conducted by the Ymir RV, modifications to the models are required. These adjustments are needed due to the Ymir RV's small size and the complex sea conditions in the Tromsø Fjord.

Paper I: The Comparison of Two Kinematic Motion Models for Autonomous Shipping Maneuvers

In Paper I, the CMM and CTRA are employed as the system models within the KF-based framework to estimate vessel navigation states. Both the CMM and CTRA used are nonlinear, which necessitates the implementation of the EKF and UKF. Regarding the filter algorithms, the system models are described in continuous-time while the measurement models are in discrete-time. Consequently, the filter algorithms are designated as CD-EKF (Continuous-Discrete Extended Kalman Filter) and CD-UKF (Continuous-Discrete Unscented Kalman Filter) in the paper.

To enhance accuracy, a second-order explicit Runge-Kutta method is utilized during the prediction step for calculating both the prior estimates and the prior error covariance. The performance of these models is evaluated through simulated maneuvers in the UiT bridge simulator. Monte Carlo-based tests are performed because the simulator provides multiple independent measurements.

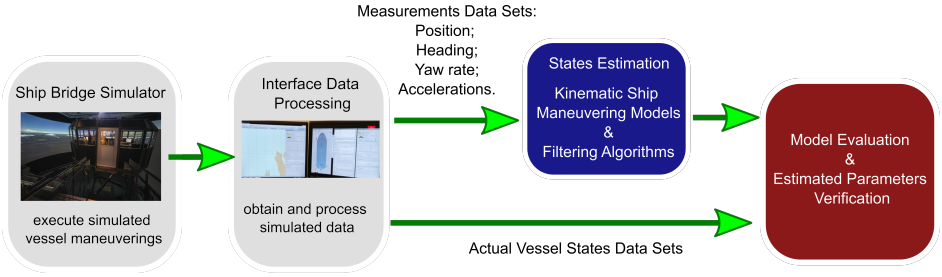

Figure 5.1: Simulated maneuvering experiment setup. (Figure from Paper I)

Figure 5.1 illustrates the acquisition of simulated maneuvering data from the UiT bridge simulator. The simulator offers a fully immersive display and an authentic replica of a ship's bridge. Navigation data from the simulated maneuvers performed on this bridge is accessible through the user interface. These datasets include both simulated measurements and actual state values.

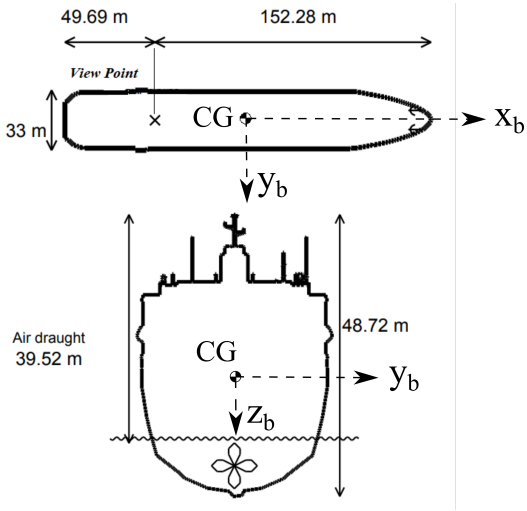

Figure 5.2: Dimensions of the vessel used in the simulator. (Figure from Paper I)

The vessel used for the simulated maneuvers is shown in Fig. 5.2. It is a large-tonnage cargo container. The simulation was conducted under calm weather conditions. Six different maneuvers were simulated: starboard turns with rudder angles of 10 and 35 degrees, port turns with rudder angles of 10 and 35 degrees, a zigzag maneuver of 20-20, and a Williamson turn. For a single ma-

neuver, the simulator can generate multiple sets of independent measurements. As a result, 100 sets of independent measurements were obtained for each maneuver. This enables Monte Carlo simulations to effectively evaluate the performance of the estimation.

Figure 5.3a and 5.3b presents several estimates of the vessel navigation states from the Starboard-35 and Port-10 maneuvers. These results are chosen from one random test in a series of 100 Monte Carlo simulations. The positions estimated by the CTRA closely match the actual values, and the accuracy of the surge velocity is notable. However, as the ship begins to turn, a noticeable gap appears between the estimated and actual values of the sway velocity. In the estimates generated by the CMM, although the velocity components in the navigation frame eventually match the true values, there is a clear delay between the estimated and actual values. Similarly, the acceleration components—a_t and a_n—exhibit constant biases, much like those observed in the sway velocity.

Figure 5.4 and 5.5 display the estimation performances through the average Root Mean Square Errors (RMSEs) derived from all the maneuvers in the Monte Carlo simulations.

The Monte Carlo-based simulations reveal that the performance difference between the EKF and the UKF is minimal. Furthermore, a comparative analysis shows that, in the CTRA, the average RMSE for surge velocity is higher than that for sway velocity. Conversely, in the CMM, the RMSE for the acceleration component a_n is an order of magnitude larger than that for a_t. The numerical results of RMSEs presented in Fig. 5.4 and 5.5 suggest that, although the estimation results shown in Fig. 5.3a and 5.3b are randomly selected from one of the 100 Monte Carlo-based tests, they are representative of the overall outcomes observed across all simulations.

Contribution by the Author

- The author conceived the ideas with other authors.
- The author developed the methodology.
- The author developed the implementation of the simulation experiments.
- The author wrote the first draft of the manuscript.

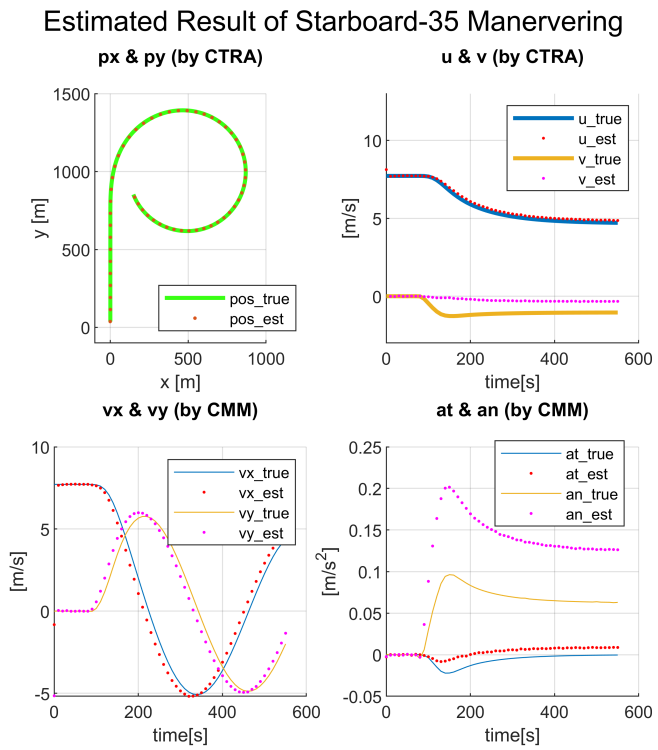

(a) Estimated results of Starboard-35 maneuver

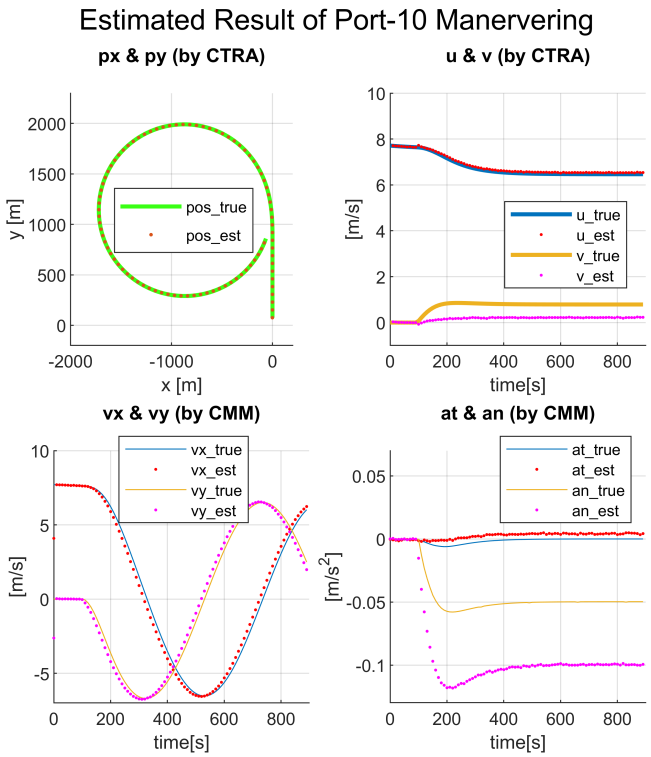

(b) Estimated results of Port-10 maneuver

Figure 5.3: Vessel state estimation results from Port-10 and Starboard-35 maneuvers. (Figure from Paper I)

TABLE 2: The Average RMSEs of CMM State Variables from 100 Monte Carlo-based Tests									
Error of State: [unit]		$\boldsymbol{p_x}$: $[\boldsymbol{m}]$	p_y: $[m]$	v_x: $[m/s]$	v_y: $[m/s]$	ψ: $[deg]$	r: $[deg/min]$	a_t: $[m/s^2]$	a_n: $[m/s^2]$
Starboard-35	E	0.736	0.706	0.558	0.535	0.270	0.054	0.010	0.069
	U	0.736	0.706	0.554	0.533	0.270	0.054	0.010	0.069
Starboard-10	E	0.514	0.652	0.389	0.467	2.534	0.056	0.005	0.049
	U	0.514	0.652	0.388	0.466	2.534	0.056	0.005	0.049
Port-35	E	0.701	0.913	0.533	0.659	4.114	0.056	0.010	0.063
	U	0.700	0.913	0.533	0.659	4.114	0.056	0.010	0.063
Port-10	E	0.541	0.510	0.406	0.385	2.433	0.056	0.004	0.048
	U	0.541	0.510	0.406	0.385	2.433	0.056	0.004	0.048
20/20-Zigzag	E	0.562	0.541	0.428	0.432	0.270	0.056	0.004	0.053
	U	0.562	0.541	0.429	0.425	0.270	0.056	0.004	0.053
Williamson	E	0.548	0.873	0.407	0.615	4.479	0.056	0.009	0.050
	U	0.548	0.874	0.405	0.617	4.479	0.056	0.009	0.050
E: State variables estimated by CD-EKF; U: State variables estimated by CD-UKF;									

Figure 5.4: Average RMSEs of CMM State Variables from 100 Monte Carlo-based Tests. (Table from Paper I)

TABLE 3: The Average RMSEs of CTRA State Variables from 100 Monte Carlo-based Tests									
Error of State: [unit]		$\boldsymbol{p_x}$: $[\boldsymbol{m}]$	p_y: $[m]$	u: $[m/s]$	v: $[m/s]$	ψ: $[deg]$	r: $[deg/min]$	a_u: $[m/s^2]$	a_v: $[m/s^2]$
Starboard-35	E	0.741	0.713	0.178	0.767	0.274	0.054	3.952×10^{-4}	4.263×10^{-4}
	U	0.741	0.713	0.183	0.767	0.274	0.054	3.952×10^{-4}	4.262×10^{-4}
Starboard-10	E	0.514	0.548	0.104	0.570	2.277	0.055	3.959×10^{-4}	3.953×10^{-4}
	U	0.514	0.548	0.103	0.569	2.277	0.055	3.959×10^{-4}	3.954×10^{-4}
Port-35	E	0.687	0.674	0.214	0.712	3.795	0.055	3.953×10^{-4}	4.166×10^{-4}
	U	0.687	0.673	0.211	0.713	3.795	0.055	3.953×10^{-4}	4.166×10^{-4}
Port-10	E	0.546	0.515	0.118	0.559	2.434	0.056	3.927×10^{-4}	4.125×10^{-4}
	U	0.546	0.515	0.116	0.560	2.434	0.056	3.928×10^{-4}	4.125×10^{-4}
20/20-Zigzag	E	0.563	0.544	0.154	0.586	0.273	0.055	4.000×10^{-4}	5.258×10^{-4}
	U	0.563	0.544	0.151	0.587	0.273	0.055	3.999×10^{-4}	5.258×10^{-4}
Williamson	E	0.518	0.579	0.137	0.579	4.154	0.055	4.440×10^{-4}	4.524×10^{-4}
	U	0.518	0.579	0.137	0.579	4.154	0.055	4.440×10^{-4}	4.524×10^{-4}
E: State variables estimated by CD-EKF; U: State variables estimated by CD-UKF;									

Figure 5.5: Average RMSEs of CTRA State Variables from 100 Monte Carlo-based Tests. (Table from Paper I)

Paper II: Kinematic motion models based vessel state estimation to support advanced ship predictors

Paper II further advances vessel state estimation by building on the kinematic motion models developed in Paper I. In light of the findings from Paper I, where certain estimates significantly deviated from the true values, the measurement models have been refined. Four estimation scenarios with varying configurations of models and algorithms are established: CMM+EKF, CMM+UKF, CTRA+EKF, and CTRA+UKF.

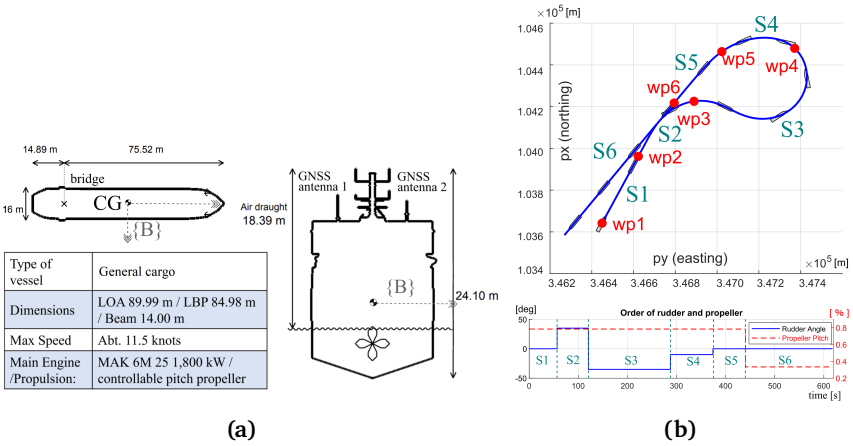

(a) **(b)**

Figure 5.6: The vessel used in the simulator and the maneuver performed. (Figure from Paper II)

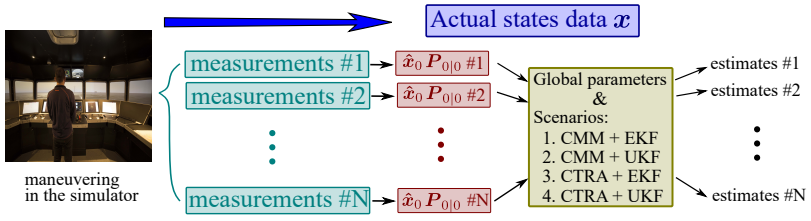

Figure 5.7: Configuration of the Monte Carlo-based simulation. (Figure from Paper II)

The evaluation involves a simulated maneuver similar to the Williamson turn, with 50 independent sets of measurements collected for this maneuver. Details regarding the vessel used, the maneuver performed, and the configuration of this Monte Carlo-based test are illustrated in Fig. 5.6 and 5.7.

To evaluate the filters in this thesis, RMSEs, along with stability and consistency tests are used. The stability test utilizes the innovation covariance matrix $\mathbf{S}$, which is integral to both the EKF and UKF. The metric for stability assessment is the reciprocal condition number of $\mathbf{S}$. A stable filter will exhibit a reciprocal

condition number close to 1, whereas an unstable filter will have a reciprocal condition number approaching 0. For the consistency test, the Normalized Innovation Squared (NIS) and autocorrelation are used. A chi-square test is used to evaluate the NIS. If the filter is well-tuned and the system model accurately represents the properties of the vessel, the NIS values should ideally follow the chi-square distribution with degrees of freedom equal to the dimension of the measurement vector. Meanwhile, the consistency test also includes a z-test with autocorrelation. This test checks whether the innovations from the estimation process are uncorrelated from one measurement to the next. In optimal estimation scenarios, such as those systems modeled by KF, the innovations should ideally be white noise. This means that they are uncorrelated and follow a normal distribution with zero mean and a variance defined by the innovation covariance matrix.

Upon analyzing 50 sets of measurement data, the stability tests reveal that the CMM+EKF configuration is the only one exhibiting instability. The instances of divergence observed in the Monte Carlo-based test comprising 50 runs are depicted in Fig. 5.8. These instances of divergence primarily occur after the ship executes a new rudder or propeller order.

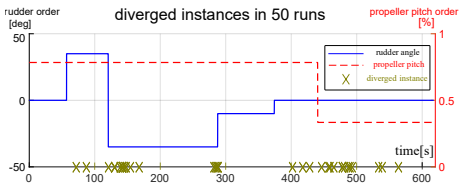

(a) Diverged instances are labeled in the time axis. The labeled positions represent the moments when the interruption occurs.

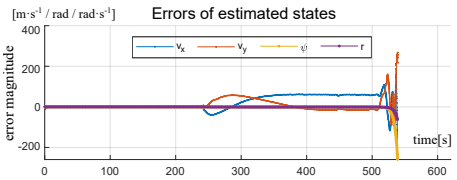

(b) The error magnitude of estimated states (v_x, v_y, ψ, r) from a diverged instance.

Figure 5.8: The stability test results of Scenario: CMM + EKF. (Figure from Paper II)

The consistency test results are depicted in Fig. 5.9. It can be seen that most of the NIS and autocorrelation values fall within the bounded area. However, at stages S2 and S3, some NIS exceed the upper bound, with a particularly large overshoot observed at S3. Similarly, a significant overshoot is also noted in the autocorrelation.

Comparing these findings with simulated maneuver data reveals that the overshoots are linked to significant changes in vessel rudder orders and shifts in heading. Specifically, at S2 and S3, the rudder executes two sharp turns: from 0 to 35 degrees, and then from 35 degrees to -35 degrees. Additionally, as the ship rotates at S3, the heading aligns with the north, causing the measured heading to switch abruptly from 360 degrees to 0 degrees. These observations suggest that the filter used in the model tends to underestimate system errors

during large steering maneuvers or sudden changes in heading.

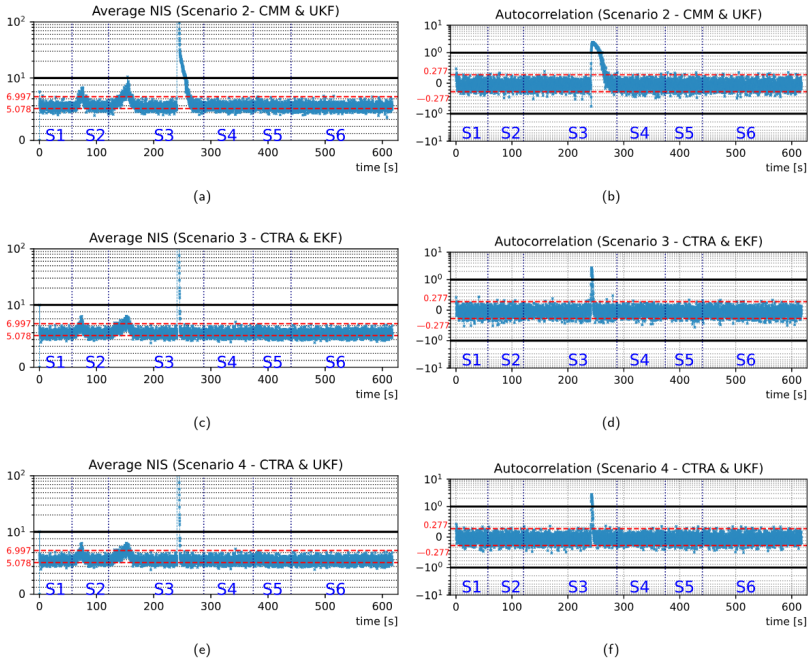

Figure 5.9: Filter consistency test based on average NIS and autocorrelation. (Figure from Paper II)

Contribution by the Author

- The author conceived the ideas with other authors.
- The author developed the methodology.
- The author developed the implementation of the simulation experiments.
- The author wrote the first draft of the manuscript.

Paper III: Coordinate Conversion and Switching Correction to Reduce Vessel Heading-Related Errors in High-Latitude Navigation.

This paper primarily addresses the heading switch issue discussed in Paper II. It further refines the combination of kinematic motion models and KF-based estimation algorithms to enhance the precision of the estimated navigation states. The focus is on improving the accuracy of vessel state estimation in high-latitude areas by tackling the challenges associated with the UTM coordinate system and heading measurements.

There are two main improvements. The first is the introduction of grid convergence into the measurement models. Grid convergence is calculated using the latitude and longitude data from the GNSS, and this calculation can be performed concurrently with the conversion of latitude and longitude to northing and easting coordinates. The second improvement involves applying a switch correction in the KF-based estimation algorithm to correct the innovation of the heading.

The vessel used is the same as in Paper II, and the simulation takes place in the Svalbard region, centered around 78° north latitude within the UTM zone 33X. Two maneuvers are executed: a straight-line course toward true north and a zigzag maneuver (see Fig. 5.10).

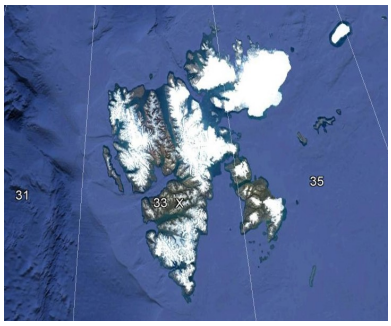

(a) Simulated area—Svalbard

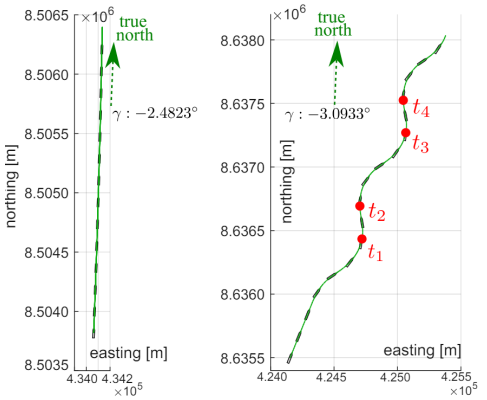

(b) The simulated straight line and zigzag maneuvers

Figure 5.10: Satellite image of the Svalbard area and vessel maneuvers (straight line and zigzag maneuver) simulated within this area from the UiT simulator. (Figure from Paper III)

For each maneuver, three scenarios are implemented for state estimation (Tab. 5.1).

The estimation results are illustrated in Fig. 5.11 to 5.13. The estimated positions

Configuration	Models with grid convergence	Algorithms with switching correction
Scenario 1	Yes	Yes
Scenario 2	Yes	No
Scenario 3	No	Yes

Table 5.1: Scenarios for vessel state estimation in simulated maneuvering executed in the UTM zone 33X.

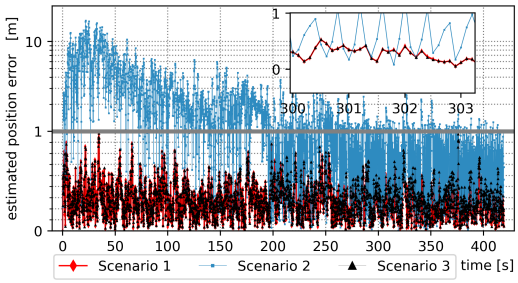

(a) straight line maneuver

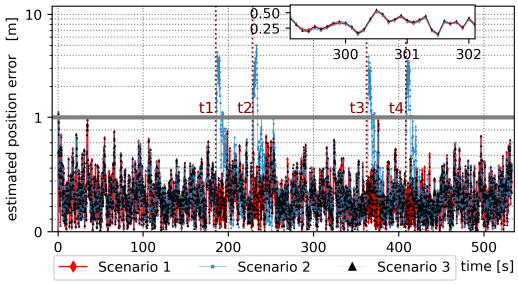

(b) zigzag maneuver

Figure 5.11: Euclidean norm of estimation position error. Errors above 1 [m] are plotted on log scale. (Figure from Paper III)

are represented by the Euclidean norm of the estimation errors. The heading estimation is shown using a specialized error metric, defined as the inner product of the angle between the two heading vectors. The surge and sway velocities are presented as both the estimated values and the actual values.

The results clearly demonstrate the importance of both modifications. The switch correction effectively resolves the algorithm's stability issues, as evidenced in Fig. 5.13, where the heading error is significantly reduced with this adjustment. Furthermore, incorporating grid convergence from coordinate conversion significantly enhances the accuracy of velocity estimates, with a notable improvement in the estimation of sway velocity (see Fig. 5.12). This improvement is crucial for accurate local-scale predictions.

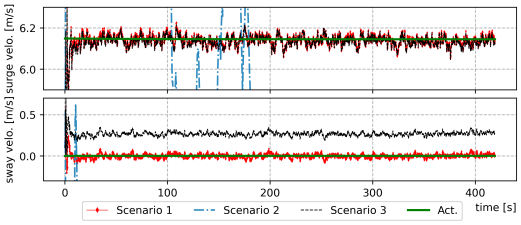

(a) straight line maneuver

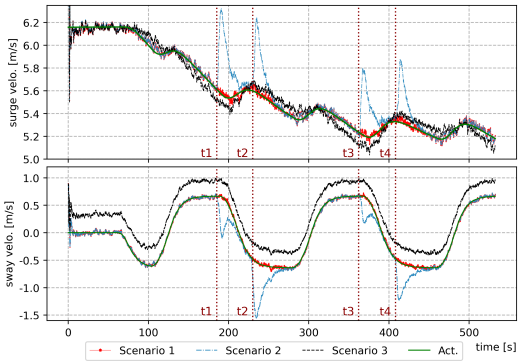

(b) zigzag maneuver

Figure 5.12: The estimated surge and sway velocity. (Figure from Paper III)

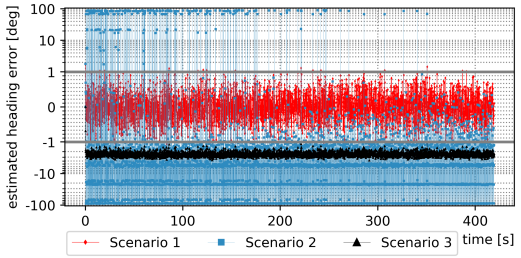

(a) straight line maneuver

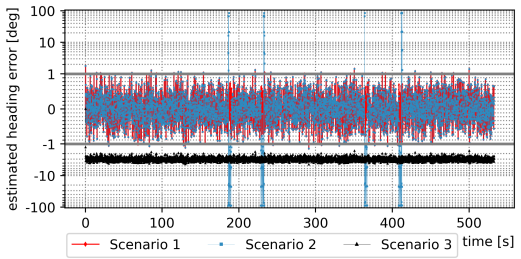

(b) zigzag maneuver

Figure 5.13: Plots of the error for heading. Errors outside $[-1°, 1°]$ are plotted on log scale. (Figure from Paper III)

Contribution by the Author

- The author conceived the ideas with other authors.
- The author developed the methodology.
- The author developed the implementation of the simulation experiments.
- The author wrote the first draft of the manuscript.

Paper IV: Adaptive Kalman Filter-Based Estimator with Sea Trail Data to Calculate Ship States in Complex Navigation Conditions.

This paper further enhances KF-based estimation by introducing an adaptive tuning algorithm. Additionally, real maneuvering data from the sea trials conducted by the Ymir RV are used to evaluate the filter's performance. An overview of the Ymir RV and the sea trial experiment is presented in Fig. 5.14. The performed maneuvers are shown in Fig. 5.15, where the measured positions are attached.

Figure 5.14: The sea trail experiment in Tromsø fjord. (Figure from Paper IV)

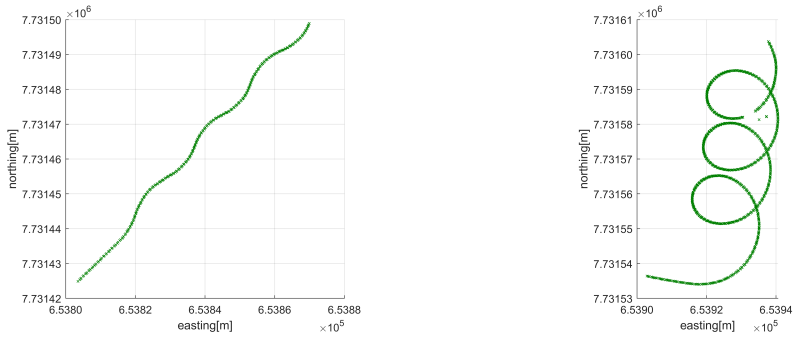

(a) zigzag maneuver **(b)** port-turning maneuver

Figure 5.15: The performed maneuvers by Ymir RV. There exist outliers of measurements in the port-tuning maneuver. (Figure from Paper IV)

To implement the adaptive tuning algorithm, a minor modification is made to the kinematic motion model. Given that filter inconsistency is triggered by steering operations, navigation states related to steering, such as heading and yaw rate, are processed separately. The CAA model is employed to describe the vessel's rotational motion with respect to the heading. Since the rudder command is not a parameter within the kinematic motion models, the innovation of turn rate can serve as an indicator of when the ship executes new rudder commands.

The CAA is designed to execute before the CMM and CTRA. When a significant

increase in turn rate r is detected, the system noise of the CMM and CTRA is adjusted by multiplying the noise covariance matrix $\mathbf{Q}$ by a scaling factor α. This paper proposes that the scaling factor α should be positively correlated with the absolute innovation of turn rate. The innovation of turn rate is denoted by $|y_r|$ in this paper. A large value of $|y_r|$ signifies that the vessel is making swift and significant maneuvers, typically in response to a substantial rudder order, which causes the ship to adjust its course more aggressively. In such cases, a larger α should be applied. However, determining the optimal α for all possible $|y_r|$ in the sea trial experiment is challenging. A practical approach is to identify several sets of best-fitting α and $|y_r|$ values through a limited number of experiments and then use regression methods to estimate the appropriate α for an unknown $|y_r|$.

This paper employs a GPR model to determine the appropriate values for α. The optimal combinations of α and $|y_r|$ are derived from the simulated maneuvers. These combination data are utilized as the training data sets for the GPR model. The simulated maneuvers are performed in the UiT simulator with a vessel similar in size and weight to that of the Ymir RV. The simulated maneuvers include multiple turns with varying rudder commands. The data sets of $|y_r|$ from the entire maneuver are categorized into four groups based on its absolute value. The original $\mathbf{Q}$ setting corresponds to the group with the smallest $|y_r|$, with α set to 1 for this group. For the other three groups, α values are assigned as 10, 20, and 30, corresponding to increasing levels of $|y_r|$. These α values used here were determined through multiple simulated maneuvers conducted in the UiT simulator. Since the simulator provides access to the vessel actual navigation state, relevant post-processing was performed to identify the optimal α. To enhance the training stability of the GPR model, zero-mean Gaussian noise is added to each value of α. The training data are presented in Fig. 5.16.

The predicted α values from the two maneuvers, based on the designed GPR model, are presented in Fig. 5.17. It is evident that the values of $|y_r|$ undergo a significant change when the Ymir RV is not engaged in a straight-line maneuver. As $|y_r|$ varies, the corresponding α values also change.

Another adaptive tuning procedure is applied to address measurement abnormalities. In the actual sea-trial experiment, a small number of measured positions were found to be abnormal. As shown in Fig. 5.15, several measured positions deviated from the expected trajectory. To handle such cases, the filters are equipped with corresponding countermeasures. When a position abnormality is detected, the measurement covariance matrix $\mathbf{R}$ is increased by a fixed scaling factor of 1000. This adjustment is based on the understanding that abnormalities are isolated incidents that occur only over a short duration. By setting a large scaling factor, the filters rely primarily on the prior

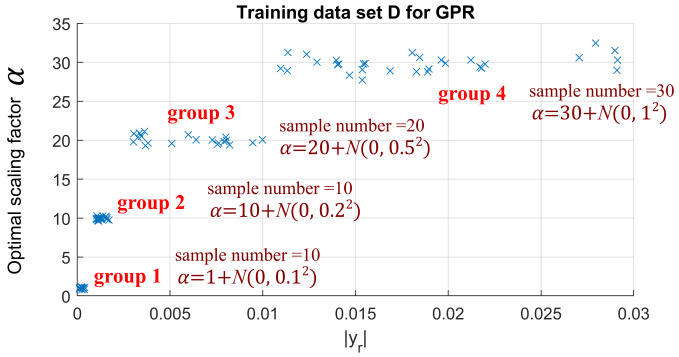

Figure 5.16: Sampled data used for the training of GPR. Noted that the values of the optimal α in each group are added with artificial white Gaussian noises. (Figure from Paper IV)

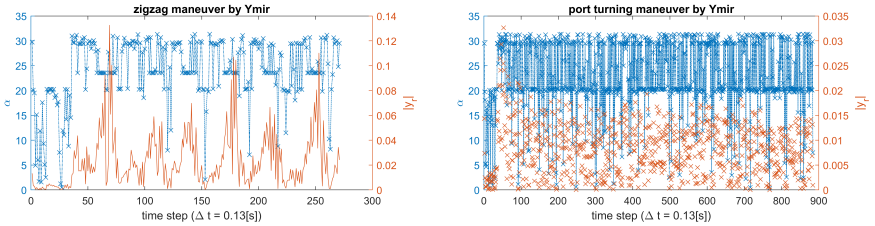

(a) Zigzag maneuver **(b)** Port-turning maneuver

Figure 5.17: Calculated $|y_r|$ and predicted α based on the GPR model. (Figure from Paper IV)

estimates during the prediction steps, minimizing the impact of the erroneous measurements.

Figure 5.18 shows the estimated velocity during the zigzag maneuver, comparing the results with and without the adaptive tuning algorithm. The results show that estimates with adaptive tuning exhibit a notably faster reaction time compared to those without it.

For the port turning maneuver, which involves several abnormal position measurements, the tuning mechanism effectively corrects these errors. As shown in Fig. 5.19, the position estimates from both models address the anomalies caused by GNSS errors. In comparison, the position estimation using the CMM performs better than that using the CTRA. The abnormal position measurements also impact the estimated velocity, leading to sudden, large-scale fluctuations. The adaptive tuning mechanism effectively mitigates these issues. However, the mitigation of the estimated sway velocity from the CTRA model is less evident compared to that from the other models (see Fig. 5.20).

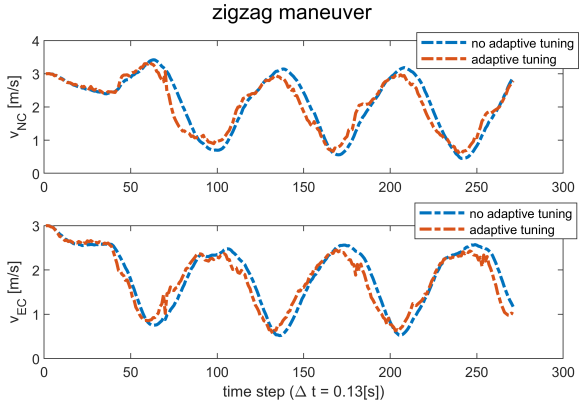

(a) Estimated velocities from the CMM

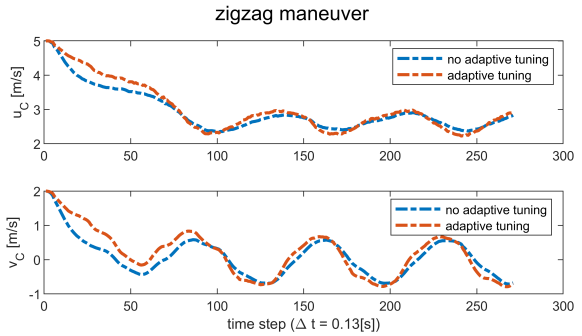

(b) Estimated velocities from the CTRA

Figure 5.18: Estimated velocities from the zigzag maneuver with and without the adaptive tuning mechanism. (Figure from Paper IV)

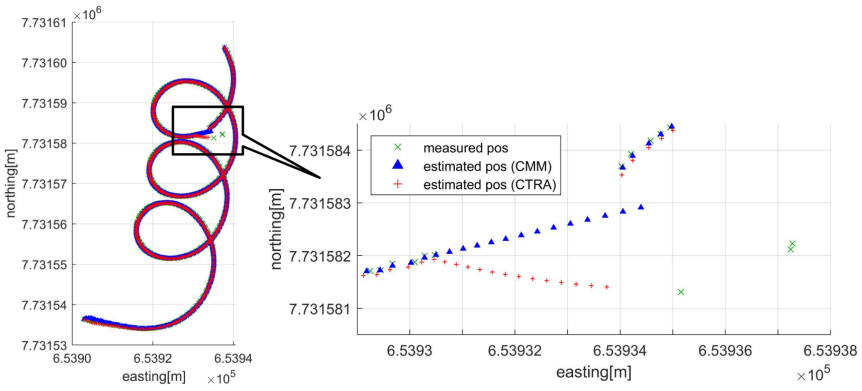

Figure 5.19: Estimated positions in the port turning maneuver. The time steps during which abnormal measurements occur are magnified for closer examination. (Figure from Paper IV)

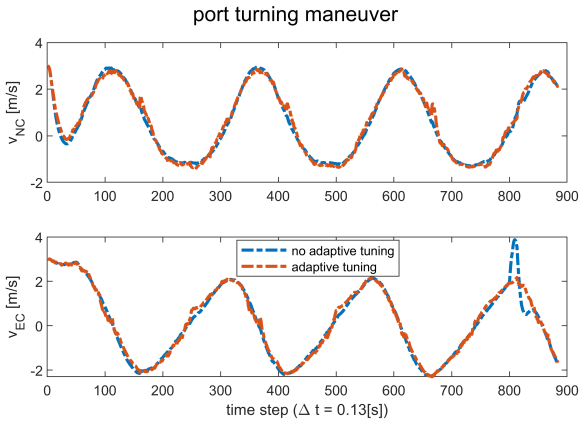

(a) Estimated velocities from the CMM

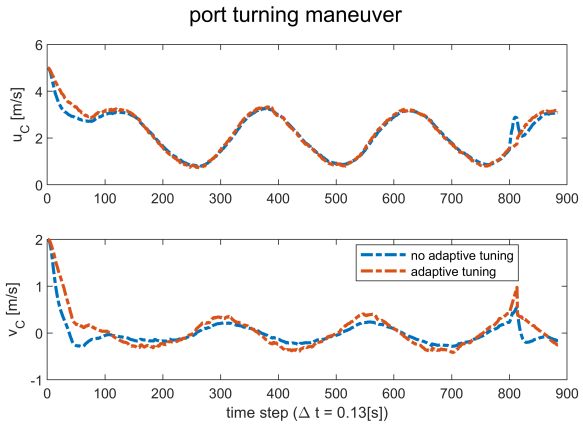

(b) Estimated velocities from the CTRA

Figure 5.20: Estimated velocities from the port turning maneuver with and without the adaptive tuning mechanism. (Figure from Paper IV)

Contribution by the Author

- The author conceived the ideas with other authors.
- The author developed the methodology.
- The author supported the configuration and sea-trail experiments of Ymir RV
- The author wrote the first draft of the manuscript.

5.2 Pivot Point-based Trajectory Prediction

This section provides a summary of trajectory prediction based on the vessel PP. This prediction relies on the estimated vessel states obtained using the methods discussed in the previous section. The estimated states are then used to calculate the location of the PP on the vessel. The trajectory prediction algorithm is designed to fully account for the influence of the PP. It generates both the position and heading of the ship. To enhance prediction accuracy, an GRU type of recurrent neural network is incorporated into the algorithm evaluation process using simulated maneuvers. The implementation of the GRU is feasible due to the availability of a large volume of maneuvering data from the UiT simulator. However, GRU support is not included in evaluations using sea trial data from the Ymir RV due to the insufficient volume of maneuvering data.

Paper V: Localized Advanced Ship Predictor for Maritime Situation Awareness with Ship Close Encounter.

Paper V compares two methods for predicting vessel trajectories on a local scale. The validation of these methods relies on simulated maneuvers from the UiT bridge simulator. The vessel used in this study is the same as that in Papers II and III. However, the onboard equipment is positioned differently. The vessel in the paper is equipped with two GNSS antennas, one at the bow and one at the stern. The IMU is situated at the geometric center of the vessel.

The kinematic motion models developed in this paper build upon the enhancements introduced in Paper IV. For vessel rotational motion, the heading, turn rate, and turn rate acceleration are detailed in the CAA. The translational motion is addressed by both the CMM and CTRA. The CMM specifically examines the behavior of the vessel's geometric center, while the CTRA is applied to describe the behavior at both the bow and stern where the GNSS antennas are located. Assuming the vessel is a rigid body, the surge velocities at the bow and stern are identical. However, the sway velocities may vary during maneuvers involving turning. Therefore, this paper determines the position of the PP by analyzing the differences in sway velocities between the bow and stern of the vessel.

In conventional ship maneuvering, experienced navigators typically estimate the PP to be located about 1/5 to 1/4 of the vessel's length from the bow when the vessel begins to turn. Consequently, this paper proposes that it is more practical to estimate the PP within a range, rather than attempting to pinpoint its exact location. Figure 5.21 presents a mapping system that designates the PP to predefined regions along the ship's centerline. This assignment is based on the sway velocities measured at the ship's bow and stern (v_1 and v_2).

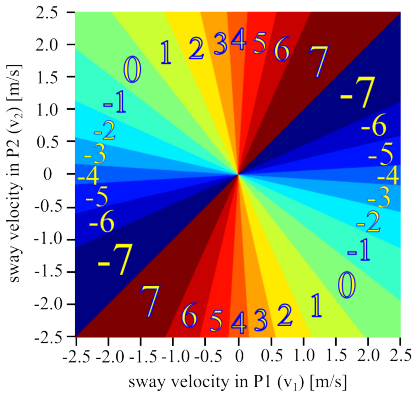

Table 4: Predefined regions and pivot point position

Region	Range in X-axis $\lvert sec\rvert = L/8$	PP coordinate in {B} (X-axis)
-7	$(-\infty, -10.5\cdot\lvert sec\rvert)$	$-20\cdot\lvert sec\rvert$
-6	$(-10.5\cdot\lvert sec\rvert, -6.5\cdot\lvert sec\rvert)$	$-8.5\cdot\lvert sec\rvert$
-5	$(-6.5\cdot\lvert sec\rvert, -4.5\cdot\lvert sec\rvert)$	$-5.5\cdot\lvert sec\rvert$
-4	$(-4.5\cdot\lvert sec\rvert, -3.5\cdot\lvert sec\rvert)$	$-4\cdot\lvert sec\rvert$
-3	$(-3.5\cdot\lvert sec\rvert, -2.5\cdot\lvert sec\rvert)$	$-3\cdot\lvert sec\rvert$
-2	$(-2.5\cdot\lvert sec\rvert, -1.5\cdot\lvert sec\rvert)$	$-2\cdot\lvert sec\rvert$
-1	$(-1.5\cdot\lvert sec\rvert, -0.5\cdot\lvert sec\rvert)$	$-1\cdot\lvert sec\rvert$
0	$(-0.5\cdot\lvert sec\rvert, 0.5\cdot\lvert sec\rvert)$	0
1	$(0.5\cdot\lvert sec\rvert, 1.5\cdot\lvert sec\rvert)$	$1\cdot\lvert sec\rvert$
2	$(1.5\cdot\lvert sec\rvert, 2.5\cdot\lvert sec\rvert)$	$2\cdot\lvert sec\rvert$
3	$(2.5\cdot\lvert sec\rvert, 3.5\cdot\lvert sec\rvert)$	$3\cdot\lvert sec\rvert$
4	$(3.5\cdot\lvert sec\rvert, 4.5\cdot\lvert sec\rvert)$	$4\cdot\lvert sec\rvert$
5	$(4.5\cdot\lvert sec\rvert, 6.5\cdot\lvert sec\rvert)$	$5.5\cdot\lvert sec\rvert$
6	$(6.5\cdot\lvert sec\rvert, 10.5\cdot\lvert sec\rvert)$	$8.5\cdot\lvert sec\rvert$
7	$(10.5\cdot\lvert sec\rvert, \infty)$	$20\cdot\lvert sec\rvert$

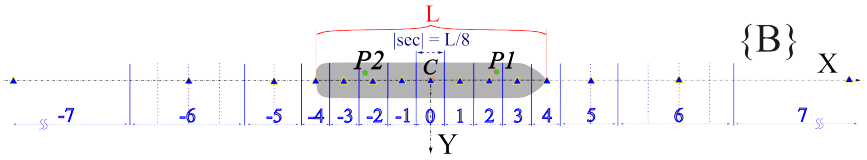

Figure 5.21: The mapping between v_1, v_2, and predefined regions of PP. (Figure from Paper V)

The vessel's centerline is divided into multiple segments, numbered from -7 to 7. The vessel PP is set to be located at the center of these segments. These regions vary in length: regions farther from the midsection (Region 5, 6, and 7) near the bow and stern are longer, while those closer to the midsection (Region 0 to 5) on the hull are shorter. When the PP is identified within a region, the trajectory prediction algorithm quantifies its position as being at the midpoint of that region.

The trajectory of the simulated maneuver used for validation is shown in Fig. 5.22. The red mark on the figure represents the position where the vessel executes a new rudder order, while the blue mark indicates the positions where the vessel has not executed any new command orders. The local-scale predictions start from all these marked positions, with a prediction horizon of 90 seconds.

The prediction is performed using two distinct methods: the kinematic-based method and the GRU-PP-based method. The kinematic-based method consistently uses kinematic motion models for predictions. It operates recursively, similar to KF-based estimation processes, yet it does not include the filtering step by measurements. The GRU-PP-based method combines the GRU neural network with the vessel PP. This GRU is trained on a large amount of vessel maneuvering data collected from the simulator. This training enables it to predict the next surge and sway velocities at the ship's bow and stern based on different rudder commands. These predicted states are used to determine the

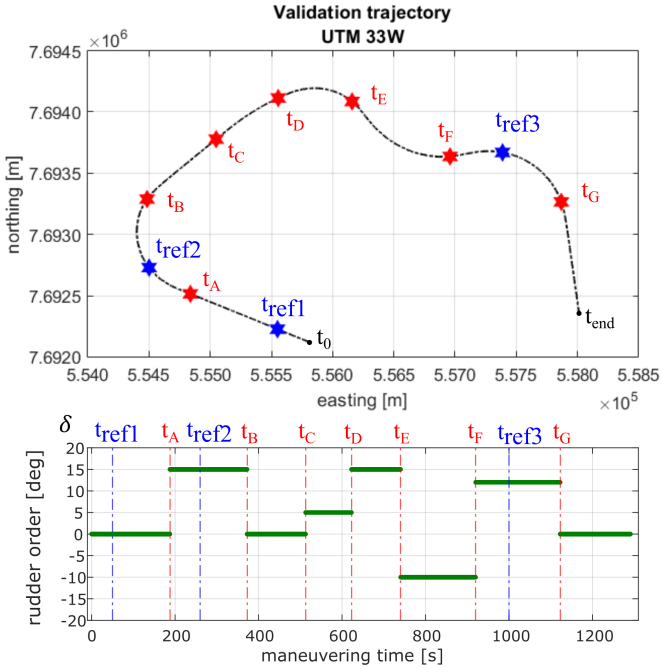

Figure 5.22: Trajectory of the validation maneuver and the related rudder order. The prediction starts from these labeled time steps. (Figure from Paper V)

vessel PP, which is considered the center of rotational motion in the horizontal plane. The final trajectory prediction algorithm employs this characteristic of the PP to accurately predict the vessel's position and heading.

The prediction results are divided into two groups. The first group (see Fig. 5.23) presents the average prediction errors corresponding to new rudder orders, highlighted by the red-marked positions in Fig. 5.22. The second group (see Fig. 5.24) shows the average prediction errors for predictions starting from the blue-marked positions, where no new rudder orders are given.

It is evident that the GRU-PP-based method offers a distinct advantage for predictions initiated with new rudder orders. This method significantly enhances accuracy within the 90-second prediction horizon. In contrast, the kinematic-based method begins to show significant errors after 45 seconds. Significant heading inaccuracies begin to emerge as soon as 30 seconds into the prediction. Each method has its own strengths depending on the conditions. Combining them could lead to a substantial improvement in local-scale prediction capabilities.

Contribution by the Author

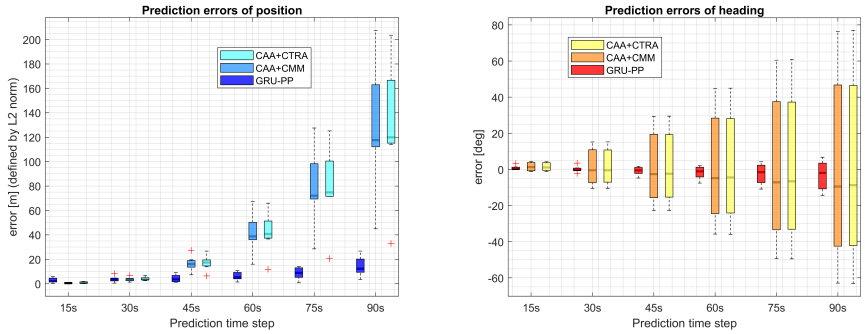

(a) Prediction errors of position **(b)** Prediction errors of heading

Figure 5.23: Average prediction errors of position and heading. Predictions start with new rudder orders. (Figure from Paper V)

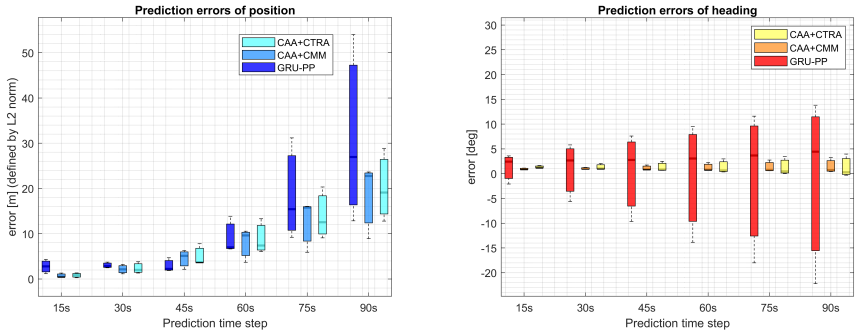

(a) Prediction errors of position **(b)** Prediction errors of heading

Figure 5.24: Average prediction errors of position and heading. Predictions start without new rudder orders. (Figure from Paper V)

- The author conceived the ideas with other authors.
- The author developed the methodology.
- The author developed the implementation of the simulation experiment.
- The author wrote the first draft of the manuscript.

Paper VI: Pivot Point Estimation based Advanced Ship Predictor Evaluation with Vessel Maneuvers under Sea Trial Conditions.

This article builds upon the work presented in Paper IV by evaluating the performance of the local-scale ASP using sea trial maneuvering data from the Ymir RV. In this evaluation, the focus is not only on vessel state estimation but also on trajectory prediction based on the vessel PP calculated by a designed GPR model.

For vessel state estimation, this paper addresses many of the practical challenges encountered during sea trials. Considering that the Ymir RV is a relatively small vessel, it exhibits sensitive seakeeping characteristics, leading to more pronounced rolling and pitching during turns or changes in rudder orders. Using CMM and CTRA to model ship maneuvering behavior in a two-dimensional plane may not be effective for the Ymir RV. Therefore, this paper considers the 3D-PV model to describe the translational motion of the Ymir RV in three dimensions. The reference frames defined and utilized in the kinematic motion models can be found in the attached paper.

The method from Paper V for calculating the vessel's PP is not suitable, as the Ymir RV cannot provide two synchronized position measurements at the current stage. Since there are no position measurements at the bow and stern, it is not possible to estimate the sway velocities at these locations. As a result, a new approach based on the GPR is introduced for the calculation of the vessel PP in this paper. The new approach assumes that the vessel is a rigid body and that its maneuverability in the sway direction is limited. Under the assumption that the vessel is a rigid body, it does not deform. Consequently, the surge velocities at all points on the vessel remain constant during turning maneuvers. Meanwhile, the sway velocities along the centerline display a linear distribution. Therefore, when the sway velocities at two distinct points on the vessel (such as the bow and stern) are known, it becomes possible to uniquely determine the sway velocity at any location on the vessel. Additionally, these sway velocities at two distinct points also uniquely determine the vessel's turn rate. The limited maneuverability in the sway direction indicates that the sway velocities during different maneuvers are relatively smaller compared with the surge velocities.

The GPR model for PP calculation is based on the assumption that the sway velocities at both the bow and stern (denoted as v_{bow} and v_{stern}) have a limited range. For example, the sway velocities of the Ymir RV are assumed to range from -5 to 5 [m/s] in this paper. All possible combinations of (v_{bow}, v_{stern}) can thus be enumerated. Each pair of (v_{bow}, v_{stern}) corresponds to a specific value of the PP location (L_{PP}) and the associated sway velocity (v_h) and turn rate (r). Here, r represents the turn rate, and v_h is the sway velocity provided by the KF-

based estimation. This process establishes a mapping from (v_h, r) to L_{PP}. Given an unknown input of (v_h, r), the GPR model can predict the corresponding L_{PP}. Figure 5.25 displays the training datasets for the GPR model. These datasets consist of 10,000 samples, each created by combining values from 100 distinct (v_{bow}) and 100 distinct (v_{stern}).

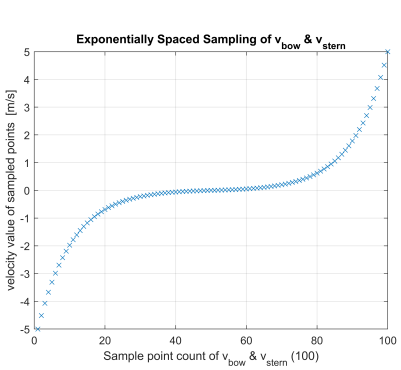

(a) The sampled values of v_{bow} and v_{stern}.

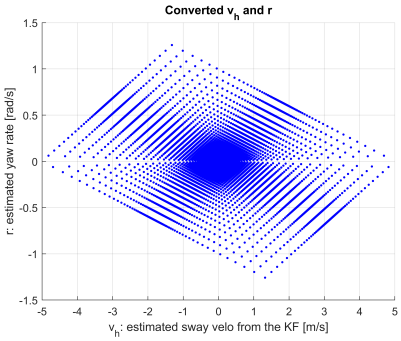

(b) The conrresond v_h and r calculated from the sampled v_{bow} and v_{stern}

Figure 5.25: The generation of training data for the GPR model (Figure from Paper VI)

Two maneuvers (Port Turning and Starboard Turning) performed by the Ymir RV are used for evaluation (Fig. 5.26 & 5.27). The local-scale predictions start from several selected time steps, with a prediction horizon of 10 seconds.

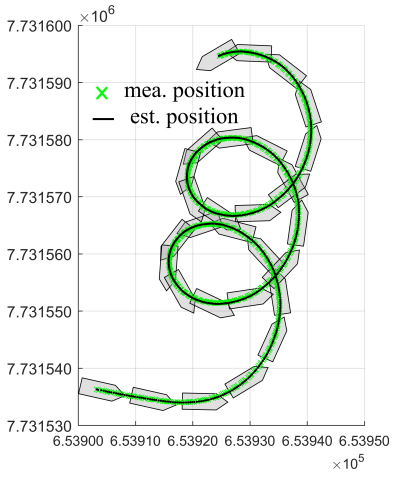

(a) estimated and measured position

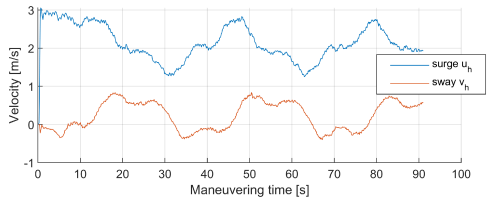

(b) estimated surge and sway velocity

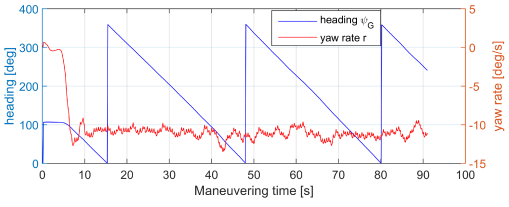

(c) estimated heading and yaw rate

Figure 5.26: Estimated vessel states from Port Turning (Figure from Paper VI)

The prediction algorithm is similar to the one used in Paper V. However, there is no support from the GRU neural network for predicting surge and sway velocities. The prediction is based on the vessel navigation states provided by

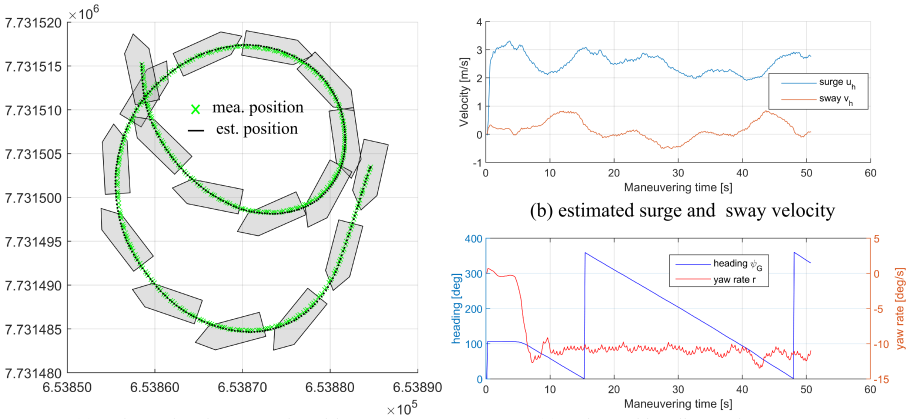

(a) estimated and measured position

(b) estimated surge and sway velocity

(c) estimated heading and yaw rate

Figure 5.27: Estimated vessel states from Starboard Turning (Figure from Paper VI)

the latest KF-based estimation step. The prediction results are illustrated in Fig. 5.28 and 5.29.

In both maneuvers, it is observed that the predictions made immediately after the rudder is activated are not entirely accurate (Fig. 5.28a and 5.29a). However, the Ymir RV demonstrates rapid response capabilities. Within just 2 seconds, the quality of the predictions improves significantly. In subsequent predictions, the predicted positions show some drift relative to the actual positions. This drift is due to the influence of sea currents in the Tromsø fjord, which the prediction algorithm does not account for. The heading predictions are of relatively accurate quality compared to the position predictions.

Contribution by the Author

- The author conceived the ideas with other authors.
- The author developed the methodology.
- The author supported the configuration and sea-trail experiments of Ymir RV
- The author wrote the first draft of the manuscript.

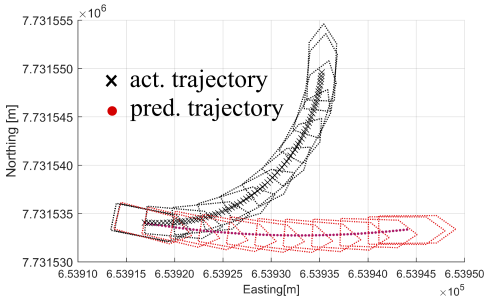

(a) prediction begins at t = 5[s]

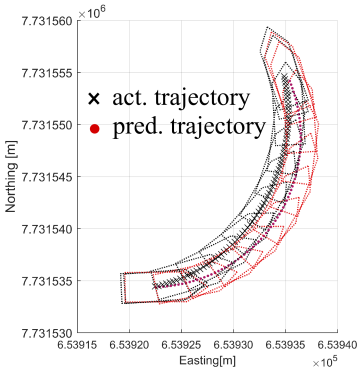

(b) prediction begins at t = 7[s]

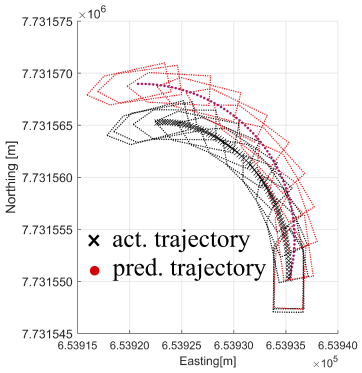

(c) prediction begins at t = 15[s]

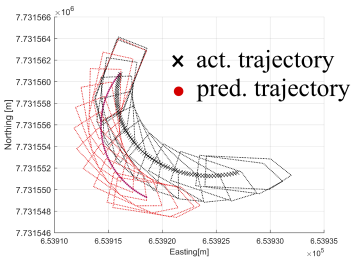

(d) prediction begins at t = 30[s]

Figure 5.28: Prediction results of Port Turning. (Figure from Paper VI)

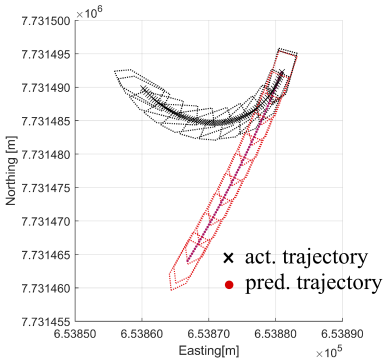

(a) prediction begins at t = 4[s]

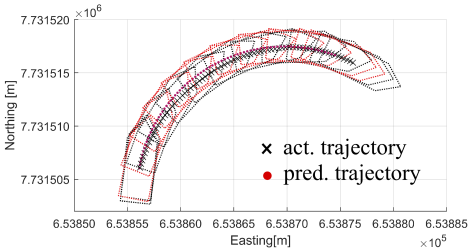

(c) prediction begins at t = 20[s]

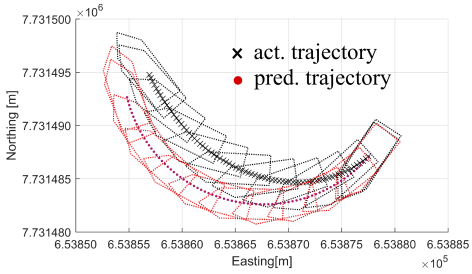

(b) prediction begins at t = 6[s]

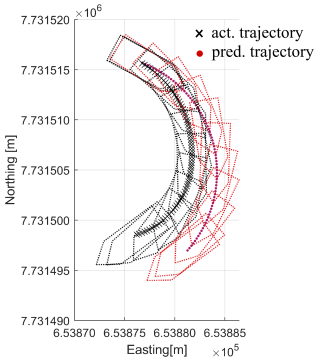

(d) prediction begins at t = 30[s]

Figure 5.29: Prediction results of Starboard Turning. (Figure from Paper VI)

Chapter 6

Results Discussion

This chapter presents a discussion of the reseoutcomearch results. The first section outlines how the appended paper contributes to the research objectives. The next section offers a more general discussion of the functionalities of the local-scale ASP in supporting level 3 situation awareness.

6.1 Summary of the Contribution to Research Objectives

The contribution of each article to the research objectives is shown in Tab. 6.1.

	RO1(i)	**RO1**(ii)	**RO2**(i)	**RO2**(ii)	**RO3**(i)	**RO3**(ii)
Paper I	× × ×	× × ×			× ×	
Paper II	× × ×	× × ×			× × ×	
Paper III	× ×	× ×			× ×	
Paper IV	× × ×	× × ×				× ×
Paper V		× ×	× × ×	× × ×	× ×	
Paper VI	× ×	× ×	× × ×	× × ×		× × ×

Table 6.1: The fulfillment of research objectives

RO1(i): Identify the kinematic motion models that best describe the ship maneuvering behaviors.

The thesis demonstrates that the kinematic motion models, CMM and CTRA, are effective alternatives for linear motion models. Both models are grounded in the representation of the vessel's general motion as curvilinear. Nonetheless, various adjustments are necessary to enhance estimation accuracy. For instance, measurement models should be adapted based on the properties of the installed sensors. Additionally, the local-scale predictions using the UTM-based position data must account for grid convergence effects at high latitudes.

When analyzing the sea trial maneuvering data, the actual sea environment proved to be more complex than the simulations suggested. To address this issue, Paper IV recommends using the CAA to specifically account for aspects of rotational motion. The CAA also acts as an indicator for detecting changes in vessel motion in response to new rudder orders. In Paper VI, the CAA and the newly introduced 3D-PV are used together to model the Ymir RV. Since the vessel is treated as a rigid body, the CAA describes its rotational motion, while the 3D-PV accounts for its translational motion. This configuration takes into account that the lightweight Ymir RV experiences significant roll and pitch motions during various maneuvers.

RO1(ii): Apply appropriate KF-based estimation algorithms to estimate the ship navigation states.

The thesis demonstrates that both EKF and UKF perform well with the nonlinear CMM and CTRA models. However, the UKF exhibits superior stability compared to the EKF in the CMM applications, as detailed in Paper II. To handle the complex sea conditions encountered during sea trial experiments, an adaptive tuning mechanism is integrated into the KF-based estimation algorithms. This mechanism adjusts the system error covariance matrix **Q** within the algorithm, with the innovation of turn rate estimated from the CAA serving as an indicator of when to apply adaptive tuning. Additionally, the adaptive tuning mechanism modifies the measurement error covariance matrix **R** when abnormalities in the GNSS measurements are detected. Through these adaptive tuning strategies, the estimation algorithms demonstrate enhanced performance and robustness in real-world applications.

RO2(i): Calculate the location of the PP based on the estimated navigation states.

Two methods for calculating the location of the PP have been developed. In the first method, the vessel PP is assigned to predefined regions based on the sway velocities measured at the bow and stern, where the GNSS antennas are installed. Using a mapping system, the location of the PP can be quickly determined. The second method calculates the PP using a GPR model. Assuming the vessel behaves as a rigid body, the estimated sway velocity at a single point

and the estimated turn rate are used to convert into sway velocities at the bow and stern. These converted velocities serve as inputs to the GPR model. The prediction results show that both methods successfully achieve the desired outcomes.

RO2(ii): Design the trajectory prediction method based on the understanding of the PP.

The trajectory prediction method in this thesis is based on the rigid body assumption, which allows the vessel's general motion to be decomposed into translational and rotational components. Under this assumption, the PP is treated as the center of rotational motion. This approach has proven effective for local-scale predictions. It provides accurate estimates of both the vessel's position and heading.

Trajectory prediction based on the vessel's PP can be further enhanced by integrating it with a GRU neural network. In the evaluation using simulated maneuvers, the GRU is trained on the simulated maneuvering datasets from the simulator. With the GRU providing predicted surge and sway velocities, the local-scale ASP is able to make predictions starting from the time steps when new rudder orders are executed.

RO3(i): The evaluation of the implemented methods through simulated maneuvering from the UiT bridge simulator.

One advantage of utilizing simulated maneuvering data is the ability to implement Monte Carlo-based simulations. In Paper I, Monte Carlo-based simulations demonstrated that both the EKF and UKF exhibit similar performance levels. Paper II built upon previous findings by incorporating consistency and stability tests. These tests revealed that the EKF could become unstable when used with highly nonlinear kinematic motion models, such as the CMM. Furthermore, the application of simulated data demonstrated that, in high-latitude regions, the use of the UTM coordinate system can lead to considerable discrepancies between grid heading and true heading. If these deviations are not corrected, they can significantly impair the accuracy of estimations.

RO3(ii): The evaluation of the implemented methods through sea-trial experimental maneuvering from the UiT research vessel-Ymir RV.

The sea trial maneuvering data indicated that the simulators cannot accurately replicate certain complex sea conditions. The use of fixed $\mathbf{Q}$ and $\mathbf{R}$ configurations in the KF-based algorithms resulted in diminished accuracy of state estimation when applied to the complex sea conditions of sea trial experiments conducted by the Ymir RV. To improve this, the kinematic motion models were

further optimized. Moreover, an adaptive tuning method was incorporated into the KF-based algorithms, as elaborated in Paper IV. The evaluation using sea trial maneuvering data highlighted the need for additional considerations to improve estimation accuracy in real sea conditions. Key factors include the performance and configuration of sensors, as well as the seakeeping abilities of the experimental vessel. These aspects are explored in Paper VI.

6.2 General Discussion

This section provides a general discussion of the functionalities of the local-scale ASP in relation to the research objectives.

6.2.1 Vessel Navigation State Estimation

In Paper I, the CMM and CTRA were employed for their ability to more accurately represent the general motion of a rigid body. Paper II improved the measurement models to better match the specific characteristics of the simulator data. Paper III corrected heading errors related to the UTM coordinate system and adjusted the CTRA accordingly. These enhancements have resulted in greater precision in the estimated vessel navigation states. However, it is important to note that the CMM's high degree of nonlinearity can lead to instability when applying the EKF algorithm.

The sea trial maneuvering data collected using the Ymir RV in Tromsø Fjord significantly differ from the data generated by the simulator. First, the Ymir RV is a relatively lightweight vessel with limited seakeeping capabilities. Additionally, the actual sea conditions in Tromsø Fjord are complex and include many elements that simulators cannot accurately replicate. Consequently, the kinematic motion models and KF-based algorithms were further refined to accommodate these sea trial maneuvering data. In Paper IV, the vessel navigation states related to rotational motion—specifically heading and turn rate—were isolated and developed into a new model termed CAA. This model represents the vessel's rotation through constant angular acceleration. The updated CMM and CTRA now primarily describe the vessel's translational motion.

Considering the Ymir RV's high maneuverability and rapid state changes in response to rudder adjustments, the KF-based algorithm was updated with adaptive tuning capabilities. This adaptive tuning mechanism correlates with the innovation of turn rate the CAA. As the kinematic motion models do not incorporate rudder angle information, the innovation of turn rate is used as an indicator to determine whether the vessel has executed a turning maneuver.

Paper VI examines the impact of the Ymir's sensitive seakeeping characteristics and the configuration of its onboard sensors. Significant roll and pitch during navigation notably affect sensor readings, especially those from the IMU. To mitigate this issue, the 3D-PV model was employed. Accelerations from the IMU were corrected before use, and these corrected values were then used as inputs to the model. The results presented in Paper VI demonstrate that the 3D-PV model, when integrated with adaptive tuning, consistently maintains filter accuracy.

Limitation

The rudder orders and engine power are not included as parameters in the kinematic motion models. Consequently, when the vessel is in an unsteady state due to changes in rudder orders or engine power, the accuracy of the estimations may decrease. The consistency test conducted in Paper II confirmed also that the filter shows inconsistencies during changes in rudder orders or engine power.

Although later improvements were made by using the CAA to detect when a new rudder order is executed, this approach relies on the assumption that the turn rate acceleration remains constant during the tuning maneuvering. However, for vessels with high maneuverability, this assumption may not hold true. Furthermore, the scale factors used for the system noise covariance ($\mathbf{Q}$) and measurement noise covariance ($\mathbf{R}$) in the KF-based estimation adaptive tuning mechanism need to be carefully evaluated. Due to the limited number of sea trial experiments, the scale factor used in Paper VI was specifically tailored to the conditions of that particular environment. Additional experiments are necessary to identify the optimal scaling factors for different conditions.

6.2.2 The PP-based Trajectory Prediction

The local-scale trajectory prediction, enhanced by the understanding of the vessel PP, demonstrates outstanding performance. Both the simulated and sea-trial maneuvering yielded good validation results. With the extensive amount of simulated maneuvering data available, combining the GRU with the PP enables immediate and accurate predictions after executing new rudder orders.

When evaluating sea trial maneuvering data, a GPR model was used to calculate the PP. The absence of adequate sea trial maneuvering data limited the use of tools like the GRU, leading to significant inaccuracies in predictions immediately following a new rudder order. However, the Ymir RV's high maneuverability allows it to quickly reach new steady states after executing rudder

commands. The prediction algorithms thus restored their accuracy once the Ymir RV returned to steady state.

Limitation

It is important to note that the vessel used in the simulator differs from the Ymir RV. The vessel used in the simulator has a larger tonnage and greater inertia. Consequently, it takes a longer reaction time to respond to new rudder orders. The longer reaction time is advantageous for making predictions over extended horizons, such as the 90-second prediction window discussed in Paper V. Furthermore, the larger inertia of the simulator's vessel makes it less susceptible to external factors such as wind, waves, and ocean currents. These factors can thus be disregarded in predictions if necessary. However, the Ymir RV is a smaller vessel with lower inertia. As a result, predicting its behavior in complex sea conditions requires taking more factors into account. For example, the strong sea currents in the Tromsø Fjord have a significant impact on smaller vessels like the Ymir RV. The prediction results presented in Paper VI demonstrate that neglecting the influence of ocean currents leads to biased outcomes. The limited amount of sea trial maneuvering data is also a significant limitation. Due to this scarcity of data, there is no GRU support for the local-scale prediction of the Ymir RV. As a result, the quality of predictions noticeably decreases when new rudder commands are issued.

6.2.3 The Support to Level 3 Situation Awareness

The designed local-scale ASP effectively supports Level 3 Situation Awareness in ship navigation. The predicted trajectories generated by the ASP provide essential guidance to both human and possibly future digital navigators that will navigate autonomous vessels. In general, large ships need time to change their motion by adjusting the rudder or altering the engine status. With the support of the local-scale ASP, collision risk can be estimated in a early stage and avoidance decisions can be made well in advance. In addition, since the local-scale prediction is based on an understanding of the vessel PP, it is particularly useful for maneuvers requiring this knowledge, such as entering a port, mooring, or avoiding nearby obstacles.

The prediction results can be integrated into ship bridge systems, such as ARPA or ECDIS, and shared with Vessel Traffic Service (VTS) centers and nearby vessels. As maritime digitization advances, future navigation safety will increasingly rely on the cooperation of multiple vessels within the same area. Sharing the predictions from the designed ASP can enhance overall situation awareness across the fleet, leading to more effective management of complex

maritime environments.

Limitation

To report prediction results, it is more appropriate to express them in terms of probability distributions. Presenting results as probability distributions offers a deeper understanding of the range of possible outcomes and highlights the inherent uncertainty in the prediction process. The results from the local-scale ASP presented in this thesis represent the most probable predictions. However, it would be even more beneficial if these predictions also accounted for and displayed all associated uncertainties. For instance, if the prediction identifies a region where a vessel has a 95% probability of being within the prediction horizon, decisions should take the entire region into account.

Additionally, it is important to note that the support for level 3 situation awareness is based on maintaining the foundations of levels 1 and 2. The predictions provided by the local-scale ASP assume that the vessel's onboard sensors are functioning properly. However, as demonstrated in Paper IV, the GNSS anomalies occurred at certain time steps. In Paper IV, an adaptive tuning method was employed to correct the impact of the GNSS data anomalies. However, it is important to note that the GNSS anomalies were infrequent and that the data quickly returned to normal. If more sensors experience anomalies or if anomalous data persist for an extended period, the KF-based estimation algorithm may fail to function properly. This is particularly concerning for autonomous shipping, where timely human intervention may be lacking. Therefore, in further development of the local-scale ASP, it should include mechanisms for detecting abnormal data states and procedures for handling data identified as abnormal.

Chapter 7

Conclusions

The conclusion of this thesis is presented in this chapter. Together, several suggestions and recommendations are also listed for the future work of the development of the local-scale ASP.

7.1 Concluding Remarks

Enhancing situation awareness is essential for ensuring safe and effective maritime navigation. Attaining the highest level of situation awareness is particularly critical in complex maritime environments where manned, remotely-controlled, and autonomous vessels operate in shared waters. Given the current limitations in achieving the highest level of situation awareness, particularly in predicting vessel behaviors, the local-scale ASP has been developed.

The workflow of the local-scale ASP consists of two main components: vessel navigation state estimation and PP-based trajectory prediction. In vessel navigation state estimation, the ASP employs the KF-based algorithms. This method incorporates various kinematic motion models and measurements from onboard equipment, treating the ship as a rigid body in the modeling process. The kinematic motion model has been continuously refined during the research process to improve estimation accuracy. For example, when simulating maneuvers with a large-tonnage ship, the model simplifies motion to a two-dimensional plane with three Degree of Freedoms (DOFs). During sea trials with the Ymir RV, a smaller vessel navigating the complex conditions of

Tromsø Fjord, the model is adjusted to three-dimensional space to accurately account for pitch and roll angles, thereby minimizing significant errors.

Since the classic KF are designed for linear models, the EKF and UKF are used for nonlinear scenarios. The estimation algorithms for nonlinear systems are further refined to handle continuous-time nonlinear models by using numerical methods to solve the system models. Additionally, the CAA is integrated into these algorithms, enabling them to incorporate adaptive tuning techniques. The vessel state estimation using KF-based algorithms has proven effective in both simulated maneuvers and sea trials. Furthermore, during the validation process, issues with using the UTM coordinate system at high latitudes were identified and adequate solutions were proposed.

In PP-based trajectory prediction, the ASP performs trajectory prediction using the vessel's PP, which is calculated from the estimated states. The prediction is conducted on a two-dimensional plane. Given that the vessel is modeled as a rigid body, the trajectory prediction includes both the vessel's position and its heading. Based on different configurations of onboard equipment, the thesis implements two methods to calculate the PP. The first method utilizes the relationship between the sway velocities at the bow and stern of the ship to locate the PP within pre-defined regions. The second method employs a GPR model, assuming the vessel's sway velocity is within a specific range. By enumerating the distribution of sway velocities at the bow and stern, relevant training data for the GPR model are generated. This GPR model then maps the sway velocity at a given point and turn rate to the corresponding PP value.

The vessel's heading is updated and adjusted based on the calculated PP, which is used as the center of rotational motion of a rigid body-assumed vessel. The PP-based trajectory prediction algorithm has demonstrated strong performance in predicting both simulated maneuvers and sea trial maneuvers. In particular, when combined with the GRU model for simulated maneuvers, the algorithm achieves accurate predictions starting from the moment when a new rudder order is executed. Incorporating the vessel PP into the trajectory prediction enables the predicting of the swept area over the prediction horizon. Anticipating this swept area in advance is vital for navigational safety, as it enables proactive assessment of potential obstacles that could impact safe navigation.

In summary, this thesis introduces a designed local-scale ASP aimed at supporting level 3 situation awareness. The performance of this ASP has been evaluated through both simulations and sea trials. These evaluations have demonstrated its effectiveness. However, it is advisable to conduct more sea trials in the future, as the simulator may not accurately predict all challenges

encountered in real-world conditions. For example, strong sea currents in Tromsø Fjord have affected prediction performance. Taking these factors into account in future tests could enhance the functionality of the ASP. Ultimately, it is anticipated that the developed local-scale ASP will be integrated into bridge systems to support a range of vessel operations, encompassing conventional manned, remotely-controlled, and autonomous vessels.

7.2 Future Work

There are two key areas for future proposals. First, there is a need to further enhance the performances of the local-scale ASP. The following suggestions are being considered:

- Further analysis will focus on how complex sea conditions affect the Ymir RV. One critical factor is the sea current. The narrowness of Tromsø Fjord results in stronger sea currents. This effect should be further investigated in the trajectory prediction.

- Apart from sea currents, another critical environmental factor affecting vessel maneuvering in Tromsø Fjord is the wave activity. Due to the relatively enclosed nature of the Tromsø Fjord, wind-driven waves and Kelvin wakes generated by passing vessels have the most significant impact on navigation in this area. Considering these environmental factors can optimize the parameter initialization in the KF-based algorithms.

- More sea trials should be conducted with the Ymir RV. Once sufficient training data sets are available, the use of GRU for the prediction with the Ymir RV will be explored.

- The probability of measurement abnormalities can also be investigated in advance.

- It is advisable to demonstrate the prediction results alongside the probability distribution. The calculation of the relevant probability distribution can be based on the confidence intervals from the KF-based estimates, as well as regression results from the GPR.

Second, this thesis examines the performance of the designed local-scale ASP specifically for the own ship. Future research should investigate how these predictions could influence decision-making during vessel maneuvering by providing level 3 situation awareness. This investigation can include the following suggested tasks:

- Develop a system for sharing predictions from the ASP among multiple vessels within the same sea area.

- Integrate the predictions into a vessel's bridge system and conduct vessel maneuvers. Initially, this experiment can be carried out using a simulator. Analyze the differences in maneuvering performance with and without the support of ASP predictions.

- Further research can focus also on how these predictions can enhance various collision alarm algorithms.

Aiello, G., Giallanza, A., and Mascarella, G. (2020). Towards shipping 4.0. a preliminary gap analysis. *Procedia Manufacturing*, 42:24–29. International Conference on Industry 4.0 and Smart Manufacturing (ISM 2019).

Ait Allal, A., Mansouri, K., Mohamed, Y., and Qbadou, M. (2018). Toward energy saving and environmental protection by implementation of autonomous ship. pages 177–180.

Ang, J. H., Goh, C., Saldivar, A. A. F., and Li, Y. (2017). Energy-efficient through-life smart design, manufacturing and operation of ships in an industry 4.0 environment. *Energies*, 10(5).

Artikis, A. and Zissis, D. (2021). *Guide to Maritime Informatics*. Springer.

Askari, H. R. and Hossain, M. N. (2022). Towards utilizing autonomous ships: A viable advance in industry 4.0. *Journal of International Maritime Safety, Environmental Affairs, and Shipping*, 6(1):39–49.

Batlle, J. and Condomines, A. (2020). *Rigid Body Kinematics*. Cambridge University Press.

Cahuantzi, R., Chen, X., and Güttel, S. (2023). *A Comparison of LSTM and GRU Networks for Learning Symbolic Sequences*, page 771–785. Springer Nature Switzerland.

Choi, H., Van Merrienboer, J. J. G., and Paas, F. (2014). Effects of the physical environment on cognitive load and learning: Towards a new model of cognitive load. *Educational Psychology Review*, 26:225–244.

Chung, J., Gulcehre, C., Cho, K., and Bengio, Y. (2014). Empirical evaluation of gated recurrent neural networks on sequence modeling.

Clark, I. (2005). *Ship Dynamics for Mariners: A Guide to the Theory of Hull Resistance, Power Requirements, Propulsion, Steering, Control Systems and Ship Motion in a Seaway*. Nautical Institute.

Dixon, W. E., Behal, A., Dawson, D. M., and Nagarkatti, S. P. (2003). *Underactuated Systems*, pages 269–335. Birkhäuser Boston, Boston, MA.

DNV-GL (2018a). Autonomous and remotely-operated ships.

DNV-GL (Sep, 2018b). Class guideline: Autonomous and remotely operated ships. Technical report, DNV-GL. DNVGL-CG-0264.

EMSA (Jun, 2023). Annual overview of marine casualties and incidents 2023. Investigation report, European Maritime Safety Agency.

Endsley, M. (1988). Design and evaluation for situation awareness enhancement. volume 32.

Endsley, M. (1995a). Endsley, m.r.: Toward a theory of situation awareness in dynamic systems. *Human Factors: The Journal of the Human Factors and Ergonomics Society*, 37:32–64.

Endsley, M. (1995b). Endsley, m.r.: Toward a theory of situation awareness in dynamic systems. human factors journal 37(1), 32-64. *Human Factors: The Journal of the Human Factors and Ergonomics Society*, 37:32–64.

Endsley, M. (2015). Situation awareness misconceptions and misunderstandings. *Journal of Cognitive Engineering and Decision Making*, 9:4–32.

Endsley, M. (2016). From here to autonomy: Lessons learned from human–automation research. *Human Factors*, 59:001872081668135.

Endsley, M. R. (2011). *Designing for Situation Awareness: An Approach to User-Centered Design, Second Edition*. CRC Press, Inc., USA, 2nd edition.

Fagnant, D. and Kockelman, K. (2015). Preparing a nation for autonomous vehicles: opportunities, barriers and policy recommendations for capitalizing on self-driven vehicles. *Transportation Research Part A*, 77:1–20.

Foot, P. (1967). The problem of abortion and the doctrine of the double effect. *Oxford Review*, 5:5–15.

García Maza, J. A. and Argüelles, R. P. (2022). Colregs and their application in collision avoidance algorithms: A critical analysis. *Ocean Engineering*,

261:112029.

Haight, J. and Kecojevic, V. (2005). Automation vs. human intervention: What is the best fit for the best performance? *Process Safety Progress*, 24:45 – 51.

Hannaford, E., Maes, P., and Van Hassel, E. (2022). Autonomous ships and the collision avoidance regulations: a licensed deck officer survey. *WMU Journal of Maritime Affairs*, 21(2):233–266.

Hewamalage, H., Bergmeir, C., and Bandara, K. (2021). Recurrent neural networks for time series forecasting: Current status and future directions. *International Journal of Forecasting*, 37(1):388–427.

Hu, L., Hu, H., Naeem, W., and Wang, Z. (2022). A review on colregs-compliant navigation of autonomous surface vehicles: From traditional to learning-based approaches. *Journal of Automation and Intelligence*, 1(1):100003.

Huang, Y. and van Gelder, P. (2020). Collision risk measure for triggering evasive actions of maritime autonomous surface ships. *Safety Science*, 127:104708.

IMO (2021). Autonomous ships: regulatory scoping exercise completed.

IMO (2022). Symposium on: Making headway on the imo mass code.

IMO (2023). 2023 imo strategy on reduction of ghg emissions from ships.

Jarrahi, M. H., Lutz, C., and Newlands, G. (2022). Artificial intelligence, human intelligence and hybrid intelligence based on mutual augmentation. *Big Data Society*, 9.

JTSB (Sep, 2023). Marine accident investigation report - cargo ship wakashio. Investigation Report MA2023-10, Japan Transport Safety Board.

Kapser, S., Abdelrahman, M., and Bernecker, T. (2021). Autonomous delivery vehicles to fight the spread of covid-19 – how do men and women differ in their acceptance? *Transportation Research Part A: Policy and Practice*, 148:183–198.

Kavallieratos, G., Katsikas, S., and Gkioulos, V. (2019). *Cyber-Attacks Against the Autonomous Ship: Methods and Protocols*, pages 20–36.

Kawase, K. (2013). Concise derivation of extensive coordinate conversion formulae in the gauss-krüger projection.

Kim, T.-e., Perera, L. P., Sollid, M.-P., Batalden, B.-M., and Sydnes, A. (2022). Safety challenges related to autonomous ships in mixed navigational environments. *WMU Journal of Maritime Affairs*, 21.

Levin, E. (1990). A recurrent neural network: Limitations and training. *Neural Networks*, 3(6):641–650.

Maritime, T. and Coastguard Agency, U. K. (2024). Navigation safety: Navigation practices relevant to restricted visibility.

Martin Cunneen, Martin Mullins, F. M. D. S. I. F. and Ryan, C. (2020). Autonomous vehicles and avoiding the trolley (dilemma): Vehicle perception, classification, and the challenges of framing decision ethics. *Cybernetics and Systems*, 51(1):59–80.

MUNIN (2012). Final report summary - munin (maritime unmanned navigation through intelligence in networks).

Murray, B. (2021). *Machine Learning for Enhanced Maritime Situation Awareness - Leveraging Historical AIS Data for Ship Trajectory Prediction*. Phd thesis, UiT The Arctic University of Norway, 6050 Stakkevolla,n N-9037 Tromsø Norway.

NTSB (May, 2024). Marine investigation preliminary report - contact of containership dali with the francis scott key bridge and subsequent bridge collapse. Investigation Report DCA24MM031, The National Transportation Safety Board.

Perera, L. P. (2019). Deep learning towards autonomous ship navigation and possible colregs failures. *Journal of Offshore Mechanics and Arctic Engineering*.

Perera, L. P. and Murray, B. (2019a). Situation awareness of autonomous ship navigation in a mixed environment under advanced ship predictor.

Perera, L. P. and Murray, B. (2019b). Situation awareness of autonomous ship navigation in a mixed environment under advanced ship predictor.

PMA (2021). Marine safety investigation report grounding of mv even given at suez canal egypt on march 23, 2021. Investigation Report R-026-2021-DIAM, Panama Maritime Authority, General Directorate of Merchant Marine, Maritime Affairs Investigation Department.

Razmjooei, D., Alimohammadlou, M., Ranaei Kordshouli, H.-A., and Askarifar, K. (2023). Industry 4.0 research in the maritime industry: a bibliometric analysis. *WMU J. Marit. Aff.*

Register, L. (2017). Ship right design and construction: Design code for unmanned marine systems. Technical report, Lloyd's Register.

Rico Lee-Ting Cho, J. S. L. and Ho, M. H.-C. (2021). The development of autonomous driving technology: perspectives from patent citation analysis. *Transport Reviews*, 41(5):685–711.

Rødseth, Ø. J., Nesheim, D. A., Rialland, A., and Holte, E. A. (2023). *The Societal Impacts of Autonomous Ships: The Norwegian Perspective*, pages 357–376. Springer International Publishing, Cham.

Rødseth, , Wennersberg, L. A., and Nordahl, H. (2021). Improving safety of interactions between conventional and autonomous ships.

Rødseth, J., Wennersberg, L. A. L., and Nordahl, H. (2023). Improving safety of interactions between conventional and autonomous ships. *Ocean Engineering*, 284:115206.

Schwab, K. (2017). *The Fourth Industrial Revolution*. Crown Publishing Group, USA.

Sherstinsky, A. (2020). Fundamentals of recurrent neural network (rnn) and long short-term memory (lstm) network. *Physica D: Nonlinear Phenomena*, 404:132306.

Thombre, S., Zhao, Z., Ramm-Schmidt, H., Garcia, J., Malkamaki, T., Nikolskiy, S., Hammarberg, T., Nuortie, H., Bhuiyan, M. Z. H., Sarkka, S., and Lehtola, V. (2022). Sensors and ai techniques for situational awareness in autonomous ships: A review. *IEEE Transactions on Intelligent Transportation Systems*, 23:64–83.

Thor, I. F. (2011). *Models for Ships, Offshore Structures and Underwater Vehicles*, chapter 7, pages 133–186. John Wiley Sons, Ltd.

Tijan, E., Jović, M., Aksentijević, S., and Pucihar, A. (2021). Digital transformation in the maritime transport sector. *Technological Forecasting and Social Change*, 170:120879.

Tusher, H. M., Munim, Z., Notteboom, T., Kim, T.-e., and Nazir, S. (2022). Cyber security risk assessment in autonomous shipping. *Maritime Economics & Logistics*, 24.

Tzeng, C.-Y. (1998). Analysis of the pivot point for a turning ship. *Journal of Marine Science and Technology*, 6.

UNCTAD (2023). Review of maritime transport 2023. *United Nations Conference on Trade and Development*.

Veitch, E. and Andreas Alsos, O. (2022). A systematic review of human-ai interaction in autonomous ship systems. *Safety Science*, 152:105778.

Vered, M., Livni, T., Howe, P. D. L., Miller, T., and Sonenberg, L. (2023). The effects of explanations on automation bias. *Artificial Intelligence*, 322:103952.

Wolsing, K., Roepert, L., Bauer, J., and Wehrle, K. (2022). Anomaly detection in maritime ais tracks: A review of recent approaches. *Journal of Marine Science and Engineering*, 10(1).

Yang, S., Yu, X., and Zhou, Y. (2020). Lstm and gru neural network performance comparison study: Taking yelp review dataset as an example. pages 98–101.

Yara (2020). The first ever zero emission, autonomous ship.

Yoganandhan, A., Subhash, S., Hebinson Jothi, J., and Mohanavel, V. (2020). Fundamentals and development of self-driving cars. *Materials Today: Proceedings*, 33:3303–3310. International Conference on Nanotechnology: Ideas, Innovation and Industries.

Zhou, X.-y., Huang, J.-j., Wang, F.-w., Wu, Z.-l., and Liu, Z.-j. (2019). A study of the application barriers to the use of autonomous ships posed by the good seamanship requirement of colregs. *Journal of Navigation*, 73:1–16.

Part III

Appended Papers

Paper I

The Comparison of Two Kinematic Motion Models for Autonomous Shipping Maneuvers

Wang, Y., Perera, L. P. and Batalden, B.-M. (2022)

Published in *Proceedings of the ASME 2022 41st International Conference on Ocean, Offshore and Arctic Engineering. Volume 5A: Ocean Engineering*

https://doi.org/10.1115/omae2022-79583

Paper II

Kinematic motion models based vessel state estimation to support advanced ship predictors

Wang, Y., Perera, L. P. and Batalden, B.-M. (2023)

Published in *Ocean Engineering*

https://doi.org/10.1016/j.oceaneng.2023.115503

Ocean Engineering 286 (2023) 115503

Contents lists available at ScienceDirect

Ocean Engineering

journal homepage: www.elsevier.com/locate/oceaneng

Kinematic motion models based vessel state estimation to support advanced ship predictors

Yufei Wang [a,*], Lokukaluge Prasad Perera [a,b], Bjørn-Morten Batalden [a]

[a] Department of Technology and Safety, UiT The Arctic University of Norway, Tromsø, Norway
[b] SINTEF Digital, Oslo, Norway

ARTICLE INFO

Handling Editor: Prof. A.I. Incecik

Keywords:
Ship maneuvering
System state estimation
Kinematic motion models
Continuous-discrete models
EKF/UKF
Monte-Carlo based simulation

ABSTRACT

Advanced ship predictors can generally be considered as a vital part of the decision-making process of autonomous ships in the future, where the information on vessel maneuvering behavior can be used as the source of information to estimate current vessel motions and predict future behavior precisely. As a result, the navigation safety of autonomous vessels can be improved. In this paper, vessel maneuvering behavior consists of continuous-time system states of two kinematic motion models—the Curvilinear Motion Model (CMM) and Constant Turn Rate & Acceleration (CTRA) Model. Two state estimation algorithms—the Extended Kalman Filter (EKF) and Unscented Kalman Filter (UKF) are implemented on these two models with certain modifications so that they can be compatible with discrete-time measurements. Four scenarios, created by combining different models and algorithms, are implemented using simulated ship maneuvering data from a bridge simulator. These scenarios are then verified through the proposed stability and consistency tests. The simulation results show that the EKF tends to be unstable combined with the CMM. The estimates from the other three scenarios can generally be considered more stable and consistent, unless sudden actions or variations in vessel heading occurred during the simulation. The CTRA is also proven to be more robust compared to the CMM. As a result, a suitable combination of mathematical models and estimation filters can be considered to support advanced ship predictors in future ship navigation.

1. Introduction

In recent years, various interdisciplinary research studies involving modern technologies (machine learning, artificial intelligence, Internet of Things, big data, etc.) have been developed to support the maritime industry and promote its development of autonomous shipping (Akbar et al., 2020; Im et al., 2018; Perera, 2019; Thombre et al., 2022). Several commercial companies and research organizations around the world have already been started relevant research and development activities on the same topic (Kongsberg, 2020; Meguri2040, 2020; Yara, 2021). The establishment of related maritime rules and regulations to deal with autonomous ships is also steadily progressing at the present stage under various maritime authorities to support the same objective (MSC, 2021; UNCTAD, 2021).

The advantages of autonomous ships are believed to be multi-dimensional, while that can also consist of various challenges. Unmanned ship operations indicate that human accommodation and life support facilities can be removed from such vessels, thus more innovative ship structures can be constructed (Kretschmann et al., 2017). The improvements of ship structures can also suggest an increase in energy efficiency and reduce greenhouse gas emissions (Munim, 2019). The shortage of experienced seafarers in shipping can also be mitigated by autonomous ships. (Wróbel et al., 2017). However, challenges posed by autonomous ships will be also there and that can change the status quo of the maritime industry probably to a large extent. The most immediate challenges in autonomous ships can be considered as the safety-related issues in vessel navigation.

The publications from European Maritime Safety Agency show that maritime accidents (collision, contact, and grounding) represent 51.4% of cargo ships from 2014 to 2020 in all sea accidents (EMSA, 2021). To avoid such accidents, accurate and trustworthy collision risk assessment approaches are essential. However, the decision-making process of ship collision avoidance for various vessel encounter situations can be complicated in a mixed environment, where autonomous, manned, and remote-controlled ships coexist, resulting higher collision risk navigation situations (Perera and Murray, 2019). It should be also pointed out that compared with manned ships, where the COLREGs can be used to

* Corresponding author.
E-mail address: yufei.wang@uit.no (Y. Wang).

https://doi.org/10.1016/j.oceaneng.2023.115503
Received 6 March 2023; Received in revised form 1 July 2023; Accepted 29 July 2023

Nomenclature

Variables

a_t, a_n	the tangential and normal acceleration components with respect to the course-speed vector
a_u, a_v	the transitional surge and sway acceleration components
$\boldsymbol{K}$	the Kalman gain
$\boldsymbol{N}$	the total iterations of a Monte Carlo-based simulation
$\boldsymbol{P}$	the states covariance
p_x, p_y	the northing and easting positions of the ship's CG in the UTM
$\boldsymbol{Q}$	the covariance matrix of system noise
$\boldsymbol{R}$	the covariance matrix of measurement noise
r	the yaw rate of ship
$\boldsymbol{S}$	the innovation covariance
(t)	the continuous-time unit
$[t_k]$	the discrete-time unit
u, v	the surge and sway velocity components
$\boldsymbol{V}$	the course-speed vector of the ship
v_x, v_y	the velocity components in northing and easting
$\boldsymbol{w_x}$	the white Gaussian system noise
$\boldsymbol{w_z}$	the white Gaussian measurement noise
z_{au}, z_{av}	the measured surge and sway acceleration from the onboard IMU
z_{px}, z_{py}	the measured positions
z_r	the measured yaw rate
z_ψ	the measured heading
α	the significance level of hypothesis test
Δt	the sensors sampling period
δt	the time step for temporal discretization
ε_z	the normalized innovation squared
λ	the initial parameter in the UKF
ψ	the measured heading
ρ	the autocorrelation function
χ	the course of a ship

Subscripts

$\blacksquare_i$	the i-th state in a state vector
$\blacksquare_{ii}$	the i-th diagonal element in a diagonal matrix
$\blacksquare\|_{\{B\}}$	variables described in the vessel body-fixed frame
$\blacksquare\|_j$	the j-th iteration in Monte Carlo-based simulations
$\blacksquare\|_{t_{k-1}\|t_k}$	prior estimates of variables in prediction steps
$\blacksquare\|_{t_k\|t_k}$	posterior estimates of variables in filtering steps

Superscripts

$\widehat{\blacksquare}$	the variable with estimated value

Acronyms

CG	Center of Gravity
CMM	Curvilinear Motion Model
CTRA	Constant Turn Rate & Acceleration (Model)
DoF	Degree of Freedom
EKF	Extended Kalman Filter
IMU	Inertial Measurement Unit
NIS	Normalized Innovation Squared
RMS	Root Mean Squared
UKF	Unscented Kalman Filter
UTM	Universal Transverse Mercator

make the respective collision avoidance decisions, there are still no relevant legal frameworks specially designed for autonomous ships (Kim et al., 2022). On the other hand, required ship technologies to support autonomous ship navigation should also be developed, in parallel to the maritime rules and regulations. Therefore, advanced ship predictor type technologies should be considered to support decision support systems for all kinds of vessels under complex navigation situations (Perera, 2019).

1.1. Ship motion prediction

The prediction methods in ship motions can be different and can also influence the respective prediction time horizon. These time horizons can be classified under both local and global prediction scales. For vessel trajectory predictions in a global scale (e.g., a period more than three or more minutes), the AIS data of vessel maneuvering can be utilized to make the required trajectory predictions (Perera and Murray, 2019). This can also be supported by accurately estimating vessel behaviors within a shorter time horizon, which can be viewed as trajectory predictions on a local scale. The improvements in situation awareness (SA) are also vital in the decision-making processes of ship navigation and collision avoidance, and that can also be supported by the same prediction methods. According to the definition of SA, the perception of information from the respective measured data sets is defined as the level one of SA (Endsley, 1995). The failure of SA at level one is reported as the main reasons for many industrial accidents, such as aviation (Grech et al., 2002), offshore drilling (Sneddon et al., 2006), and collisions between attendant vessels and offshore facilities (Sandhåland et al., 2015). From this aspect, a precise estimation of vessel behaviors should be guaranteed to enhance SA in future vessels, i.e., autonomous ships.

Regarding ship maneuvering behavior predictions, the required mathematical concepts are still to be developed due to complex motions of vessels, and some of such challenges are listed in this section. The first one is nonlinear maneuvering behaviors of ships, such as the underactuated property (Do and Pan, 2009). The induced external forces and moments caused by irregular waves or wind can also bring additional complexity in nonlinear ship maneuvering behaviors (Janssen et al., 2017). The second issue lies in the implementation of simplistic mathematical models, which are mainly employed in ship behavior prediction (Perera, 2017). These models are assumed to operate under constant state and parameter conditions; therefore, their performance may be degraded when exposed to varying environmental conditions. It should be also noted that many ship maneuvering behavior prediction applications from bridge systems are supported by the Automatic Radar Plotting Aid (ARPA) and Electronic Chart Display and Information Systems (ECDIS), where linear estimations of vessel positions through a point representation are executed. Such linear estimations can also be problematic in complex navigation environments since not only vessels' positions but also orientations need to be considered in closed encounter situations. That information can also be used to estimate the navigation risk in ship encounter situations.

1.2. Ship maneuvering models

State estimation typically begins with creating mathematical models of the relevant systems. Traditionally, systems are modeled based on the governing laws of nature, also known as physics-based models, which regulate how the systems change over time. More recently, data-driven models have also been developed as an alternative approach. Advances in artificial intelligence and big data technologies make this method more feasible in some applications. A data-driven model can be created by utilizing real data collected from real-world applications, without relying on an underlying physical law. Several recent studies provide a succinct comparison between these two methods (Rahman et al., 2018; Willard et al., 2020).

Data-driven models have been considered to be an effective method in many maritime-related fields (Coraddu et al., 2019; Murray and Perera, 2020; Triepels et al., 2018). However, a major restriction of this approach is that a large number of high-quality data sets should be available, and such data sets can be difficult to obtain or may have low data quality due to limitations in some real-world sensor and data acquisition systems. Another drawback is that data-driven models may have low interpretability or trustworthiness; the contributing factors that cause errors and faults can be thus difficult to identify in some situations (Chakraborty et al., 2020; Ribeiro et al., 2016; Vellido et al., 2012). One should also note that modern data-driven techniques will continue to emerge, resulting in various analysis results based on big data. There are studies that integrate physics-based and data-driven modeling applications have also been proposed (Hanachi et al., 2019; Wang et al., 2022a), yet the availability of large high quality data sets is still mandatory in such applications.

For physics-based models of ship maneuvering, the Newton's laws of motion can be considered as a fundamental concept. The ship maneuvering models can be classified into kinematic and dynamic motion models. The term "kinematics" here refers to the studies of ship motions regardless of external forces and moments that cause it, whereas "dynamic" indicates the influences of external forces and moments into ship maneuvering models. General mathematical expressions of dynamic motion models for ship maneuvering can be seen in recent studies (Fossen, 2010), where most of these expressions are a set of dynamic system equations. The maneuvering model group (MMG) is another dynamic model approach, where the rudder deflection angle and propeller revolutions are used as the model inputs and proposed by Yasukawa and Yoshimura (2014). For a vessel state estimation process, the implementation of dynamic motion models can introduce additional challenges as discussed before. This is mainly due to nonlinear hydrodynamic forces and moments which can be a part of the dynamic motion models but difficult to be measured directly and accurately by on-board sensors (Perera and Murray, 2019). Without adequate sensor measurements, certain iterative estimation algorithms may not converge and thus fail to capture vessel behaviors. A more common way that determines related hydrodynamics coefficients of external forces and moments is to calculate through model scale tests in towing tanks or ocean basins, and then to extrapolate the respective results into full scale vessels. However, such approach may not be accurate due to system-model related erroneous conditions, also not to mention various navigation and environmental conditions which can alter hydrodynamic coefficients of forces and moments significantly due to their time-varying nature.

By using kinematic motion models, model identification difficulties due to external forces and moments can be avoided. The measurements obtained from vessel translational and rotational motions can be used with the mathematical models, i.e., kinematic motion models, directly in such situations, and the variations in accelerations can be considered as model uncertainties. As for the applications of trajectory prediction and then the utilization of the same for collision detection, the models which describe related motions in curved paths under planar motions (Best and Norton, 1997; Li and Jilkov, 2003) are more general. From the view of vehicle maneuvers, the planar motions models indicate three DoFs (i.e., surge, sway, and yaw) and the respective model states represent the relevant maneuvering behaviors (Schubert et al., 2008; Stellet et al., 2015).

1.3. Vessel state estimation

The Kalman filter (KF) is a widely used estimation algorithm for linear systems, and it has extensions for nonlinear systems, such as the extended Kalman filter (EKF) and unscented Kalman filter (UKF) (Daum, 2005; Wan and Merwe, 2000). To use Kalman filter-based algorithms, it is necessary to represent related systems in a state space form. This involves expressing the evolution of state variables through a collection of first-order differential equations that represent the system models. Measurable states are represented as outputs and used to create measurement models. Because of the digital nature, measurement models are frequently applied with the sensor measurements collected in discrete-time. In contrast, many system models can be represented in continuous-time since many mechanical systems are analog. A combination of system and measurement models but with different time representations is also proposed in the recent research studies (Leander et al., 2014; Mbalawata et al., 2012).

When dealing with nonlinear systems, it can be challenging to obtain analytical solutions for nonlinear differential equations in continuous-time system models. Therefore, the temporal discretization technique is necessary to generate numerical solutions, even though they may contain some degree of truncation errors. The order of the truncation errors is positively correlated to the magnitude of the time step (δt) used in the temporal discretization (Ames, 1977). The most common case is to use the δt which is equal to the sampling period of the respective data acquisition system that collects the sensor data (Δt). However, this method is not always reliable because Δt has limitations such that a small value of δt may introduce high level of sensor noise. Additionally, using a small value for Δt can introduce unnecessary noise and redundancy, which is not preferable in estimation algorithms either (Miguel et al., 2017). On the other hand, choosing a larger value for δt can lead to unstable numerical solutions, which may cause estimation algorithms to become unstable and diverge (Butcher, 1996).

In some studies, an appropriate value of δt which is usually a factor of Δt is used in the temporal discretization for numerical solutions of nonlinear system models (Frogerais et al., 2012; Sarkka, 2007; Takeno and Katayama, 2012). The EKF and UKF thus need modifications that each prediction step contains nested iterations based on δt. The Runge–Kutta explicit higher order method is further considered to reduce the truncation errors with less iterations (Frogerais et al., 2012; Takeno and Katayama, 2012). The EKF and UKF with the above-mentioned modifications are considered in this study since the proposed kinematic motion models for ship maneuvering is also highly nonlinear and difficult to find its analytical solutions.

It should also be noted that ships, particularly those with large tonnage, exhibit specific maneuvering behaviors (Molland, 2008). Ocean-going vessels are prone to drift due to underactuated conditions, which can result in potential near-miss or collision situations during navigation (Perera, 2017). Accurate estimation of ships' states, especially in the sway direction in order to find the ship's pivot point, is necessary (Seo, 2016). Consequently, the established state-space models and algorithms must be capable of providing precise estimates under such circumstance. Estimated states in sway direction with a longer convergence period (Perera, 2017), or a large delay and bias (Wang et al., 2022b), need to be avoided.

In this study, vessel maneuvering behavior is described by the system states of two kinematic motion models, where the Kalman filter-based approaches are applied to estimate the same system states. To verify the applied models and estimation algorithms, a two-step approach has been taken. Firstly, the models and algorithms have been verified in the bridge simulator environment, and the lessons learned from this process have been documented in this study. Secondly, the verification and demonstration on the same models and estimation algorithms will be conducted on actual vessel navigation using the UiT autonomous test vessel in a future study. Considering that the verification under simulated environments can be crucial prior to conducting future sea trials in a real environment, this paper focuses on the first step of this process. The paper is organized under the following sections: Section 2 presents the literature review of different system modeling methods and the Kalman filter-based estimation algorithms; Section 3 gives extensive details of the proposed kinematic motion models; Section 4 introduces the proposed state estimation algorithms; Section 5 presents the evaluation methods (Monte Carlo-based simulation, algorithm stability and consistency tests) to verify the performances of the filters; The

simulation results, discussions, and conclusions are shown in the last parts of this paper.

2. Kinematic motion models

Kinematic motion models are selected to capture ship maneuvering behavior in this study. The position, velocity, acceleration, and heading states are the important parameters that can reflect the characteristics of relevant ship maneuvers and have been selected for model development in this study.

2.1. State vectors

In a state-space model, the states of a system can be expressed in a vector form. In this paper, two different navigation state vectors (1) and (2) are used, as they are related to the CMM and CTRA for ship maneuvering (see Fig. 1).

$$\boldsymbol{x} = \left[p_x, p_y, v_x, v_y, \psi, r, a_t, a_n\right]^T \text{(in the CMM)}\# \tag{1}$$

$$\boldsymbol{x} = \left[p_x, p_y, u, v, \psi, r, a_u, a_v\right]^T \text{ (in the CTRA)}\# \tag{2}$$

In both models, the values of p_x and p_y are based on the Universal Transverse Mercator (UTM) coordinate system. The unit in the Cartesian grid layout of the UTM is in meters. In the CMM, the course-speed vector V decomposes along the inertial reference frame into v_x and v_y, whereas along the vessel body-fixed reference frame into u and v in the CTRA. The acceleration at and an are the normal and tangential components with regard to V.

All the states in Fig. 1 are related to the ship's apparent CG. Due to added mass effects, the apparent CG can shift during maneuvers. However, to simplify the mathematical models, an assumption is made that such a shift can be neglected by considering that the ship maneuvers are conducted in calm water conditions. As explained in the following section, since the IMU collects the simulated data from the apparent CG, this is a favorable reference frame for generating the respective mathematical models.

2.2. System models

The CMM and CTRA mathematical models are based on the curvilinear motion equation (3), which can be written as:

$$\dot{\chi} = a_n / V$$

$$\dot{V} = a_t$$

$$\dot{p}_x = v_x = V\cos(\chi)$$

$$\dot{p}_y = v_y = V\sin(\chi)\# \tag{3}$$

This system model has a very flexible generality in that it can reduce to several special cases such as constant velocity linear motion ($a_n = 0$, $a_t = 0$), constant acceleration linear motion ($a_n = 0$, $a_t \neq 0$), constant turn motion ($a_n \neq 0$, $a_t = 0$), and more complex cases, where both a_n and a_t are non-zero (Li and Jilkov, 2003).

The model derivation starts with a reference frame transformation, where v_x and v_y in the local inertial reference frame are represented by u and v in the vessel body-fixed reference frame:

$$v_x = u\cos(\psi) - v\sin(\psi)\# \tag{4}$$

$$v_y = u\sin(\psi) + v\cos(\psi)\# \tag{5}$$

The acceleration components in the local inertial reference frame (a_x and a_y) can be thus written as:

$$a_x = \dot{v}_x = \left.\frac{du}{dt}\right|_{\{B\}}\cos(\psi) - u\frac{d\psi}{dt}\sin(\psi) - \left.\frac{dv}{dt}\right|_{\{B\}}\sin(\psi) - v\frac{d\psi}{dt}\cos(\psi)$$

$$= a_u\cos(\psi) - u\,r\sin(\psi) - a_v\sin(\psi) - v\,r\cos(\psi)\# \tag{6}$$

$$a_y = \dot{v}_y = \left.\frac{du}{dt}\right|_{\{B\}}\sin(\psi) + u\frac{d\psi}{dt}\cos(\psi) + \left.\frac{dv}{dt}\right|_{\{B\}}\cos(\psi) - v\frac{d\psi}{dt}\sin(\psi)$$

$$= a_u\sin(\psi) + u\,r\cos(\psi) + a_v\cos(\psi) - v\,r\sin(\psi)\# \tag{7}$$

With the combination of (4)-(7), the expressions of a_u and a_v can be further written as:

$$a_u = \left(a_x + r\,v_y\right)\cos(\psi) + \left(a_y - r\,v_x\right)\sin(\psi)\# \tag{8}$$

$$a_v = \left(a_y - r\,v_x\right)\cos(\psi) - \left(a_x + r\,v_y\right)\sin(\psi)\# \tag{9}$$

It should be noted that au and av are translational accelerations that represent the rate of change of u and v in the vessel body-fixed frame of reference. The measurements of the accelerations in both surge and sway directions also contain a rotational accelerations component, which will be derived in the following subsection. A summary of the CMM and CTRA models is shown in Table 1. The system nonlinearity is modeled as a Gaussian-distributed noise with a zero-mean. The determination of the covariance matrix of the Gaussian—$\boldsymbol{Q}$ can be complex

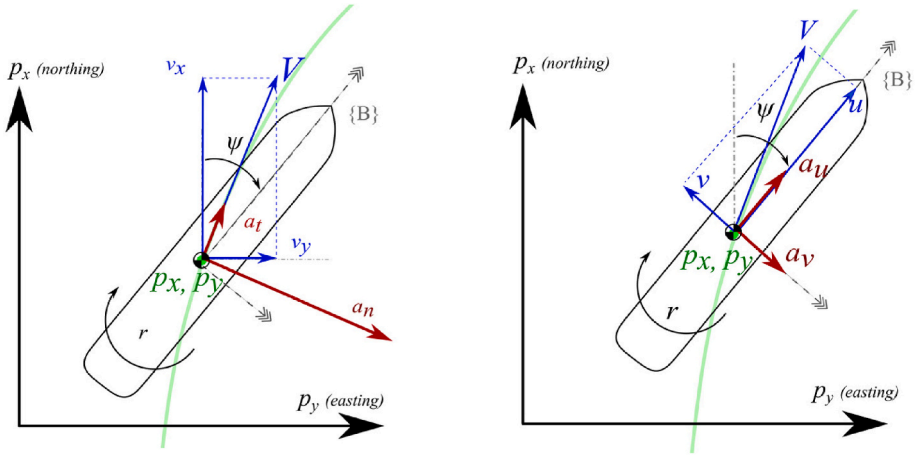

(a) state in the CMM (b) state in the CTRA

Fig. 1. Two different navigation state vectors in the UTM coordinate system. It is assumed that the apparent CG of ship does not shift greatly.

Table 1
System models of ship maneuvering.

Model	CMM	CTRA
state vector	$\boldsymbol{x}(t) = [p_x, p_y, v_x, v_y, \psi, r, a_t, a_n]^T$	$\boldsymbol{x}(t) = [p_x, p_y, u, v, \psi, r, a_u, a_v]^T$
system models with continuous-time step t $\boldsymbol{w_x} \sim \mathcal{N}(\boldsymbol{0}, diag(\boldsymbol{Q}) \in \mathbb{R}^{8\times 8})$	$\dot{\boldsymbol{x}}(t) = f_{CMM}(\boldsymbol{x}(t)) + \boldsymbol{w_x}$ $\begin{bmatrix} v_x \\ v_y \\ a_t f^{vx} - a_n f^{vy} \\ a_t f^{vy} + a_n f^{vx} \\ r \\ 0 \\ 0 \\ 0 \end{bmatrix} + w_x$ $\left(f^{vx} = \frac{v_x}{\sqrt{v_x^2+v_y^2}}, f^{vy} = \frac{v_y}{\sqrt{v_x^2+v_y^2}}\right)$	$\dot{\boldsymbol{x}}(t) = f_{CTRA}(\boldsymbol{x}(t)) + \boldsymbol{w_x}$ $\begin{bmatrix} u\cos(\psi) - v\sin(\psi) \\ v\cos(\psi) + u\sin(\psi) \\ a_u \\ a_v \\ r \\ 0 \\ 0 \\ 0 \end{bmatrix} + w_x$

Table 2
Measurement models.

measurement vector (used by both models)	$z = [z_{px}, z_{py}, z_\psi, z_r, z_{au}, z_{av}]^T$	
Model	CMM	CTRA
measurement models with discrete-time step $t_k = k \bullet \Delta t$ $(k = 1, 2, \ldots)$ $\boldsymbol{w_z} \sim \mathcal{N}(\boldsymbol{0}, diag(\boldsymbol{R}) \in \mathbb{R}^{6\times 6})$	$z[t_k] = h_{CMM}(\boldsymbol{x}[t_k]) + \boldsymbol{w_z}$ $\begin{bmatrix} p_x \\ p_y \\ \psi \\ r \\ h_{u1}\cos(\psi) + h_{u2}\sin(\psi) - v\,r \\ h_{v1}\cos(\psi) - h_{v2}\sin(\psi) + u\,r \end{bmatrix} + w_z$ $(h_{u1} = a_t f^{vx} - a_n f^{vy} + r v_y)$ $(h_{v1} = a_t f^{vy} + a_n f^{vx} - r v_x)$ $(h_{u2} = a_t f^{vy} + a_n f^{vx} - r v_x)$ $(h_{v2} = a_t f^{vx} - a_n f^{vy} + r v_y)$ Where f^{vx} & f^{vy} are shown in Table 1	$z[t_k] = h_{CTRA}(\boldsymbol{x}[t_k]) + \boldsymbol{w_z}$ $\begin{bmatrix} p_x \\ p_y \\ \psi \\ r \\ a_u - v\,r \\ a_v + u\,r \end{bmatrix} + w_z$

and sometimes needs experimental data or practical intuition. A general processing method is used with a diagonal matrix to represent $\boldsymbol{Q}$.

2.3. Measurement models

The measurements are from the respective sensors measured by a data acquisition system in discrete-time. Hence, the state variables in the measurement model are discrete. Regarding the measurements, it is considered that the relevant position, heading, yaw rate, and acceleration values of a selected vessel are obtained from the on-board sensors. These sensors can be categorized as GNSS systems, gyroscopes, IMUs, and yaw rate indicators. The multiple measurements can also be written as a vector:

$$z = \left[z_{px}, z_{py}, z_\psi, z_r, z_{au}, z_{av}\right]^T \# \tag{10}$$

The measured positions z_{px} and z_{py} in Eq. (10) are projected from the raw latitude/longitude data into the northing/easting in the UTM coordinate system. One should note that z_{px} and z_{py} indicate the position of the ship's GNSS antenna receivers which may not be the ship's apparent CG. Certain calibration should be done to correct z_{px} and z_{py} to the ship's apparent CG. The elements—z_ψ and z_r are the measured heading (with reference to the axis of northing) and the measured yaw rate (see Fig. 1). These states are available from the fiber optic gyroscope with high precision information. The respective accelerations can be measured by the accelerometers embedded in the IMUs. The mathematical expressions of measured accelerations that are used with respect to a selected vessel with 6 DoFs can be referred in Hover and Michael S (2010). In this study, two assumptions on the IMU are made: its body frame is well aligned with the vessel body-fixed reference frame and it is located close to the vessel's apparent CG. One should note that if these assumption cannot be held in realistic ocean-going vessels, additional mathematical transformations should be introduced to transfer actual measurements into the required model measurements. Furthermore, the acceleration components caused by gravity are also removed from the final outputs of the IMU since heave, pitch, and roll motions are not considered in the motion models. The mathematical expressions of measured accelerations z_{au} and z_{av} can be hence expressed as (11) and (12) when only 3 DoFs are considered.

$$z_{au} = a_u - v\ r \# \tag{11}$$

$$z_{av} = a_v + u\ r \# \tag{12}$$

One should note that the measurement models that have shown in Table 2 share the same measurement vector with a discrete-time step of Δt. The measurement uncertainty is also modeled as the Gaussian noise with a zero mean. Because sensors measure the respective parameters independently, it is reasonable to assume that the covariance matrix of the measurement noise—$\boldsymbol{R}$ is also diagonal. The diagonal elements in $\boldsymbol{R}$ can be determined in advance, e.g., through sensor operation manuals or independent experiments by observing sensor noise conditions.

3. Estimation algorithms

The EKF and UKF are applied for state estimation under the respective system and measurement models. The parameter estimation process of these two algorithms is usually conceptualized in two steps which execute iteratively: prediction and filtering step. The parameter initialization phase should be included before the parameter estimation process. Since the system and measurement models are described in different time steps, the EKF and UKF algorithms need certain modifications to coordinate the respective iterative steps.

3.1. Time step modification

Since the kinematic-based system models are nonlinear and difficult to obtain analytical solutions, the temporal discretization must be considered. Fig. 2 shows the relationship of various time steps that are considered in this study. In each prediction step, the numerical solutions of prior estimation are calculated through the temporal discretization with δt. The measurements have a sampling period of Δt, so that the measurement innovation, the Kalman gain, and the posterior estimates are calculated every Δt. One should note that the time steps have the units of seconds. An overview of the EKF and UKF with the modifications is illustrated in Figs. 3 and 4. The second-order Runge–Kutta explicit method is used in this study, and further the details can be referred to Frogerais et al. (2012); Takeno and Katayama(2012); Wang et al. (2022b).

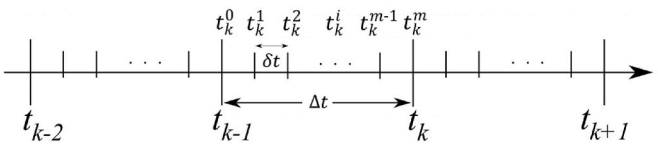

Fig. 2. Time step δt in temporal discretization and measurements sampling period Δt.

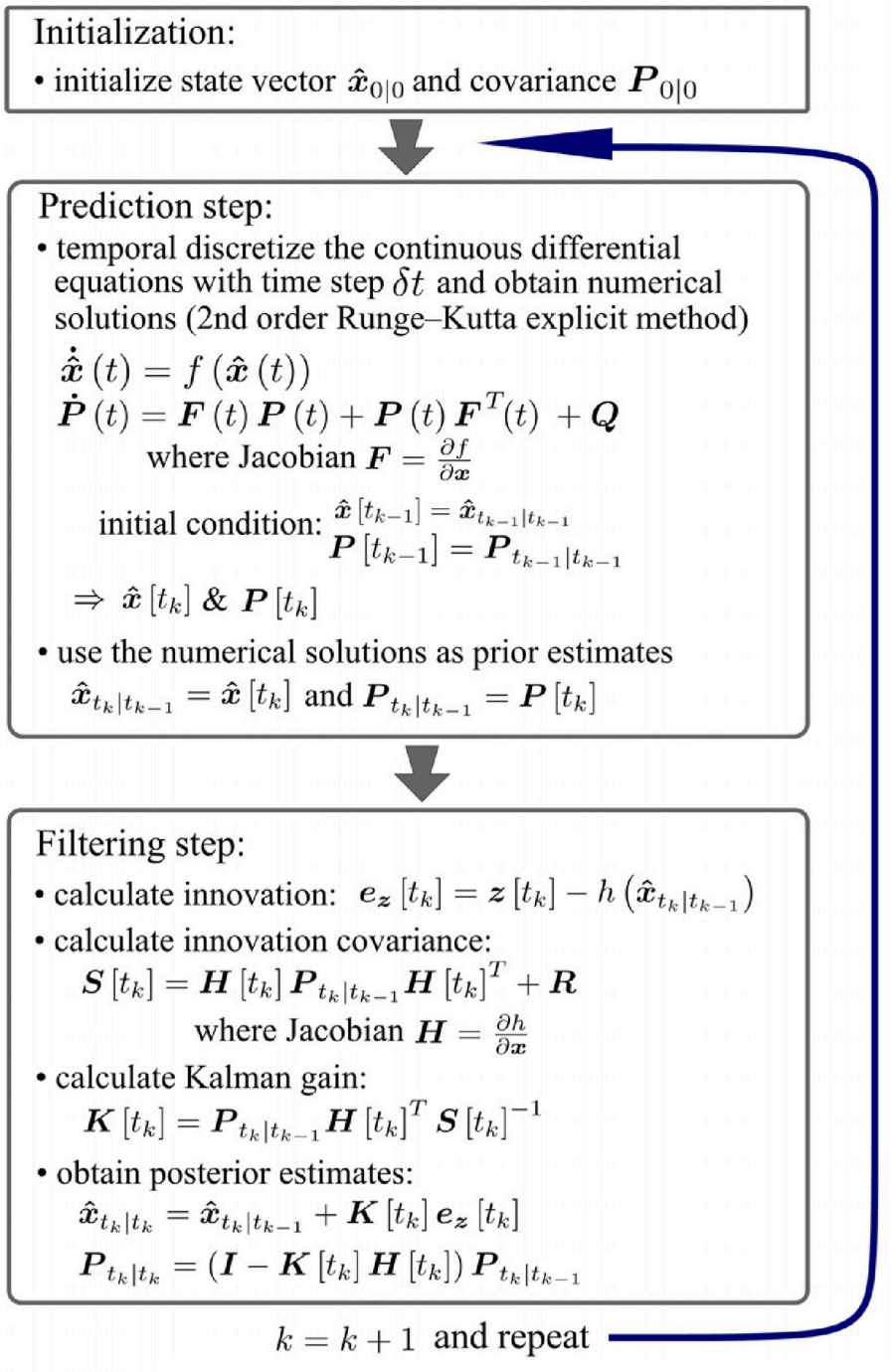

Fig. 3. Chart flow of the EKF.

3.2. State vector initialization

Since the EKF and UKF are suboptimal estimation algorithms, they can diverge in some situations resulted with erroneous estimated parameters (Barrau, 2015). To secure the parameter estimation accuracy, the initial states should be approximately close to the true values as possible. If the initial states are purely guessed and far away from the actual values, the estimation results can diverge. From a practical point of view, some states can be measured directly from sensors. Therefore, the measurements of those states can be used to approximate the initial values of both measurable and non-measurable states. Additionally, it will be explained later that a Monte Carlo-based simulation approach will be used, which allows for multiple iterations with different initialized values within a given parameter range to evaluate the algorithm's performance.

In this study, the initial state vector in each Monte Carlo-based run is randomly generated from a Gaussian distribution (13). This is feasible for initializing the position, heading, and yaw rate values (14)–(15). The velocities in the CMM can be estimated roughly through two historical position values in the beginning (16)–(17). These initialized values can further be used to approximate the respective velocities in the CTRA (18)–(19). All accelerations are initialized as with zero values, since vessel speeds vary relatively slow in general. Therefore, the respective acceleration values should have relatively smaller values.

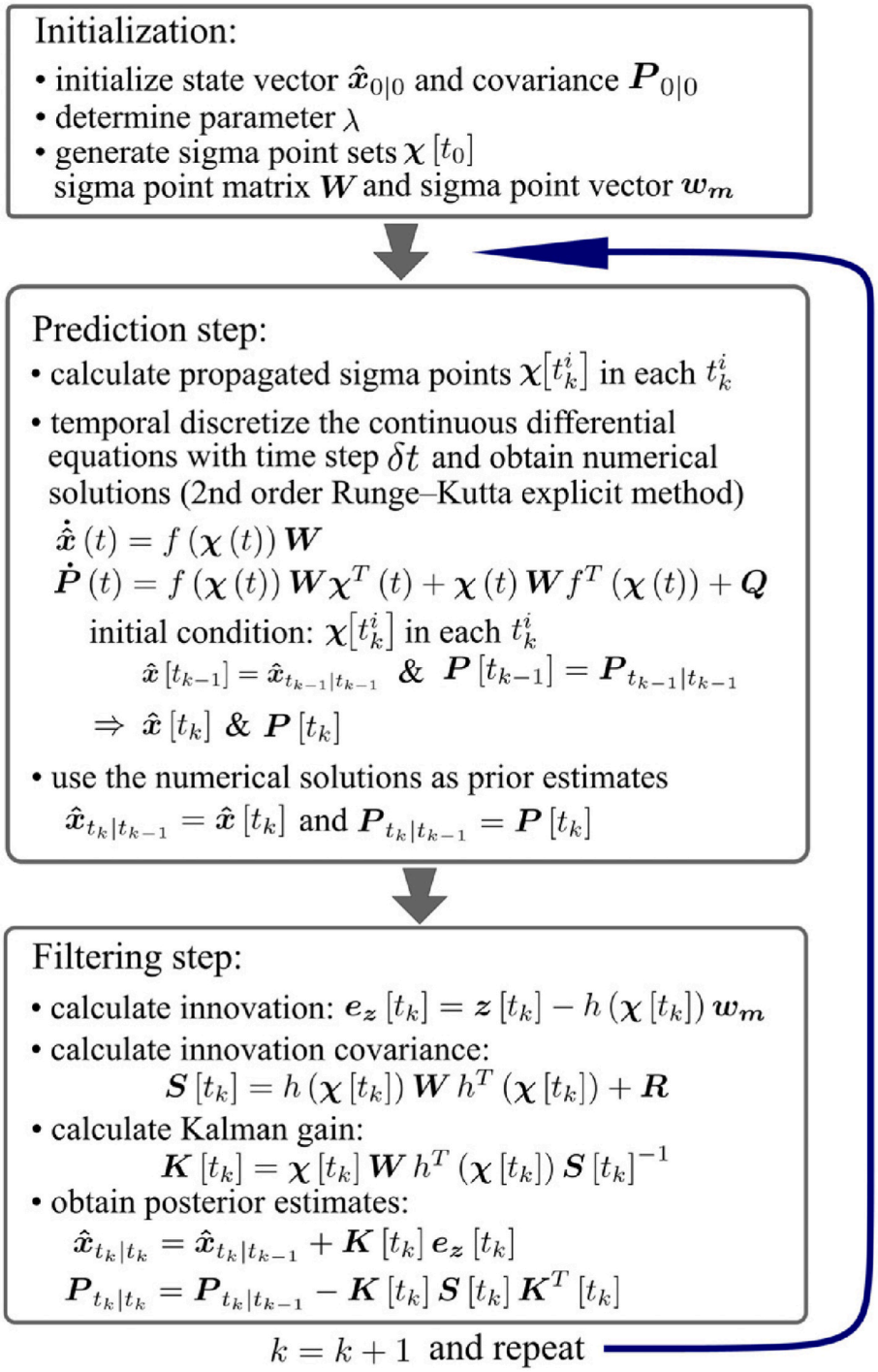

Fig. 4. Chart flow of the UKF.

For $\boldsymbol{P}_{0|0}$, the covariance matrix elements related to the measured states can share the same values as they are in $\boldsymbol{R}$. A two-point differencing method is applied for the correlation between positions and velocities (Bar-Shalom et al., 2002). It should be noted that the initially estimated $\boldsymbol{P}_{0|0}$ is not strictly correct for $\boldsymbol{x}[t_0]$ in the CTRA. The correlations between vessel position and surge/sway velocities can have complex relationships (Svensson, 2019). However, during a normal cruising stage where the sway velocity is not significant compared to the surge velocity, the format of $\boldsymbol{P}_{0|0}$ can be approximately accepted.

$$\hat{\boldsymbol{x}}_{0|0} \sim \mathcal{N}(\boldsymbol{x}[t_0], \boldsymbol{P}_{0|0})\# \tag{13}$$

$$\boldsymbol{x}[t_0] = [z_{px}, z_{py}, v_x, v_y, z_\psi, z_r, 0, 0]^T (\text{for CMM})\# \tag{14}$$

$$\boldsymbol{x}[t_0] = [z_{px}, z_{py}, u, v, z_\psi, z_r, 0, 0]^T (\text{for CTRA})\# \tag{15}$$

$$v_x[t_0] = \frac{z_{px}[t_0] - z_{px}[t_{-1}]}{\Delta t}\# \tag{16}$$

$$v_y[t_0] = \frac{z_{py}[t_0] - z_{py}[t_{-1}]}{\Delta t}\# \tag{17}$$

$$u[t_0] = v_x[t_0]\cos(z_\psi[t_0]) + v_y[t_0]\sin(z_\psi[t_0])\# \tag{18}$$

$$v[t_0] = -v_x[t_0]\sin(z_\psi[t_0]) + v_y[t_0]\cos(z_\psi[t_0])\# \tag{19}$$

$$\boldsymbol{P}_{0|0} = \begin{bmatrix} \boldsymbol{P1}_{4\times4} & \boldsymbol{0}_{4\times4} \\ \boldsymbol{0}_{4\times4} & \boldsymbol{P2}_{4\times4} \end{bmatrix}\# \tag{20}$$

$$\boldsymbol{P1}_{4\times4} = \begin{bmatrix} R_{11} & 0 & \frac{R_{11}}{\Delta t} & \frac{R_{22}}{\Delta t} \\ 0 & R_{22} & 0 & 0 \\ \frac{R_{11}}{\Delta t} & 0 & \frac{2R_{11}}{\Delta t^2} & 0 \\ \frac{R_{22}}{\Delta t} & 0 & 0 & \frac{2R_{22}}{\Delta t^2} \end{bmatrix}\# \tag{21}$$

$$\boldsymbol{P2}_{4\times4} = \begin{bmatrix} R_{33} & 0 & 0 & 0 \\ 0 & R_{44} & 0 & 0 \\ 0 & 0 & R_{55} & 0 \\ 0 & 0 & 0 & R_{66} \end{bmatrix}\# \tag{22}$$

4. Filter verification

The filter verification is implemented to examine the stability and consistency of the estimation algorithms. The necessary data sets used in this study are obtained from simulated ship maneuvers performed in the UiT bridge simulator (see Fig. 5). Ship maneuvers in the bridge simulator are generated from certain dynamic motion models. These models are developed by the respective bridge manufacturer, and these models are unknown for this study. It is assumed that these ship maneuvers are similar to real navigation situations, where the dynamics properties of real ship motions can be difficult to capture precisely.

4.1. Monte Carlo-based simulation

After several ship maneuvering exercises in the bridge simulator, several data sets are collected. That data set consists of vessel states as well as simulated measurements of the respective vessel states. There are four scenarios which are made by different combinations of the models and algorithms are utilized on the same data sets. These scenarios share the same global parameters. Each scenario is executed N times with different initial values and measurements. Such an approach is thus equivalent to offline multiple running, i.e., Monte Carlo-based simulations. Fig. 6 shows how the Monte Carlo-based simulations are performed with the respective scenarios.

The values of the global parameters that are used for the Monte Carlo-based simulation are listed in Table 3. Since there are 50 independent measurements that can be collected, the Monte Carlo-based simulation is run 50 iterations. The sampling period of measurements is 0.1 s. The time step for the temporal discretization is set to 0.005 s, resulting in 20 internal iterations for the numerical calculations in each prediction step. One should note that as the time step for the temporal discretization increases, the numerical solutions from the explicit methods (such as the Runge-Kutta explicit method in this study) can become unstable (Butcher, 1996). Hence, the value of 0.005 s used in this study to satisfy the required stability requirement. The definition of parameter λ in the UKF should be referred to Wan and Merwe (2000).

Fig. 5. UiT bridge simulator.

4.2. Estimation algorithm stability

The Kalman gain $\boldsymbol{K}$ is vital for precise estimation of the vessel states. Since the calculations of $\boldsymbol{K}$ contain the inverse matrix operation of innovation covariance $\boldsymbol{S}$, this matrix should be well-conditioned such that the inverse operation should not be sensitive to the respective perturbations. In this study, the reciprocal condition number (Rcond) is used as a criterion to examine the condition of $\boldsymbol{S}$ (Cline et al., 1979). It can be defined as:

$$Rcond(\boldsymbol{S}) = \frac{1}{\|\boldsymbol{S}^{-1}\|_1 \bullet \|\boldsymbol{S}\|_1}\# \tag{23}$$

$$\text{where, } \|\boldsymbol{S}\|_1 = \max_{1\le j\le \dim(\boldsymbol{S})} \sum_{i=1}^{\dim(\boldsymbol{S})} |a_{ij}|\# \tag{24}$$

If $\boldsymbol{S}$ is well-conditioned, $Rcond\ (\boldsymbol{S})$ is near 1, otherwise an ill-conditioned $\boldsymbol{S}$ will have the Rcond close to 0. One should note that the threshold that determines whether a matrix is well-conditioned depends on the specific problem and the desired level of the parameter estimation accuracy. In this study, the threshold value is set to 1×10^{-10} which is an iteratively observed value. With this threshold value, the small estimated errors can have a major impact on the inverse of $\boldsymbol{S}$. The executions of both algorithms are designed to be interrupted if an ill-conditioned $\boldsymbol{S}$ is detected, where the parameter estimation process can be classified as divergence. If an interruption occurs during the execution of an estimation algorithm, the related algorithm can be thus considered as diverged. It is important to note that an algorithm may not exhibit divergence in a single trial, which is why multiple runs are necessary. This is also why the Monte Carlo-based simulation are implemented in this study.

4.3. Estimation algorithm consistency

The consistency test for estimation algorithms is necessary to verify whether the estimated states converge to the actual states. The calculated innovations $\boldsymbol{e}_z$ can be used to evaluate the consistency of the estimation algorithms. The consistency test should be performed based on simulated data before applying parameter estimation algorithms to real-world data, as actual states may not always be available in real-world applications. The respective criteria for the consistency of an algorithm can be categorized as:

(1) Innovations should be accepted as the zero mean and own magnitude commensurate with the innovation covariance matrix;
(2) Innovations should be accepted as the white Gaussian noise. The normalized innovation squared (NIS) is used to verify the first criteria in general, and it is defined as:

$$\varepsilon_z[t_k] = \boldsymbol{e}_z^T[t_k]\boldsymbol{S}_{t_k|t_{k-1}}^{-1}\boldsymbol{e}_z[t_k]\# \tag{25}$$

For the Monte Carlo-based simulations which provide the (N-run) average NIS $\bar{\varepsilon}_z$, a chi-square test for hypothesis testing can be implemented (Chew, 1966):

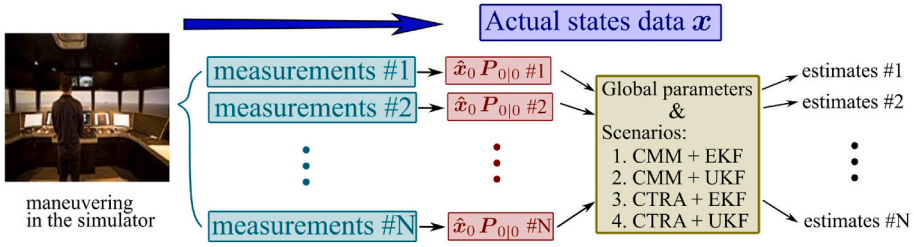

Fig. 6. Monte Carlo-based simulation.

Table 3
Global parameters assignment.

Global parameters	
N	50
Δt	0.1 [s]
δt	0.005 [s]
$\boldsymbol{Q}$	$diag(10^{-1}, 10^{-1}, 10^{-3}, 10^{-3}, 10^{-5}, 10^{-5}, 10^{-1}\pi/180, 10^{-5}\pi/180)$
$\boldsymbol{R}$	$diag(1^2, 1^2, (0.5\pi/180)^2, (10^{-3}\pi/180)^2, 0.01^2, 0.01^2)$
λ	1.72 (only used in the UKF)

H0 criterion (1) is established;
H1 *criterion (1) is NOT established or inconclusive;*

Test statistic:

$\chi^2 = \bar{\varepsilon}_z$ with the DoFs $N \cdot \dim(z)$

Critical value:
(two-sided test with a significant level $\boldsymbol{\alpha} = 0.05$)

$$\left[\chi^2_{N\bullet\dim(z)}(0.025), \chi^2_{N\bullet\dim(z)}(0.975)\right]$$

The (N-run) average autocorrelation $\bar{\rho}$ can be used as the test statistics for the criterion (2), and the Z-test as a hypothesis test can be applied (Bar-Shalom et al., 2002):

H0 criterion (2) is established;
H1 *criterion (2) is NOT established or inconclusive; Test statistic:*

$$Z = \bar{\rho}(k, k+1) = \frac{1}{\sqrt{\dim(z)}} \frac{num_1}{den_1 \ den_2} \# \tag{26}$$

where : $num_1 = \sum_{j=1}^{N} \boldsymbol{e}_z^T[t_k]\boldsymbol{e}_z[t_{k+1}]\big|_j$

$$den_1 = \sqrt{\sum_{j=1}^{N} \left(\boldsymbol{e}_z^T[t_k]\boldsymbol{e}_z[t_k]\right)\big|_j}$$

$$den_2 = \sqrt{\sum_{j=1}^{N} \left(\boldsymbol{e}_z^T[t_{k+1}]\boldsymbol{e}_z[t_{k+1}]\right)\big|_j}$$

Critical value:
(two-sided test with a significant level $\boldsymbol{\alpha} = 0.05$)

$$\left[-1.96 \Big/ \sqrt{N}, 1.96 \Big/ \sqrt{N}\right]$$

One should also note that the EKF and UKF are suboptimal estimation filters. The estimated states may not be optimal in the sense of minimizing the mean squared errors with respect to the true states, where the estimation algorithm can be diverged in some situations. The non-zero estimated errors may be achieved so that the complete consistency is not possible. Therefore, the estimation algorithm consistency test also needs to examine the behavior of the estimation errors. The root mean squared (RMS) errors are used in this study, and the RMS error of a single state x_i in step t_k from the Monte Carlo-based simulations with N-run can be defined as:

$$RMS(x_i[t_k]) = \sqrt{\frac{1}{N}\sum_{j=1}^{N} (\hat{x}_i[t_k] - x_i[t_k])\big|_j \#} \tag{27}$$

where: $x_i[t_k]$ is the actual value in step t_k.

5. Simulation results and discussion

A selected vessel used in the bridge simulator is illustrated in Fig. 7. It is a general cargo ship equipped with a single controllable pitch propeller and a single rudder. The position of the apparent CG is located midships, and it is assumed that the apparent CG does not shift largely during ship maneuvers.

5.1. Simulated ship maneuvers

Several ship maneuvers are conducted in the UiT bridge simulator (see Fig. 8). The trajectory made from these maneuvers is similar to the Williamson turn (Ian, 2004). Calm weather conditions are implemented in the bridge simulator, which means that impacts from wind and waves are insignificant. In addition, the speed of the surrounding ocean currents is also set to be 0 so that the SOG is identical to the STW. Based on the maneuvers, six voyage segments can be divided. These segments include:

S1 (wp1 → wp2) steady-state cruising (11.43 knots with the propeller pitch 0.78);
S2 (wp2 → wp3) place the rudder to starboard with a deflection angle of 35°;
S3 (wp3 → wp4) place the rudder to port with 35° when the heading reaches 90°;
S4 (wp4 → wp5) reduce the rudder to 10 degrees of port when the heading reaches 300°;
S5 (wp5 → wp6) place the rudder amidships when the heading reaches 230°;
S6 (wp6 → end) decrease the propeller pitch to 0.33 when the heading reaches 210°.

Since typical ship maneuvers, such as cruising, turning, and slow-up are all included, the analyses are divided by different time intervals to examine each voyage segment.

5.2. Estimation algorithm stability

The estimation algorithms follow the procedure stated in Section 4.1. The simulation results show that Scenario 1 (the CMM with EKF) is the only unstable combination. The diverged instances in Scenario 1 during the Monte Carlo based simulation with 50 runs are labeled in Fig. 9a. The distribution of the diverged instances illustrates that they mostly occur after the vessel executes a new rudder or propeller order. For a diverged instance, the errors of estimated states (v_x, v_y, ψ, and r) are depicted in Fig. 9b. It can be observed that the errors of $\hat{v}_x$ and $\hat{v}_y$ have significant increases in the middle of the execution period. In the last moments before the interruption, the errors of $\hat{v}_x$ and $\hat{v}_y$ demonstrate a

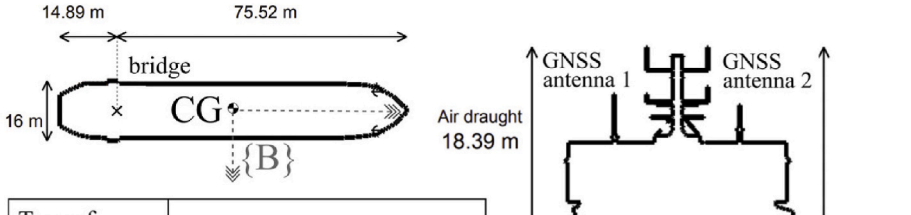

Type of vessel	General cargo
Dimensions	LOA 89.99 m / LBP 84.98 m / Beam 14.00 m
Max Speed	Abt. 11.5 knots
Main Engine /Propulsion:	MAK 6M 25 1,800 kW / controllable pitch propeller

Fig. 7. The vessel used in the simulator.

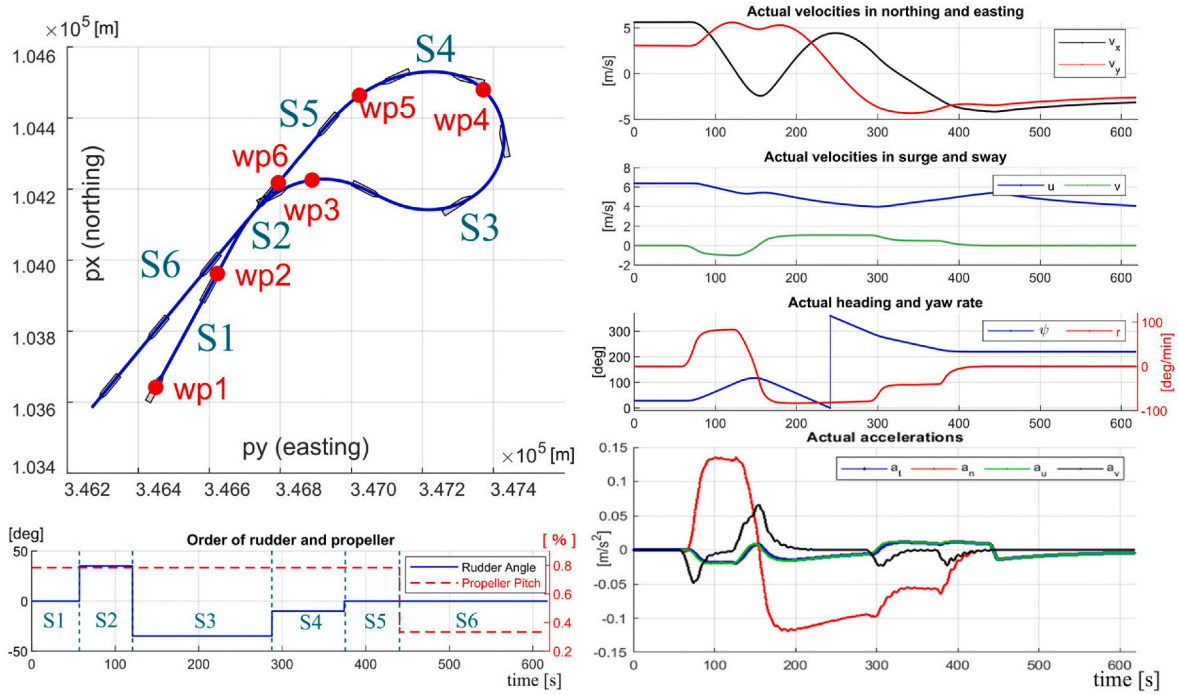

Fig. 8. The simulated maneuver in the UiT bridge simulator. The actual latitude/longitude data sets are transferred into the UTM coordinate system. The vessel icons are shown every 50 s.

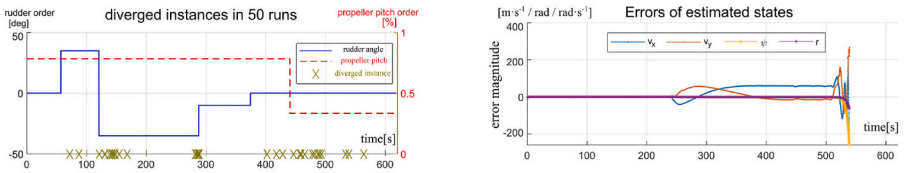

(a).Diverged instances are labeled in the time axis. The labeled positions represent the moments when the interruption occurs.

(b) The error magnitude of estimated states (v_x, v_y, ψ, r) from a diverged instance.

Fig. 9. The stability test results of Scenario 1 (CMM + EKF).

trend of unstable oscillations. Meanwhile, the errors of $\hat{\psi}$ and $\hat{r}$ are showing approximately exponential growth. Since these estimated states contribute to the components of Jacobian $\boldsymbol{F}$ and $\boldsymbol{H}$ in the EKF, $\boldsymbol{F}$ and $\boldsymbol{H}$ can thus diverge and cause the ill condition of $\boldsymbol{S}$ consequently.

The truncation errors from a first order Taylor series expansion in the EKF as well as the nonlinearity in both the system and measurement models of the CMM can be considered as the reasons to introduce such an instability of Scenario 1. Because both estimated prior and posterior error covariances require the $\boldsymbol{F}$ and $\boldsymbol{H}$, the truncation errors thus will remain in the solutions after each iteration. Upon closer examination of

Fig. 9b, it becomes apparent that the estimated errors begin to accumulate to a larger value, which means that the EKF fails to compensate for the estimation errors. The execution of new control orders accelerates the error accumulation processes. In comparison with the UKF in Scenario 2, where the Taylor series expansion is not applied, the respective truncation errors do not impact the solution of the error covariance matrix. Therefore, the unscented transformation in the UKF is clearly more robust for the nonlinearity in the CMM.

It should also be emphasized that the nonlinearity of both the system and measurement models of the CTRA is relatively smooth, compared with the nonlinearities in the CMM. The smoothness can be understood as that the functions in both the system and measurement models of the CTRA are continuously differentiable, and there are no discontinuous or sudden changes of the derivatives. As a result, these functions are well-behaved and mathematically tractable. The EKF can hence converge with the CTRA, as observed in the results. By contrast, the terms f^{vx} and f^{vy} in the CMM indicate that the respective derivatives can exhibit sudden changes as either v_x or v_y approaches 0.

5.3. Estimation algorithm consistency

The (N-run) average NIS and autocorrelation (one step apart) of Scenario 2, 3, and 4 are presented in Fig. 10. As can be seen, there are three unbounded periods that the average NIS is greater than the upper bound in S2 and S3 for all scenarios (over the logarithmic scale). The average NIS only slightly exceeds the upper bound in the first and second periods, whereas a great exceedance can be observed in the last period when the heading switches. For the autocorrelation, there is only one unbounded period which happens in S3.

The percentage of the bounded test statistics are shown in Table 4 and Table 5. Except for S2 and S3, approximately 70%–80% of the average NIS and over 90% of the autocorrelation function are within the critical values. In each voyage segment, it can also be confirmed that there are situations where the average NIS are less than the lower bound (roughly 20%), and these average NIS are evenly distributed and the values do not significantly exceed the lower bound.

When comparing Scenario 2 and 3 (or Scenario 2 and 4), it is perceptible that the average NIS in the first and second unbounded period in Scenario 2 is slightly higher. In the last unbounded period, it takes a longer time for the average NIS converges to the critical value range again in Scenario 2. The autocorrelation shares a similar behavior in that the re-converge time in Scenario 2 is longer. The test results also show that the test statistics of Scenario 3 and 4 are fairly close to each other.

The three unbounded periods overlap within three events: the first and second unbounded periods correspond to the rudder order in S2 and S3; the last unbounded period is due to switching of the vessel heading between 0 to 360°. The first and second events are thought to cause the modeling errors in the CMM and CTRA. Because the mean values of accelerations and yaw rate are assumed to be 0 in both models (see Table 1), and sudden actions (such as rudder to starboard/port with 35°) can produce significant changes of the respective translational and rotational accelerations or yaw rate, there exists thus a discrepancy between the models and the real maneuvering behaviors after these actions. A shorter re-convergence periods can manifest that the CTRA is more robust, whereas the CMM can be sensitive towards sudden actions. The switching of the vessel heading is thought to cause numerical errors in the estimation algorithms. Once the vessel heading is aligned with the true north, the heading measurements of heading can switch between

Table 4
Percentage of the bounded average NIS.

Stages	S1	S2	S3	S4	S5	S6
Scenario 2 (CMM + UKF)	77%	77%	67%	80%	77%	72%
Scenario 3 (CTRA + EKF)	73%	80%	74%	77%	77%	74%
Scenario 4 (CTRA + UKF)	73%	80%	74%	77%	77%	74%

Table 5
Percentage of the bounded autocorrelation.

Stages	S1	S2	S3	S4	S5	S6
Scenario 2 (CMM + UKF)	94%	95%	81%	93%	93%	95%
Scenario 3 (CTRA + EKF)	92%	94%	92%	96%	96%	95%
Scenario 4 (CTRA + UKF)	93%	94%	93%	95%	93%	95%

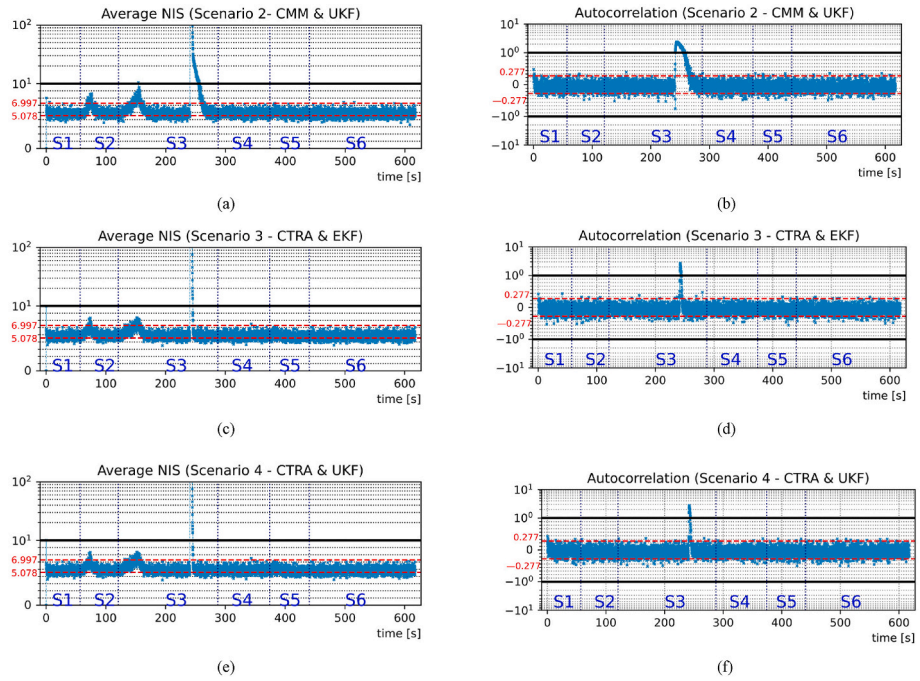

Fig. 10. Filter consistency test based on average NIS and autocorrelation. Areas above and below the black lines are on a logarithmic scale. The related critical values of test statistics are shown in red lines.

0 and 360°, which leads to great numerical errors in the innovation calculations.

Since the upper unbounded values of the NIS indicate that the estimated error can be underestimated, ship maneuvering behavior predictions in a local scale based underestimated errors can be thus too optimistic so that potential collision risks can be overlooked. In contrast, the lower unbounded NIS represents the overestimation of errors, which causes an inefficiency in the estimation algorithm. Since the consistency tests show that the lower unbounded NIS (roughly 20%) is evenly distributed and not significantly exceeded, the impact on the prediction error is considered negligible.

5.4. Root mean square errors

The RMS errors from the Monte Carlo-based simulations of Scenario 2, 3 and 4 are illustrated (see Figs. 11–13). The suboptimal property of proposed nonlinear filters can be used to explain the non-zero RMS errors. One can observe that a modest increase of the RMS errors during the first and second unbounded periods due to the sudden actions. The most significant increases in the RMS errors happen after the switching of the vessel heading. Although both the EKF and UKF can converge the estimation algorithm again, the re-convergence time can be longer for some states, and this is more obvious in Scenario 2. Therefore, it can be inferred that the frequent switching of the vessel heading, such as continuous northward navigation or zigzag maneuvers, can cause large estimation errors and cause estimation algorithms to diverge.

It is also obvious in Figs. 11–13 that the estimation accuracy of velocities and accelerations is guaranteed in the proposed state-space models. The state-space models used in this study validate the speculations that ship motions in the sway direction can have a greater influence on the state estimation process, causing the large drifts and biases in the estimated velocities and accelerations (Wang et al., 2022b). When comparing Scenario 3 and Scenario 4, it can be observed that the performances of the EKF and UKF are almost the same. Since the computational cost of the UKF is usually higher, the EKF can be a better choice for real-time applications with limited computational resources.

Based on the above discussion, it can be considered that Scenarios 2, 3, and 4 are consistent, except for sudden rudder orders or vessel heading variations. To mitigate the estimation algorithm errors due to such sudden actions, an increase in the model uncertainty can be introduced, and such a method requires an adaptive tuning mechanism of the system noise matrix. For vessel heading variations (i.e., between 0 and 360°), a special wrapping treatment towards the vessel heading inside the estimation algorithms should be developed in the future.

6. Conclusion

Two kinematic motion models—the CMM and CTRA are used as the system models in continuous-time for vessel state estimation. Combining with the measurement models in discrete-time, the EKF and UKF with corresponding modifications are applied. Based on the simulated maneuvering data sets from the UiT bridge simulator, the Monte Carlo-based simulations are performed on four scenarios, and the simulation results are further used for the estimation algorithm stability and consistency tests. The results of the stability test show that the combination of the CMM and EKF (Scenario 1) is an unstable scenario. For the other three scenarios, except for periods when sudden maneuvering actions or vessel heading variations occur, the estimation algorithm can be considered as consistent, even though small scale estimation errors exist.

It is apparent that Scenario 1 should be avoided in actual vessel maneuvering situations. For other scenarios, the estimated parameters with a relevant consistent test can be used to evaluate the estimation accuracy of ship maneuvering behavior in a local scale. However, it should be noted that sudden maneuvers of ocean-going vessels can often lead to high-risk ship encounter situations. Due to changes in translational and rotational accelerations or yaw rate caused by sudden maneuvering actions, the vessel state predictions based on the CMM and CTRA may not be sufficient so that potential collision risks may be higher. To increase the prediction accuracy, it may require a large amount of vessel state measurements for a longer period, but this may result in a shorter reaction time for the decision-making process during a ship close encounter situation. Switching of the vessel's heading can cause larger estimation errors compared to sudden maneuvers. It is expected that degraded vessel state predictions may occur after such situations. Therefore, certain methods that can reduce the heading-related errors need to be considered (Wang et al., 2023). Regarding the simulation results, it is worth mentioning that multiple simulations involving different types of vessels are conducted, and they yielded similar results. However, for the sake of representativeness, this paper presents only the results for a general cargo ship.

The bridge simulator-based experiment can be viewed as the foundation for verifying the models and algorithms in the second step. Future work will involve verifying these models and algorithms using real navigation data obtained from sea-trial experiments. It is expected that certain errors may arise during sea trails, especially under rough weather or sea conditions. Furthermore, real vessels equipped with complex control and power systems may exhibit unexpected maneuvering behaviors, which can introduce additional uncertainties. Therefore, further work will be also planned to find solutions for these factors.

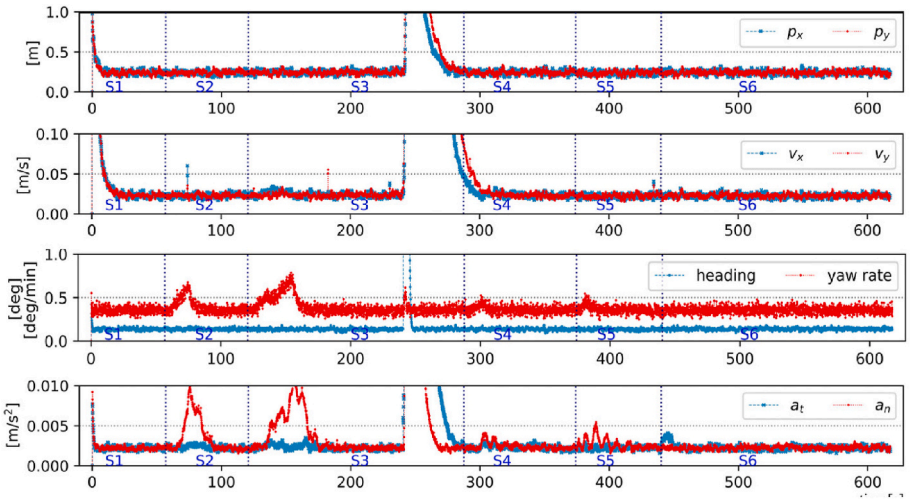

Fig. 11. The RMS errors of estimated states (50 runs) in Scenario 2 (CMM + UKF).

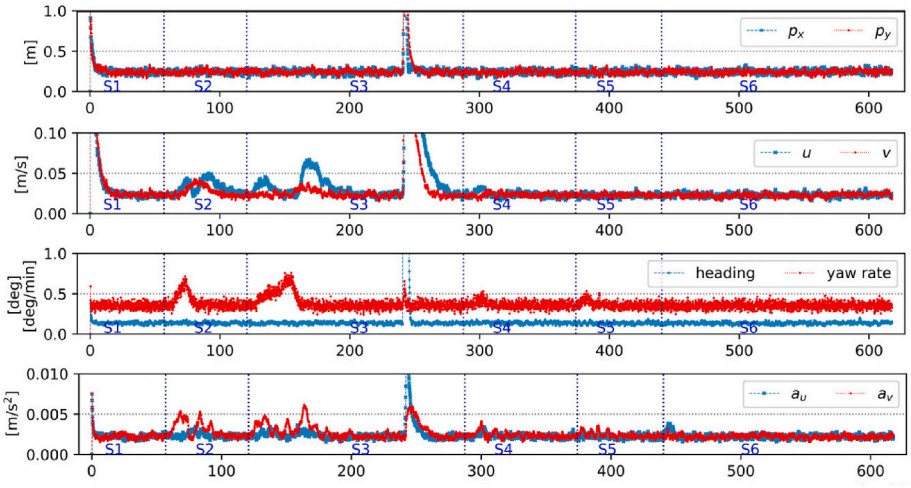

Fig. 12. The RMS errors of estimated states (50 runs) in Scenario 3 (CTRA + EKF).

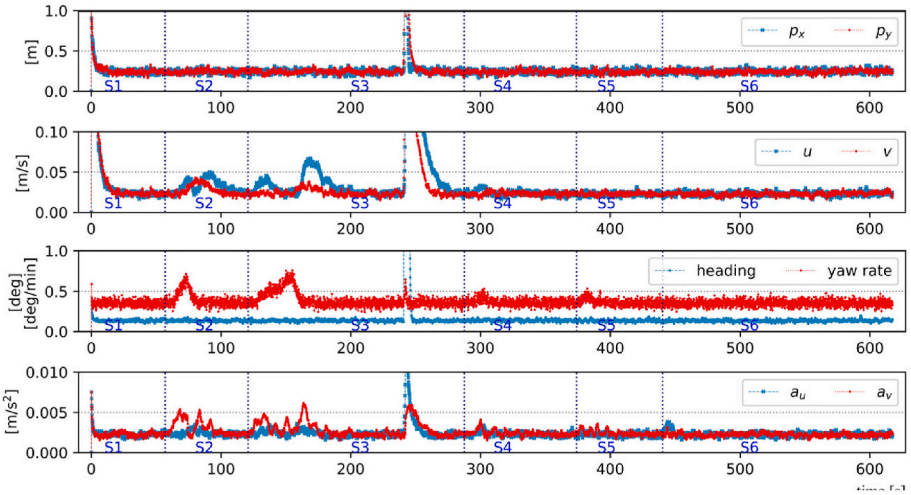

Fig. 13. The RMS errors of estimated states (50 runs) in Scenario 4 (CTRA + UKF).

CRediT authorship contribution statement

Yufei Wang: Conceptualization, Methodology, Programming, Validation, Writing – original draft, preparation. **Lokukaluge Prasad Perera:** Methodology, Validation, Supervision, Writing – review & editing. **Bjørn-Morten Batalden:** Supervision, Writing – review & editing.

Declaration of competing interest

The authors declare that they have no known competing financial interests or personal relationships that could have appeared to influence the work reported in this paper.

Data availability

Data will be made available on request.

References

Akbar, A., Aasen, A., Msakni, M.K., Fagerholt, K., Lindstad, E., Meisel, F., 2020. An economic analysis of introducing autonomous ships in a short-sea liner shipping network. Int. Trans. Oper. Res. 28 https://doi.org/10.1111/itor.12788.

Ames, William F., 1977. Numerical Methods for Partial Differential Equations, second ed. Academic Press, pp. 1–40. 9780120567607.

Barrau, A., 2015. Non-linear state error based extended Kalman filters with applications to navigation. Automatic. Mines Paristech, English. NNT:. tel-01247723.

Bar-Shalom, Y., Rong, X., L, Kirubarajan, T., 2002. Estimation with applications to tracking and navigation: theory. Algorithms and Software.John Wiley & Sons, Inc. 5, 247.

Best, R.A., Norton, J.P., 1997. A new model and efficient tracker for a target with curvilinear motion. IEEE Trans. Aero. Electron. Syst. 33, 1030–1037.

Butcher, J., 1996. A history of Runge-Kutta methods. Appl. Numer. Math. 20, 247–260. https://doi.org/10.1016/0168-9274(95)00108-5. URL: https://www.sciencedirect.com/science/article/pii/0168927495001085.

Chakraborty, D., Başağaoğlu, H., Winterle, J., 2020. Interpretable vs. noninterpretable machine learning models for data-driven hydro- climatological process modeling. Expert Syst. Appl. 170, 114498 https://doi.org/10.1016/j.eswa.2020.114498.

Chew, V., 1966. Confidence, prediction, and tolerance regions for the multivariate normal distribution. J. Am. Stat. Assoc. 61, 605–617. URL: http://www.jstor.org/stable/2282774.

Cline, A.K., Moler, C.B., Stewart, G.W., Wilkinson, J.H., 1979. An estimate for the condition number of a matrix. SIAM J. Numer. Anal. 16, 368–375. https://doi.org/10.1137/0716029.

Coraddu, A., Oneto, L., Baldi, F., Cipollini, F., Atlar, M., Savio, S., 2019. Data-driven ship digital twin for estimating the speed loss caused by the marine fouling. Ocean Engineering 186, 106063. https://doi.org/10.1016/j.oceaneng.2019.05.045.

Daum, F., 2005. Nonlinear filters: beyond the kalman filter. IEEE Aero. Electron. Syst. Mag. 20, 57–69. https://doi.org/10.1109/MAES, 2005.1499276.

Do, K.D., Pan, J., 2009. Control of Ships and Underwater Vehicles, 1 ed. Springer London. https://doi.org/10.1007/978-1-84882-730-1.

EMSA, 2021. Annual Overview of Marine Casualties and Incidents 2021. European Maritime Safety Agency. Report.

Endsley, M.R., 1995. Toward a theory of situation awareness in dynamic systems. Hum. Factors 37, 32–64. https://doi.org/10.1518/001872095779049543.

Fossen, T.I., 2010. Handbook of Marine Craft Hydrodynamics and Motion Control. John Wiley & Sons Ltd.

Frogerais, P., Bellanger, J., Senhadji, L., 2012. Various ways to compute the continuous-discrete extended kalman filter. IEEE Trans. Automat. Control 57, 1000–1004.
Grech, M.R., Horberry, T., Smith, A., 2002. Human error in maritime operations: analyses of accident reports using the leximancer tool. In: Proceedings of the Human Factors and Ergonomics Society Annual Meeting, vol. 46, pp. 1718–1721. https://doi.org/10.1177/154193120204601906.
Hanachi, H., Yu, W., Kim, I.Y., Liu, J., Mechefske, C., 2019. Hybrid data-driven physics-based model fusion framework for tool wear prediction. Int. J. Adv. Des. Manuf. Technol. 101 https://doi.org/10.1007/s00170-018-3157-5.
Hover, F.S., Michael S, T., 2010. Chapter 10: vehicle internal dynamics. In: System Design for Uncertainty. MIT OpenCourseWare, Cambridge MA. URL: https://ocw.mit.edu/courses/2-017j-design-of-electromechanical-robotic-systems-fall-2009/resources/mit2_017jf09_ch10/.MIT.
Ian, C., 2004. Ship Dynamics for Mariners. The Nautical Institute, p. 114.
Im, I., Shin, D., Jeong, J., 2018. Components for smart autonomous ship architecture based on intelligent information technology. Proc. Comput. Sci. 134, 91–98. https://doi.org/10.1016/j.procs.2018.07.148.
Janssen, W.D., Blocken, B., van Wijhe, H.J., 2017. Cfd simulations of wind loads on a container ship: Validation and impact of geometrical simplifications. J. Wind Eng. Ind. Aerod. 166, 106–116. URL: https://www.sciencedirect.com/science/article/pii/S0167610517300818.
Kim, T.E., Perera, L.P., Sollid, M.P., Batalden, B.M., Sydnes, A., 2022. Safety challenges related to autonomous ships in mixed navigational environments. WMU J. Marit.Aff. https://doi.org/10.1007/s13437-022-00277-z.
Kongsberg, M., 2020. Kongsberg maritime and massterly to equip and operate two zero-emission autonomous vessels for asko. URL:https://www.kongsberg.com/maritime/about-us/news-and-media. . (Accessed 20 September 2022).
Kretschmann, L., Burmeister, H.C., Jahn, C., 2017. Analyzing the economic benefit of unmanned autonomous ships: an exploratory cost- comparison between an autonomous and a conventional bulk carrier. Res. Transport. Bus. & Manag. 25, 76–86. URL: https://www.sciencedirect.com/science/article/pii/S2210539516301328.
Leander, J., Lundh, T., Jirstrand, M., 2014. Stochastic differential equations as a tool to regularize the parameter estimation problem for continuous time dynamical systems given discrete time measurements. Math. Biosci. 251, 54–62. https://doi.org/10.1016/j.mbs.2014.03.001. URL: https://www.sciencedirect.com/science/article/pii/S0025556414000510.
Li, X.R., Jilkov, V.P., 2003. Survey of maneuvering target tracking. part i. dynamic models. IEEE Trans. Aero. Electron. Syst. 39, 1333–1364.
Mbalawata, I., Särkkä, S., Haario, H., 2012. Parameter estimation in stochastic differential equations with Markov chain Monte Carlo and non- linear kalman filtering. Comput. Stat. 28 https://doi.org/10.1007/s00180-012-0352-y.
Meguri2040, 2020. The nippon foundation meguri2040 fully autonomous ship program. URL: https://www.nippon-foundation.or.jp/en/news/articles/2022/20220118-66716.html. (Accessed 20 September 2022).
Miguel, M.R., Felipe, E., Alfredo, G., 2017. Analysis of the optimal sampling rate for state estimation in sensor networks with delays. ISA (Instrum. Soc. Am.) Trans. 68, 293–301. https://doi.org/10.1016/j.isatra.2017.03.007.
Molland, A., 2008. The Maritime Engineering Reference Book, 1 ed. Butterworth-Heinemann.
MSC, 2021. Outcome of the Regulatory Scoping Exercise for the Use of Maritime Autonomous Surface Ships (MASS).Report MSC.1/Circ.1638. Maritime Safety Committee IMO.
Munim, Z.H., 2019. Autonomous ships: a review, innovative applications and future maritime business models. Supply Chain Forum Int. J. 20, 266–279. https://doi.org/10.1080/16258312.2019.1631714.
Murray, B., Perera, L.P., 2020. A dual linear autoencoder approach for vessel trajectory prediction using historical ais data. Ocean Engineering 209, 107478. https://doi.org/10.1016/j.oceaneng.2020.107478.
Perera, L.P., 2017. Navigation vector based ship maneuvering prediction. Ocean Engineering 138, 151–160.
Perera, L.P., 2019. Deep learning toward autonomous ship navigation and possible colregs failures. J. Offshore Mech. Arctic Eng. 142 https://doi.org/10.1115/1.4045372.
Perera, L.P., Murray, B., 2019. Situation awareness of autonomous ship navigation in a mixed environment under advanced ship predictor. In: ASME 2019 38th International Conference on Ocean. Offshore and Arctic Engineering. V07BT06A029.
Rahman, S.M., San, O., Rasheed, A., 2018. A hybrid approach for model order reduction of barotropic quasi-geostrophic turbulence. Fluid 3, 86. https://doi.org/10.3390/fluids3040086.
Ribeiro, M.T., Singh, S., Guestrin, C., 2016. Model-agnostic interpretability of machine learning. URL: https://arxiv.org/abs/1606.05386.
Sandhåland, H., Oltedal, H., Eid, J., 2015. Situation awareness in bridge operations – a study of collisions between attendant vessels and offshore facilities in the north sea. Saf. Sci. 79, 277–285. https://doi.org/10.1016/j.ssci.2015.06.021.
Sarkka, S., 2007. On unscented kalman filtering for state estimation of continuous-time nonlinear systems. IEEE Trans. Automat. Control 52, 1631–1641.
Schubert, R., Richter, E., Wanielik, G., 2008. Comparison and Evaluation of Advanced Motion Models for Vehicle Tracking, pp. 1–6. https://doi.org/10.1109/ICIF.2008.4632283.
Seo, S., 2016. Safer and more efficient ship handling with the pivot point concept. The Int.J.Marine Navig.Safety of Sea Transport. 10.
Sneddon, A., Mearns, K., Flin, R., 2006. Situation awareness and safety in offshore drill crews. Cognit. Technol. Work 8, 255–267. https://doi.org/10.1007/s10111-006-0040-1.
Stellet, J.E., Straub, F., Schumacher, J., Branz, W., Zöllner, J.M., 2015. Estimating the process noise variance for vehicle motion models. In: 2015 IEEE 18th International Conference on Intelligent Transportation Systems, pp. 1512–1519. https://doi.org/10.1109/ITSC.2015.212.
Svensson, D., 2019. Derivation of the discrete-time constant turn rate and acceleration motion model. In: 2019 Sensor Data Fusion: Trends, Solutions, Applications. SDF), pp. 1–5. https://doi.org/10.1109/SDF.2019.8916654.
Takeno, M., Katayama, T., 2012. A numerical method for continuous-discrete unscented kalman filter. Int. J. Innovat. Comput. Inf. Control 8-3 (B), 2261–2274.
Thombre, S., Zhao, Z., Ramm-Schmidt, H., Vallet García, J.M., Malkamäki, T., Nikolskiy, S., Hammarberg, T., Nuortie, H., Bhuiyan, H., M, Z., Särkkä, S., Lehtola, V. V., 2022. Sensors and ai techniques for situational awareness in autonomous ships: a review. IEEE Trans. Intelligent Transport. Sys. 23, 64–83. https://doi.org/10.1109/TITS.2020.3023957.
Triepels, R., Daniels, H., Feelders, A., 2018. Data-driven fraud detection in international shipping. Expert Syst. Appl. 99, 193–202. URL: https://www.sciencedirect.com/science/article/pii/S0957417418300083.
UNCTAD, 2021. Review of Maritime Transport 2021. Report. United Nations Conference on Trade and Development.
Vellido, A., Martín-Guerrero, J.D., Lisboa, P.J.G., 2012. Making machine learning models interpretable. In: European Symposium on Artificial Neural Networks, Computational Intelligence and Machine Learning.
Wan, E., Merwe, R., 2000. The Unscented Kalman Filter for Nonlinear Estimation, pp. 153–158. https://doi.org/10.1109/ASSPCC.2000.882463.
Wang, J., Li, Y., Gao, R.X., Zhang, F., 2022a. Hybrid physics-based and data-driven models for smart manufacturing: modelling, simulation, and explainability. J. Manuf. Syst. 63, 381–391. URL. https://www.sciencedirect.com/science/article/pii/S0278612522000541.
Wang, Y.F., Perera, L.P., Batalden, B.M., 2022b. The comparison of two kinematic motion models for shipping maneuvers (79583. In: The 42nd International Conference on Ocean, Offshore and Arctic Engineering (OMAE).
Wang, Y.F., Perera, L.P., Batalden, B.M., 2023. Coordinate conversion and switching correction to reduce vessel heading related errors in highlatitude navigation. In: The 22nd World Congress of the International Federation of Automatic Control. IFAC, 2023.
Willard, J.D., Jia, X., Xu, S., Steinbach, M.S., Kumar, V., 2020. Integrating Physics-Based Modeling with Machine Learning: A Survey, 04919. ArXiv abs/2003.
Wróbel, K., Montewka, J., Kujala, P., 2017. Towards the assessment of potential impact of unmanned vessels on maritime transportation safety. Reliab. Eng. Syst. Saf. 165, 155–169. URL: https://www.sciencedirect.com/science/article/pii/S0951832016303337.
Yara, I., 2021. Yara to start operating the world's first fully emission-free container ship. URL. https://www.yara.com/corporate-releases/yara-to-start-operating-the-worlds-first-fully-emission-free-container-ship. (Accessed 20 September 2022).
Yasukawa, H., Yoshimura, Y., 2014. Introduction of mmg standard method for ship maneuvering predictions. J. Mar. Sci. Technol. 20, 37–52. https://doi.org/10.1007/s00773-014-0293-y.

Paper III

Coordinate Conversion and Switching Correction to Reduce Vessel Heading-Related Errors in High-Latitude Navigation

Wang, Y., Perera, L. P. and Batalden, B.-M. (2023)

Published in *The 22nd World Congress of the International Federation of Automatic Control (IFAC 2023). 56-2, 11590–11595*

https://doi.org/10.1016/j.ifacol.2023.10.477

Available online at www.sciencedirect.com

ScienceDirect

IFAC PapersOnline CONFERENCE PAPER ARCHIVE

IFAC PapersOnLine 56-2 (2023) 11602–11607

Coordinate conversion and switching correction to reduce vessel heading related errors in high-latitude navigation

Yufei Wang * **Lokukaluge P. Perera** * **Bjørn-Morten Batalden** *

* *UiT The Arctic University of Norway, Tromsø, 9037 Norway (yufei.wang@uit.no; prasad.perera@uit.no; bjorn.batalden@uit.no)*

Abstract: Considering the distortion errors of projected coordinates and the switching property of vessel heading, coordinate conversion and switching correction methods are proposed to modify a kinematic motion model and the Unscented Kalman Filter (UKF). The coordinate conversion method utilizes the grid convergence from a Universal Transverse Mercator (UTM) projection to correct the vessel heading. The switching correction is embedded in the UKF so that the innovations of vessel heading can be calculated correctly. The simulation results demonstrate that the proposed modifications in both model and algorithm can generate more accurate estimated vessel states from two simulated maneuvers. Since a reliable estimation of vessel maneuvers is the prerequisite in many intelligent systems that support various decision-making processes in maritime transportation, the proposed modifications can be therefore implemented into these systems to support navigation safety in high latitude areas.

Keywords: vessel state estimation, kinematic motion model, Unscented Kalman Filter, UTM coordinate system, navigation in high latitudes, circular data.

1. INTRODUCTION

The recent development in industrial digitization brings new opportunities and challenges to the traditional maritime industry. Many latest intelligence systems supported by artificial intelligence and big data become highly involved in various maritime applications, i.e., energy efficiency, equipment maintenance, navigation, and accident prevention, etc (Munim et al., 2020). Since future vessels will be navigated by intelligent systems, the threshold for navigation errors should be minimized, especially in high latitudes. On the other hand, human navigation activities in high latitudes have an increasing trend in recent years. With global warming and the gradual disappearance of the Arctic ice caps, the potential of Arctic shipping routes is being constantly highlighted (Aksenov et al., 2017).

As for intelligence systems to support ship navigation, safety can be an important factor. It is imperative to obtain reliable navigation data sets which are related to the vessel's maneuvering behaviors for the same purpose. These data sets can be used to estimate vessel states online, and the accuracy of estimated states needs to be guaranteed since poor quality of estimated states can cause the wrong prediction of vessel behaviors and finally lead to collisions or near-miss situations. Maneuvering behavior of vessels can be described by kinematic motion models in several studies (Li and Jilkov, 2003; Perera, 2017; Wang et al., 2022), and navigation states of vessels can be estimated by Kalman filter-based (KF) techniques with relatively high accuracy. However, as an implicit assumption that measured positions used in most kinematic motion models are actually the projected coordinates of the raw latitude/longitude data from GNSS systems, where the UTM coordinate system has generally been used. Similar processing methods which use the UTM coordinate system in maritime research studies are also presented (Mu et al., 2019; Kim et al., 2022). The projected coordinates can introduce larger distortion errors in high-latitude areas, especially if the models are associated with heading measurements that can cause various erroneous conditions in state estimation. Consequently, a direct implementation of kinematic motion models in high latitudes can be problematic due to the same reasons.

Another factor that is usually omitted in applications of ship maneuvering is that the measured heading belongs to circular data (Philipp, 2009), which is different from other non-circular data, such as positions and velocities. Measured headings from advanced optical gyroscopes can show the switching property so that the readings can jump discontinuously from 0 to 360° when the ship's actual heading measurements are close to true north. The measurements of the discontinuous heading (i.e., varying among 0°+ and 360°- values) can finally cause the estimation algorithms to diverge during vessel operations in such regions. There are several modified methods to handle the circular data, such as the quaternion-based estimation (Zhang et al., 2012) and the Invariant Extended Kalman Filter (Barrau, 2015). The distinctive feature of these methods is the representation of circular data to the unit quaternions and the Lie groups, respectively.

This paper proposes a novel methodology, i.e., coordinate conversion and switch correction method that work on the kinematic motion model with the UKF algorithms as a solution to the above-mentioned problem. These modifications can be conveniently applied to the same

Peer review under responsibility of International Federation of Automatic Control.
10.1016/j.ifacol.2023.10.477

model and estimation algorithm. Simulated or actual vessel maneuvers in high-latitude areas can use the proposed methodology to improve their navigation integrity. The remainder is organized as follows: Section 2 introduces the utilized coordinate conversion method of the UTM; the kinematic motion model is presented in Section 3; Section 4 describes the UKF algorithms; Section 5 shows the simulation settings and results; the conclusion and plans in next step are summarized in the final.

2. UTM COORDINATE CONVERSION

The UTM coordinate system is a commonly used projection coordinate system that can represent geographic positions in a Cartesian coordinate system. This system has extensively been used in ship navigation. The mechanism of the UTM projection is roughly shown in Fig. 1, and the details can be referred to Osborne (2013).

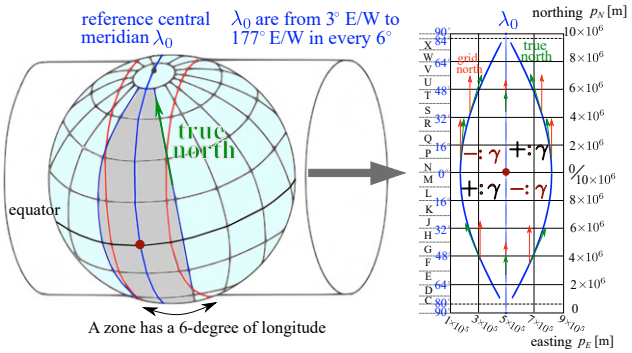

Fig. 1. The schema of UTM projection and coordinate system. There are 60 divided zones in total.

There are various methods that convert latitude and longitude (ϕ, λ) into northing and easting (p_N, p_E) in the UTM system. In this study, the method proposed by Kawase (2012) which consists of (2) to (11) is used since it is more convenient for computer programming. This methodology, i.e., the coordinate conversion method, is based on the WGS84 spatial reference system that describes the Earth as an oblate spheroid along the north-south axis with an equatorial radius a and a flattening f. Some preliminary constant parameters based on a and f can be calculated at first.

$$a = 6378.137[km];\ 1/f = 298.257223563 \tag{1}$$

$$n = \frac{f}{2-f};\ A = \frac{a}{1+n}\left(1 + \frac{n^2}{4} + \frac{n^4}{64} + \cdots\right) \tag{2}$$

$$\alpha_1 = \frac{1}{2} - \frac{2}{3}n^2 + \frac{5}{16}n^3; \alpha_2 = \frac{13}{48}n^2 - \frac{3}{5}n^3; \alpha_3 = \frac{61}{240}n^3 \tag{3}$$

The origin of the projected area lies in the intersection of the equator and the reference central meridian λ_0 (see Fig. 1). The point scale at the reference central meridian k_0 is specified to be 0.9996. To avoid negative position values, the origin of northing N_0 is set to 0[km] in the northern hemisphere and 10000[km] in the southern hemisphere. The origin of easting E_0 starts with 500[km]. With a measured ϕ and λ, p_N, p_E, local point scale k, and grid convergence γ can be calculated as:

$$p_N = N_0 + k_0 A\left(\xi^{'} + \sum_{j=1}^{3}\alpha_j\, sin\left(2j\xi^{'}\right) cosh\left(2j\eta^{'}\right)\right) \tag{4}$$

$$p_E = E_0 + k_0 A\left(\eta^{'} + \sum_{j=1}^{3}\alpha_j\, cos\left(2j\xi^{'}\right) sinh\left(2j\eta^{'}\right)\right) \tag{5}$$

$$k = \frac{k_0 A}{a}\sqrt{\left(1 + \left(\frac{1-n}{1+n}tan\phi\right)^2\right)\frac{\sigma^2 + \tau^2}{t^2 + cos^2(\lambda - \lambda_0)}} \tag{6}$$

$$\gamma = tan^{-1}\left(\frac{\tau\sqrt{1+t^2} + \sigma\, t\, tan(\lambda - \lambda_0)}{\sigma\sqrt{1+t^2} - \tau\, t\, tan(\lambda - \lambda_0)}\right) \tag{7}$$

where:

$$t = sinh\left(tanh^{-1}(sin\phi) - \frac{2\sqrt{n}}{1+n}tanh^{-1}\left(\frac{2\sqrt{n}}{1+n}sin\phi\right)\right) \tag{8}$$

$$\xi^{'} = tan^{-1}\left(\frac{t}{cos(\lambda - \lambda_0)}\right); \eta^{'} = tanh^{-1}\left(\frac{sin(\lambda - \lambda_0)}{\sqrt{1+t^2}}\right) \tag{9}$$

$$\sigma = 1 + \sum_{j=1}^{3} 2j\alpha_j\, cos\left(2j\xi^{'}\right) cosh\left(2j\eta^{'}\right) \tag{10}$$

$$\tau = \sum_{j=1}^{3} 2j\alpha_j\, sin\left(2j\xi^{'}\right) sinh\left(2j\eta^{'}\right) \tag{11}$$

Grid convergence γ is the difference between true north and grid north, and the sign of γ is shown in Fig. 1. The value of γ is zero in the equator and the central meridian. As objects move away from these axes, γ increases and will reach a higher value in high-latitude areas. Local point scale k in the UTM projection is determined by the located ϕ and λ. A maximum value of k can reach 1.0010 at the zone boundaries in the equator, which indicates a projected distance falls short of the true scale by 1 unit in 1000. For general collision avoidance, this projection error can be neglected.

3. SHIP MOTION MODEL

A kinematic motion model—Constant Turn Rate and Acceleration (CTRA) model is used in this study to model ship maneuvering behavior. It is assumed that the center of gravity (CG) does not shift greatly during maneuvering. The relevant navigation states which describe the CG of a vessel are shown in Fig. 2. It should be noted that

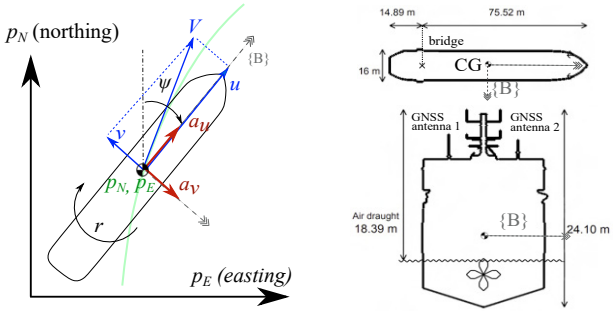

Fig. 2. The system states in the CTRA and the geometry information of the vessel used in the simulation

the heading as a system state in the CTRA model is based on the northing axis, i.e., grid north. As for the measurements, it is designed so that the vessel position, heading, yaw rate, and acceleration can be measured from on-board sensors as discrete-time signals. The measured position can be calibrated to the CG of the vessel. It is also assumed that IMUs are well located in the CG so that the measured accelerations do not contain any misaligned noises. In particular, optical gyroscopes are considered so that the measured heading is based on true north. Through the state-space representation method, a continuous-time system model and a discrete-time measurement model are considered and that can be written as:

$$\boldsymbol{x}(t) = [p_N, p_E, u, v, \psi, r, a_u, a_v]\,|_{(t)} \tag{12}$$

$$\dot{\boldsymbol{x}}(t) = f(\boldsymbol{x}(t)) + \boldsymbol{w_x} \tag{13}$$

$$= \begin{bmatrix} u(t)\,cos(\psi(t)) - v(t)\,sin(\psi(t)) \\ v(t)\,cos(\psi(t)) + u(t)\,sin(\psi(t)) \\ a_u(t) \\ a_v(t) \\ 0 \\ 0 \\ r(t) \\ 0 \end{bmatrix} + \boldsymbol{w_x} \tag{14}$$

where:

$$\boldsymbol{w_x} \sim \mathcal{N}\left(0,\, diag\left(\boldsymbol{Q} \in R^{8\times 8}\right)\right)$$

$$\boldsymbol{z}[t_k] = [z_{p_N}, z_{p_E}, z_{au}, z_{av}, z_\psi, z_r]\,|_{[t_k]} \tag{15}$$

$$\boldsymbol{z}[t_k] = h(\boldsymbol{x}[t_k]) + \boldsymbol{w_z} = \begin{bmatrix} p_N[t_k] \\ p_E[t_k] \\ a_u[t_k] - v[t_k]\,r[t_k] \\ a_v[t_k] + u[t_k]\,r[t_k] \\ \psi[t_k] + \gamma \\ r[t_k] \end{bmatrix} + \boldsymbol{w_z} \tag{16}$$

where:

$$\boldsymbol{w_z} \sim \mathcal{N}\left(0,\, diag\left(\boldsymbol{R} \in R^{6\times 6}\right)\right); t_k = k \cdot \Delta t \;\; (k = 0, 1, ...)$$

Both the system noise $\boldsymbol{w_x}$ and measurement noise $\boldsymbol{w_z}$ are assumed to be Gaussian noise, with their respective covariances being diagonal matrices. In the measurement model, p_N, p_E, and γ can be calculated based on the raw latitude/longitude data according to (4), (5), and (7). Since the change of γ is a small value in a local area, it is treated as a constant during the simulated maneuvers. Note that the calculated heading from the measurement models in (16) may not locate between 0° and 360°, which is inconsistent with z_ψ in (15). A modification towards the measurement innovations of heading is thus necessary.

4. STATE ESTIMATION ALGORITHM

The UKF is selected to estimate the states in the CTRA. The main feature of the UKF is that a set of sigma points ($\boldsymbol{s}$) with pre-defined weights (W) generated from unscented transformation can be used to approximate vessel states and error covariances. The calculation of Jacobians is not required in the UKF, and this is also a benefit for highly nonlinear systems. Since the system model consists of continuous differential equations, exact analytical solutions cannot be found in some situations, numerical methods are therefore developed to solve the prior states in prediction steps (Takeno and Katayama, 2012; Wang et al., 2022).

4.1 Switching correction of heading

After the prediction step, the filtering step will be executed. The posterior states are given by the combination of the prior estimates ($\hat{\boldsymbol{x}}_{t_k|t_{k-1}}$), Kalman gain ($K$), and the measurement innovation ($\boldsymbol{z}[t_k] - \hat{\boldsymbol{z}}_{t_k|t_{k-1}}$) which is also known as the measurement residual.

$$\hat{\boldsymbol{x}}_{t_k|t_k} = \hat{\boldsymbol{x}}_{t_k|t_{k-1}} + K\left(\boldsymbol{z}[t_k] - \hat{\boldsymbol{z}}_{t_k|t_{k-1}}\right) \tag{17}$$
$$\text{where: } \hat{\boldsymbol{z}}_{t_k|t_{k-1}} = h(\boldsymbol{s}[t_k])\,W$$

It should be noted that the difference operation of the measurement innovation in (17) is not suitable for the heading. Because of the switching property, the wrapping effect should be considered, e.g., the difference between 359° and 1° should be 2° instead of 358°. Therefore, a special treatment for the heading should be included. In this study, a switching correction is considered (see Alg. 1). This proposed methodology is based on the assumption that the yaw rate of ships is limited due to the low maneuverability compared with ground vehicles and aircraft. A sharp change of heading is thus unlike to happen for general ships, especially with large tonnages. A threshold value r_{lim} can be consequently applied to modify the innovations.

Algorithm 1
Switching correction for the heading in prediction step

Calculate the innovation of heading:
$res_\psi = z_\psi[t_k] - \hat{\psi}_{t_k|t_{k-1}}$

if $res_\psi \geq r_{lim}\,\Delta t$ **then**
  $res_\psi = res_\psi - 2\pi$
else if $res_\psi < -r_{lim}\,\Delta t$ **then**
  $res_\psi = res_\psi + 2\pi$
end if

After obtain the Kalman Gain K:
$\hat{\psi}_{t_k|t_k} = \left\langle \hat{\psi}_{t_k|t_{k-1}} + K \cdot res_\psi \right\rangle$
where $\langle . \rangle := mod(mod(.\,, 2\pi) + 2\pi, 2\pi)$

4.2 Proposed error for heading

There are various types of errors based on the difference between actual and estimated states to evaluate the estimation accuracy of the respective algorithms. Obviously, the difference operation is not suitable for the switching properties of vessel heading. A vector-based error representation for vessel heading is used in this study (see Fig.3). The heading is converted into the heading vector which has the unit length and the initial point at the origin of the UTM coordinate. The magnitude of error is defined as the angle between two related heading vectors, where the angle can be calculated from the inner product. The sign of error is determined by the quadrants in UTM coordinate after a clockwise rotation of the heading vectors.

5. SIMULATION RESULTS AND DISCUSSION

Data sets from a ship bridge simulator that has the geographic data in the Svalbard area are used in this study. These data sets consist of two ship maneuvers, actual

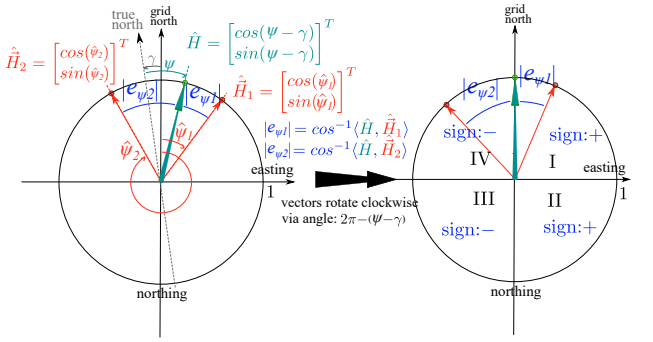

Fig. 3. The designed error representation for heading. Note that the actual heading (green vector) starts from true north; the estimated headings (2 red vectors) start from grid north.

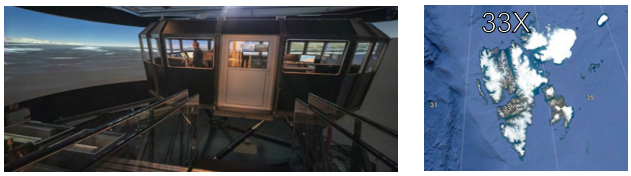

Fig. 4. The UiT ship bridge simulator. The satellite image of the Svalbard area is obtained from Google Earth.

vessel states and measurements (see Fig. 4). In order to verify the effectiveness of the proposed methodology, three scenarios are used to estimate the vessel states under the same initialized conditions (see table 1).

Table 1. Scenarios for state estimation

Config. name	grid convergence in the CTRA	switching correction in the UKF
Scenario 1	Yes	Yes
Scenario 2	Yes	No
Scenario 3	No	Yes

5.1 Simulated maneuvers

The simulated maneuvers are a straight line maneuver towards true north and a zigzag-like maneuver (see Fig. 5). The maneuver towards true north can actually happen in all navigation areas and provide highly discontinuous heading measurements that switch frequently between 0°+ to 360°−. Such a maneuver can be considered as an extreme situation, where the robustness of relevant state estimation algorithms can be degraded. The switching of heading can also happen in zigzag maneuvers. The zigzag maneuver showed in Fig. 5 suffers the switch of heading in time steps—t_1 to t_4. This maneuver can be frequently executed at high latitudes to avoid obstacles like ice conditions.

5.2 Parameter initialization

The related parameter initialization is shown in table 2. The variable δt is used as a temporal unit for the numerical calculation in the prediction steps. The parameters α, β, and κ are used in the UKF to tune the sigma points. The initialized state $\boldsymbol{x_0}$ can be generated from two historical measurements before the filter starts to work. The covariance matrices of both system and measurement noise ($\boldsymbol{Q}$ and $\boldsymbol{R}$) are assumed as diagonal matrices. The detail of the initialization process can be referred to Wang et al. (2022).

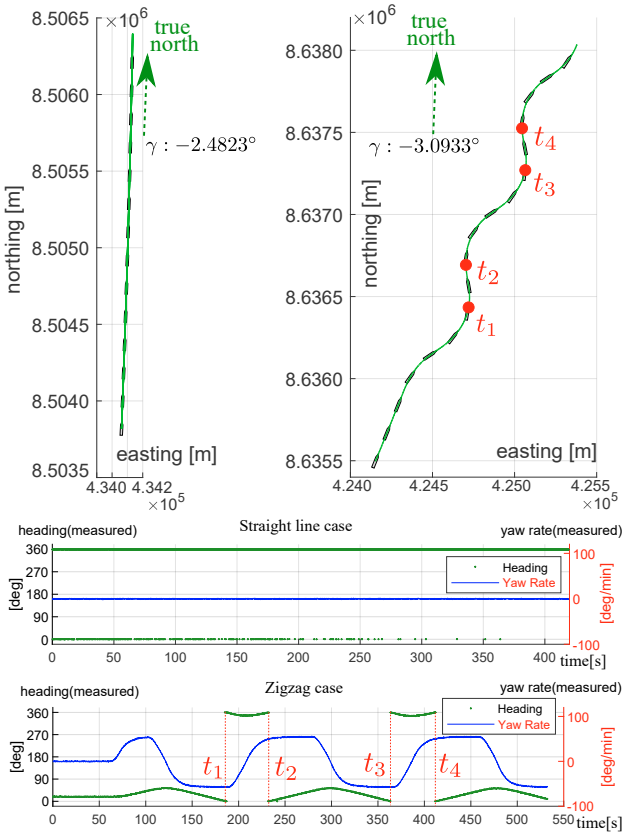

Fig. 5. The simulated straight line and zigzag maneuvers. The vessel position is recorded every 30 seconds. The measured heading and yaw rate are attached.

Table 2. Initilized parameters

Δt	$0.1[s]$	δt	$0.005[s]$
γ (line)	$-2.4823°$	γ (zigzag)	$-3.0933°$
r_{lim}	$^{50\pi}/_{180}[s^{-1}]$	α	0.3
β	2	κ	100
$\boldsymbol{Q}$	$diag(10^{-1}, 10^{-1}, 10^{-3}, 10^{-3}, 10^{-5}, 10^{-5}, {}^{10^{-1}\pi}/_{180}, {}^{10^{-5}\pi}/_{180})$		
$\boldsymbol{R}$	$diag(1, 1, (0.01)^2, (0.01)^2, ({}^{0.5\pi}/_{180})^2, ({}^{10^{-2}\pi}/_{180})^2)$		
$\boldsymbol{x_0}$ (line)	$[8503821, 434061, 5.5, 0.1, 0, 0, 3.14, 0]$		
$\boldsymbol{x_0}$ (Zigzag)	$[8635500, 424155, 6.7, 0.9, 0, 0, 0.31, 0]$		

5.3 Simulation results

Figure 6 shows the Euclidean norm of the estimated position errors. In the straight line case, it can be seen clearly the larger estimated position error from Scenario 2 where the UKF does not contain the switch correction. In the zigzag case, there are occasions when the errors from Scenario 2 increase sharply. The moments that these occasions happen coincide with the time steps—t_1 to t_4 when the measured heading hits true north. However, during other time periods when the measured heading leaves away from true north, the errors from all of the scenarios are less than 1[m]. It can be also observed that the position errors from Scenario 1 and Scenario 3 are

similar in both maneuvering cases. The impact of grid convergence on the accuracy of position estimation in the CTRA is thus smaller. This can be interpreted as the predicted p_N and p_E will not change much without considering γ based on (14), and the measurements of p_N and p_E can also fix the errors in prediction steps.

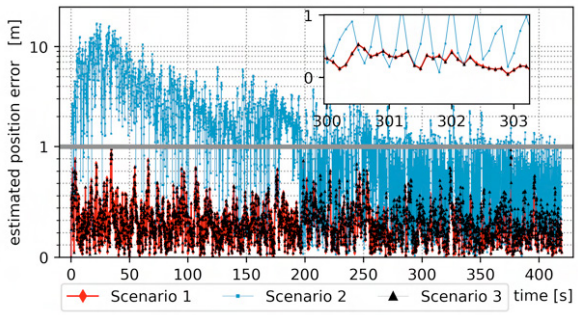

(a) straight line maneuver

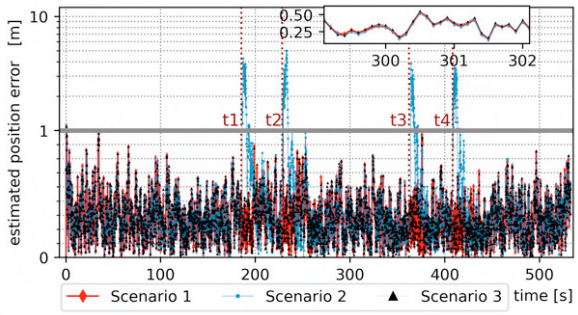

(b) zigzag maneuver

Fig. 6. Euclidean norm of estimation position error. Errors above 1 [m] are plotted on log scale.

The estimated surge and sway velocities (u and v) are demonstrated in Fig.7, and it can be seen that the estimates from Scenario 1 are strongly aligned with the actual values in both maneuvers. In the straight line maneuver, the estimates from Scenario 2 diverge completely, and the divergence behavior of the related algorithm can be noted in Fig. 7a. The estimated u from Scenario 3 are well converged to the actual values, whereas the estimated v has a constant bias. In the zigzag maneuver, a constant bias of the estimated v from Scenario 3 also exists, where a minor bias in the estimated u can also be seen. The estimates from Scenario 2 are similar to those from Scenario 1, except that larger errors occur when the heading switches in the labeled time steps in Fig. 7b. The algorithm diverges in these situations but will also converge after a considerable time period.

The results from Fig.7 indicate that constant biases of estimated v exist when γ is neglected in the CTRA. This can be explained by that v is highly sensitive to the vessel actual heading. It can be seen from Fig.2 that v does not exist if the vessel heading is aligned with the course vector. However, if the estimates of vessel heading are inaccurate due to, for example, the ignoring of projection error, this can lead to extra velocity components in the sway direction. Sway velocities are generally omitted in kinematic models with respect to ground vehicles, but can play a vital role in ship maneuvering and decision-making for collision avoidance. A vessel with additional sway velocity can induce extra swept areas, and thus increase the risk of collision, contact, or near-miss accidents. Therefore, sway velocities must be included and precisely estimated for ship maneuvering.

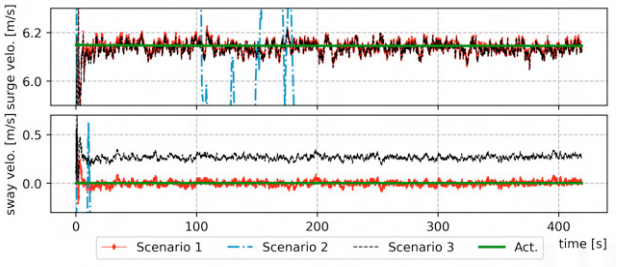

(a) straight line maneuver

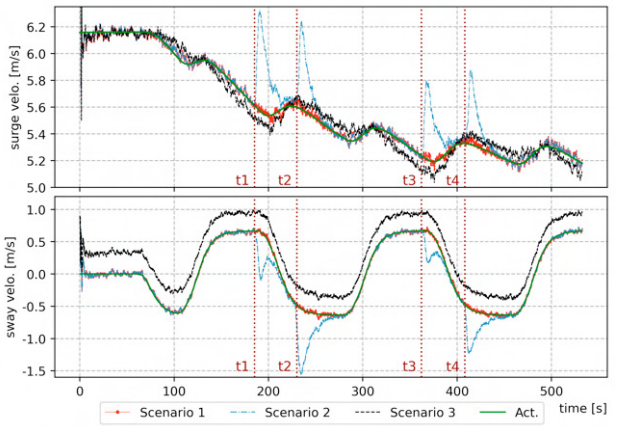

(b) zigzag maneuver

Fig. 7. The estimated surge and sway velocity

The evaluation of the estimated heading is based on the vector-based error representation (see Fig.3). It can be observed that the estimated heading from Scenario 2 becomes diverged when the vessel heading switches in both maneuvers. The estimated heading from Scenario 3 has a constant bias, and this is due to the reason that the grid convergence is not considered in this situation. One should note that the UKF without the switching correction is able to correct large estimation errors once the measured heading well behaves again. However, it takes a relatively long time for the positions and velocities to become converged, especially for the velocities under the same conditions. From this point of view, it can be considered that the switching correction also has a positive effect on the estimation accuracy of the positions and velocities in the CTRA. This is also attributed to the mathematical equations (14) that both positions and velocities are coupled with the heading. A heading innovation without the switching correction can corrupt the posterior estimates in the prediction step of the UKF. Since the UKF algorithm executes iteratively, these corrupted posterior estimates will be implemented in the next prediction step as the inputs to calculate the prior estimates. The uncorrected innovations of vessel heading hence spread to the position and velocity estimates.

The estimates of yaw rate and accelerations are summarized through the root mean square error (RMSE) in

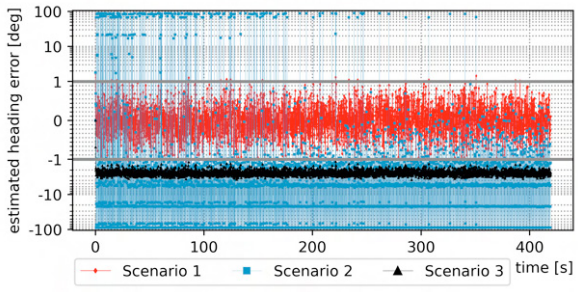

(a) straight line maneuver

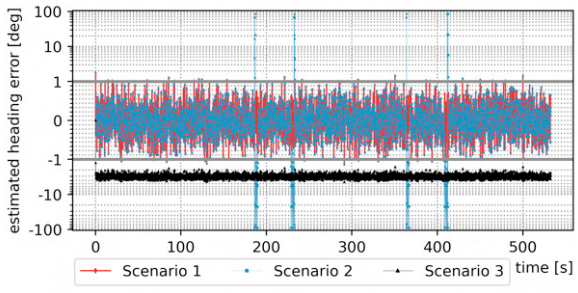

(b) zigzag maneuver

Fig. 8. Plots of proposed error for heading. Errors outside $[-1°, 1°]$ are plotted on log scale.

table 3 and table 4. The RMSEs of yaw rate and accelerations by all scenarios are similar to each other and have the same order of magnitude.

Table 3. RMSE in straight line maneuver

RMSE	Scenario 1	Scenario 2	Scenario 3
$r : [°/min]$	3.53×10^{-1}	3.56×10^{-1}	3.53×10^{-1}
$a_u : [m/s^2]$	4.85×10^{-2}	4.85×10^{-2}	4.85×10^{-2}
$a_v : [m/s^2]$	2.38×10^{-3}	2.39×10^{-3}	2.38×10^{-3}

Table 4. RMSE in zigzag maneuver

RMSE	Scenario 1	Scenario 2	Scenario 3
$r : [°/min]$	3.94×10^{-1}	3.94×10^{-1}	3.94×10^{-1}
$a_u : [m/s^2]$	4.81×10^{-3}	5.44×10^{-3}	6.09×10^{-3}
$a_v : [m/s^2]$	2.61×10^{-3}	3.70×10^{-3}	2.77×10^{-3}

6. CONCLUSIONS AND FUTURE WORK

The UTM projection can result in non-neglectable heading associated errors in high latitudes, and the switching of measured heading can cause significant inaccuracies in vessel state estimation. To mitigate these errors, two proposed solutions are introduced. As the innovative points, these methods consider the grid convergence that is embedded in the system and measurement model of the CTRA, and the correction of heading switching in the UKF. With these proposed methods, the UKF becomes more robust and can handle highly discontinuous measurements of vessel heading. By incorporating the correction made by the grid convergence, the estimation accuracy of vessel states in the CTRA can be further improved. As a result, these improvements can be applied to ship intelligence systems that support navigation safety in high-latitude areas. Future work involves conducting sea-trial experiments in the Tromsø area, which is also located in high latitudes.

ACKNOWLEDGEMENTS

This work has been conducted under the Autonomous ship Program in UiT-The Arctic University of Norway, which aims to develop the digital helmsman as a part of the ship intelligence to operate future vessels supported by the MARKOM II project under the project title “Onshore Operation Center for Remotely Controlled Vessels (OOC 2023)" under the contract number PMK-2022-10014.

REFERENCES

Aksenov, Y., Popova, E.E., Yool, A., Nurser, A.G., Williams, T.D., Bertino, L., and Bergh, J. (2017). On the future navigability of arctic sea routes: high-resolution projections of the arctic ocean and sea ice. *Marine Policy*, 75, 300–317.

Barrau, A. (2015). *Non-linear state error based extended Kalman filters with applications to navigation*. Thesis.

Kawase, K. (2012). Concise derivation of extensive coordinate conversion formulae in the gauss-krueger projection.

Kim, J.S., Lee, D.H., Kim, D.W., Park, H., Paik, K.J., and Kim, S. (2022). A numerical and experimental study on the obstacle collision avoidance system using a 2d lidar sensor for an autonomous surface vehicle. *Ocean Engineering*, 257, 111508. doi: https://doi.org/10.1016/j.oceaneng.2022.111508.

Li, X.R. and Jilkov, V.P. (2003). Survey of maneuvering target tracking. part i. dynamic models. *IEEE Transactions on Aerospace and Electronic Systems*, 39(4), 1333–1364.

Mu, X., He, B., Zhang, X., Song, Y., Shen, Y., and Feng, C. (2019). End-to-end navigation for autonomous underwater vehicle with hybrid recurrent neural networks. *Ocean Engineering*, 194, 106602. doi: https://doi.org/10.1016/j.oceaneng.2019.106602.

Munim, Z.H., Dushenko, M., Jimenez, V.J., Shakil, M.H., and Imset, M. (2020). Big data and artificial intelligence in the maritime industry: a bibliometric review and future research directions. *Maritime Policy & Management*, 47(5), 577–597. URL `https://doi.org/10.1080/03088839.2020.1788731`.

Osborne, P. (2013). *The Mercator Projections*. doi: 10.5281/zenodo.35392.

Perera, L.P. (2017). Navigation vector based ship maneuvering prediction. *Ocean Engineering*, 138, 151–160.

Philipp, B. (2009). Circstat: a matlab toolbox for circular statistics. *Journal of Statistical Software*, 31. doi: 10.18637/jss.v031.i10.

Takeno, M. and Katayama, T. (2012). A numerical method for continuous-discrete unscented kalman filter. *International Journal of Innovative Computing, Information and Control*, 8.

Wang, Y.F., Perera, L.P., and Batalden, B.M. (2022). The comparison of two kinematic motion models for shipping maneuvers (79583). In *The 42nd International Conference on Ocean, Offshore and Arctic Engineering (OMAE)*.

Zhang, Z.Q., Meng, X.L., and Wu, J.K. (2012). Quaternion-based kalman filter with vector selection for accurate orientation tracking. *IEEE Transactions on Instrumentation and Measurement*, 61(10), 2817–2824.

Paper IV

Adaptive Kalman Filter-Based Estimator with Sea Trail Data to Calculate Ship States in Complex Navigation Conditions

Wang, Y., Perera, L. P. and Batalden, B.-M. (2024)

Published in *The 34th International Ocean and Polar Engineering Conference (ISOPE 2024)*

Adaptive Kalman Filter-based Estimator with Sea Trail Data to Calculate Ship States in Complex Navigation Conditions

Yufei Wang[1], Lokukaluge P. Perera[1,2], and Bjørn-Morten Batalden[1]
[1]UiT The Arctic University of Norway, Tromsø, Norway
[2]SINTEF Digital, SINTEF AS, Oslo, Norway

ABSTRACT

With the progress of innovative technologies, ships in future with different autonomy levels are anticipated to enter the realm of maritime transportation. As a result, the scenarios of multi-ship encounters at sea can become more complex and the risk of potential collisions can be difficult to elevate. To support navigation safety and guarantee the required situation awareness level, it is therefore essential to acquire ship navigation states with a greater degree of precision. The Kalman Filter (KF)-based techniques are one of the popular approaches for deriving the ship navigation state by merging the prior estimates from physics-based models with measurements from onboard sensors. However, many KF-based estimates are calculated by assuming constant system and measurement uncertainties during the iterative process. In this study, an adaptive tuning mechanism in the KF-based techniques is utilized to estimate ship navigation states. This approach enables the estimation processes to skillfully reduce both system and measurement noises estimations. Consequently, it results in the generation of smoother and more responsive estimates of the respective vessel states, particularly when confronted with variations in rudder orders or encountering abnormal measured positions.

KEY WORDS: State estimation; Kalman Filter (KF); Unscented Kalman Filter (UKF); Kinematic motion model; Adaptive tuning mechanism; Gaussian Process Regression.

INTRODUCTION

Autonomous shipping is expected to exist and show its benefits in maritime transportation in the coming future. With respect to the current development of autonomous ships, onboard sensors are considered as one of the fundamental parts (Perera, 2019;Thombre et al., 2022). These sensors are specifically designed to provide digital navigators of autonomous ships with precise navigation information, ensuring the maintenance of adequate situation awareness. Since not all ship navigation information can be directly measured, and the measurements from sensors may contain measurement noise, it is generally considered to implement KF-based techniques to generate estimated states with higher precision.

Given the convenience of kinematic motion models, using KF-based estimation combined with these models is a favorable choice (Li and Jilkov, 2003). One advantage of employing kinematic motion models is the ignorance of hydrodynamic coefficients which are associated with external forces and moments. The influences of external disturbances can be modeled as system noises in kinematic motion models. The curvilinear motion model (CMM) and the constant turn rate and acceleration model (CTRA) represent two kinematic motion models which can encompass diverse motions exhibited by ships. As a result, these models are widely employed in numerous research studies to provide essential ship navigation states (Perera, 2017;Wang et al., 2023). Nevertheless, it is important to recognize that these kinematic motion models operate under the assumption of constant accelerations and turn rates. Clearly, this assumption becomes invalid when ships execute new rudder orders or adjust engine power. Consequently, the utilization of constant system noises in the CMM and CTRA within the KF-based estimation can lead to less precise estimates. Another crucial factor to consider is the potential for measurement bias when utilizing GNSS systems. To enhance measurement precision, the augmentation of GNSS is actively encouraged. However, it is important to note that while such augmentation can improve precision, it does not guarantee the elimination of measure abnormalities (Baybura et al., 2019). When the measured outliers exceed certain thresholds, the KF-based estimation may yield questionable results.

Therefore, from a practical perspective, the application of KF-based techniques should incorporate adaptive tuning of system and

measurement noises to enhance robustness. This adjustment ensures that the filtering process remains resilient to varying conditions, contributing to more reliable and precise state estimates.

Adaptive filtering

There are several approaches which are used for tuning system and measurement noises adaptively. The first approach involves a statistical analysis of the innovation (Hu et al., 2003). In the KF-based techniques, the innovation is the difference between the observed measurements and the prior estimates. Through an examination of the statistical properties of innovations, one can assess the evolving characteristics of the associated system and measurement noises over time. An alternative adaptive approach utilizes the innovation as a criterion to identify the occurrence of new maneuvers of ships. When new maneuvers are identified, a scale factor is employed to adjust the system noises (Efe et al., 1999;Almagbile et al., 2010). Instead of the scale factor, there are studies which introduce the forgetting factor with a comparable function for adjusting system noises (Ohhira et al., 2021;Wu et al., 2021). There are also proposed approach which contains multiple models, such as Interacting Multiple Models (IMM) and Multiple Model Adaptive Estimation (MMAE) (Mazor et al., 1998;Alsuwaidan et al., 2011). These methods incorporate multiple models to account for system uncertainties. IMM employs an interaction mechanism facilitating seamless transitions between different models based on measurements. In contrast, MMAE is designed to dynamically select the most suitable model from a set of candidates, adapting to the evolving characteristics of measurements.

In the first category of methods, the accurate determination of the statistical properties of innovation necessitates the specification of the quantity of historical data. An analysis relying on a smaller dataset may fail to accurately reflect the proper statistical properties, while an analysis utilizing a larger dataset runs the risk of averaging out these statistical properties. Within the second category of methods, the determination of both the scale factors and forgetting factors needs to be done artificially. Furthermore, it is essential to explore multiple factors associated with optimal maneuver fits in advance. Concerning IMM and MMAE, a significant portion of the computational cost is allocated to identifying the most suitable models. The MMAE may struggle in situations where there is uncertainty or ambiguity in the selection of appropriate models, which can impact its overall performance. The IMM is sensitive to model switching so that incorrect model switching decisions can happen in rapidly changing or unpredictable environments. It is worth noting that models which can be utilized in the IMM framework must share identical system states. This constraint serves as a limitation when employing the IMM.

In this study, an adaptive tuning mechanism is designed for ship navigation state estimation using KF-based techniques and kinematic motion models. The design takes into account that ships, often of substantial tonnage, primarily undergo maneuvers triggered by different rudder orders rather than changes in engine states. Considering measurements obtained from onboard sensors, the adaptive tuning mechanism primarily focuses on outliers in GNSS measurements. This is rational as the precision of GNSS measurements relies on the operational status of satellites and ground equipment, factors not under the control of ships. Therefore, the proposed adaptive tuning mechanism for ship maneuvers primarily deals with two scenarios: new rudder orders and abnormal GNSS measurements.

The paper follows a structured outline. The next section, Preliminaries, encompasses all the methods employed in this study. Subsequently, the Simulation and Experiment Setup section makes a brief presentation of the simulated and sea-trial experiments. This is succeeded by the presentation of Experiment Results and Related Discussions. The section of Conclusions is in the last.

METHODOLOGY

Kinematic motion models

Three kinematic motion models will be used to describe the ship maneuvers—the Constant Angular Acceleration (CAA) model, the Curvilinear motion model (CMM), and the Constant Turn Rate & Acceleration (CTRA) model. The states described by these models are illustrated in Fig.1. The onboard sensors, including the GNSS, gyroscope, and IMU, are assumed to be positioned at the geometric center of the ship, denoted as point C. The acquired measurements include the UTM coordinates of C (Z_{NC}, Z_{EC}), ship's true heading (z_{ψ_T}), turn rate (z_r), and the accelerations in the vessel body reference frame (Z_{au}, Z_{av}). It is essential to highlight that, as the measured position is converted into UTM coordinates, the heading utilized in the CMM and CTRA is adjusted to align with grid north ψ_G. Given that the measured heading ψ_T is in true north, a deviation which is denoted as grid convergence γ can exist. Specific corrections are necessary, and details on correction methods can be found in (Kawase, 2013).

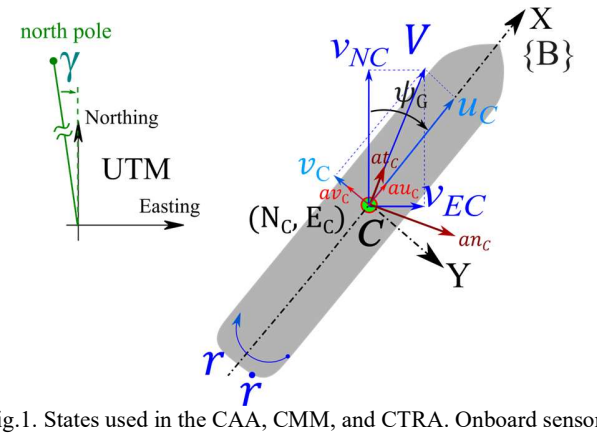

Fig.1. States used in the CAA, CMM, and CTRA. Onboard sensors (GNSS, gyroscope, and IMU) are installed in C.

The system and measurement models of the utilized kinematic motion models are listed in Tab.1-3. In the KF-based state estimation, the CAA is initially executed to generate estimated values for heading, turn rate, and angular acceleration. These estimates are then utilized as parameters in the CMM and CTRA (Eq.4-6). It is crucial to emphasize that the kinematic motion models are constructed on the assumption of constant accelerations and turn rates. When the ship adopts new rudder orders, these assumptions are no longer valid. Consequently, the uncertainties $\boldsymbol{w_x}$ and $\boldsymbol{w_z}$ must be adaptively reevaluated to ensure enhanced estimation precision. As $\boldsymbol{w_x}$ and $\boldsymbol{w_y}$ is assumed to be white Gaussian noises, the covariance matrix $\boldsymbol{Q}$ and $\boldsymbol{R}$ are thus needs to be adaptively assigned.

Table 1:

CAA:	$\boldsymbol{x}(t) = [\psi_T, r, \dot{r}]^T; \quad \boldsymbol{z}[t_k] = [z_{\psi_T}, z_r]$
system model:	$\dot{\boldsymbol{x}}(t) = \begin{bmatrix} 0 & 1 & 0 \\ 0 & 0 & 1 \\ 0 & 0 & 0 \end{bmatrix} \cdot \boldsymbol{x}(t) + \boldsymbol{w_x} \quad (1)$ $\left(\boldsymbol{w_x} \sim \mathcal{N}(\boldsymbol{0}, \boldsymbol{Q} \in \mathbb{R}^{3\times3})\right)$
measurement model:	$\boldsymbol{z}[t_k] = \begin{bmatrix} 1 & 0 & 0 \\ 0 & 1 & 0 \end{bmatrix} \boldsymbol{x}[t_k] + \boldsymbol{w_z} \quad (2)$ $\left(\boldsymbol{w_z} \sim \mathcal{N}(\boldsymbol{0}, \boldsymbol{R} \in \mathbb{R}^{2\times2})\right)$

Table 2:

CMM:	$\boldsymbol{x}(t) = [N_C, E_C, v_{NC}, v_{EC}, at_C, an_C]^T$ $\boldsymbol{z}[t_k] = [Z_{NC}, Z_{EC}, z_{au}, z_{av}]$
system model:	$\dot{\boldsymbol{x}}(t) = \begin{bmatrix} v_{NC} \\ v_{EC} \\ at_C\, f^{v_{NC}} - an_C\, f^{v_{EC}} \\ at_C\, f^{v_{EC}} + an_C\, f^{v_{NC}} \\ 0 \\ 0 \end{bmatrix} + \boldsymbol{w_x}$ (3) $(\boldsymbol{w_x} \sim \mathcal{N}(\boldsymbol{0}, \boldsymbol{Q} \in \mathbb{R}^{6\times6}))$ $f^{v_{NC}} = \frac{v_{NC}}{V}, f^{v_{EC}} = \frac{v_{EC}}{V} \left(V = \sqrt{v_{NC}^2 + v_{EC}^2}\right)$
measurement model:	$\boldsymbol{z}[t_k] = \begin{bmatrix} Z_{NC} \\ Z_{EC} \\ h_1 \cos(\psi_G) + h_2 \sin(\psi_G) \\ h_1 \cos(\psi_G) - h_2 \sin(\psi_G) \end{bmatrix} + \boldsymbol{w_z}$ (4) $(\boldsymbol{w_z} \sim \mathcal{N}(\boldsymbol{0}, \boldsymbol{R} \in \mathbb{R}^{4\times4}))$ $h_1 = at_c\, f^{v_{NC}} - an_c\, f^{v_{EC}} + r\, v_{EC}$ $h_2 = at_c\, f^{v_{EC}} + an_c\, f^{v_{NC}} - r\, v_{NC}$

Table 3:

CTRA:	$\boldsymbol{x}(t) = [N_C, E_C, u_C, v_C, au_C, av_C]^T$ $\boldsymbol{z}[t_k] = [Z_{NC}, Z_{EC}, z_{au}, z_{av}]$
system model:	$\dot{\boldsymbol{x}}(t) = \begin{bmatrix} u_C \cos(\psi_G) - v_C \sin(\psi_G) \\ v_C \cos(\psi_G) + u_C \sin(\psi_G) \\ au_C \\ av_C \\ 0 \\ 0 \end{bmatrix} + \boldsymbol{w_x}$ (5) $(\boldsymbol{w_x} \sim \mathcal{N}(\boldsymbol{0}, \boldsymbol{Q} \in \mathbb{R}^{6\times6}))$
measurement model:	$\boldsymbol{z}[t_k] = \begin{bmatrix} Z_{NC} \\ Z_{EC} \\ z_{au} - v_C\, r \\ z_{av} + u_C\, r \end{bmatrix} + \boldsymbol{w_z}$ (6) $(\boldsymbol{w_z} \sim \mathcal{N}(\boldsymbol{0}, \boldsymbol{R} \in \mathbb{R}^{4\times4}))$

KF-based state estimation

It is evident that CAA and CTRA are linear models, while CMM is nonlinear. In this study, the KF is employed for estimating states in CAA and CTRA, and the UKF is utilized in CMM for estimating related states. As the system models are described in continuous-time, the KF-based estimation requires the implementation of numerical solutions for the corresponding continuous-time differential equations. The algorithms for KF and UKF are presented in Fig.2 and 3. These algorithms are based on the constant $\boldsymbol{Q}$ and $\boldsymbol{R}$ which required to be initialized in the initialization stage.

In the execution of the KF-based estimation, the states in the CAA will be estimated firstly. This is attributed to the fact that the innovation of the turn rate in the CAA (y_r) can be employed as the criterion to assess whether the ship maintains a constant turn rate. A variation in the turn rate is anticipated to result in altered values of y_r. When deviated values of y_r are identified, $\boldsymbol{Q}$ in the CMM and CTRA will be increased by multiplying it with a scale factor α. The establishment of a relationship between y_r and α is essential. Details of this relationship will be elaborated upon in the following subsection.

Regarding $\boldsymbol{R}$ in the CMM and CTRA, the innovations of the position, denoted as y_N and y_E, are employed to identify potential biases in the measured positions (Fig.4). If the innovation exceeds a predefined threshold, a substantial scaling factor is implemented on $\boldsymbol{R}$, prioritizing the computation of the Kalman gain. The threshold is determined through GNSS testing. In this study, the threshold is set to 2 [m] and a scaling factor of 1000 will be multiplied to $\boldsymbol{R}$ if the innovations are larger than the threshold. It is important to note that the assumption is made that abnormal data from the GNSS occur infrequently, typically during short navigation periods. The occurrence of abnormal GNSS data over an extended period could lead to issues in inertial navigation, which is beyond the scope of this paper.

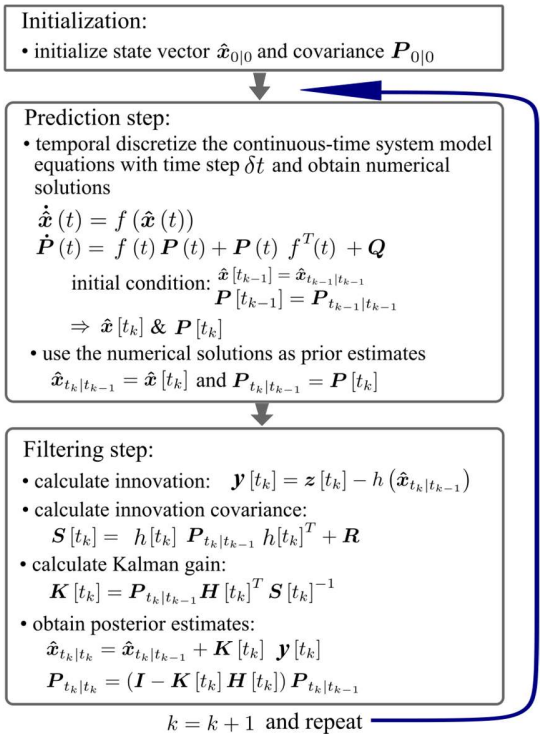

Fig. 2. KF algorithm (used for the CAA and CTRA)

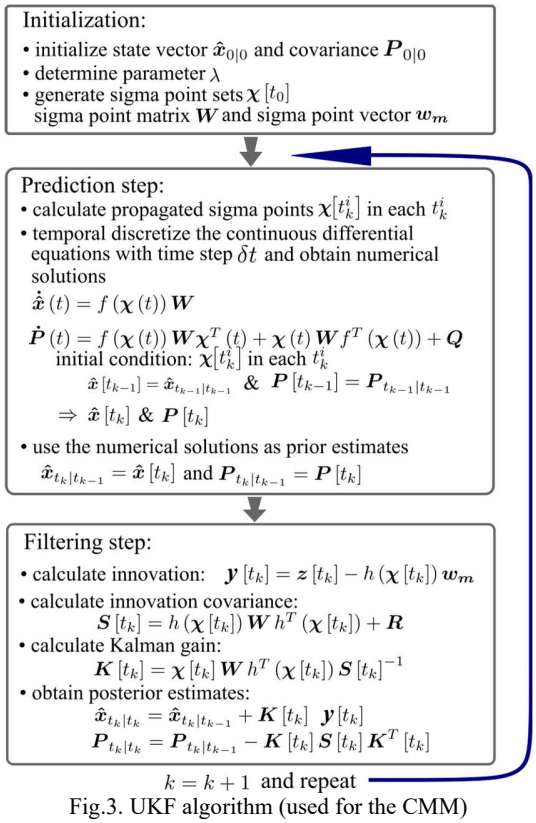

Fig.3. UKF algorithm (used for the CMM)

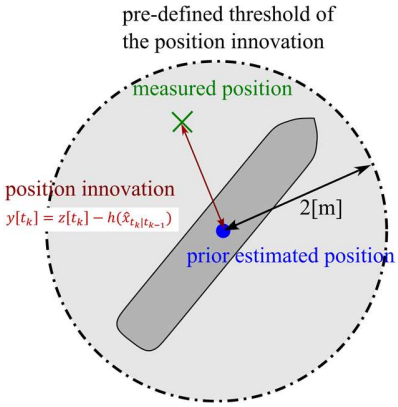

Fig.4. The measurement noise $\boldsymbol{R}$ will be modified if position innovations are outside the colored circle that is regulated by a pre-defined threshold.

Gaussian process regression in adaptive tuning

Gaussian process regression (GPR) is widely utilized in machine learning and statistical analysis. GPR models demonstrate exceptional proficiency in capturing complex relationships within datasets, drawing on foundational principles rooted in probability theory. For an input with arbitrary N samples $(\boldsymbol{x_1}, \boldsymbol{x_2}, \dots, \boldsymbol{x_N})$, if the corresponding output $\boldsymbol{f} = \big(f(\boldsymbol{x_1}), \boldsymbol{f}(\boldsymbol{x_2}), \dots, \boldsymbol{f}(\boldsymbol{x_N})\big)$ follows a multiple Gaussian distribution $\mathcal{N}(\boldsymbol{\mu}, \boldsymbol{K})$, it can be defined that $\boldsymbol{f}$ follows a Gaussian process:

$$\boldsymbol{f} \sim GP(\boldsymbol{\mu}, \boldsymbol{K}) \tag{7}$$

where $\boldsymbol{\mu} = \big(\mu(\boldsymbol{x_1}), \mu(\boldsymbol{x_2}), \dots, \mu(\boldsymbol{x_N})\big)$, $K_{nn'} = k(\boldsymbol{x_n}, \boldsymbol{x_{n'}})$.

In many cases, through suitable data transformations, it is often feasible to assume $\boldsymbol{\mu}$ as 0, making the explicit modeling of $\boldsymbol{\mu}$ unnecessary. The elements $K_{nn'}$ in the covariance matrix $\boldsymbol{K}$ are referred to as the kernel function. This function possesses the property that if two inputs exhibit similarity, the corresponding element in the matrix will have a higher value. In this study, the squared exponential kernel function is used (Eq.8).

$$k(\boldsymbol{x_n}, \boldsymbol{x_{n'}} | \boldsymbol{\theta}) = \theta_1 \exp\left(-\frac{(\boldsymbol{x_n} - \boldsymbol{x_{n'}})^T (\boldsymbol{x_n} - \boldsymbol{x_{n'}})}{2\,\theta_2}\right) + \theta_3 \delta(\boldsymbol{x_n}, \boldsymbol{x_{n'}}) \tag{8}$$

where δ is the Kronecker-delta.

Given the known datasets $\mathcal{D} = \{(x_1, y_1), \dots, (x_N, y_N)\}$, if the function $\boldsymbol{f}$ which satisfies $\boldsymbol{y} = \boldsymbol{f}(\boldsymbol{x})$ is generated by $GP\big(0, k(\boldsymbol{x_n}, \boldsymbol{x_{n'}})\big)$, the output of a unknown input x^* can be also represented by a Gaussian distribution (Eq.9).

$$p(y^* | x^*, \mathcal{D}) = \mathcal{N}\left(k_*^T K^{-1} y, k_{**} - k_*^T K^{-1} k_*\right) \tag{9}$$

where: $k_* = k(\boldsymbol{x_n}, x^* | \boldsymbol{\theta}), k_{**} = k(x^*, x^* | \boldsymbol{\theta})$

Based on Eq.9, the expectation of y^* is equal to $k_*^T K^{-1} y$. It should be noted that Eq.9 only covers the case where the input x^* is single, which is the primary focus of this study. However, it is worth mentioning that GPR is also applicable to scenarios involving multiple unknown inputs.

Another task involving the utilization of GPR is the determination of the hyperparameter $\boldsymbol{\theta}$. Given that the elements $k(\boldsymbol{x_n}, \boldsymbol{x_{n'}} | \boldsymbol{\theta})$ are influenced by $\boldsymbol{\theta}$, the matrix $\boldsymbol{K}$ is consequently dependent on $\boldsymbol{\theta}$. In this scenario, the probability of y based on dataset D can be expressed as:

$$p(y|\mathcal{D}) = \mathcal{N}(y|0, K_{\boldsymbol{\theta}}) = \frac{1}{(2\pi)^{N/2}} \frac{1}{|K_{\boldsymbol{\theta}}|^{1/2}} \exp\left(-\frac{1}{2} y^T K_{\boldsymbol{\theta}}^{-1} y\right) \tag{10}$$

The method of maximum likelihood estimation can be employed to determine $\boldsymbol{\theta}$. The logarithm of $p(y|\mathcal{D})$ can be expressed as:

$$L = \log p(y|\mathcal{D}) \propto -log|K_\theta| - y^T K_\theta^{-1} y + const \tag{11}$$

with:

$$\frac{\partial L}{\partial \theta} = \frac{\partial L}{\partial K_\theta} \frac{\partial K_\theta}{\partial \theta} = -tr\left(K_\theta^{-1} \frac{\partial K_\theta}{\partial \theta}\right) + \left(K_\theta^{-1} y\right)^T \frac{\partial K_\theta}{\partial \theta} \left(K_\theta^{-1} y\right) \tag{12}$$

Utilizing the gradient of L (Eq.12), optimization algorithms can be applied to estimate $\boldsymbol{\theta}$. In this study, the L-BFGS algorithm is chosen to compute $\boldsymbol{\theta}$, and further details about this algorithm can be found in (Andrew and Gao, 2007).

In this study, the absolute value of the innovation of turn rate $|y_r|$ and the optimally-fitted scaling factor α undergo initial testing through simulated maneuvers in the UiT bridge simulator. The training dataset is consequently formed by pairs of $|y_r|$ and α. Figure 5 illustrates the comprehensive workflow of the proposed adaptive tuning mechanism. In each iteration, $|y_r|$ from the CAA is employed in the trained GPR model to dynamically determine α. The system noise $\boldsymbol{Q}$ is consequently modified by α, resulting in $\boldsymbol{Q}^*$ in the CMM and CTRA. Concurrently, the innovations y_N and y_E from the CMM and CTRA are utilized to assess whether the measured positions exhibit abnormal behavior. When abnormalities are detected, $\boldsymbol{R}$ is substituted with $\boldsymbol{R}^*$ to ensure that the filters reduce the emphasis on the measured data.

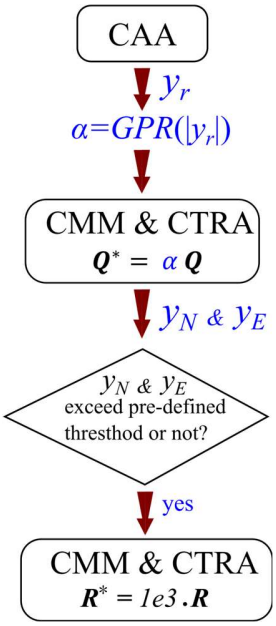

Fig.5. The workflow of the proposed adaptive tuning mechanism

EXPERIMENT PREPARATION

In this study, both simulated and sea-trial experiments will be conducted to validate the adaptive tuning mechanism. The simulated experiment takes place in the UiT bridge simulator (Fig.6).

Fig.6. UiT bridge simulator and the execution of simulated maneuvers

The sea-trial experiment is conducted using the UiT autonomous ship named "Ymir" in the Tromsø area (Fig.7). The ship is equipped with a variety of sensors, and a specialized data collection platform is designed to acquire the necessary measurements from selected sensors.

Fig.7. The equipped sensors in the autonomous ship "Ymir" and the sea trail experiment in Tromsø area.

Training data sets

During simulated maneuvers, the actual ship navigation states can be obtained directly from the simulator. Consequently, the optimal α with respect to $|y_r|$ can be determined through multiple offline trials. It is noteworthy that one of the advantages of employing GPR is that it does not necessitate an excessive number of experimental trials, implying significant cost savings. The training data sets are obtained from a simulated maneuver which contains straight line, starboard turning, and port turning. In Fig.8, it can be observed that $|y_r|$ have significant change in several time steps which imply that the ship has a new rudder order in the related steps. The innovation is further categorized into four groups by different levels of values.

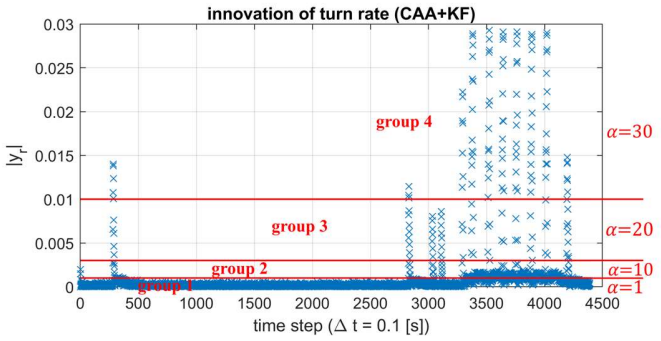

Fig.8. The absolute value of innovation of turn rate from the CAA. The maneuver is executed in the UiT bridge simulator. The $|y_r|$ values are categorized into four distinct groups, each assigned with an optimal α.

The training dataset $\mathcal{D}$ is randomly chosen from the four groups, with a slightly greater number of samples from groups exhibiting a larger range of (Fig.9). Artificial noises are introduced to each group's optimal α. The introduction of artificial noises has a negligible impact on estimation precision, yet it plays a role in enhancing the fitting within the Gaussian process.

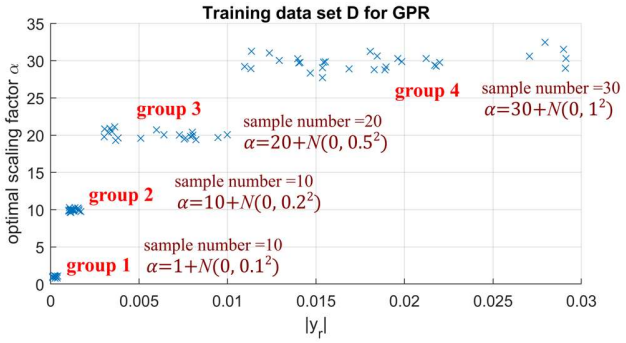

Fig.9. Sampled data set $\mathcal{D}$ used for the training of GPR. Noted that the values of the optimal α in each group are added with artificial white Gaussian noises.

RESULTS AND DISCUSSIONS

Parameters initialization.

The parameters requiring initialization are outlined in Tab.4. The initial values for $\boldsymbol{Q}$ in all kinematic motion models are optimized for straight-line maneuvers, while the initialization of $\boldsymbol{R}$ is based on the sensors' performance characteristics. For the numerical solution in both the KF and UKF, the second-order Runge–Kutta explicit method is employed with a discretized time step δt.

Table.4. initialized parameters used in the KF-based estimation

parameters	value
dt	$0.13[s]$ (time interval between consecutive measurements)
δt	0. 0065 [s] (time interval used in temporal discretization)
$\boldsymbol{Q}$ (CAA)	$diag\left(\left(\frac{0.1\pi}{180}\right)^2, \left(\frac{0.01\pi}{180}\right)^2, \left(\frac{0.001\pi}{180}\right)^2\right)$
$\boldsymbol{Q}$ (CMM)	$diag(1^2, 1^2, 0.5^2, 0.5^2, 0.25^2, 0.25^2)$
$\boldsymbol{Q}$ (CTRA)	$diag(0.3^2, 0.3^2, 0.1^2, 0.1^2, 0.03^2, 0.03^2)$
$\boldsymbol{R}$ (CAA)	$diag\left(\left(\frac{0.5\pi}{180}\right)^2, \left(\frac{0.01\pi}{180}\right)^2\right)$
$\boldsymbol{R}$ (CMM)	$diag(1^2, 1^2, 0.01^2, 0.01^2)$
$\boldsymbol{R}$ (CTRA)	$diag(1^2, 1^2, 0.01^2, 0.01^2)$
λ	1.72 (unscented transform parameter used in the UKF)
$\boldsymbol{\theta}$	$(\theta_1, \theta_2, \theta_3) = (0.2, 0.4, 0.15)$ (hyperparameters in the kernel function)

Gaussian Process Regression Training

The regression outcome derived from the data set $\mathcal{D}$ is illustrated in Fig.10. The red solid line depicts the expected values of predicted α across a range of 300 $|y_r|$, spanning from 0 to 0.03. The plot also includes 95% prediction intervals. Following training, the optimal $\boldsymbol{\theta}$ is determined to be $(0.0023, 8.7554, 0.7914)$. It is noticeable that the predicted α exhibits a gradual increase between distinct groups, with the predicted values in group 3 and group 4 displaying linear distributions.

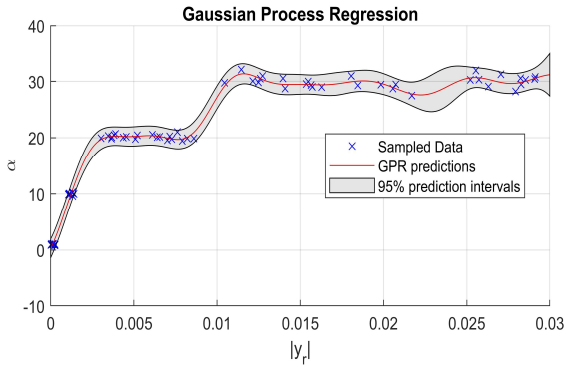

Fig.10. The predicted scaling factor α with the sampled data sets $\mathcal{D}$ from the simulated maneuver.

State estimation with sea-trail data

Two maneuvers conducted by "Ymir" serve as the basis for evaluating the proposed adaptive tuning mechanism. These maneuvers encompass a zigzag and a port-turning maneuver, with Fig.11 illustrating the measured positions during these maneuvers. Notably, during the port-turning maneuver, unusual measurements become evident as the ship undergoes the turning phase, with recorded positions remaining static for several seconds. Due to the absence of actual true data from sea-trial experiments, innovations are employed to assess the estimation performances of the CMM and CTRA. Large values of innovations can suggest a suboptimal fit or model inaccuracies. Therefore, it is anticipated that the innovations should be maintained on a small scale for precise estimation.

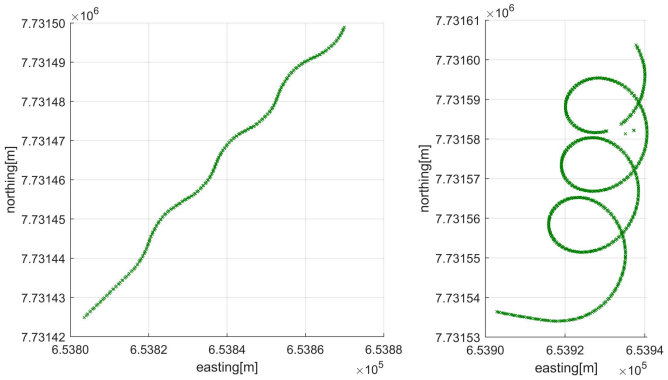

Fig.11. The measured position of the zigzag and port-turning maneuver. There exist outliers of measurements in the port-tuning maneuver.

In the zigzag maneuver, the predicted scaling factor α is depicted in Fig.12. It is evident that as the magnitude of $|y_r|$ increases, a comparatively higher α is computed using the trained GPR model. The adaptive tuning facilitated by this GPR model results in the scaling factor α tending to be larger when the ship executes a zigzag maneuver. This observation implies that the final estimates will assign greater importance to the measured data during the zigzag stage.

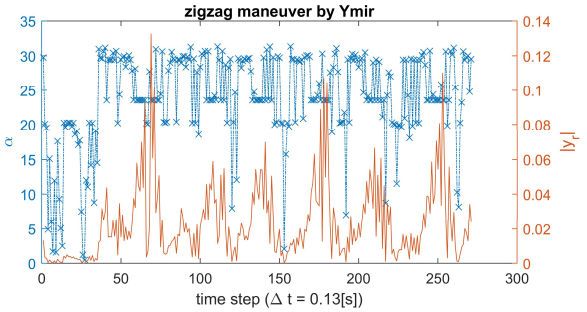

Fig. 12. $|y_r|$ and predicted α of the zigzag maneuver

The innovations of northing and easting (y_N & y_E) are illustrated in Fig.13. In the absence of adaptive tuning, the innovations exhibit significant fluctuations during the zigzag stage. Conversely, the adaptive tuning mechanism mitigates these fluctuations, resulting in lower innovations during the same stage. This indicates that with tuned $\boldsymbol{Q}$, both the CMM and CTRA demonstrate higher accuracy compared to the same models with constant $\boldsymbol{Q}$.

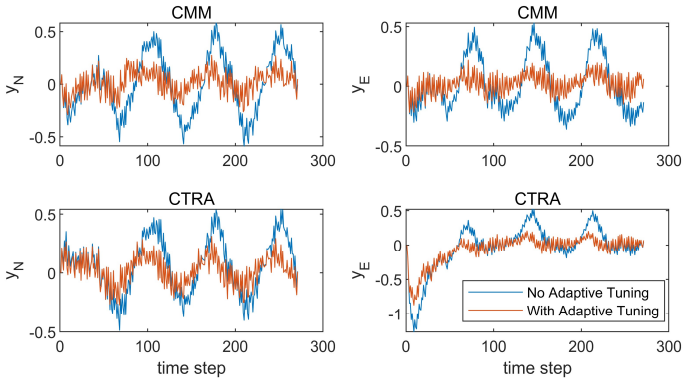

Fig. 13. The comparison between the y_N and y_E w/o adaptive tuning in the CMM and CTRA (zigzag maneuver).

The estimated velocities are presented in Fig.14-15. It is noticeable that velocities estimated with adaptive tuning exhibit a relatively faster reaction time when the ship receives new rudder orders. This attribute holds significance in real-time applications that necessitate swift responses to environmental changes.

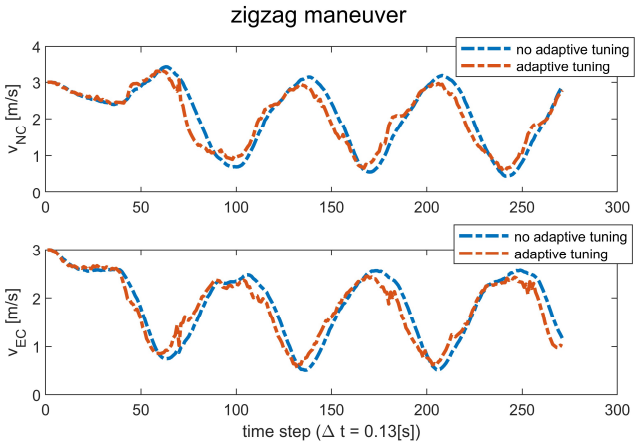

Fig. 14. Estimated velocities (v_{NC} & v_{EC}) from the CMM

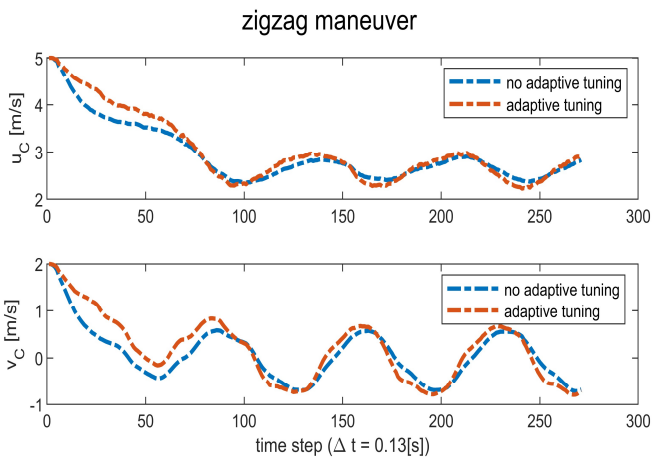

Fig. 15. Estimated velocities (u_C & v_C) from the CTRA

The computed α for the port-turning maneuver is depicted in Fig16. It is evident that α tends to exhibit higher values once the ship initiates the turning process. The significant magnitude of $|y_r|$ during the turning stage suggests that the ship encounters disturbances more frequently than in the initial phase when executing a straight-line maneuver. These disturbances during the turning stage are attributed partly to the influence of a strong sea current, as evidenced by the measured positions indicating the ship's drift (Fig.11(b)).

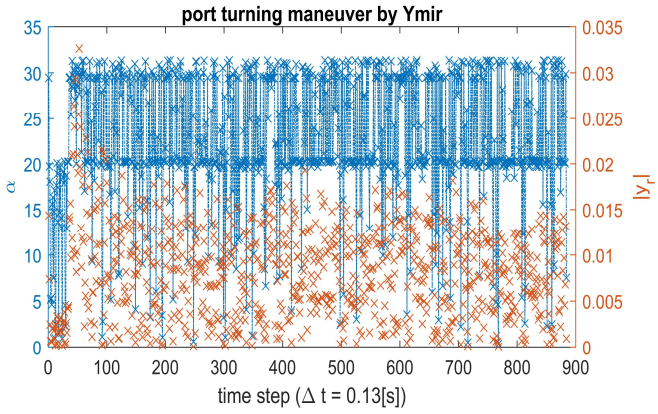

Fig. 16. $|y_r|$ and predicted α of the port turning maneuver

The innovations of northing and easting from the port turning maneuver are illustrated in Fig.17. Similar to the zigzag scenario, the innovations exhibit less fluctuation with the adaptive tuning mechanism. However, a significant deviation in the innovations is noticeable during time steps when abnormal measured positions are recorded. In such cases, the adaptive tuning of $\boldsymbol{R}$ is activated. The estimated positions and velocities are presented in Fig.18-20. It is observed that with the adaptive tuning of $\boldsymbol{R}$, the posterior estimates rely more on the system models once abnormal measurements are detected. The estimated velocities with adaptive tuning appear smoother compared to those with constant $\boldsymbol{Q}$ and $\boldsymbol{R}$.

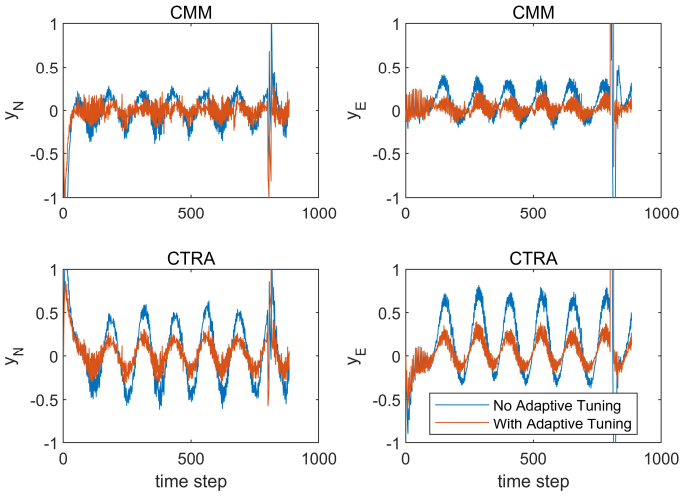

Fig. 17. The comparison between the y_N and y_E w/o adaptive tuning in the CMM and CTRA (port turning maneuver). The large value of innovations is caused by the outliers of measured positions.

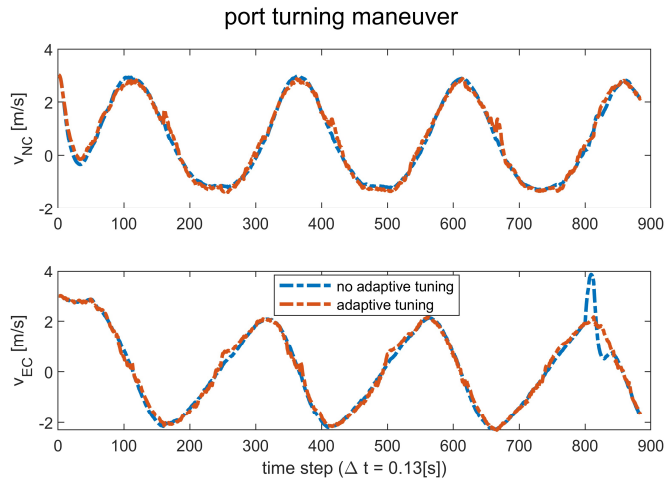

Fig. 18. Estimated velocities (v_{NC} & v_{EC}) from the CMM

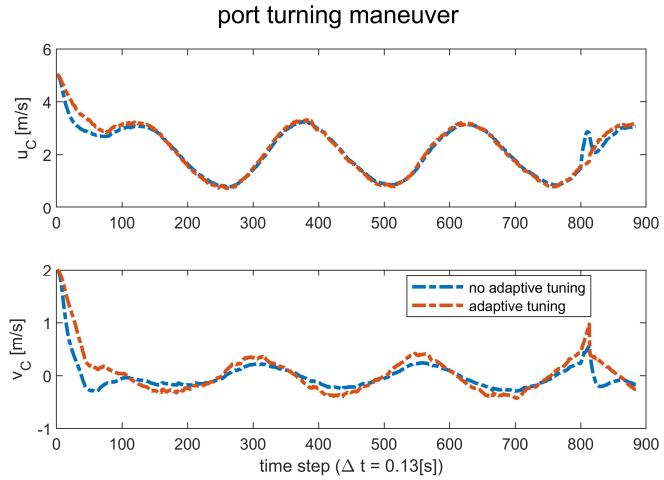

Fig.19. Estimated velocities (u_C & v_C) from the CTRA

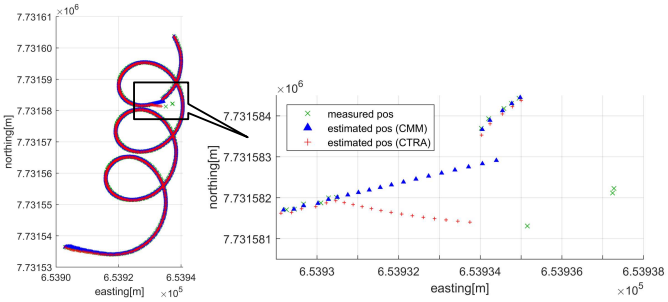

Fig.20. Estimated positions in the port turning maneuver. The time steps during which abnormal measurements occur are magnified for closer examination.

Additionally, it can be observed that the CMM exhibits greater robustness than the CTRA when confronted with abnormal measured positions. The positions estimated by the CMM appear smoother than those from the CTRA. The estimated sway velocity from the CTRA still displays discontinuous jumping. This indicates that the ship navigation states used in the CTRA can be more sensitive to measurement outliers.

CONCLUSIONS

An adaptive tuning mechanism is implemented in the KF-based state estimation, where the system models are generated by the kinematic motion models. Simulated maneuvers from the UiT bridge simulator are utilized to determine the optimal scaling factor for the system noise $\boldsymbol{Q}$. Subsequently, a GPR model is trained by using the sampled simulated data. The sea-trial experiment data from the vessel 'Ymir,' comprising zigzag and port-turning maneuvers, is used to further evaluate the adaptive tuning mechanism. The results reveal that, with the adaptive tuning mechanism, the innovations in positions exhibited reduced fluctuations compared to positions estimated with constant $\boldsymbol{Q}$ and $\boldsymbol{R}$. The estimated velocities adapt more swiftly to new rudder orders. In instances where the measured positions contained abnormalities, the adaptive tuning mechanism contributed to the enhanced smoothness of the estimated states.

In this research, the assessment of the adaptive tuning mechanism is constrained to relying solely on innovations due to the absence of actual ship navigation states. Consequently, the upcoming sea-trial experiment aims to collect a more diverse range of data from the installed onboard sensors through multiple trails so that more comprehensive evaluations by various criteria can be feasible. Additionally, the exploration of training a GPR model using datasets from the sea-trial experiment is under consideration. These datasets encompass unforeseen uncertainties stemming from the complex navigation environment.

ACKNOWLEDGEMENTS

This work has been conducted under the Autonomous ship Program in UiT-The Arctic University of Norway, which aims to develop the digital helmsman as a part of the ship intelligence to operate future vessels supported by the MARKOM II project under the project title “Onshore Operation Center for Remotely Controlled Vessels (OOC 2023)" under the contract number PMK-2022-10014.

REFERENCES

Almagbile, A., J. Wang and W. Ding (2010). "Evaluating the Performances of Adaptive Kalman Filter Methods in GPS/INS Integration." Journal of Global Positioning Systems **9**.

Alsuwaidan, B., J. Crassidis and Y. Cheng (2011). "Generalized Multiple-Model Adaptive Estimation using an Autocorrelation Approach." Aerospace and Electronic Systems, IEEE Transactions on **47**: 2138-2152.

Andrew, G. and J. Gao (2007). Scalable training of L1-regularized log-linear models. Proceedings of the 24th international conference on Machine learning. Corvalis, Oregon, USA, Association for Computing Machinery**:** 33–40.

Baybura, T., İ. Tiryakioğlu, M. A. Uğur, H. İ. Solak and Ş. Şafak (2019). "Examining the Accuracy of Network RTK and Long Base RTK Methods with Repetitive Measurements." Journal of Sensors **2019**: 3572605.

Efe, M., J. A. Bather and D. P. Atherton (1999). An adaptive Kalman filter with sequential rescaling of process noise. Proceedings of the 1999 American Control Conference (Cat. No. 99CH36251).

Hu, C., W. Chen, Y. Chen and D. Liu (2003). "Adaptive Kalman Filtering for Vehicle Navigation." Journal of Global Positioning Systems **2**: 42-47.

Kawase, K. (2013). Concise Derivation of Extensive Coordinate Conversion Formulae in the Gauss-Krüger Projection.

Li, X. R. and V. P. Jilkov (2003). "Survey of maneuvering target tracking. Part I. Dynamic models." IEEE Transactions on Aerospace and Electronic Systems **39**(4): 1333-1364.

Mazor, E., A. Averbuch, Y. Bar-Shalom and J. Dayan (1998). "Interacting multiple model methods in target tracking: a survey." IEEE Transactions on Aerospace and Electronic Systems **34**(1): 103-123.

Ohhira, T., A. Shimada and T. Murakami (2021). "Variable Forgetting Factor-Based Adaptive Kalman Filter With Disturbance Estimation Considering Observation Noise Reduction." IEEE Access **9**: 100747-100756.

Perera, L. (2019). "Deep Learning towards Autonomous Ship Navigation and Possible COLREGs Failures." Journal of Offshore Mechanics and Arctic Engineering.

Perera, L. P. (2017). "Navigation vector based ship maneuvering prediction." Ocean Engineering **138**: 151-160.

Thombre, S., Z. Zhao, H. Ramm-Schmidt, J. M. V. García, T. Malkamäki, S. Nikolskiy, T. Hammarberg, H. Nuortie, M. Z. H. Bhuiyan, S. Särkkä and V. V. Lehtola (2022). "Sensors and AI Techniques for Situational Awareness in Autonomous Ships: A Review." IEEE Transactions on Intelligent Transportation Systems **23**(1): 64-83.

Wang, Y., L. P. Perera and B.-M. Batalden (2023). "Kinematic motion models based vessel state estimation to support advanced ship predictors." Ocean Engineering **286**: 115503.

Wu, M., L. Qin, G. Wu, Y. Huang and C. Shi (2021). "State of Charge Estimation of Power Lithium-ion Battery Based on a Variable Forgetting Factor Adaptive Kalman Filter." Journal of Energy Storage **41**: 102841.

Paper V

Localized Advanced Ship Predictor for Maritime Situation Awareness with Ship Close Encounter

Wang, Y., Perera, L. P. and Batalden, B.-M. (2024)

Published in *Ocean Engineering*

https://doi.org/10.1016/j.oceaneng.2024.117704

Ocean Engineering 306 (2024) 117704

Contents lists available at ScienceDirect

Ocean Engineering

journal homepage: www.elsevier.com/locate/oceaneng

Research paper

Localized advanced ship predictor for maritime situation awareness with ship close encounter

Yufei Wang [a,*], Lokukaluge Prasad Perera [a,b], Bjørn-Morten Batalden [a]

[a] Department of Technology and Safety, UiT The Arctic University of Norway, Tromsø, Norway
[b] SINTEF Digital, Oslo, Norway

ARTICLE INFO

Keywords:
Maritime situation awareness
Ship trajectory prediction
Kinematic motion models
Gated recurrent unit
Pivot point

ABSTRACT

The marine navigation environment can become further complex when ships with different autonomy levels are introduced. To ensure navigation safety in such a mixed environment, advanced ship predictor type technologies are essential in aiding ship navigators to attain the highest levels of situation awareness (SA). Consequently, precise ship trajectory prediction, specifically within a short prediction horizon, should be included in such predictors as an indispensable component. This study introduces two methods for ship trajectory prediction on a local scale: the kinematic-based method and the Gate Recurrent Unit (GRU)-Pivot Point (PP)-based method. The first method utilizes kinematic motion models to predict a ship trajectory. In the second method, the GRU is trained to generate the predictions of related ship navigation states. The ship's PP is then extracted from these predicted states, subsequently providing the predicted ship trajectory. Both methods are validated using simulated maneuvering exercises to assess their effectiveness, with a prediction horizon of 90 s. The results show that the kinematic-based method excels in the predictions during ship's stable stages, i.e., steady-state conditions. Meanwhile, the GRU-PP-based method exhibits robust performances in cases when new rudder orders are executed, i.e., transient conditions. It is considered that these applications can provide significant benefits in maritime SA in present and future ship navigation.

1. Introduction

1.1. Complex navigation environment

In recent years, significant progress has been made in the development of autonomous ships, propelled by advancements in sensor technologies, artificial intelligence, and the Internet of Things (UiT, 2021; Birkeland, 2022; MEGURI2040, 2022; AVATAR, 2023; Kongsberg, 2023). The ongoing research and development of autonomous ships aim to revolutionize the industry by tackling several critical challenges. These challenges include reducing maritime accidents attributable to human errors (Hoem et al., 2019; Kohn et al., 2019), improving energy efficiency to reduce greenhouse gas emissions (Munim, 2019; Kim et al., 2021), and alleviating shortages of skilled and professional seafarers (Porathe et al., 2014; Wróbel et al., 2017).

Until the present time, the definitions of ships' autonomy level can be found in various institutions and research studies (NFAS, 2017; IMO, 2019; Rødseth, 2019; Fukuto, 2021). As for the development of autonomous ships, it is important to acknowledge that it is not realistic to implement the same autonomous levels to various ship types and flags simultaneously. Even with the same degree of autonomy, ships can manifest unique individual variations. Consequently, it is considered that close encounter situations among ships can become significantly complex when ships with varying levels of autonomy—such as fully autonomous, remotely-controlled, and manned ships—coexist within the same navigation area (Perera, 2019; Chang et al., 2021; Kim et al., 2022).

Considering this complexity, maneuvering and navigating to avoid potential collisions can pose significant challenges. One of the challenges lies in communication. Conventional manned ships primarily communicate directly through radio, visual, or audio signals. However, communication with remotely-operated or autonomous ships may adopt varied styles and utilize different protocols. Coordinating and ensuring seamless communication among ships with different autonomy levels can thus present challenges (Ait Allal et al., 2020; Koo et al., 2023). Some studies also suggest that due to the reliance of remotely-operated

* Corresponding author.
E-mail address: yufei.wang@uit.no (Y. Wang).

https://doi.org/10.1016/j.oceaneng.2024.117704
Received 19 January 2024; Received in revised form 18 March 2024; Accepted 27 March 2024
Available online 4 May 2024

and autonomous ships on designed algorithms, it can be challenging for human operators to grasp how remotely-operated and autonomous ships perceive and respond to a complex and varying navigation environment (Abilio Ramos et al., 2019; Veitch and Andreas Alsos, 2022). Given that remotely-controlled and autonomous ships can rely heavily on various sensors to perceive their surroundings, it is crucial to examine the sensors' capabilities. This includes the understanding of how the limitations of sensors' performance could affect SA (Thombre et al., 2022). It is also worth noting that cybersecurity needs to be emphasized for remotely-operated and autonomous vessels since they can be susceptible to cyberattacks (Amro et al., 2022; Oruc et al., 2022). All the challenges mentioned above emphasize the fact that maintaining SA in a complex navigation environment can differ from conventional shipping practices. Therefore, the development of innovative technologies and tools is essential to support the future of maritime transportation.

1.2. Situation awareness in ship navigation

In maritime transportation, maintaining SA is vital to ensure the safety of ships, particularly in scenarios of close encounter situations. It is ruled therefore by the Convention on the International Regulations for Preventing Collisions at Sea (COLREGs) that all vessels shall at all times maintain a proper lookout by sight and hearing so that the operators can fully appraise the situations with the risk of collision. A common definition of SA is based on three ascending levels (Endsley, 1995): the perception of the elements in the environment within a volume of time and space; the comprehension of their meaning; and the projection of their status in the near future. Given the above-mentioned challenges in a complex navigation environment, it is considered that the importance of having the highest level of SA can be further emphasized (Perera and Batalden, 2019; Zhou et al., 2019; Rødseth et al., 2023). By assessing the current ship navigation states and predicting the evolution of the same states, navigators can proactively maneuver through challenging circumstances. This ability is particularly advantageous for maneuvering in congested areas, narrow passages, and high-traffic zones (Lee et al., 2016; Lu et al., 2018). Meanwhile, considering the longer response times of large-tonnage ships when making adjustments in rudder or engine power, proactive maneuvering is also required (Wickens et al., 2019). Furthermore, it is important to acknowledge that unforeseen events can occur at any time, especially among ships operating at different autonomy levels. Accurate predictions can aid navigators in creating temporal and spatial buffers, affording them the necessary margin and flexibility to effectively address these unexpected events.

The integration of sophisticated technologies like Global Navigation Satellite Systems (GNSS), advanced gyroscopes, Inertial Measurement Units (IMUs), Automatic Identification System (AIS), Electronic Chart Display and Information System (ECDIS), Advanced Precision Radar Aids (APRA), and other navigation systems significantly contributes to enhancing maritime SA. With the aid of these technologies and equipment, improving perception and understanding of nearby situations becomes achievable, particularly in scenarios with limited visibility. However, it is crucial to note that many of these systems still rely on simplistic linear mathematical models for ship trajectory prediction (Perera, 2017). Linear predictions may pose a risk of significant errors, particularly by overlooking potential collision points in close encounter situations. Therefore, the knowledge and experience of navigators continue to be a critical component in decision-making during close ship encounter situations.

1.3. Advanced ship predictors

The proposal of advanced ship predictors serves as innovative tools to enhance maritime SA and support decision-making processes. The workflow of advanced ship predictors can be segmented into different stages. Various methods and techniques are applied within these stages to fulfill their respective functionalities. Considering the characteristics of ship maneuvering, it is proposed in (Perera and Murray, 2019) that advanced ship predictors should be utilized across both long time periods (global scale) and short time periods (local scale). The same study further suggest that global-scale prediction can be primarily based on AIS data, while local-scale prediction mainly utilizes measurements from onboard sensors such as GNSS systems, gyroscopes, IMUs, and others.

For the prediction on a local scale, it can be generally segmented into two stages: ship navigation state estimation and trajectory prediction. The KF-based techniques are widely employed in the first stage to estimate the required ship navigation states by fusing various onboard sensors' measurements (Bar-Shalom et al., 2002; Perera et al., 2012; Wang et al., 2023a,b). These estimates can subsequently be used to predict the ship trajectory in the second stage through various methods. One method is to directly employ the same models used in the KF-based techniques to predict trajectories. Particularly, the models can be combined with some practical tips in ship maneuvering so that the prediction can become more accurate and actionable. The implementation of a ship's pivot point is a good practice to support the local scale trajectory prediction (Perera, 2017). Another method involves employing different neural networks. Neural networks have proven effective in various domains, serving as powerful tools for addressing nonlinear problems. Furthermore, recent advancements in sensor and database technologies enable the collection and processing of large datasets, thus facilitating more efficient training of diverse neural networks. Many neural networks designed for ship trajectory prediction are trained using Automatic Identification System (AIS) datasets (Capobianco et al., 2020; Murray and Perera, 2021; Zhang et al., 2021). However, given the characteristics of AIS data, utilizing neural networks trained with AIS may not be the most suitable option for local scale predictions. These characteristics include data anomalies (Wolsing et al., 2022) and varying sampling rates (Artikis and Zissis, 2021). Several studies employ anomaly detection and linear interpolation techniques to preprocess the collected AIS data (Zhao et al., 2018; Suo et al., 2020). However, it is important to note that the predicted results have a relatively large time step and cover a wide navigation area. For local scale predictions that require more precise results with smaller time steps, these methods may not provide adequate support.

This study primarily focuses on the ship trajectory prediction on a local scale. Considering the importance of simulation verification before actual sea trials, the proposed method is currently being verified using simulated data from a ship bridge simulator. The remainder of the paper is structured as follows: Section 2 reviews the related research studies on advanced ship predictors; Section 3 offers detailed insights into the methods proposed and utilized in this study; Section 4 introduces the preparation for the simulation exercises and outlines the initialized parameters; Section 5 presents the simulation results and relevant discussions. Conclusions are drawn in the final sections of this paper.

2. Literature review

This review examines the methods and techniques utilized in the two stages of local scale predictions, namely ship navigation state estimation and trajectory prediction.

2.1. Ship navigation state estimation

In the first stage, the Kalman Filter (KF) and its variants—including the Extended Kalman Filter (EKF), Unscented Kalman Filter (UKF), Particle Filter (PF), and other related—are widely employed to estimate the ship navigation state. The implementation of KF-based state estimation requires system models that describe how the related system states evolve and how they are influenced by systematic uncertainties. Kinematic motion models are widely used in system modeling. External disturbances, such as external forces and moments, can be modeled as

uncertainties in these models. This treatment can reduce extensive efforts in identifying relevant hydrodynamic coefficients (Perera and Murray, 2019). Relevant studies on the implementation of kinematic motion models can be found in (Best and Norton, 1997; Perera and Guedes Soares, 2012; Wang et al., 2023a,b), where the applications of nonlinear system models like the Curvilinear Motion Model (CMM) and Constant Turn Rate and Acceleration (CTRA) are used to describe general ship behaviors. Regarding the kinematic motion models, it is important to note that the mathematical derivation processes of these models are rooted in a Cartesian coordinate, i.e., the Universal Transverse Mercator (UTM) coordinate system. A correction to address the project distortions in the UTM is suggested in the study by (Wang et al., 2023a,b), where the grid convergence is calculated to adjust ship headings in kinematic motion models.

In this study, the ship will be treated as a rigid body. This is based on the necessity to emphasize the relatively large geometric size of ships during short prediction periods. With the rigid body-based assumption, the ship's navigation states can exhibit variations at different locations (Batlle and Condomines, 2020). Therefore, when integrating kinematic motion models for a ship with the rigid body assumption, it is important to state the reference point at which the ship navigation state is characterized. Additionally, with the dispersion of onboard sensors across ships, it is also crucial to make adjustments to measurements associated with reference points.

2.2. Ship trajectory prediction

The prediction of a ship's trajectory typically starts from the current time step and relies on previously estimated navigation states. The kinematic motion models themselves can be directly employed to predict a ship's trajectory in the future, known as the kinematic-based method. In this method, it is assumed that the kinematic motion models remain applicable during the prediction horizon. However, it is essential to recognize that this assumption may not hold during a transient phase of ship maneuvering. For instance, the constant accelerations and yaw rates specified in the CMM and CTRA are not met when ships follow new rudder orders.

Predictions based on neural networks represent another popular prediction method. The remarkable capability of Recurrent Neural Networks (RNNs) in handling time-series data has gained notable attention in recent times. These kinds of networks are commonly preferred for making predictions due to their adaptation to utilizing internal states to process diverse input sequences (Lipton et al., 2015). However, RNNs with general structures face the challenge of vanishing or exploding gradients (Pascanu et al., 2013). In response to this issue, alternatives like RNNs with gated memory structures, such as Long Short-Term Memory (LSTM) (Hochreiter and Schmidhuber, 1997) and Gated Recurrent Unit (GRU) (Chung et al., 2014), are gaining more practical applications.

Ship trajectory prediction based on RNNs can be found in numerous research studies. In research (Murray and Perera, 2021), the authors employ the GRU with an encoder-decoder architecture to forecast ship trajectories. In another study (Capobianco et al., 2020), the authors combine the encoder-decoder architecture with the LSTM for ship trajectory prediction. Furthermore, several research studies propose modified structures of the RNNs, including bidirectional GRU (Wang et al., 2020), bidirectional LSTM (Zhang et al., 2021), and the combination of RNNs with Deep Neuron Network (DNN) (Li et al., 2022) and Convolutional Neural Network (CNN) (Syed and Ahmed, 2023). However, as previously mentioned, all these studies uniformly train the RNNs with AIS data. Therefore, it is considered that the corresponding predictions may lack precision at a local scale.

The GRU is chosen in this study and the datasets used for training are collected from the KF-based estimated navigation states. This is due to the limited quantity of these KF-based estimates compared to AIS. Many research studies state that the GRU outperforms LSTM with a relatively smaller amounts of training data (Suo et al., 2020; Yang et al., 2020; Cahuantzi et al., 2023). Another feature of the used GRU is that the outputs are the surge and sway velocities, rather than positions and headings in a selected vessel. The surge and sway velocities obtained from the GRU are used to determine the location of the ship pivot point (PP).

2.3. Pivot point

The concept of a ship's PP has significant importance in ship maneuvering. Given that ships in general have substantial geometrical dimensions, turning maneuvers can result in expansive swept areas. Local-scale predictions must account for these areas. The size of the swept area is closely linked to the position of PP on ships (Seo, 2016). Therefore, the knowledge utilization of the PP serves as a fundamental technique in ship-handling education and training (Clark, 2005; Kjerstad, 2021). Experienced ship helmsmen usually rely on their expertise to estimate the PP, enabling them to predict ship positions and headings within a short time period.

The PP can be defined as follows: it is a specific point along the ship's centerline, measured from the ship's center of gravity (CG), where the sway velocity is zero during a turn maneuver (Tzeng, 1998). The distance between the ship CG and the PP–$dist_{CG\rightarrow PP}$ can be calculated as the ratio between the sway velocity at the CG (v_{CG}) and the yaw rate (r):

$$dist_{CG\rightarrow PP} = -v_{CG} / r \tag{1}$$

It should be noted that the determination of the PP based on (1) can pose challenges in real applications. One of the challenges arises from the effects of added mass in ship maneuvering. The added mass of a ship, also denoted as the extra mass of fluid that accelerates due to ship motions, can have the same comparable order of magnitude with respect to the ship mass (Fossen, 2011). This phenomenon highlights the importance of using the ship apparent center of gravity (ACG) rather than the CG when applying Newton's laws. However, the added mass can vary under different maneuvering and environmental conditions (Korotkin, 2008), making the ACG a non-fixed point. Another challenge lies in the calculation of the quotient in (1). It can become unstable when ships experience relatively small yaw rates. In such cases, the results may diverge and lack practical significance.

A novel approach to determine the position of PP is introduced in this study. In conventional ship maneuvering, it is well-known to experienced helmsmen that the PP of a turning ship typically situates around 1/5 to 1/4 of the ship length aft of the bow (Kjerstad, 2021). With this consideration, this study suggests that it can be more practical to estimate a range along the ship's centerline where the PP is likely to be found, rather than precisely determining the exact location of the PP.

3. Methodology

The complete workflow of the proposed localized advanced ship predictor development is depicted in Fig. 1. In Stage 1, the ship navigation states used in the kinematic motion models are estimated by the KF-based algorithm. The trajectory prediction in Stage 2 starts subsequently from the current step, utilizing the estimates obtained before. This paper primarily focuses on ship trajectory prediction; hence, the statistical properties and quality of the estimates from Stage 1 will not be addressed in this paper. For further details, reference can be made to (Wang et al., 2023a,b). This research study demonstrates that the estimated ship navigation states from the CMM and CTRA converge and maintain good precision. In this study, the ship trajectory prediction is carried out through two independent methods: the kinematic-based method and GRU-PP-based method. Both methods can generate a predicted trajectory that contains the ship's positions and headings over a shorter prediction horizon.

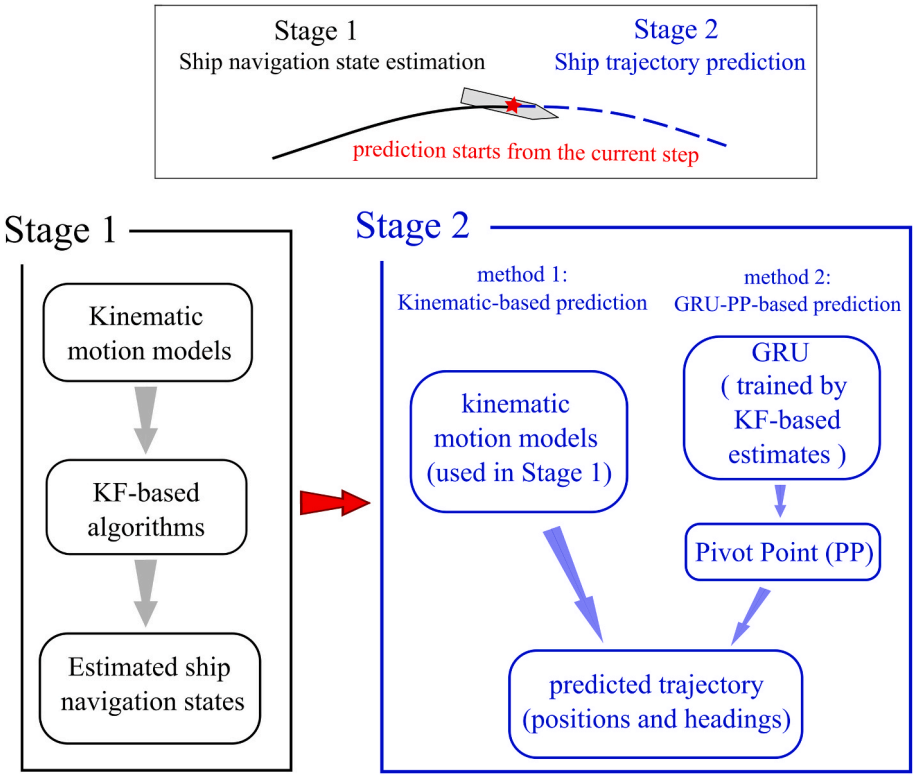

Fig. 1. The workflow of the localized advanced predictor involves two stages (Stage 2 is the primary focus of this paper).

3.1. Kinematic-based prediction

Three kinematic motion models are used in this section. The first model focuses on the rotation of the ship by using the constant angular acceleration (CAA) model (see Table 1). It can be observed that the CAA is a linear model (3), allowing the KF to generate optimal estimates. Additionally, this approach offers the advantage of deriving the angular acceleration–$\dot{r}$, which can be used for the correction of measurements. It should be noted that the heading ψ_T in the CAA is the true north. This configuration is based on the capability of advanced gyroscopes to directly measure ψ_T, as outlined in the measurement model of the CAA.

The other two models are the CTRA and CMM. Unlike the vessel states in the CAA, those in the CTRA and CMM must be explicitly defined with reference points on the ship. In the CTRA, two reference points P1 and P2 (see Table 2) are used. These two points are symmetrically positioned about the geometric center of the ship (C) and correspond to the measured positions by the GNSS system. The CTRA will consequently execute twice, providing vessel states in (6) with respect to both P1 and P2. Under the assumption that the ship's hull is incompressible, the velocity and acceleration (u and a_u) in the ship's surge direction is the same at both P1 and P2. The geometric center of the ship (C) is the reference point in the CMM (see Table 3). It should be noted that the CAA will be executed prior to the CTRA and CMM. The estimated states of the CAA (2) can therefore be utilized as constant parameters in the CTRA and CMM.

With respect to the measured positions from the GNSS system, the raw data sets are latitude and longitude (z_φ, z_λ) in the geographic coordinate system. A conversion is thus necessary to transform these latitude and longitude coordinates into the corresponding northing and easting of the UTM coordinate system. In addition, it is important to emphasize that ψ_G in both the CMM and CTRA represents the grid north in relation to the northing. Another modification is thus required to convert the true north ψ_T into the grid north ψ_G. In this study, the functions $f_N(z_\varphi, z_\lambda)$ and $f_E(z_\varphi, z_\lambda)$ are used to calculate the related northing and easting from a collected (z_φ, z_λ). Furthermore, the function $f_\gamma(z_\varphi, z_\lambda)$ is used to calculate the grid convergence γ which is the difference between ψ_T and ψ_G. The details of the conversion functions of $f_N(,)$, $f_E(,)$ and $f_\gamma(,)$ can be referred to (Kawase, 2013). As the onboard sensors are located in different positions, adjustments are also required for the measurement models (9), (10), and (14). These adjustments operate under the assumption that the ship's ACG is positioned around the geometric center of the ship, i.e., point C. The uncertainties related

Table 1
Constant angular acceleration (CAA) model.

	System model	Measurement model
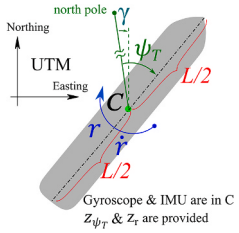	$\boldsymbol{x}(t) = [\psi_T, r, \dot{r}]^T$ (2) $\dot{\boldsymbol{x}}(t) = \begin{bmatrix} 0 & 1 & 0 \\ 0 & 0 & 1 \\ 0 & 0 & 0 \end{bmatrix} \bullet \boldsymbol{x}(t) + \boldsymbol{w}_x (\boldsymbol{w}_x \sim \mathcal{N}(\boldsymbol{0}, \boldsymbol{Q} \in \mathbb{R}^{3\times3}))$ (3)	$z[t_k] = [z_{\psi_T}, z_r]$ (4) $z[t_k] = \begin{bmatrix} 1 & 0 & 0 \\ 0 & 1 & 0 \end{bmatrix} \boldsymbol{x}[t_k] + \boldsymbol{w}_z (\boldsymbol{w}_z \sim \mathcal{N}(\boldsymbol{0}, \boldsymbol{R} \in \mathbb{R}^{2\times2})) t_k = k \bullet \Delta t \ (k = 1, 2, \ldots)$ (5)

Table 2
Constant turn rate & acceleration model (CTRA) (reference point: P1 & P2).

	System model	Measurement model
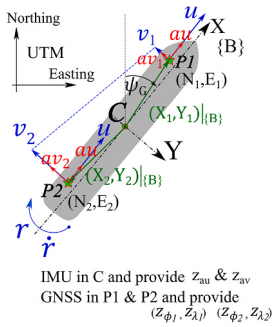 IMU in C and provide z_{au} & z_{av} GNSS in P1 & P2 and provide $(z_{\phi 1}, z_{\lambda 1})$ $(z_{\phi 2}, z_{\lambda 2})$	$\boldsymbol{x}(t) = [N_i, E_i, u, v_i, au, av_i]^T$ (6) $(i = 1,2)$ $\dot{\boldsymbol{x}}(t) = \begin{bmatrix} u\cos(\psi_G) - v_i\sin(\psi_G) \\ v_i\cos(\psi_G) + u\sin(\psi_G) \\ au \\ av_i \\ 0 \\ 0 \end{bmatrix} + \boldsymbol{w_x}$ $(\boldsymbol{w_x} \sim \mathcal{N}(\boldsymbol{0}, \boldsymbol{Q} \in \mathbb{R}^{6\times6}))$ (7) $i = 1,2\ \psi_G = \psi_T - f_\gamma(z_\varphi, z_\lambda)$	$z[t_k] = [f_N(z_{\varphi i}, z_{\lambda i}), f_E(z_{\varphi i}, z_{\lambda i}), z_{au}, z_{av}]$ (8) For P1: $z[t_k] = \begin{bmatrix} N_1 \\ E_1 \\ au - v_1 r - \dot{r} Y_1 - r^2 X_1 \\ av_1 + u r + \dot{r} X_1 - r^2 Y_1 \end{bmatrix} + \boldsymbol{w_z}$ (9) For P2: $z[t_k] = \begin{bmatrix} N_2 \\ E_2 \\ au - v_2 r - \dot{r} Y_2 - r^2 X_2 \\ av_2 + u r + \dot{r} X_2 - r^2 Y_2 \end{bmatrix} + \boldsymbol{w_z}$ $(\boldsymbol{w_z} \sim \mathcal{N}(\boldsymbol{0}, \boldsymbol{R} \in \mathbb{R}^{4\times4}))$ (10)

Table 3
Curvilinear motion model (CMM) (reference point: C).

Table 3. Curvilinear Motion Model (CMM) (reference point: C)

	system model	measurement model
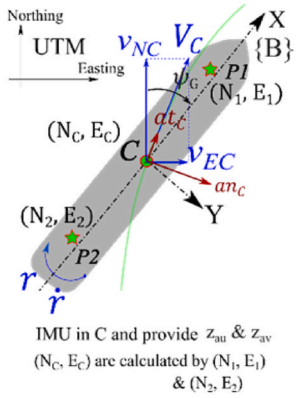 IMU in C and provide z_{au} & z_{av} (N_C, E_C) are calculated by (N_1, E_1) & (N_2, E_2)	$\boldsymbol{x}(t) = [N_C, E_C, v_{NC}, v_{EC}, at_C, an_C]^T$ (11) $\dot{\boldsymbol{x}}(t) = \begin{bmatrix} v_{NC} \\ v_{EC} \\ at_C f^{v_{NC}} - an_C f^{v_{EC}} \\ at_C f^{v_{EC}} + an_C f^{v_{NC}} \\ 0 \\ 0 \end{bmatrix} + \boldsymbol{w_x}$ $(\boldsymbol{w_x} \sim \mathcal{N}(\boldsymbol{0}, \boldsymbol{Q} \in \mathbb{R}^{6\times6}))$ (12) $f^{v_{NC}} = \frac{v_{NC}}{\sqrt{v_{NC}^2 + v_{EC}^2}}$ $f^{v_{EC}} = \frac{v_{EC}}{\sqrt{v_{NC}^2 + v_{EC}^2}}$	$\boldsymbol{z}[t_k] = [N_C, E_C, z_{au}, z_{av}]$ (13) $\boldsymbol{z}[t_k] = \begin{bmatrix} N_C \\ E_C \\ h_1\cos(\psi_G) + h_2\sin(\psi_G) - r\, g_1 \\ h_2\cos(\psi_G) - h_1\sin(\psi_G) + r\, g_2 \end{bmatrix} + \boldsymbol{w_z}$ $(\boldsymbol{w_z} \sim \mathcal{N}(\boldsymbol{0}, \boldsymbol{R} \in \mathbb{R}^{4\times4}))$ (14) (14) $N_C = 0.5(N_1 + N_2) + 3.6\sin(\psi_G);$ $E_C = 0.5(E_1 + E_2) + 3.6\cos(\psi_G);$ $\psi_G = \psi_T - f_\gamma(z_\phi, z_\lambda);$ $h_1 = at_C f^{v_{NC}} - an_C f^{v_{EC}} + r\, v_{EC};$ $h_2 = at_C f^{v_{EC}} + an_C f^{v_{NC}} - r\, v_{NC};$ $g_1 = v_{NC}\cos(\psi) + v_{EC}\sin(\psi);$ $g_2 = -v_{NC}\sin(\psi) + v_{EC}\cos(\psi);$

to this assumption are incorporated into the system and measurement noises.

The kinematic-based prediction utilizes the system models (3), (7), and (11). When the prediction starts, the estimated states (2), (6), and (11) from the current step are inputted into the system models to calculate the states for the next steps. This calculation can be iteratively executed until the defined prediction horizon is reached. The calculated positions and headings can thus be extracted to generate the ship's predicted trajectory. In this study, kinematic-based predictions are based on these two combinations of models: CAA + CMM and CAA + CTRA. The predicted headings are derived from the CAA, while the predicted positions are obtained from the CMM or CTRA. The measurement models (5, 9, 10, 14) will not be utilized in the trajectory prediction. Instead, they are employed in Stage 1 by the KF-based algorithms to produce estimated navigation states and the details can be seen in (Wang et al., 2023a,b).

3.2. GRU-PP-based method

The second prediction method integrates the GRU and the ship PP. The GRU is employed to generate the ship surge and sway velocities over the prediction horizon. These predicted states can later determine the location of the PP along the ship's centerline. After identifying the location of the PP, the ship's movement can be decomposed into two components: the translation of an arbitrary point and the rotation around the PP. The ship's positions and headings can then be determined using a rigid body motion-based algorithm.

3.2.1. The gated recurrent unit

The GRU is a simplified version of the LSTM that aims to enhance computational efficiency. In contrast to the LSTM's three-gate structure,

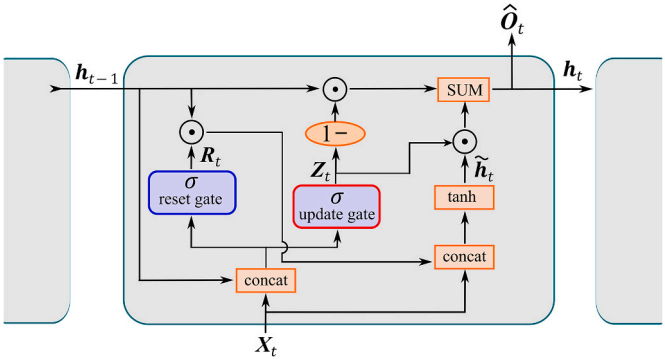

Fig. 2. GRU cell structure.

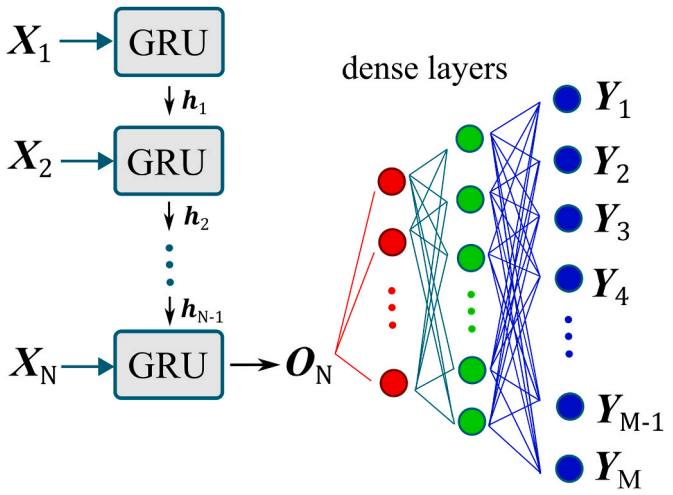

Fig. 3. The generation of predictions from the GRU and the attached dense layers.

the GRU simplifies the architecture to feature only two gates: the reset gate and the update gate. The two gates in the GRU can adaptively adjust the balance between the "remembering" and "forgetting" during the training process. Despite the reduction in the number of gates, the GRU incorporates a specialized mechanism aimed at achieving equivalent levels of accuracy to the LSTM. The cell of the GRU is shown in Fig. 2.

The reset gate and update gate work together to perform the regression of latent state h_t at each time step t. This procedure can be formulated in (15)–(18).

$$\boldsymbol{Z}_t = \sigma(\boldsymbol{W}_z \boldsymbol{X}_t + \boldsymbol{U}_z \boldsymbol{h}_{t-1} + \boldsymbol{b}_z) \tag{15}$$

$$\boldsymbol{R}_t = \sigma(\boldsymbol{W}_R \boldsymbol{X}_t + \boldsymbol{U}_R \boldsymbol{h}_{t-1} + \boldsymbol{b}_r) \tag{16}$$

$$\widetilde{\boldsymbol{h}}_t = \tanh(\boldsymbol{W}_h \boldsymbol{X}_t + \boldsymbol{U}_h(\boldsymbol{R}_t \odot \boldsymbol{h}_{t-1}) + \boldsymbol{b}_h) \tag{17}$$

$$\boldsymbol{h}_t = (1 - \boldsymbol{Z}_t) \odot \boldsymbol{h}_{t-1} + \boldsymbol{Z}_t \odot \widetilde{\boldsymbol{h}}_t \tag{18}$$

where $\boldsymbol{X}_t$ is the input vector, $\boldsymbol{Z}_t$ is the update gate vector, $\boldsymbol{R}_t$ is the reset gate vector, $\boldsymbol{h}_t$ is the latent state vector, $\widetilde{\boldsymbol{h}}_t$ is the candidate activation vector, and $\boldsymbol{O}_t$ is the output vector. $\boldsymbol{W}, \boldsymbol{U},$ and $\boldsymbol{b}$, each denoted with different subscripts, are related parameter matrices and vectors. The operators $\sigma(,)$ and $\odot$ represent the logistic activation function and Hadamard product, respectively. The update gate plays a pivotal role in adjusting the rate of new memories and determines the weights assigned to updating the long-term memory (15). The reset gate is responsible for regulating the rate of memory decay and generates the weights allocated to resetting during memory processing (16). Following this, the reset value, denoted as $\boldsymbol{R}_t$, is utilized to prepare $\widetilde{\boldsymbol{h}}_t$ for the subsequent memory update (17). Finally, the long-term memory undergoes an update for $\boldsymbol{h}_t$ by utilizing a weighted ratio of $\boldsymbol{h}_{t-1}$ and $\widetilde{\boldsymbol{h}}_t$ (18).

The output $\boldsymbol{O}_t$ from the final GRU cell is used to produce a time series of predictions via dense layers (see Fig. 3). In this study, the predictions ranging from $\boldsymbol{Y}_1$ to $\boldsymbol{Y}_M$ represent the time series of the predicted surge and sway velocities, i.e., u, v_1, and v_2 over the prediction horizon M. The input vector $\boldsymbol{X}_t$ is derived from the states outlined in (2), (6), and (11). During the training process, the Mean Square Error (MSE) is used as the loss function. The adjustment of parameters in the neural network are guided by the backpropagation algorithm, which is designed to minimize the MSE.

3.2.2. *Training of the GRU*

Since the training of the GRU must be conducted in advance, a series of historical simulated exercises of ship maneuvers is collected. One of the examples is depicted in Fig. 4. Following the workflow of Stage 1 (see Fig. 1), the ship's navigation states depicted in (2), (6), and (11) can be acquired for the entire duration of maneuvering. Some states from (2), (6), and (11) are selected and processed to generate the vector denoted by $\boldsymbol{X}$ (19). The parameters δ and β_C in $\boldsymbol{X}$ are not the states in the kinematic models. δ represents the rudder order. β_C denotes the drift angle which is defined as the difference between the heading and the course. The course can be determined using the v_{NC} and v_{EC} as outlined in (11).

$$\boldsymbol{X} = (\delta, \psi_G, r, \beta_C, V_C, at_C, an_C, au, av_1, av_2, u, v_1, v_2) \tag{19}$$

A time series of the vector (19) can be obtained which cover from t_0 to t_{end}. Since the GRU is introduced to improve prediction precision in scenarios where the selected ship executes new rudder orders, the training dataset only includes the vectors from a defined timeframe both before and after the release of the new rudder order. Fig. 5 illustrates the processing of training samples extracted from the time series of vector (19) shown in Fig. 4. Each training sample encompasses a time span of 30 s preceding the issuance of a new rudder order and 90 s following its execution. This configuration is based on the consideration that the well-trained GRU can effectively analyze historical navigation states occurring 30 s before a new rudder order to forecast subsequent states for the following 90 s. Given that the state estimation occurs at 0.1-s intervals, the input has a lag of 300 and the output spans a prediction horizon of 900 steps. The first ten elements in the vector (19) form the input of GRU. With the identical input, the GRU is structured to produce three distinct outputs: u, v_1, and v_2. Because these outputs are generated independently, the GRU thus requires three separate training processes for each distinct result.

A normalization procedure is also included to optimize the training

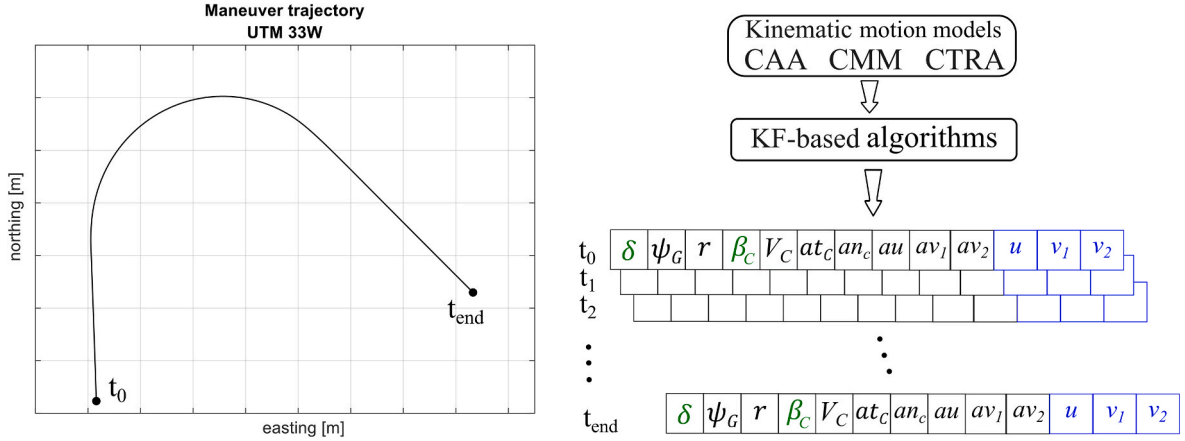

Fig. 4. Time series of the vector are generated from the estimated ship navigation states from a simulated exercise of maneuver.

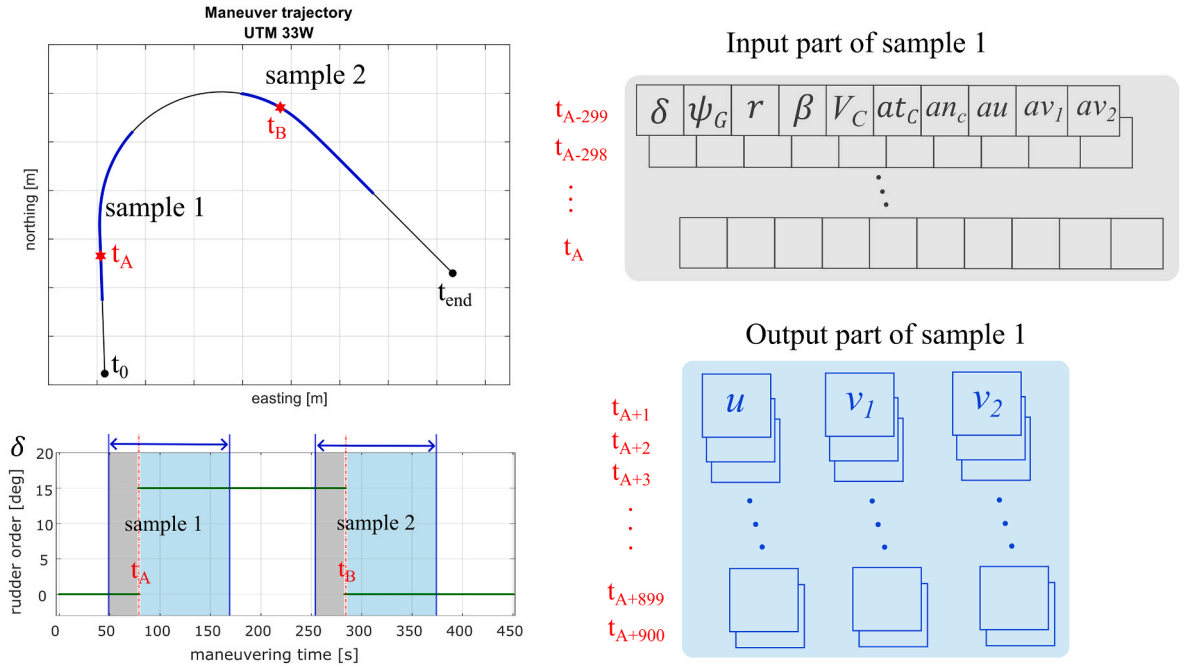

Fig. 5. Extracting training samples from a simulated exercise of maneuver. Each training sample spans a 120-s period, with new rudder commands issued at the 30th second of each interval (estimates are obtained in every 0.1[s]).

process. This procedure scales all the ship navigation states to fit within the −1 to 1 range, using the minimum and maximum values from the samples. Subsequently, a corresponding denormalization process will be applied to the outputs based on (20).

$$X_{train} = \frac{X - min(X)}{max(X) - \min(X)} \times 2 - 1 \quad (\max(\delta) = 45°, \min(\delta) = -45°) \tag{20}$$

3.2.3. Rigid body-based algorithm

Since the ship is treated as a rigid body, its motions can be decomposed into translational and rotational motions. The motion decomposition of a rigid body may not be unique in some situations. However, for practical purposes in analyzing ship maneuvers, it is more beneficial to decompose the motion such that the translational movement aligns with u and the rotational motion centers around the PP. It is crucial to differentiate the PP from the instant center of rotation. The depiction in Fig. 6 illustrates that the PP acts as the center for rotational movement concerning the ship's sway velocities, while also being involved in transitional motion. The assumption of a rigid body implies also that sway velocities are linearly distributed along the ship's length. With this premise, the position of the PP on the ship's centerline can be

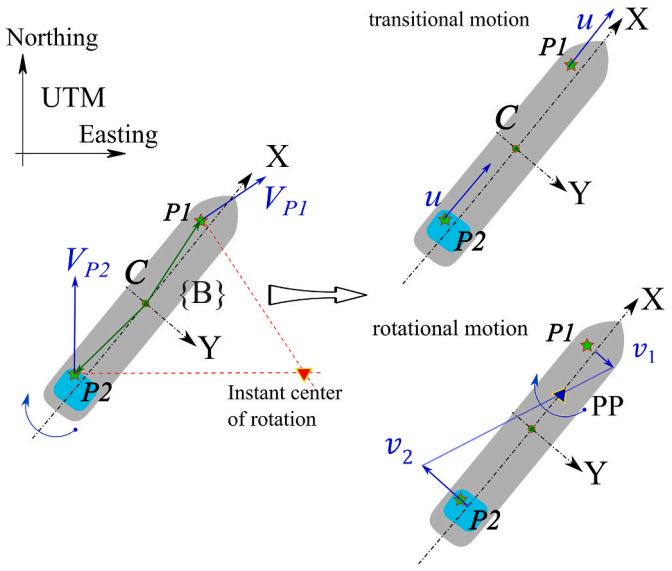

Fig. 6. Decomposition of the motion of a ship.

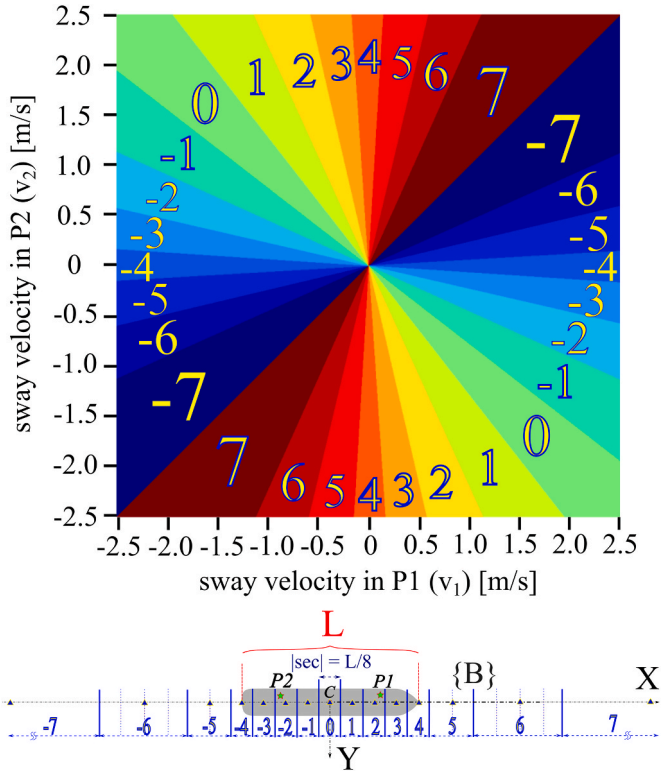

Fig. 7. The mapping between v_1, v_2, and predefined regions of pivot point.

Table 4
Predefined regions and pivot point position.

Region	Range in X-axis ($\|sec\| = L/8$)	PP coordinate in X-axis of {B}
−7	$(-\infty, -10.5 \bullet \|sec\|)$	$-20 \bullet \|sec\|$
−6	$(-10.5 \bullet \|sec\|, -6.5 \bullet \|sec\|)$	$-8.5 \bullet \|sec\|$
−5	$(-6.5 \bullet \|sec\|, -4.5 \bullet \|sec\|)$	$-5.5 \bullet \|sec\|$
−4	$(-4.5 \bullet \|sec\|, -3.5 \bullet \|sec\|)$	$-4 \bullet \|sec\|$
−3	$(-3.5 \bullet \|sec\|, -2.5 \bullet \|sec\|)$	$-3 \bullet \|sec\|$
−2	$(-2.5 \bullet \|sec\|, -1.5 \bullet \|sec\|)$	$-2 \bullet \|sec\|$
−1	$(-1.5 \bullet \|sec\|, -0.5 \bullet \|sec\|)$	$-1 \bullet \|sec\|$
0	$(-0.5 \bullet \|sec\|, 0.5 \bullet \|sec\|)$	0
1	$(0.5 \bullet \|sec\|, 1.5 \bullet \|sec\|)$	$1 \bullet \|sec\|$
2	$(1.5 \bullet \|sec\|, 2.5 \bullet \|sec\|)$	$2 \bullet \|sec\|$
3	$(2.5 \bullet \|sec\|, 3.5 \bullet \|sec\|)$	$3 \bullet \|sec\|$
4	$(3.5 \bullet \|sec\|, 4.5 \bullet \|sec\|)$	$4 \bullet \|sec\|$
5	$(4.5 \bullet \|sec\|, 6.5 \bullet \|sec\|)$	$5.5 \bullet \|sec\|$
6	$(6.5 \bullet \|sec\|, 10.5 \bullet \|sec\|)$	$8.5 \bullet \|sec\|$
7	$(10.5 \bullet \|sec\|, \infty)$	$20 \bullet \|sec\|$

determined using v_1 and v_2.

In this study, a mapping system is established to assign the PP to the predefined regions along the ship's centerline based on v_1 and v_2. As shown in Fig. 7, these predefined regions are designated within the range of −7 to 7, with a deliberate emphasis on concentration between the bow and stern (region −4 to 4). Moving away from both the bow and stern, the size of these regions is progressively expanded. This design is based on the experience with the selected vessel in the simulated maneuvering, where the PP is primarily located within the ship. Additionally, a rigid body motion-based algorithm is utilized to generate the predicted trajectory. When the PP is far from the ship, its precise numerical value gradually becomes of minimal impact on the algorithm's outcome. Therefore, the regions outside the ship are designed to expand progressively.

When allocating the PP to a specific region, a fixed distance between the PP and the ship's center (C) will be determined according to Table 4. The distance between the PP and C will be further converted into the distance between the PP and P2—$dist_{PP\to P2}$. As it is later demonstrated that the bridge and the GNSS are positioned around P2, the distance $dist_{PP\to P2}$ gains more practical significance.

Supported by this mapping system, the prediction of the ship's trajectory becomes feasible once the predicted u, v_1, and v_2 are established from the GRU. The translational motion (L_{trans}) can be derived solely from u. Because the cargo carrier has the bridge located astern, the distance between PP and P2 ($dist_{PP\to P2}$) and v_2 are used to calculate the angular speed of the rotational motion (ω). It is evident that ω displays minimal sensitivity to the variation of $dist_{PP\to P2}$ when this distance is significantly large. This characteristic underlies the reason for the predefined regions that have relatively extensive ranges away from both the bow and stern of the vessel.

Given the ship navigation states in current time step t_k, and the time series of predictions of (u, v_1, v_2) from time step t_{k+1} to t_{k+N} by the GRU, the predicted ship trajectory from t_{k+1} to t_{k+N} can be calculated by the provided algorithm:

Rigid body motion-based algorithm for ship trajectory prediction:

Given ship navigation states in t_k, and prediction of u, v_1, and v_2 from t_{k+1} to t_{k+N} for $i = k+1$ to $k+N$ do:
(translational calculation)
$L_{trans}[t_i] = u[t_i] \bullet dt$,
(rotational calculation)
determine the position of PP by $v_1[t_i]$ & $v_2[t_i]$ via the mapping system
calculate $dist_{PP\to P2}[t_i]$,
$\omega[t_i] = \frac{v_2[t_i]}{dist_{PP\to P2}[t_i]}$,
(heading in next time step)
$\psi_G[t_i] = \psi_G[t_{i-1}] + \omega[t_i] \bullet dt$,
(position of C in next time step)
$N_C[t_i] = N_C[t_{i-1}] + L_{trans}[t_i] \bullet \cos(\psi_G[t_i])$,
$E_C[t_i] = E_C[t_{i-1}] + L_{trans}[t_i] \bullet \sin(\psi_G[t_i])$.

It is worth noting that the operations of translational and rotational calculations in this algorithm are non-commutative. Different calculation sequences lead to discrepancies in prediction outcomes. To reduce these discrepancies, using a smaller value of dt is advisable.

4. Preparation for the simulation experiment

4.1. Simulation environment

All the maneuvering data sets used in this study are obtained from the simulated exercises conducted within the UiT bridge simulator (see Fig. 8). The bridge simulator serves as a platform for nautical education, enabling students to practice various maneuvers and enhance their seamanship skills. A substantial volume of ship exercise maneuvering data sets is thus accessible through the simulator. It is also important to highlight that maneuvers in the simulator are generated using specific nonlinear dynamic motion models that are unknown to the users. This reflects real-world navigation scenarios, where accurately capturing the dynamic properties of ships remains a challenging task.

A general cargo carrier (see Fig. 9) is selected from the simulator to generate various maneuvers. One should note that due to the relatively large size and tonnage of this cargo carrier, The primary method used to change ship navigation states, such as for collision avoidance, is the adjustment of the rudder rather than altering the engine power. Calm weather conditions are set during maneuvers so that the ship will not have significant pitch and roll motions. The cargo carrier is equipped with multiple sensors, including the gyroscope and IMU situated at a selected location of the ship that is closer to the vessel center of mass. Two GNSS antennas are symmetrically positioned relative to point C, recording the positional data of the bow (P1) and stern (P2), respectively. The measurements from these sensors will be used in the KF-based estimation to generate the required ship navigation states.

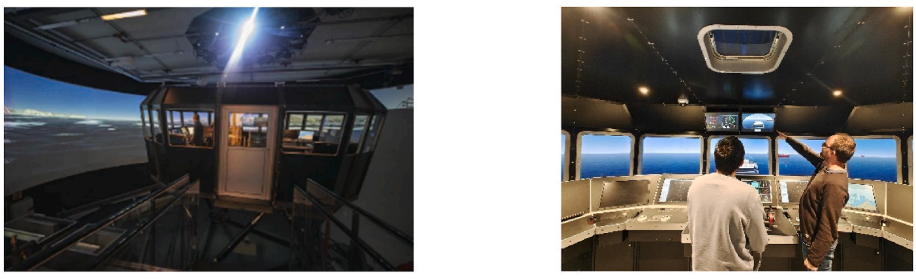

(a) View of the simulator from outside (b) Inside the UiT bridge simulator

Fig. 8. The UiT bridge simulator.

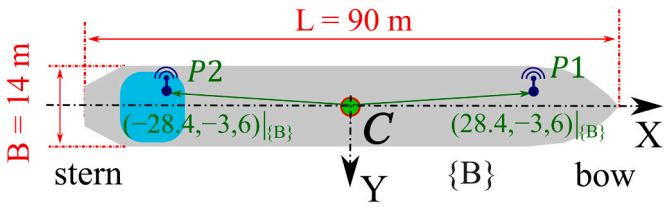

The advanced gyroscope and IMU are installed in C;
The GNSS antennas are installed in P1 and P2.

Type of vessel	General Cargo Carrier
Dimensions	LOA 90.00 m/ Beam 14.00 m
Draft	Ca. 6.5 m
Max Speed	Ca. 11.5 knots
Main Engine / Propulsion:	MAK 6M 25 1,800 kW/ controllable pitch propeller
gross tonnage / net tonnage	2,999 t / 1,639 t

Fig. 9. The general cargo carrier used in the UiT bridge simulator.

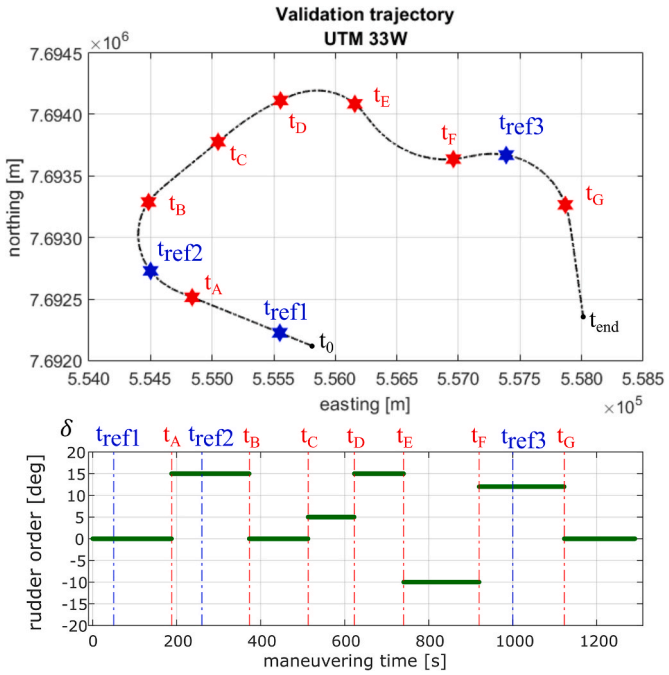

Fig. 10. Trejectory of the validation maneuver and the related rudder order. The trajectory prediction starts from these labeled time steps.

4.2. The simulated exercise for validation

To evaluate the prediction performances of both methods, a simulated maneuver performed by the same cargo carrier is executed in the simulator. Fig. 10 illustrates the trajectory alongside the corresponding rudder orders over the maneuvering time. The time steps when the predictions start are labeled in Fig. 10. The time steps highlighted in red directly follow a new rudder order, while the blue-labeled steps do not include any new rudder orders.

4.3. Parameters initialization

Two groups of parameters need to be determined in advance. The first group consists of parameters used in the ship navigation state estimation. Table 5 lists the parameters for state estimation. The values in the measurement noise covariances $\boldsymbol{R}$ are based on the sensors' performance characteristics, while the system noise covariance $\boldsymbol{Q}$ is determined through multiple trials to optimize the estimates.

The second group of parameters is related to the GRU structure and the training process (Table 6). Two hidden layers are used to correct the latent state vector $\boldsymbol{h}_t$ and the output vector $\boldsymbol{y}_t$. To assess how well the GRU with the initialized parameters generalizes to unseen data, there are 20% of the training samples are used as the validation samples.

5. Simulation results and discussion

5.1. The training of the GRU

The training outcomes of the GRU are depicted in Fig. 11, where the training and validation loss over 100 epochs are plotted. In Fig. 11(a) and (b), the training loss curves start with higher values, gradually decreasing and stabilizing as the training proceeds. Simultaneously, the validation loss curves exhibit a similar decreasing trend, eventually converging with the training loss curves. This convergence indicates the model's proficiency in effective learning and robust generalization to new datasets. However, a distinct pattern emerges in Fig. 11(c), where the validation loss curve initially mirrors the training loss but gradually diverges after approximately 40 epochs. This deviation suggests a potential issue with overfitting, implying that the model might be excessively tailored to the training data and could encounter difficulties in generalizing to unfamiliar datasets. To mitigate this concern and obtain an optimal balance between model fit and generalization, implementing early stopping as a strategy is worth considering.

5.2. Validation of ship trajectory prediction

The ship trajectory predictions start from step t_A to t_G with new rudder orders are illustrated in Fig. 12. The ship icons shown in these plots give a direct image of the predicted position and heading in everything 15 s over the prediction horizon of 90 s. In these cases, the superiority of the GRU-PP-based prediction over the prediction horizon is evident. The prediction results can provide navigators with a comprehensive understanding of the ship's states after a decision to change the rudder order. Given the emphasis in maritime transportation on making decisions ahead of time to prevent collisions, the prediction results can offer navigators generous safety margins in both temporal and spatial domains. Additionally, early decision-making allows for a balanced consideration of safety alongside other critical factors like time and cost. Since the GRU-PP-based prediction also has the ability to assess the effectiveness of a rudder order, it can serve also as a tool in optimizing decision-making processes for collision avoidance.

The detailed quantitative analyses of the predictions start at t_A, t_C, and t_E are presented in Fig. 13 which displays the prediction errors of positions and headings. The prediction errors of positions are determined by the Euclidean distance between the actual and predicted positions. Regarding the prediction errors of headings, both the related actual and predicted headings are represented as unit vectors in a Cartesian coordinate system. Following this, the errors are calculated as the angle between these two vectors. The prediction results from the kinematic-based methods demonstrate a similar level of accuracy compared to the GRU-PP-based method during the initial stage of the prediction horizon. However, as predictions progress, the errors in the kinematic-based predictions tend to increase significantly. These significant increases in errors arise from the assumptions made about constant accelerations and yaw rates in the kinematic motion models. The increases of errors are also proportional to the magnitude of the

Table 5
The initialized parameters of ship navigation state estimation.

Model	Para.	Definition	Value	Method of estimation
CAA	dt	time interval between consecutive measurements	0.1 [s]	Estimates are acquired every 0.1 s.
	Q	noise covariance matrix of system model	$\begin{pmatrix} dt^4/20 & dt^3/8 & dt^2/6 \\ dt^3/8 & dt^2/3 & dt/2 \\ dt^2/6 & dt/2 & 1 \end{pmatrix} \bullet q_r$ $q_r = 10^{-12}\,\pi/180$	A general noise covariance matrix for constant acceleration models
	R	noise covariance matrix of measurement model	$\begin{pmatrix} (0.5\,\pi/180)^2 & 0 \\ 0 & (0.01\,\pi/180)^2 \end{pmatrix}$	Values are referred to the sensors' performance property
CTRA	dt	time interval between consecutive measurements or updates	0.1 [s]	Estimates are acquired every 0.1 s.
	Q	noise covariance matrix of system model	$Diag(10^{-2}, 10^{-2}, 10^{-4}, 10^{-4}, 10^{-6}, 10^{-6})$	Determined by multiple trials to obtain the optimal estimates
	R	noise covariance matrix of measurement model	$Diag(1, 1, 10^{-4}, 10^{-4})$	Values are referred to the sensors' performance property
CMM	dt	time interval between consecutive measurements or updates	0.1 [s]	Estimates are acquired every 0.1 s.
	δt	time interval in the temporal discretization of nonlinear model	0.005 [s]	A trade-off value balancing accuracy and stability
	Q	noise covariance matrix of system model	$Diag(10^{-1}, 10^{-1}, 10^{-3}, 10^{-3}, 10^{-5}, 10^{-5})$	Determined by multiple trials to obtain the optimal estimates
	R	noise covariance matrix of measurement model	$Diag(1, 1, 10^{-4}, 10^{-4})$	Values are referred to the sensors' performance property
	λ	Tunning parameter used in the UKF	1.72	Recommended value suggested in (Wan and Merwe, 2000)

Table 6
The initialized parameters of the GRU.

Type	Para.	Definition	Value	Notation
Training samples	N_{train}	Total number of training samples	107	collection from 5 h' maneuvering
	N_{valid}	Total number of validation samples	22	20% of the N_{train}
Neuron network structure	n_c	Number of GRU cell	300	corresponding to input lag 300
	n_h	the number of dense layers	2	
	n_{h1}	the number of nodes in 1st dense layer	240	with activation function "ReLU"
	n_{h2}	the number of nodes in 2nd dense layer	120	with activation function "ReLU"
	n_o	the number of nodes in the output layer	900	corresponding to prediction horizon 900
Back-propagation training	lr	Fixed learning rate	0.001	
	batch	size of batch for training	64	
	epoch	epochs of training	100	proven to be converged

rudder angle. For example, predictions starting at t_C with a rudder change from 0 to 5 [deg] exhibit less errors compared to predictions starting at t_A and t_E. It is worth noting that the rise in prediction errors for heading occurs earlier than that of positions. This can imply that as for the used cargo carrier, the heading experiences a shorter response delay following a new rudder order compared to the course.

The prediction results and errors for cases without new rudder orders are depicted in Figs. 14 and 15. In these predictions, it is apparent that both prediction methods exhibit comparable performances. Particularly in the scenario beginning from t_{ref2}, the kinematic-based method surpasses the performance of the GRU-based method. It is essential to note that the training samples for the GRU always include a new rudder order in inputs. However, the presentation in Fig. 14 shows that the designed GRU can still generate reasonably predictions when inputs does not contain new rudder orders. Nonetheless, it is important to acknowledge that such predictions carry uncertainties, as evidenced by Fig. 14(b) which shows substantial prediction errors gradually.

The statistical analysis of the prediction results is depicted in Figs. 16 and 17. In Fig. 16, all the prediction errors start with new rudder orders (from $t_A - t_G$) are aggregated to generate boxplots for selected time steps. It is evident that the GRU-PP-based method exhibits superior performance when predictions start with new rudder angles. Conversely, the kinematic-based prediction can only maintain better precision over a shorter duration. A similar analysis is conducted for predictions starting without rudder angle orders, i.e., the predictions from t_{ref1}, t_{ref2}, and t_{ref3}. The performance of the kinematic-based method surpasses that of the GRU-PP-based method (see Fig. 17). The kinematic-based method demonstrates its reliability during steady ship stages. Considering the strengths and weaknesses of each prediction method, a combination of both approaches could be implemented to enhance SA in ship navigation safety and address challenges in future complex navigation environments.

6. Conclusion

In this research, ship trajectory prediction at a local scale is examined using two distinct methods through simulated maneuvering within the UiT bridge simulator. In the kinematic-based method, trajectory predictions are achieved through combinations of kinematic motion models (CAA + CMM and CAA + CTRA). In the GRU-PP-based method, the neural network-based predictions are integrated with the pivot point and a rigid body motion-based algorithm. The GRU generates predictions for the ship's surge and sway velocities in two different reference points. These sway velocities are then utilized to determine the location of the pivot point through a predefined mapping system. Finally, trajectory prediction is achieved using the rigid body motion-based algorithm.

A simulated maneuver which contains multiple rudder operations is used to validate these two prediction methods. Regarding the simulation results, firstly, the kinematic-based method demonstrates superiority during the ship's steady maneuvering phases. Kinematic motion models are proven to be robust for both linear and circular steady motions of the ship. Secondly, when predictions commence with a new rudder order, the GRU-PP-based method demonstrates a significant reduction in prediction errors compared to the kinematic-based method. The significant prediction errors observed in the kinematic-based method once again highlight the limitations of kinematic motion models in the ship trajectory prediction. As the third level of Situational Awareness (SA)

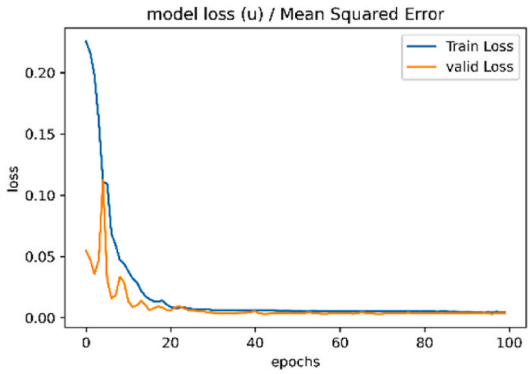

(a) training loss of u

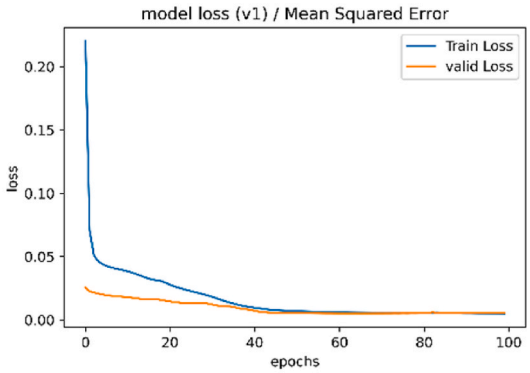

(b) training loss of v_1

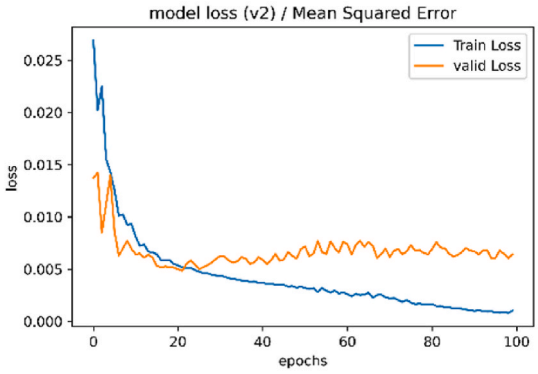

(c) training loss of v_2

Fig. 11. Training and validation loss of the GRU.

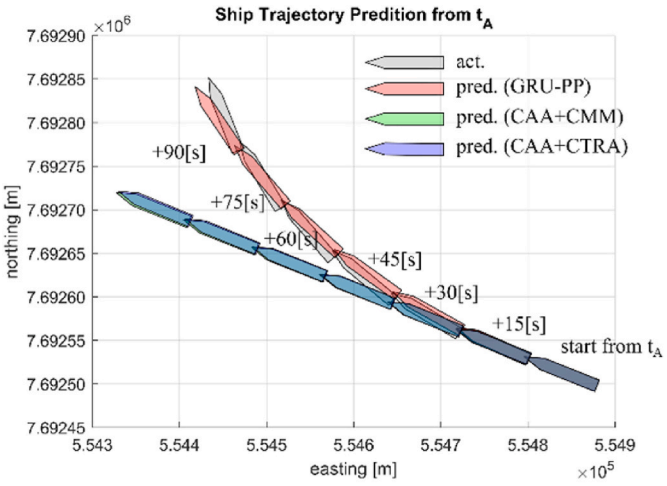

(a) Prediction from t_A

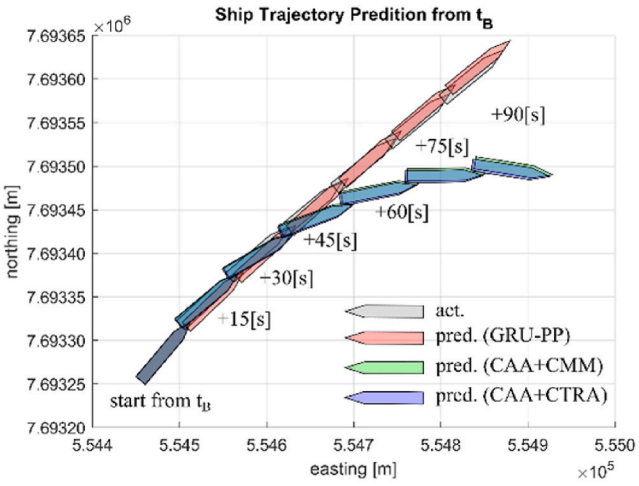

(b) Prediction from t_B

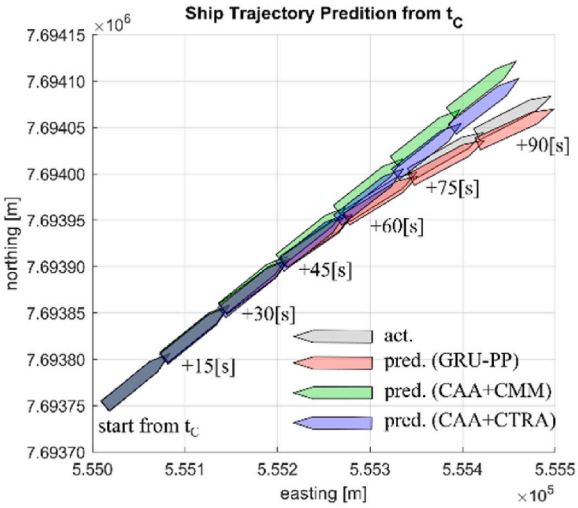

(c) Prediction from t_C

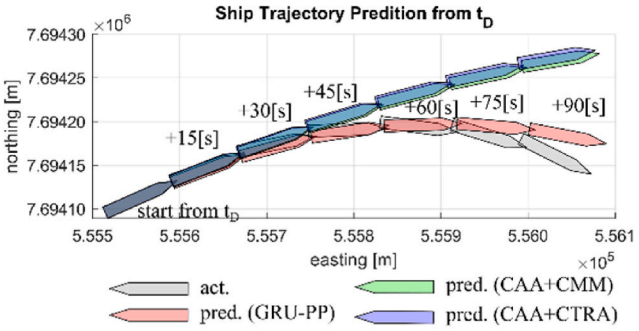

(d) Prediction from t_D

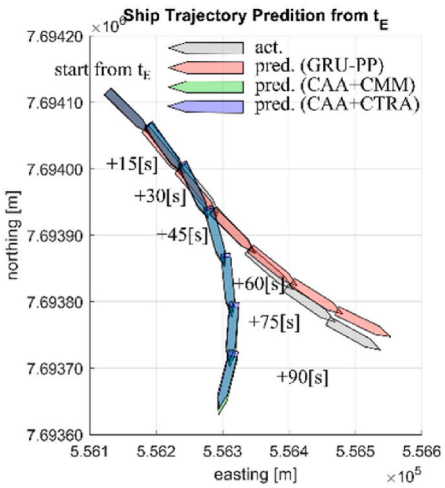

(e) Prediction from t_E

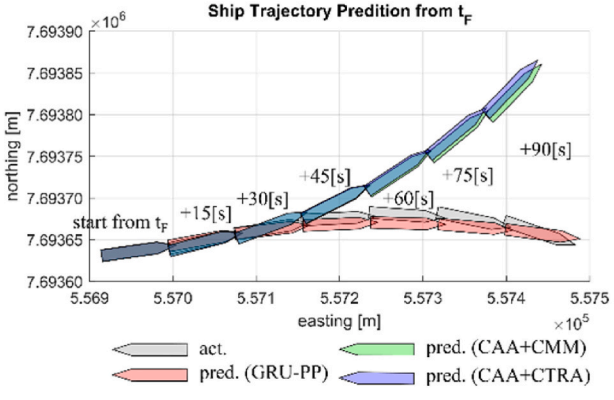

(f) Prediction from t_f

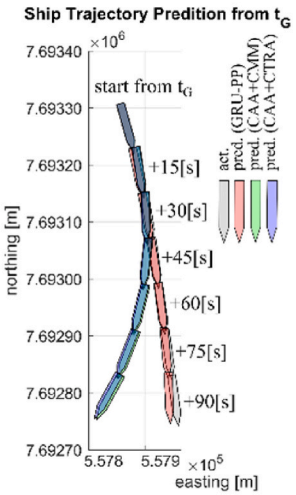

(g) Prediction from t_g

Fig. 12. Ship trajectory predictions from time steps when new rudder orders are issued.

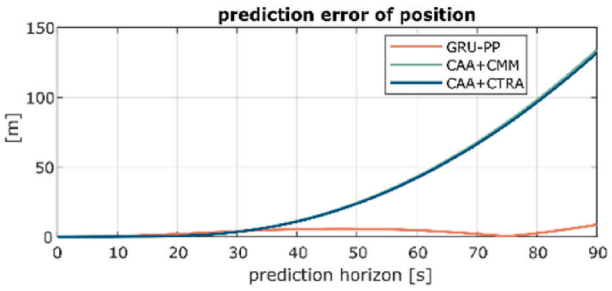

(a) error of predicted position from t_A

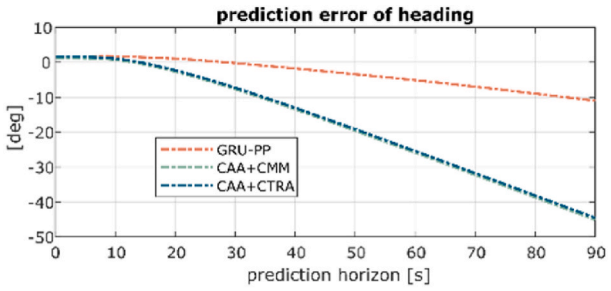

(b) error of predicted heading from t_A

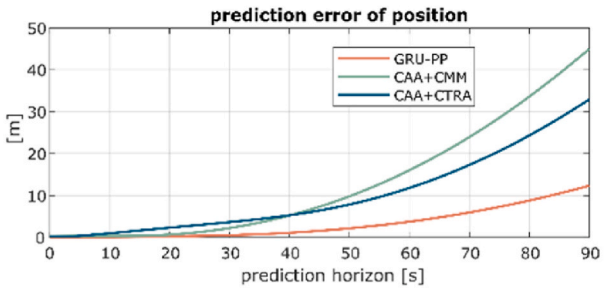

(c) error of predicted position from t_C

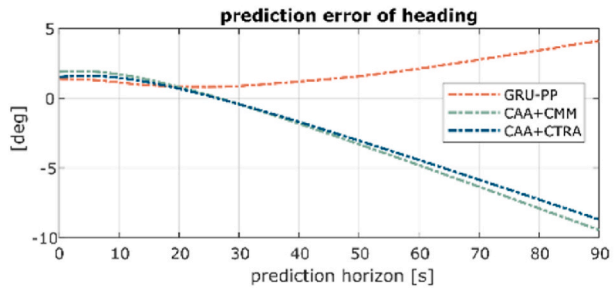

(d) error of predicted heading from t_C

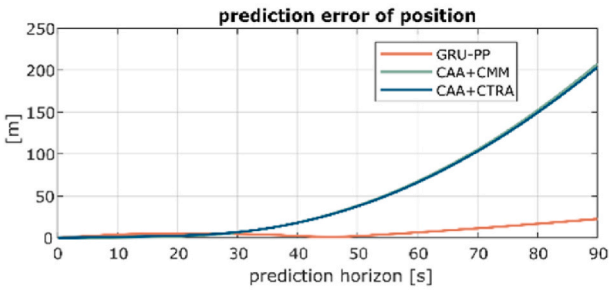

(e) error of predicted position from t_E

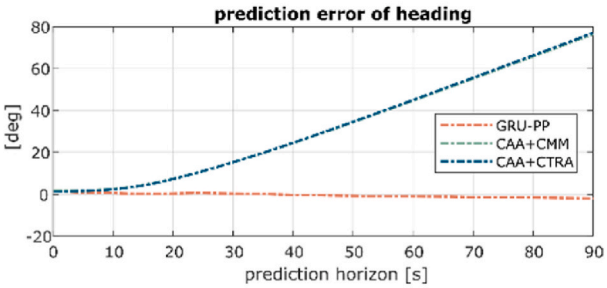

(f) error of predicted heading from t_E

Fig. 13. Prediction error from step t_A, t_C, and t_E.

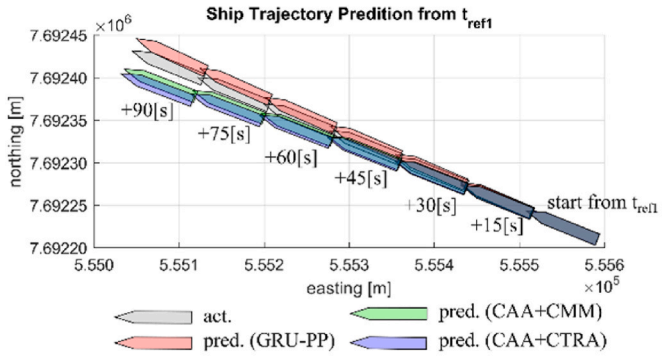

(a) Prediction from t_{ref1}

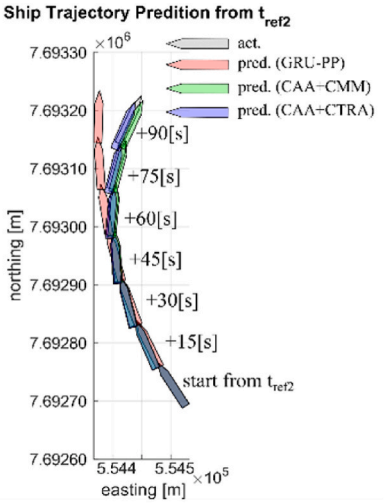

(b) Prediction from t_{ref2}

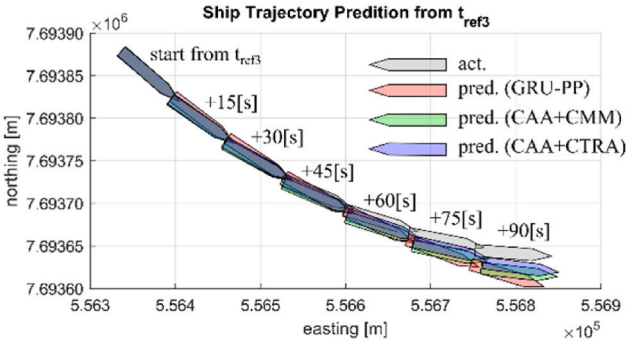

(c) Prediction from t_{ref3}

Fig. 14. Ship trajectory prediction from time steps without new rudder orders.

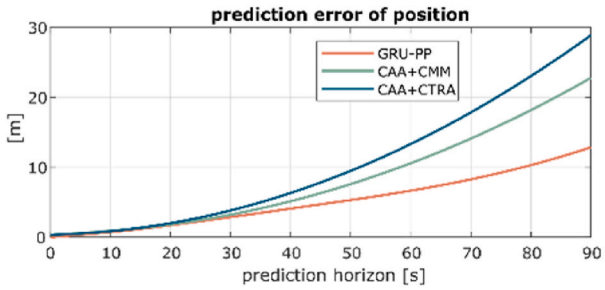

(a) error of predicted position from t_{ref1}

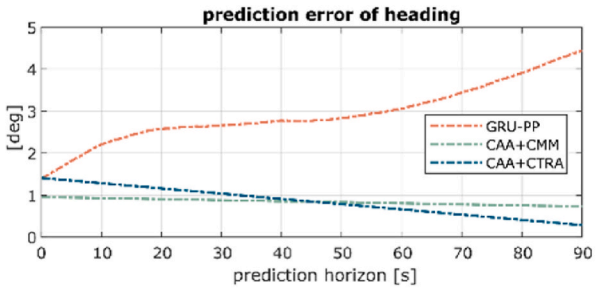

(b) error of predicted heading from t_{ref1}

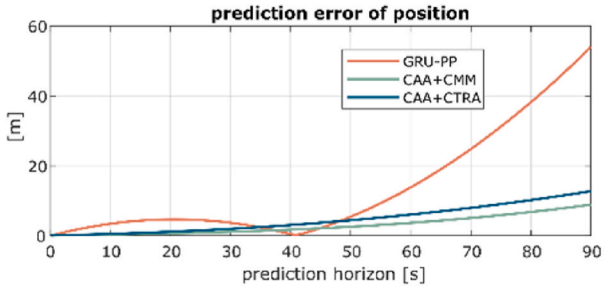

(c) error of predicted position from t_{ref2}

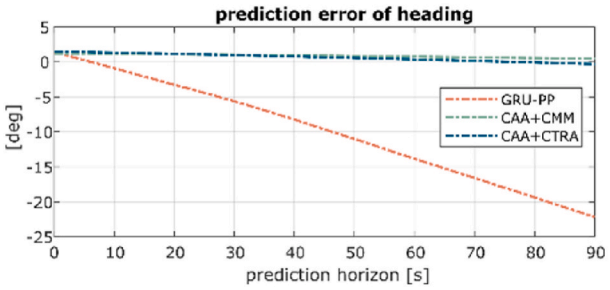

(d) error of predicted heading from t_{ref2}

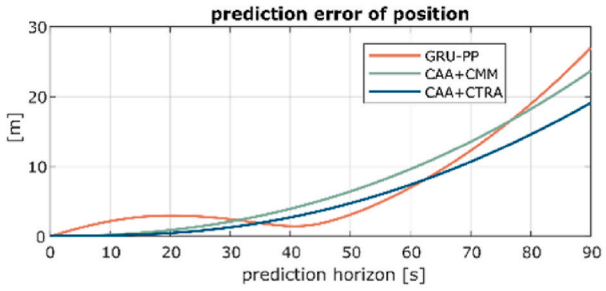

(e) error of predicted position from t_{ref3}

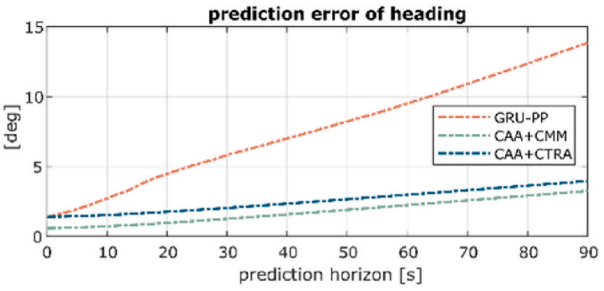

(f) error of predicted heading from t_{ref3}

Fig. 15. Prediction error from step t_{ref1}, t_{ref2}, and t_{ref3}.

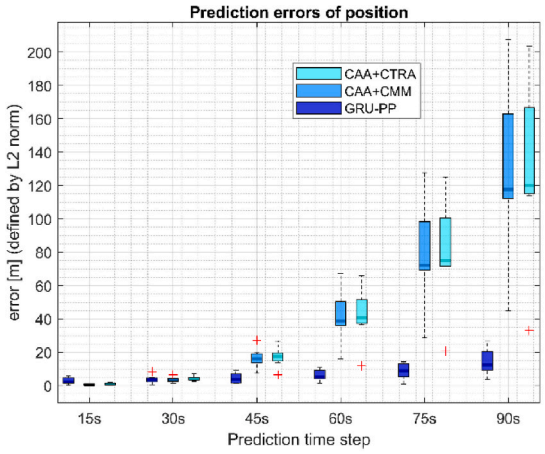

(a) prediction errors of position

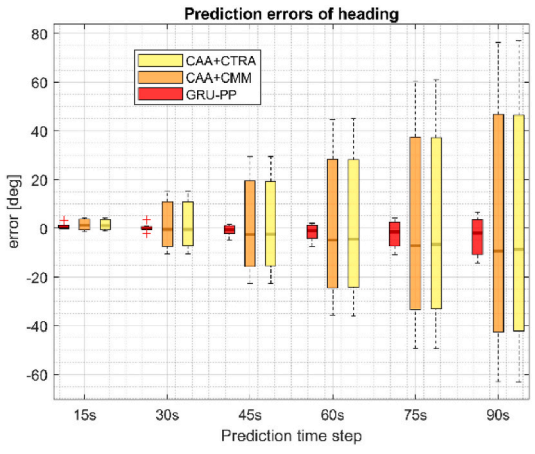

(b) prediction errors of heading

Fig. 16. Statistical analysis of the prediction results. Boxplots are generated using predicted values across all scenarios from time point t_A to t_G.

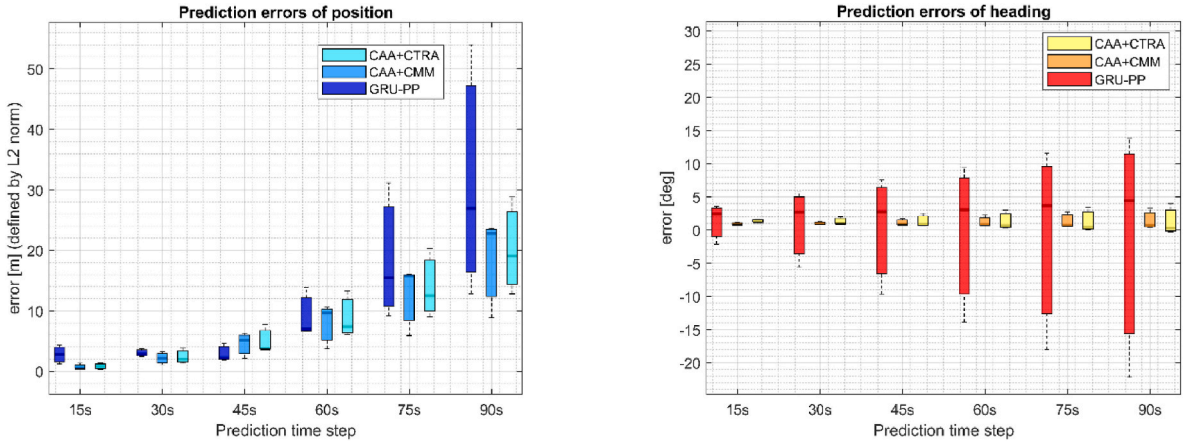

(a) prediction errors of position (b) prediction errors of heading

Fig. 17. Statistical analysis of the prediction results. Boxplots are generated using predicted values across all scenarios from time point t_{ref1}, t_{ref2}, and t_{ref3}.

requires projecting ship states into the near future, these predictions spanning a horizon of 90 s can thus serve as an effective tool to enhance SA.

However, the findings in this study are subject to a limitation in terms of the simulated data. The main reason is that this study focuses on demonstrating the capabilities of the proposed advanced predictors in a simulated environment. In this environment, actual ship models are highly nonlinear and remain unknown. Since the capabilities of the proposed advanced predictors are quantified, then these algorithms are ready to implement with the data sets from ocean going ships and that is the future step of this study. One should also note that real sea-trial data can encompass additional unexpected factors from the sea environment, i.e., the sensor noise may be higher due to rough wind or wave conditions, which are challenging to replicate in simulated environments. Furthermore, the training datasets used for the GRU do not incorporate features from the sea environment and weather conditions. Consequently, the GRU designed and trained using the simulated data may not be compatible with real navigation data in some situations, as the sea environment and weather conditions can significantly influence the ship's maneuvering. Therefore, future efforts will involve conducting sea-trial experiments and collecting real ship navigation data. Additional work will be required in designing the GRU to ensure that environmental factors are also reflected in the final predictions.

CRediT authorship contribution statement

Yufei Wang: Writing – original draft, Visualization, Validation, Methodology, Investigation, Formal analysis, Data curation, Conceptualization. **Lokukaluge Prasad Perera:** Writing – review & editing, Supervision, Software, Resources, Project administration, Funding acquisition. **Bjørn-Morten Batalden:** Writing – review & editing, Supervision, Resources, Project administration, Funding acquisition.

Declaration of competing interest

The authors declare that they have no known competing financial interests or personal relationships that could have appeared to influence the work reported in this paper.

Data availability

Data will be made available on request.

Acknowledgements

This work has been conducted under the Autonomous ship Program in UiT-The Arctic University of Norway, which aims to develop the digital helmsman as a part of the ship intelligence to operate future vessels supported by the MARKOM II project under the project title "Onshore Operation Center for Remotely Controlled Vessels (OOC 2023)" under the contract number PMK-2022-10014.

Appendix A. Supplementary data

Supplementary data to this article can be found online at https://doi.org/10.1016/j.oceaneng.2024.117704.

References

Abilio Ramos, M., Utne, I.B., Mosleh, A., 2019. Collision avoidance on maritime autonomous surface ships: operators' tasks and human failure events. Saf. Sci. 116, 33–44.
Ait Allal, A., Amrani, L., Haidine, A., Mansouri, K., Mohamed, Y., 2020. Implementation of 5G communication network for a safe operation of autonomous and conventional ships. Int. J. Eng. Res. Afr. 51, 229–248.
Amro, A., Oruc, A., Gkioulos, V., Katsikas, S., 2022. Navigation data anomaly analysis and detection. Information 13, 104.
Artikis, A., Zissis, D., 2021. Guide to Maritime Informatics. Springer Nature Switzerland AG 2021, pp. 10–11.
AVATAR, 2023. Interreg VB North Sea Region Programme. Retrieved 8, Nov, 2023, from. https://northsearegion.eu/avatar/.
Bar-Shalom, Y., Li, X.R., Kirubarajan, T., 2002. State estimation for nonlinear dynamic systems. In: Estimation with Applications to Tracking and Navigation, pp. 371–420.
Batlle, J.A., Condomines, A.B., 2020. Rigid Body Kinematics. Cambridge University Press, Cambridge, England.
Best, R.A., Norton, J.P., 1997. A new model and efficient tracker for a target with curvilinear motion. IEEE Trans. Aero. Electron. Syst. 33 (3), 1030–1037.
Birkeland, Y., 2022. The First Zero Emission, Autonomous Ship: Yara International. Retrieved 8, Nov, 2023. www.yara.com/knowledge-grows/game-changer-for-the-environment/.
Cahuantzi, R., Chen, X., Güttel, S., 2023. A comparison of LSTM and GRU networks for learning symbolic sequences. In: Science and Information Conference. Springer.
Capobianco, S., Millefiori, L., Forti, N., Braca, P., Willett, P., 2020. Deep learning methods for vessel trajectory prediction based on recurrent neural networks. IEEE Trans. Aero. Electron. Syst. 57.
Chang, C.-H., Kontovas, C., Yu, Q., Yang, Z., 2021. Risk assessment of the operations of maritime autonomous surface ships. Reliab. Eng. Syst. Saf. 207, 107324.
Chung, J., Gulcehre, C., Cho, K., Bengio, Y., 2014. Empirical Evaluation of Gated Recurrent Neural Networks on Sequence Modeling arXiv preprint arXiv:1412.3555.
Clark, I.C., 2005. Ship Dynamics for Mariners. Nautical Institute, London, England.
Endsley, M., 1995. Endsley, M.R.: toward a theory of situation awareness in dynamic systems. Hum. Factors: J. Human Fact. Erg. Soc. 37, 32–64.
Fossen, T., 2011. Handbook of Marine Craft Hydrodynamics and Motion Control. John Wiley & Sons, Nashville, TN.
Fukuto, J., 2021. Automation Levels of Automated/Autonomous Ships. ClassNK.

Hochreiter, S., Schmidhuber, J., 1997. Long short-term memory. Neural Comput. 9, 1735–1780.
Hoem, Å., Rødseth, Ø., Fjørtoft, K., 2019. Addressing the accidental risks of maritime transportation: could autonomous shipping technology improve the statistics? TransNav, Int. J. Marine Navig. Safety Sea Transp. 13.
IMO, 2019. Autonomous Shipping. Retrieved 8, Nov, 2023. https://en.uit.no/prosjekter/prosjektp_document_id=668855.
Kawase, K., 2013. Concise Derivation of Extensive Coordinate Conversion Formulae in the Gauss-Krüger Projection.
Kim, S., Yun, S., You, Y., 2021. Eco-friendly speed control algorithm development for autonomous vessel route planning. J. Mar. Sci. Eng. 9.
Kim, T.-e., Perera, L., Sollid, M.-P., Batalden, B.-M., Sydnes, A., 2022. Safety challenges related to autonomous ships in mixed navigational environments. WMU J. Maritime Aff. 21.
Kjerstad, N., 2021. Fremføring av skip med navigasjonskontroll [Advancement of ships with navigation and control]. Fagbokforlaget 11–12.
Kohn, S., Momen, A., Wiese, E., Lee, Y.-C., Shaw, T., 2019. The consequences of purposefulness and human-likeness on trust repair attempts made by self-driving vehicles, 63, 222–226.
Kongsberg, 2023. Autonomous Ships Equipment/Products/Systems - Kongsberg Maritime. Retrieved 8, Nov, 2023. https://www.kongsberg.com/maritime/ship-types/autonomous-ships/.
Koo, H., Chae, J., Kim, W., 2023. Design and experiment of satellite-terrestrial integrated gateway with dynamic traffic steering capabilities for maritime communication. Sensors 23, 1201.
Korotkin, A.I., 2008. Added Masses of Ship Structures. Springer, New York, NY.
Lee, C.-K., Moon, S.-B., Jeong, T.-G., 2016. The investigation of ship maneuvering with hydrodynamic effects between ships in curved narrow channel. Int. J. Nav. Archit. Ocean Eng. 8 (1), 102–109.
Li, M.-W., Xu, D.-Y., Geng, J., Hong, W.-C., 2022. A hybrid approach for forecasting ship motion using CNN–GRU–AM and GCWOA. Appl. Soft Comput. 114.
Lipton, Z.C., Berkowitz, J., Elkan, C., 2015. A Critical Review of Recurrent Neural Networks for Sequence Learning arXiv preprint arXiv:1506.00019.
Lu, Z., Kang, L., Gao, S., Meng, Q., 2018. Determination of minimum distance to obstacle avoidance in the Singapore strait. Transport. Res. Rec.: J. Transport. Res. Board 2672.
MEGURI2040, 2022. The Nippon Foundation MEGURI2040 Fully Autonomous Ship Program. Retrieved 8, Nov, 2023, from. https://www.nippon-foundation.or.jp/en/what/projects/meguri2040.
Munim, Z., 2019. Autonomous ships: a review, innovative applications and future maritime business models. Supply Chain Forum 20, 266–279.
Murray, B., Perera, L.P., 2021. An AIS-based deep learning framework for regional ship behavior prediction. Reliab. Eng. Syst. Saf. 215, 107819.
NFAS, 2017. Definition for Autonomous Merchant Ships, Norwegian Forum for Autonomous Ships.
Oruc, A., Amro, A., Gkioulos, V., 2022. Assessing cyber risks of an INS using the MITRE ATT&CK framework. Sensors 22, 8745.
Pascanu, R., Mikolov, T., Bengio, Y., 2013. On the difficulty of training recurrent neural networks. In: International Conference on Machine Learning. Pmlr.
Perera, L., 2019. Deep learning towards autonomous ship navigation and possible COLREGs failures. J. Offshore Mech. Arctic Eng.
Perera, L., Batalden, B.-M., 2019. Possible COLREGs Failures under Digital Helmsman of Autonomous Ships.
Perera, L., Guedes Soares, C., 2012. Detections of Potential Collision Situations by Relative Motions of Vessels under Parameter Uncertainties, pp. 705–713.
Perera, L., Murray, B., 2019. Situation awareness of autonomous ship navigation in a mixed environment under advanced ship predictor. In: Proceedings of the 38th International Conference on Ocean, Offshore and Arctic Engineering (OMAE 2019). Glasgow, Scotland, UK.
Perera, L., Oliveira, P., Guedes Soares, C., 2012. Maritime traffic monitoring based on vessel detection, tracking, state estimation, and trajectory prediction. IEEE Trans. Intell. Transport. Syst. 13.
Perera, L.P., 2017. Navigation vector based ship maneuvering prediction. Ocean Eng. 138, 151–160.
Porathe, T., Prison, J., Man, Y., 2014. Situation awareness in remote control centres for unmanned ships. In: Proceedings of Human Factors in Ship Design & Operation, London, UK.
Rødseth, Ø., 2019. Defining ship autonomy by characteristic factors. In: Proceedings of ICMASS 2018 Busan, Korea. SINTEF Academic Press.
Rødseth, Ø.J., Wennersberg, L.A.L., Nordahl, H., 2023. Improving safety of interactions between conventional and autonomous ships. Ocean Eng. 284.
Seo, S.-G., 2016. Safer and more efficient ship handling with the pivot point concept. TransNav, Int. J. Marine Navig. Safety Sea Transp. 10, 605–612.
Suo, Y., Chen, W., Claramunt, C., Yang, S., 2020. A ship trajectory prediction framework based on a recurrent neural network. Sensors 20.
Syed, M.A., Ahmed, I., 2023. A CNN-LSTM architecture for marine vessel track association using automatic identification system (AIS) data. Sensors 23. https://doi.org/10.3390/s23146400.
Thombre, S., Zhao, Z., Ramm-Schmidt, H., García, J.M.V., Malkamäki, T., Nikolskiy, S., Hammarberg, T., Nuortie, H., Bhuiyan, M.Z.H., Särkkä, S., Lehtola, V.V., 2022. Sensors and ai techniques for situational awareness in autonomous ships: a review. IEEE Trans. Intell. Transport. Syst. 23 (1), 64–83.
Tzeng, C.-Y., 1998. Analysis of the pivot point for a turning ship. J. Mar. Sci. Technol. 6 (1).
UiT, 2021. UiT Autonomous Ship Program. Retrieved 8, Nov, 2023, from. https://en.uit.no/prosjekter/prosjekt?p_document_id=668855.
Veitch, E., Andreas Alsos, O., 2022. A systematic review of human-AI interaction in autonomous ship systems. Saf. Sci. 152, 105778.
Wan, E.A., Merwe, R.V.D., 2000. The unscented Kalman filter for nonlinear estimation. In: Proceedings of the IEEE 2000 Adaptive Systems for Signal Processing, Communications, and Control Symposium (Cat. No.00EX373).
Wang, C., Ren, H., Li, H., 2020. Vessel trajectory prediction based on AIS data and bidirectional GRU. In: 2020 International Conference on Computer Vision, Image and Deep Learning (CVIDL).
Wang, Y., Perera, L.P., Batalden, B.-M., 2023a. Coordinate conversion and switching correction to reduce vessel heading-related errors in high-latitude navigation. In: The 22nd World Congress of the International Federation of Automatic Control (IFAC 2023). Yokohama, Japan, pp. 11590–11595. **56-2**.
Wang, Y., Perera, L.P., Batalden, B.-M., 2023b. Kinematic motion models based vessel state estimation to support advanced ship predictors. Ocean Eng. 286, 115503.
Wickens, C., Williams, A., Clegg, B., Smith, C.A.P., 2019. Nautical collision avoidance: the cognitive challenges of balancing safety, efficiency, and procedures. Hum. Factors: J. Human Fact. Erg. Soc. 62.
Wolsing, K., Roepert, L., Bauer, J., Wehrle, K., 2022. Anomaly detection in maritime AIS tracks: a review of recent approaches. J. Mar. Sci. Eng. 10 https://doi.org/10.3390/jmse10010112.
Wróbel, K., Montewka, J., Kujala, P., 2017. Towards the assessment of potential impact of unmanned vessels on maritime transportation safety. Reliab. Eng. Syst. Saf. 165, 155–169.
Yang, S., Yu, X., Zhou, Y., 2020. LSTM and GRU neural network performance comparison study: taking yelp review dataset as an example. In: 2020 International Workshop on Electronic Communication and Artificial Intelligence (IWECAI).
Zhang, S., Wang, L., Zhu, M., Chen, S., Zhang, H., Zeng, Z., 2021. A Bi-directional LSTM ship trajectory prediction method based on attention mechanism. In: 2021 IEEE 5th Advanced Information Technology, Electronic and Automation Control Conference (IAEAC).
Zhao, L., Shi, G., Yang, J., 2018. Ship trajectories pre-processing based on AIS data. J. Navig. 71 (5), 1210–1230.
Zhou, X., Liu, Z., Wu, Z., Wang, F., 2019. Quantitative processing of situation awareness for autonomous ships navigation. TransNav, Int. J. Marine Navig. Safety Sea Transp. 13, 25–31.

Paper VI

Pivot Point Estimation based Advanced Ship Predictor Evaluation with Vessel Maneuvers under Sea Trial Conditions

Wang, Y., Perera, L. P. and Batalden, B.-M. (2024)

Submitted in *Ocean Engineering*

Pivot Point Estimation based Advanced Ship Predictor Evaluation with Vessel Maneuvers under Sea Trial Conditions

Yufei Wang[a,*], Lokukaluge Prasad Perera[a,b] , and Bjørn-Morten Batalden[a]
[a]*Department of Technology and Safety, UiT The Arctic University of Norway, Tromsø, Norway*
[b]*SINTEF Digital, Oslo, Norway*

Abstract:

To enhance situation awareness (SA) in the context of autonomous ship navigation within a complex navigation environment, the Advanced Ship Predictor (ASP) is proposed as a solution framework aimed at predicting ship maneuvers. This can be used to identify potential ship close encounters and collision scenarios in advance, where appropriate collision avoidance actions should be taken. The implementation of the localized ASP is divided into three stages. In the first stage, Kalman filter (KF)-based techniques with kinematic motion models are employed to estimate vessel navigation states. Subsequently, the pivot point (PP) is calculated from these estimates using a Gaussian process regression model. The ASP development considers an ocean-going vessel as a rigid body and decomposes its dynamics into translational and rotational motion components, where the PP serves as the center of the rotational motions. This study aims to validate the local-scale prediction of the ASP by using sea trial experimental data in real ocean environments. Therefore, several data sets from two ship maneuvers executed by the UiT research vessel, Ymir RV, are used to validate the proposed ASP. The real-world validation results demonstrate that the applied KF-based algorithms and kinematic motion models are consistent with the simulation results. It is concluded that the ASP-based vessel estimates and PP information can achieve better vessel maneuvering prediction capabilities in real ship navigation situations and that can be used to avoid possible collision or near-miss situations.

Keywords:

Maritime situation awareness
Collision avoidance
Kinematic motion models
Kalman filter-based estimation
Gaussian Process Regression
Pivot point
Ship trajectory prediction

1. Introduction

The rapid advancements in sensor technologies, big data, the Internet of Things, and artificial intelligence lead to a significant trend toward maritime digitalization, where autonomous and remotely operated vessels represent a major research focus. Nowadays, there are numerous ongoing research and development projects focused on autonomous ships and their supporting applications (UiT, 2021;MEGURI2040, 2022;Kongsberg, 2023). The development of autonomous shipping is further supported by the International Maritime Organization (IMO), which is involved in establishing a code to regulate Maritime Autonomous Surface Ships (MASS) in 2025 (IMO, 2024). Given that as much as 90% of international trade is transported across oceans, securing navigation safety and reducing maritime accidents are always the major focus in the shipping industry. According to the European Maritime Safety Agency (EMSA), collisions were the primary type of casualty event from 2014 to 2022, accounting for 21.6% of the occurrences with ships (EMSA, 2024). In addition, the EMSA report also emphasizes that human actions were the main contributing factor to such marine accidents. Therefore, research studies on collision avoidance mechanisms for autonomous and remotely operated ships are critical to secure ship navigation in the future.

1.1 Maritime situation awareness

Situation awareness (SA) is a crucial component of effective decision-making in many navigation environments. It is the process of understanding a relevant environment, the elements around it, and how these changes with

respect to time or other factors can occur. In the definition proposed in (Endsley, 1995), SA is formulated into three levels: the perception of the elements in the environment within a volume of time and space (level 1); the comprehension of their meaning (level 2); and the projection of their status in the near future (level 3). It is important to note that the introduction of autonomous navigation-related technologies in shipping will be a gradual process (Munim, 2019). Conventional manned, remotely operated, and autonomous ships with varying degrees of autonomy are likely to share the same navigation environment. Consequently, close encounter situations among these different types of ships can introduce various issues of navigation safety in the near future (Perera and Batalden, 2019;Kim et al., 2022).

To ensure navigation safety in this new and challenging environment, it is suggested that ships should maintain the highest level of SA (Endsley and Jones, 2004;Perera and Murray, 2019). If relevant supportive systems not only provide information on the ship's current navigation states but also offer reliable predictions of how these states will evolve in the future, such information could greatly improve the effectiveness of collision avoidance decisions in complex navigation environments. In addition, reliable vessel maneuvering predictions are also considered essential for conducting proactive collision avoidance maneuvers, rather than merely reacting to imminent threats (Kufoalor et al., 2018;Murray and Perera, 2021).

1.2 Advanced ship predictor

Modern ships are equipped with advanced sensor systems, such as Global Navigation Satellite Systems (GNSS), Inertial Measurement Units (IMU), and the Automatic Identification System (AIS) that observes vessel motions. These systems are indispensable for maritime SA, as they provide critical navigational data that can be transformed into useful information (Thombre et al., 2022). Other supportive systems, such as Advanced Precision Radar Aids (APRA) and the Electronic Chart Display and Information System (ECDIS), further assist navigators in understanding the ship’s status based on the respective sensor measurements. However, one should note that even these modern sensors and display systems have limitations in supporting the level 3 of SA (Endsley, 2000), where trajectory prediction is one of the major tasks.

As for the ship trajectory prediction, many of these systems still rely on simplistic linear mathematical models or linear extrapolation (Perera, 2017). Linear model-based estimation and prediction approaches may pose significant prediction errors, particularly by overlooking potential nonlinear vessel maneuvering behavior. As a matter of fact, the knowledge and experience of navigators remain critical factors in decision-making during close encounter situations to avoid potential collisions, and that knowledge should be considered in vessel behavior predictions. However, as highlighted in the EMSA report (EMSA, 2024), human knowledge and experience alone do not consistently ensure navigation safety and should be supported by modern decision-support tools. Therefore, innovative SA support systems should be developed, such as ASP-type of technologies.

In (Perera and Murray, 2019), an ASP can be used for two types of predictions: global-scale and local-scale. The global-scale prediction is designed to cover relatively long prediction horizons, such as several tens of minutes (Murray, 2021). In comparison, the local-scale prediction corresponds to shorter prediction horizons, such as predictions within a few seconds. Different data sources are utilized to support these two types of predictions. The global-scale prediction primarily uses AIS data, which follows established maritime industry standards (Artikis and Zissis, 2021). The local-scale prediction relies on onboard sensor data, such as GNSS receivers, gyroscopes, and IMUs. The measurements from these sensors typically provide a more immediate reflection of vessels' current states, accurately compared to AIS data. The implementation and validation of local scale prediction is the focus of recent research studies (Perera, 2017;Wang et al., 2024). One should note that the workflow of the local scale predictions aligns with the three levels of SA in the studies. The predictors first gather real-time measurement data from various onboard sensors to estimate the current state of a selected vessel. Then, the predictor interprets the estimates to comprehend their implications through the concept of the PP (Capt. Cauvier, 2008). The PP is an important concept in maritime education and training. Determining the location of the PP is essential for many ship maneuvers. Particularly for local-scale operations, the geometric dimensions of a ship often need to be considered. Ultimately, the highest level of SA provided by the predictor is its ability to predict the vessel state evolvement in the future. One should note that the validation of the above-mentioned local-scale predictions is based on the data sets from the simulated ship maneuvers, such as ship maneuvers are executed from a selected bridge simulator. To ensure the robustness and reliability of the relevant methods, it is essential to validate them through real experimental data from ship maneuvers. In this study, the performances of local-scale ASP are validated through sea trial experiments that are executed on the UiT research vessel, Ymir RV, around the Tromsø fjord area (UiT, 2023).

The remainder of the paper is structured as follows: Section 2 examines the methods and techniques utilized in local-scale ASP; Section 3 offers detailed insights into the methods proposed and utilized in this study; Section 4 introduces the preparation information on the sea trial experiments and outlines the initialized parameters; Section 5 presents the experimental results and relevant discussions. Conclusions are drawn in the final sections of this paper.

2. Literature Review

2.1 Vessel navigation state estimation

Ship maneuvers can often be influenced by various weather and sea conditions. Such ship maneuvers are frequently observed through the measurements from the onboard sensors, which usually contain sensor noises and/or errors. Consequently, KF-based estimations are widely utilized to filter such measurement uncertainties in many industrial applications (Montella, 2011). The application of KF-based estimation requires the establishment of system and measurement models. The system models describe how the relevant vessel navigation states evolve with time in the vessel state estimation problems. Kinematic motion models are widely used in the mathematical representations of ship maneuvering in such situations (Li and Jilkov, 2003). Using kinematic motion models helps avoid difficulties in modeling and/or identifying external forces and moments that can be difficult to measure in some situations due to their nonlinear nature.

Given that ships have large dimensions in general, when making trajectory predictions over short prediction horizons, it is crucial to account for the entire size of the ship. Therefore, it is not advisable to reduce ships to mere point masses in local-scale predictions. When the prediction is visualized in a two-dimensional coordinate plane, the heading of the ship is equally important and must together be provided (Perera and Guedes Soares, 2012;Wang et al., 2023). In the same studies, the relevant model states including heading, position, and velocity are used. The ship heading information typically interacts with vessel motion models through trigonometric functions that can introduce model nonlinearities. In (Wang et al., 2024), the ship heading and related states such as yaw rate and yaw acceleration are distinguished and modeled separately. This approach allows a nonlinear model to be decomposed into two linear models. In this scenario, the standard Kalman Filter (KF) is considered an effective tool compared to nonlinear filters, due to its lower computational resource requirements.

Measurement models in KF-based estimation show how real measurements connect to system states. These models usually include data like positions and accelerations from onboard sensors, such as GNSSs and IMUs. However, in practical applications, sensor readings must be calibrated because the measurements can be actually recorded based on the sensor's reference frame (Hover and Chin, 2009;Tedaldi et al., 2014). This issue particularly affects the accuracy of measurements for acceleration and heading values. Additionally, the added mass in ship maneuvering can also influence the ship mass, therefore its influence cannot be ignored (Korotkin, 2008). This factor must also be considered when processing sea trial data with the respective ship maneuvering models. Therefore, both system and measurement models need to be adjusted according to actual conditions in real-time applications.

2.2 Concept of pivot point

The concept of PP in ship maneuvering plays a crucial role in understanding the respective vessel motions, especially during turning or circular maneuvers (Clark, 2005;Capt. Cauvier, 2008;Kjerstad, 2021). Since ships generally have substantial geometrical dimensions, turning maneuvers can result in expansive swept areas due to varying locations of the PP (Seo, 2016). All obstacles within the swept area can pose a threat to navigation safety. Therefore, local-scale predictions should take these areas into account, where a proper vessel domain should be considered (Clark, 2005;Zinchenko et al., 2022)

In (Tzeng, 1998), the PP of a ship during turning maneuvering is defined as the point that satisfies (1).

$$X_{PP} = -v_{CG}/r \tag{1}$$

where:
v_{CG} is defined as positive directed toward the starboard side;
r is defined as positive when turning toward the starboard.

The result X_{PP} from (1) gives the location of the PP measured from the ship center of gravity (CG). According to this definition, the PP is characterized by having zero sway velocity during the ship's turning maneuver and is located on the centerline. One should note that the PP calculations in (1) may not be a simple approach in actual ship navigation, where such calculations can become unstable when ships experience relatively low yaw rates. In such cases, the results may diverge and lose its practical relevance in ship navigation. Additionally, due to the presence of added mass during ship maneuvering, the estimated sway velocity obtained in real applications may not align with the sway velocity at the ship CG, denoted the v_{CG} in (1). This uncertainty should be also included during the PP calculations.

Based on the rigid body assumption of ocean-going vessels, the PP can also be determined by sway velocities at two points along the ship's centerline. The calculation of PP in (Wang et al., 2024) is established within predefined regions, rather than pinpointing its exact location under the same calculations. The predefined region can be likened to a statistical confidence interval where the range of uncertainty can be confined. However, this approach is somewhat subjective, as the definition of the region where the PP is located can vary among different ships. Additionally, determining the sway velocity at two points to support PP calculations requires measurements from two distinct GNSS locations. This can increase the measurement system's complexity, i.e., the number of required sensors, in practical experiments.

Once the PP is determined, the subsequent trajectory prediction on a local scale can utilize the same calculations. This prediction method is informed by the practices of experienced ship navigators who typically predict ship positions and headings by applying their understanding of the PP (Kjerstad, 2021). In (Perera, 2017), a navigation vector-based prediction method is proposed for the same conditions. The determination of PP in this study is based on (1) through the estimated sway velocity and yaw rate. The prediction method used in (Wang et al., 2024) decomposes vessel motions into two components: the translation of an arbitrary point and the rotation around the PP. In this paper, it continues to utilize the thought of motion decomposition in vessel trajectory prediction. A novel method is implemented to determine the PP based on real data from sea trial experiments by the same study.

3. Methodology

Figure 1 demonstrates a maneuver executed by the UiT research vessel—Ymir RV in Tromsø fjord area. The workflow of the designed local-scale predictor is divided into three stages that cover various methods.

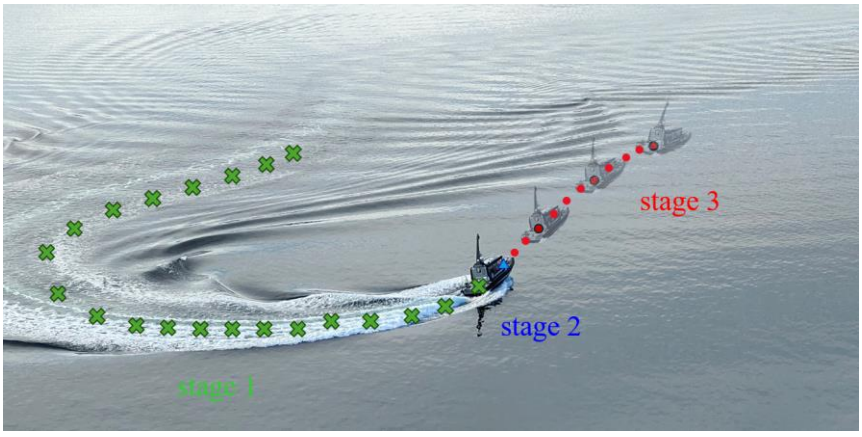

Fig.1. Sea trial experiment executed by Ymir RV in Tromsø fjord area. The local-scale prediction contains three stages.

In the first stage, vessel maneuvering models and KF-based algorithms are employed to estimate the vessel's navigation states. This stage continues until the current time when the trajectory prediction starts. The second stage contains the calculation of the vessel PP based on the estimated navigation states. The final stage involves initiating trajectory prediction, with the algorithm specifically designed to incorporate the impact of the PP on predicting vessel position and heading.

3.1 Mathematical models

Ships can experience several translational and rotational motions due to their six degrees of freedom: surge, sway, heave, yaw, pitch, and roll. For collision avoidance purposes, a simplified analysis of ship motions is typically conducted on the degrees of freedom of surge, sway, and yaw. However, due to the small size and low weight, Ymir RV is less stable and more susceptible to rough sea conditions. Compared to larger vessels, Ymir RV exhibits sensitive seakeeping characteristics, resulting in more pronounced rolling, pitching, and heaving during turns or changes in rudder orders. Therefore, the effects of roll, pitch, and heave are considered when implementing ship maneuvering models for Ymir RV. However, for trajectory prediction, since the vessel's position projected on the sea level and its heading are the most crucial information, the relevant prediction algorithm is thus based on the assumption of horizontal planar motion.

3.1.1 Reference frames

This part introduces the different reference frames used in the description of the vessel maneuvering models. A navigation reference frame $\{\boldsymbol{N}\}$ is set up to represent the navigation state vector (see Fig.2). This navigation frame is defined by three axes, where the axes N and E represent northing and easting from the Universal Transverse Mercator (UTM) coordinate system. The UTM coordinate system is well-suited for local navigation due to several key advantages, such as its metric-based grid system, high accuracy in small areas, and the integration with topographic maps and related geographic information systems. It is important to note that the UTM projection can cause a discrepancy between grid north (the direction of northing) and true north (the direction towards the geographic North Pole). The heading used in the mathematical models, denoted as ψ_G, is measured clockwise from the grid north. A vertical axis H is perpendicular to the UTM coordinate plane. The origin of this vertical axis is based on the surface of the WGS 84 reference ellipsoid.

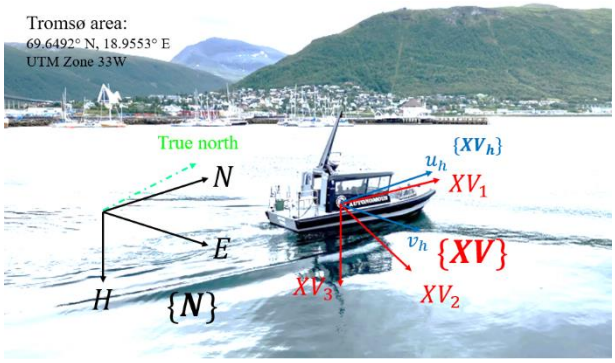

Fig.2. The defined navigation reference frame $\{\boldsymbol{N}\}$ and vessel reference frame $\{\boldsymbol{XV}\}$. The UTM zone covers Tromsø area is the 33W where the central meridian is 15° E.

The vessel reference frame, denoted as $\{\boldsymbol{XV}\}$, is established by three orthogonal axes: XV_1, XV_2, and XV_3. The axes XV_1 and XV_2 define the vessel's horizontal plane, with XV_1 oriented forward toward the bow and XV_2 directed toward the starboard side. The axis XV_3 is perpendicular to the horizontal plane and extends downward. The origin of $\{\boldsymbol{XV}\}$ is the vessel apparent center of gravity (ACG). One should note that due to the added mass effect, the position of ACG may not be a fixed point. In this study, the offsets between the ACG and the origin of $\{\boldsymbol{XV}\}$ are considered as model uncertainties that are incorporated into the system noises.

The angular position of the vessel is determined by the heading, pitch, and roll angles ($\psi_G, \theta, and\ \phi$). These angles are derived from the rotational transformation between the $\{\boldsymbol{N}\}$ and $\{\boldsymbol{XV}\}$. Given an acceleration vector $(A_{XV1}, A_{XV2}, A_{XV3})^T$ expressed in $\{\boldsymbol{XV}\}$ the corresponding components $(A_N, A_E, A_H)^T$ in $\{\boldsymbol{N}\}$ are represented by the rotational transformation as follows:

$$\begin{pmatrix} A_N \\ A_E \\ A_H \end{pmatrix} = R_{\psi_G} \cdot R_{\theta} \cdot R_{\phi} \begin{pmatrix} A_{XV1} \\ A_{XV2} \\ A_{XV3} \end{pmatrix} \quad (2)$$

where:

$$R_{\psi_G} = \begin{pmatrix} \cos(\psi_G) & \sin(\psi_G) & 0 \\ -\sin(\psi_G) & \cos(\psi_G) & 0 \\ 0 & 0 & 1 \end{pmatrix} \quad (3)$$

$$R_\theta = \begin{pmatrix} \cos(\theta) & 0 & \sin(\theta) \\ 0 & 1 & 0 \\ -\sin(\theta) & 0 & \cos(\theta) \end{pmatrix} \quad (4)$$

$$R_\phi = \begin{pmatrix} 1 & 0 & 0 \\ 0 & \cos(\phi) & -\sin(\phi) \\ 0 & \sin(\phi) & \cos(\phi) \end{pmatrix} \quad (5)$$

In addition to $\{\boldsymbol{N}\}$ and $\{\boldsymbol{XV}\}$, the vessel horizontal frame $\{\boldsymbol{XV_h}\}$ is also introduced, characterized by three orthogonal axes: XV_{h1}, XV_{h2}, and XV_{h3}. In this study, the vessel surge and sway velocities used for the local-scale prediction are defined based on $\{\boldsymbol{XV_h}\}$. Given the velocity vector $(V_N, V_E, V_H)^T$ represented in $\{\boldsymbol{XV}\}$, the surge and sway velocity can be represented as:

$$\begin{pmatrix} u_h \\ v_h \end{pmatrix} = \begin{pmatrix} \cos(\psi_G) & \sin(\psi_G) \\ -\sin(\psi_G) & \cos(\psi_G) \end{pmatrix} \begin{pmatrix} V_N \\ V_E \end{pmatrix} \quad (6)$$

This reference frame does not account for the effects of roll and pitch, as it is specified that trajectory prediction is exclusively concerned with horizontal planar motion. The surge and sway velocities, as defined by (6), will be subsequently utilized in the calculation of the vessel PP and in the prediction of its trajectory.

3.1.1 System models

The subsequent step involves the development of system and measurement models to estimate the required vessel navigation states that can be used for the trajectory prediction. In this study, two kinematic motion models are implemented. The first model, referred to as 3D-PV, considers the motion of vessel ACG in three dimensions. Given the ship navigation states which contain the position vector $\boldsymbol{P} = (P_N, P_E, P_H)^T$, velocity vector $\boldsymbol{V} = (V_N, V_E, V_H)^T$, and acceleration vector $\boldsymbol{A} = (A_N, A_E, A_H)^T$ at an arbitrary discrete time step t_k, the 3D-PV model can be summarized as:

$$\begin{bmatrix} P_N \\ P_E \\ P_H \\ V_N \\ V_E \\ V_H \end{bmatrix}_{t_k} = \boldsymbol{A} \cdot \begin{bmatrix} P_N \\ P_E \\ P_H \\ V_N \\ V_E \\ V_H \end{bmatrix}_{t_{k-1}} + \boldsymbol{B} \cdot \begin{bmatrix} A_N \\ A_E \\ A_H \end{bmatrix}_{t_{k-1}} + w_x \quad (7)$$

where:

$$\boldsymbol{A} = \begin{bmatrix} 1 & 0 & 0 & dt & 0 & 0 \\ 0 & 1 & 0 & 0 & dt & 0 \\ 0 & 0 & 1 & 0 & 0 & dt \\ 0 & 0 & 0 & 1 & 0 & 0 \\ 0 & 0 & 0 & 0 & 1 & 0 \\ 0 & 0 & 0 & 0 & 0 & 1 \end{bmatrix};$$

$$\boldsymbol{B} = \begin{bmatrix} dt^2/2 & 0 & 0 & dt & 0 & 0 \\ 0 & dt^2/2 & 0 & 0 & dt & 0 \\ 0 & 0 & dt^2/2 & 0 & 0 & dt \end{bmatrix}^T;$$

$w_x \sim \mathcal{N}(0, \boldsymbol{Q}^{6\times 6})$.

In this system model, the acceleration is treated as the system input. This combination can simplify the model and reduce computational resources, thus enabling real-time operation. The second model is based on the constant angular acceleration (CAA) assumption. The heading, yaw rate, and yaw acceleration can thus be represented as:

$$\begin{bmatrix} \psi_G \\ r \\ \dot{r} \end{bmatrix}_{t_k} = \begin{bmatrix} 1 & dt & dt^2/2 \\ 0 & 1 & dt \\ 0 & 0 & 1 \end{bmatrix} \begin{bmatrix} \psi_G \\ r \\ \dot{r} \end{bmatrix}_{t_{k-1}} + w_x \quad (8)$$

where:
$w_x \sim \mathcal{N}(0, \boldsymbol{Q}^{3\times3})$

Since the roll and pitch motions will not be considered in the trajectory prediction stage, the CAA model is only designed for the heading predictions.

3.1.2 Measurement models

The measurements from Ymir RV are obtained through the GNSS system, the gyroscope, and the IMU (see Fig.3).

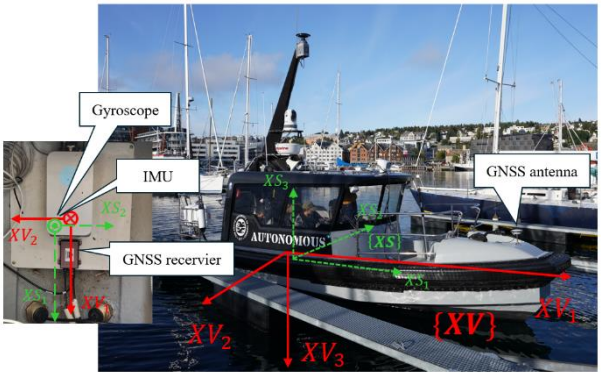

Fig.3. The sensors used for measurement. The measurements from the gyroscope and IMU are based on the sensor reference frame $\{\boldsymbol{XS}\}$

The GNSS system consists of a GPS antenna and a receiver. As illustrated in Fig.3, the GNSS antenna and receiver are positioned differently on the vessel; the antenna is installed at the bow, while the receiver is situated near the vessel's center. Through post-processing, the position initially measured by the antenna is adjusted to reflect the receiver's location. The measured positions, which include latitude, longitude, and height, are all based on the WGS 84 standard. The measured latitude and longitude will subsequently be converted into northing and easting coordinates of the UTM coordinate system. The utilized conversion function to transfer the measured latitude and longitude into northing and easting is detailed in (Kawase, 2013). The measurement model of the 3D-PV is illustrated in (9).

$$\begin{bmatrix} Z_{P_N} \\ Z_{P_E} \\ Z_{P_H} \end{bmatrix}_{t_k} = \begin{bmatrix} 1 & 0 & 0 \\ 0 & 1 & 0 \\ 0 & 0 & 1 \end{bmatrix} \begin{bmatrix} P_N \\ P_E \\ P_H \end{bmatrix}_{t_{k-1}} + w_z \quad (9)$$

where:
$w_z \sim \mathcal{N}(0, \boldsymbol{R}^{3\times3})$

Both the IMU and gyroscope are positioned closely to the origin of $\{\boldsymbol{XV}\}$. The IMU contains a three-axis accelerometer and provides the relevant accelerations. The gyroscope is a fiber-optic type and supplies measurements of heading, pitch, and roll motions, along with their respective rates. It is important to note that all measurements from the IMU and gyroscope are inherently taken in the sensor reference frame $\{\boldsymbol{XS}\}$ which is defined by three axes: XS_1, XS_2, and XS_3. As shown in Fig.3, there exist misalignments between $\{\boldsymbol{XV}\}$ and $\{\boldsymbol{XS}\}$. A rough misalignment is evident as XS_2 and XS_3 face different directions compared to XV_2 and XV_3. This misalignment can be corrected by the following axis inversions so that the new sensor axis (XS_1', XS_2', XS_3') can be written as:

$$XS_1' = XS_1, XS_2' = -XS_2, XS_3' = -XS_3 \quad (10)$$

After this rough misalignment, the fine misalignment is determined to correct the small residual angular offsets between the new sensor axis $(XS_1', XS_2', XS_3')^T$ and $\{\boldsymbol{XV}\}$. These residual angular offsets (denoted as ψ_{miss}, θ_{miss}, and ϕ_{miss}) are determined in advance by comparing the system output with another reference system. After the

alignment process, the gyroscope can provide the measured heading, pitch, and roll motions as defined in $\{\boldsymbol{XV}\}$. Given the measured heading and yaw rate (Z_{ψ_G} and Z_r), the measurement model for the CAA is presented in (11).

$$\begin{bmatrix} Z_{\psi_G} \\ Z_r \end{bmatrix} = \begin{bmatrix} 1 & 0 & 0 \\ 0 & 1 & 0 \end{bmatrix} \begin{bmatrix} \psi_G \\ r \\ \dot{r} \end{bmatrix} + w_z \quad (11)$$

where:
$w_z \sim \mathcal{N}(0, \boldsymbol{R}^{2\times 2})$

One should note that the measured heading from the fiber-optic gyroscope is oriented from the true north. To obtain the corresponding heading from grid north ψ_G, the respective grid convergence is calculated from the measured latitude and longitude. The details of the heading conversion can be referred to (Wang et al., 2023).

3.1.3 Acceleration vector as input

The IMU provides the measured acceleration components in $\{\boldsymbol{XS}\}$. Once the measured acceleration components $(A_{XS1}, A_{XS2}, A_{XS3})^T$ are obtained, the corresponding components in $\{\boldsymbol{XV}\}$ can be calculated as follows:

$$\begin{pmatrix} A_{XV1} \\ A_{XV2} \\ A_{XV3} \end{pmatrix} = - R_{\psi_{miss}} \cdot R_{\theta_{miss}} \cdot R_{\phi_{miss}} \begin{pmatrix} A_{XS1} \\ -A_{XS2} \\ -A_{XS3} \end{pmatrix} \quad (12)$$

The minus sign on the right-hand side of (12) indicates that the IMU measures the opposite direction of the respective acceleration. The components $(A_{XV1}, A_{XV2}, A_{XV3})^T$ can be further converted into $(A_N, A_E, A_H)^T$ using the rotational transformation shown in (2). The final calculation results serve as the input for the 3D-PV model.

3.2 Kalman filter estimation

3.2.1 Estimation algorithm

The Kalman filter is used to estimate the states from both the 3D-PV and CAA. The algorithm can be summarized as:

Algorithm 1: Kalman filtering
Given the system model $\boldsymbol{x}[t_k] = \boldsymbol{A}\,\boldsymbol{x}[t_k] + \boldsymbol{B}\,\boldsymbol{u}[t_k] + \boldsymbol{q}, \left(\boldsymbol{q} \sim \mathcal{N}(\boldsymbol{0}, \boldsymbol{Q})\right)$
and measurement model $\boldsymbol{z}[t_k] = \boldsymbol{C}\,\boldsymbol{x}[t_k] + \boldsymbol{r}, \left(\boldsymbol{r} \sim \mathcal{N}(\boldsymbol{0}, \boldsymbol{R})\right)$

Initialization:
initial state vector $\hat{\boldsymbol{x}}_{0|0}$ and covariance $\boldsymbol{P}_{0|0}$
Prediction step:
predicted prior state estimate: $\hat{\boldsymbol{x}}_{t_k|t_{k-1}} = \boldsymbol{A}\,\hat{\boldsymbol{x}}_{t_{k-1}|t_{k-1}} + \boldsymbol{B}\,\boldsymbol{u}_{t_{k-1}}$
predicted prior estimate covariance: $\boldsymbol{P}_{t_k|t_{k-1}} = \boldsymbol{A}\,\boldsymbol{P}_{t_{k-1}|t_{k-1}}\boldsymbol{A}^{\boldsymbol{T}} + \boldsymbol{Q}$
Filtering step:
calculate innovation: $\boldsymbol{e_z}[t_k] = \boldsymbol{z}[t_k] - \boldsymbol{C}\,\hat{\boldsymbol{x}}_{t_k|t_{k-1}}$
calculate innovation covariance: $\boldsymbol{S}[t_k] = \boldsymbol{C}\,\boldsymbol{P}_{t_k|t_{k-1}}\,\boldsymbol{C}^T + \boldsymbol{R}$
obtain Kalman gain: $\boldsymbol{K}[t_k] = \boldsymbol{P}_{t_k|t_{k-1}}\boldsymbol{C}^T\boldsymbol{S}^{-1}[t_k]$
obtain posterior state estimate: $\hat{\boldsymbol{x}}_{t_k|t_k} = \hat{\boldsymbol{x}}_{t_k|t_{k-1}} + \boldsymbol{K}[t_k]\,\boldsymbol{e_z}[t_k]$
obtain posterior estimate covariance: $\boldsymbol{P}_{t_k|t_k} = (\boldsymbol{I} - \boldsymbol{K}[t_k]\boldsymbol{C})\boldsymbol{P}_{t_k|t_{k-1}}$

Considering the system and measurement uncertainty, the minimal sensitivity of the fiber-optic gyroscope to cross-axis influences—such as vibration, acceleration, and shock—supports the rationale for assuming that the covariance matrices $\boldsymbol{Q}$ and $\boldsymbol{R}$ in the Constant Angular Acceleration (CAA) model remain constant.

Regarding the 3D-PV, considering that there are an adequate number of satellites in the sea trial area to reduce the vessel position error, the related elements in $\boldsymbol{R}$ about the position uncertainties are also set to constant values. However, the constant assumption of $\boldsymbol{Q}$ in the 3D-PV may not be reasonable since the vessel can have different

maneuvers and position accuracy can degrade some situations. Consequently, the system noise in the 3D-PV model is adaptively tuned during iterations of the KF algorithm. The detection of a maneuver change is facilitated by the estimated $\dot{r}$ from the CAA. When $\dot{r}$ exceeds a predefined threshold, the variable $\boldsymbol{Q}$ in the 3D-PV model is increased by scaling it with a scaling factor α. If $\dot{r}$ does not surpass this threshold, $\boldsymbol{Q}$ is reset to its original value.

3.2.2 Performance evaluation

Because there is no actual true data from the sea trial experiments, the filter consistency test is implemented to evaluate the performance of the KF. The Normalized Innovation Squared (NIS) test is a statistical tool to perform consistency checking in KF applications.

The NIS is defined as:

$$NIS[t_k] = \boldsymbol{e_z}[t_k]^T \, \boldsymbol{S}[t_k]^{-1} \, \boldsymbol{e_z}[t_k] \quad (13)$$

where $\boldsymbol{e_z}$ is the innovation and $\boldsymbol{S}$ innovation covariance calculated from the Algorithm 1.

In ideal cases, the values of NIS should follow a χ^2 distribution with degrees of freedom $dim(\boldsymbol{e_z})$. Two thresholds from the χ^2 distribution for a confidence level can be determined. These thresholds can define what values of NIS are expected if the KF works properly. If the NIS is lower than the lower threshold, it indicates that the filter may overestimate the error more than it really is. Conversely, if the NIS exceeds the upper threshold, it signifies that the noise is underestimated.

3.3 Pivot point-based trajectory prediction

3.3.1 Rigid body assumption

The determination of the vessel PP relies on the assumption that an ocean-going vessel behaves as a rigid body. This assumption implies that the surge velocities at every point on the vessel are uniform, and the sway velocities along the vessel centerline are linearly distributed. The position of the PP can be considered as the point where the sway velocity along the vessel's centerline is zero. Figure 4 illustrates the relationship between the PP and the sway velocities v_{bow} and v_{stern}.

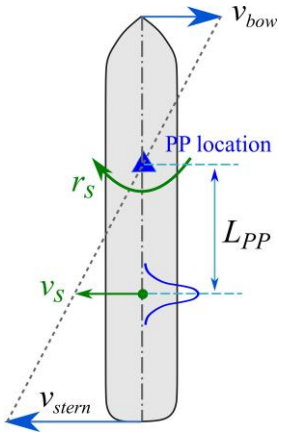

Fig.4. The determination of PP based on the rigid body assumption. The value of L_{PP} will be added with a Gaussian noise.

If v_{bow} and v_{stern} have opposite signs, the PP is located inside the vessel. When v_{bow} and v_{stern} have the same sign but differ in value, the PP is positioned outside the vessel. If v_{bow} and v_{stern} share both the same sign and the same non-zero value, this indicates that the vessel is undergoing purely transverse motion, suggesting that the PP can be considered as located at infinity. The special case that both v_{bow} and v_{stern} are zero is excluded.

One should note that once a combination of sway velocities (v_{bow}, v_{stern}) is known, the sway velocity at a selected point along the vessel (v_s) and the yaw rate (r_s) are also uniquely determined. Consequently, a mathematical mapping can be formulated between (v_{bow}, v_{stern}) and (v_s, r_s). The mapping is crucial for this

study because there is no information source to obtain v_{bow} and v_{stern} of Ymir RV. Instead, the KF-based estimation provides the estimated v_h and r, as shown in (6) and (8). The values of (v_h, r) obtained from the KF-based estimation can thus be used to derive the mapped values of (v_{bow}, v_{stern}).

In this circumstance, the distance between the point where v_h is estimated and the PP (denoted as L_{PP}) can be determined. Since the estimated v_h is assumed to be located at the vessel ACG, and the shift in the ACG is treated as Gaussian noise, L_{PP} is adjusted for this uncertainty using Gaussian noise.

3.3.2 Gaussian Process Regression

Due to the limited maneuverability of vessels in the sway direction, the values of v_{bow} and v_{stern} are typically constrained within a certain range. Various combinations of v_{bow} and v_{stern} can thus be enumerated to describe all the possible maneuvers in the vessel sway direction. The combinations of (v_{bow}, v_{stern}) can be converted into (v_h, r), together with the corresponding L_{PP}. With a new pair of (v_h, r), the related L_{PP} can be determined using regression methods.

A Gaussian Process Regression (GPR) model is implemented in this study as a non-parametric Bayesian approach to determine the PP. The GPR model is characterized by the selected kernel function, the Automatic Relevance Determination (ARD) exponential kernel function, as described in (14).

$$k(\boldsymbol{x_n}, \boldsymbol{x_m}\,|\boldsymbol{\theta}) = \sigma_f^2 \exp\left(-\frac{1}{2}\sum_{d=1}^{dim\,(x)} \frac{(x_n^d - x_m^d)^2}{l_i^2}\right) + \sigma_n^2\,\delta(\boldsymbol{x_n}, \boldsymbol{x_m}) \quad (14)$$

where x_n^d represents the d-th component of $\boldsymbol{x_n}$, σ_f is the signal standard deviation, l_i is the characteristic length scale for each dimension i, σ_n is the standard deviation of measurement noise, and δ is the Kronecker delta. The hyperparameters $\boldsymbol{\theta} = \left(\sigma_f, \sigma_n, l_i\,;\; i = 1, \dots, \dim(\boldsymbol{x})\right)$ are optimized by maximizing the log marginal likelihood function.

Based on the Gaussian Process assumption, given the training datasets $\left\{\mathcal{D} = \left(\boldsymbol{x}^i = \left(v_h^i, r^i\right), y^i = L_{PP}^i\right); i = 1, \dots, N\right\}$, the value of the response variable y^i for a new input $\boldsymbol{x}^*$ follows the Gaussian distribution shown in (15).

$$p(y^i|\boldsymbol{x}^*, \mathcal{D}) = \mathcal{N}(\boldsymbol{k}_*^T\boldsymbol{K}^{-1}\boldsymbol{y}, \boldsymbol{k}_{**} - \boldsymbol{k}_*^T\boldsymbol{K}^{-1}\boldsymbol{k}_*) \quad (15)$$

where $K_{ij} = k\left(\boldsymbol{x}_i, \boldsymbol{x}_j|\boldsymbol{\theta}\right) \in \boldsymbol{K}, k_* = k(\boldsymbol{x_i}, \boldsymbol{x}^*\,|\boldsymbol{\theta})$, and $k_{**} = k(\boldsymbol{x}^*, \boldsymbol{x}^*\,|\boldsymbol{\theta})$ $(i, j = 1, \dots, N)$.

From (15), one should note that one significant advantage of the GPR model is its ability to provide not only the expectation as the optimal results of L_{pp} but also a quantification of the related uncertainty.

3.3.3 Trajectory prediction

Based on the rigid body dynamics, the planar motion of a vessel can be decomposed into translational and rotational motions (see Fig.5). Using this decomposition, trajectory prediction can be performed using the Algorithm 2.

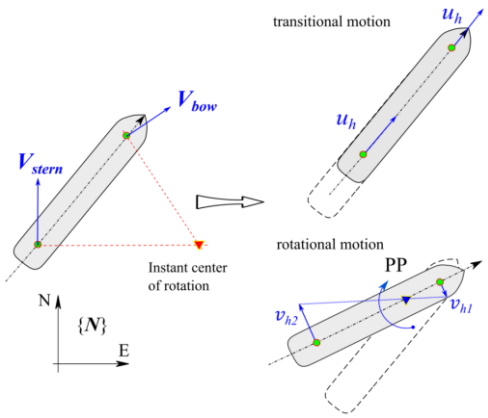

Fig.5. The planar motion of a vessel can be decomposed into translational and rotational motions based on rigid body assumption.

Algorithm 2: PP-based algorithm for ship trajectory prediction

Initialization:

- Given that the prediction starts at time step t_k;
- Obtain the estimated navigation states $P_N, P_E, \psi_G, u, v, r$ in t_k;
- Determine the PP based on the GPR model with v and r in step t_k;

Trajectory prediction: (prediction horizon t_{k+1} to t_{k+N})

for $i = k+1$ to $k+N$:

$$\Delta L = u \cdot \Delta t;$$
$$\Delta\psi_G = r \cdot \Delta t;$$

$$P'_N = P_N[t_i] + \Delta L \cdot cos(\psi_G[t_i]);$$
$$P'_E = P_E[t_i] + \Delta L \cdot sin(\psi_G[t_i]);$$

$$PP_N = P'_N + L_{PP} \cdot cos(\psi_G)$$
$$PP_E = P'_E + L_{PP} \cdot sin(\psi_G)$$

$$P_N[t_{i+1}] = \cos(\Delta\psi_G)\,(P'_N - PP_N) - \sin(\Delta\psi_G)\,(P'_E - PP_E) + PP_N$$
$$P_E[t_{i+1}] = \sin(\Delta\psi_G)\,(P'_N - PP_N) + \cos(\Delta\psi_G)\,(P'_E - PP_E) + PP_E$$
$$\psi_G[t_{i+1}] = \psi_G[t_i] + \Delta\psi_G$$

4. Sea trial experiment

4.1 Vessel and hardware structure

The vessel "Ymir RV" is a part of the UiT autonomous ship project as presented before. The vessel is constructed with a composite sandwich structure, where the core material serves both structural and insulation purposes. The key features of the vessel are listed in Tab.1.

Tab.1: Design parameters of Ymir RV

Vessel name	Ymir
Length	8 [m]
Width	2.8[m]
Draft	0.7[m] - 1[m]
Dry weight	ca. 3000 [kg]
Max load weight	ca. 750 [kg]
Max speed	ca. 30 [kt]
Engine type	4 stroke diesel engine

As it is shown in Fig.6, the measurements from different sensors are transmitted to the hardware workstation via Ethernet. To ensure data integrity and transmission reliability, the TCP protocol is utilized. A graphical user interface (GUI) is designed and implemented on the workstation to visualize the measurements. Additionally, all measurements are saved on the workstation for further data analysis.

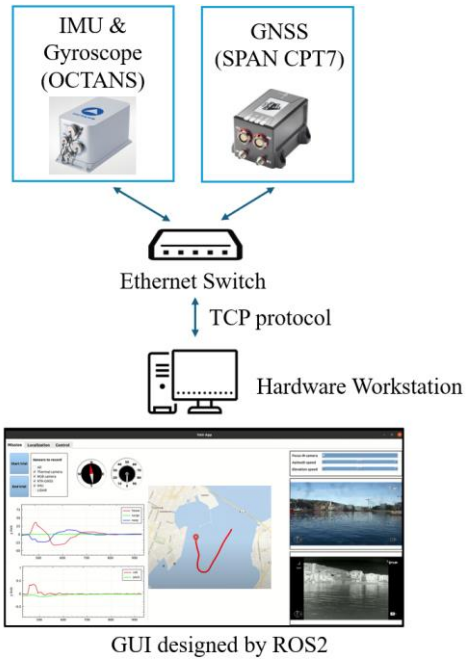

Fig.6. hardware structure in Ymir RV and GUI for measurements display

4.2 Sea trial maneuvering

The sea trial experiments are conducted in the Tromsø fjord area, which is located at 69°N. The UTM zone for this area is 33W, with the central meridian at 15°E longitude. Two maneuvers are selected to validate the trajectory prediction method: a port turning (PT) and a starboard turning (SBT). Figure 7 presents the measured latitude and longitude datasets of these two maneuvers in the map provided by OpenStreetMap (OpenStreetMap, 2024).

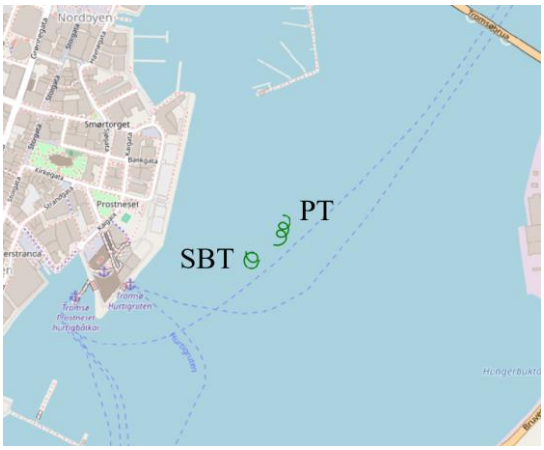

Fig.7. The PT and SBT maneuvers in the Tromsø fjord area.
The map is from the OpenStreetMap.

4.3 Parameter initialization

The parameters used in the KF and GPR model need to be initialized. Table 2 lists the parameters for KF state estimation. The values of elements in the measurement noise covariances $\boldsymbol{R}$ are based on the sensors' performance characteristics, while the system noise covariance $\boldsymbol{Q}$ is determined through multiple trials.

Table 2: The initialized parameters in the KF estimation				
Model	Para.	Definition	Value	Notation

3D-PV	Δt	time interval between two measurements	0.13 [s]	Estimates are acquired every 0.13 seconds.
	$\boldsymbol{Q}$	the noise covariance matrix of the system model	$\begin{pmatrix} \frac{q1\,dT^4}{4} & 0 & 0 & \frac{q1\,dT^3}{2} & 0 & 0 \\ 0 & \frac{q2\,dT^4}{4} & 0 & 0 & \frac{q2\,dT^3}{2} & 0 \\ 0 & 0 & \frac{q3dT^4}{4} & 0 & 0 & \frac{q3\,dT^3}{2} \\ \frac{q1\,dT^3}{2} & 0 & 0 & q1\,dT^2 & 0 & 0 \\ 0 & \frac{q2\,dT^3}{2} & 0 & 0 & q2\,dT^2 & 0 \\ 0 & 0 & \frac{q3\,dT^3}{2} & 0 & 0 & q3\,dT^2 \end{pmatrix}$ $q1 = 0.25; q_2 = 0.125; q_3 = 0.0625$	A general noise covariance matrix for constant acceleration models
	α	the scaling factor for $\boldsymbol{Q}$	1.015 (when estimated $\dot{r}$ is larger then 0.02)	Determined by multiple trials to obtain the optimal estimates
	$\boldsymbol{R}$	the noise covariance matrix of measurement model	$Diag((0.15)^2, (0.1058)^2, (0.2121)^2)$	Values are referred to the sensor performance
CAA	dt	the time interval between consecutive measurements or updates	0.13 [s]	Estimates are acquired every 0.1 seconds.
	$\boldsymbol{Q}$	the noise covariance matrix of the system model	$\begin{pmatrix} dt^4/20 & dt^3/8 & dt^2/6 \\ dt^3/8 & dt^2/3 & dt/2 \\ dt^2/6 & dt/2 & 1 \end{pmatrix} \cdot q_\psi$ $q_\psi = 3.6642 \times 10^{-5}$	Determined by multiple trials to obtain the optimal estimates
	$\boldsymbol{R}$	the noise covariance matrix of the measurement model	$Diag(0.005^2, 0.0375^2)$	Values are referred to the sensor performance

For the GPR model, the training data sets consist of 10000 samples, each formed by combining values from 100 distinct v_{bow} and 100 v_{stern} values. The values of v_{bow} and v_{stern} are within an interval of -5 to $5[m/s]$. These 100 values for both v_{bow} and v_{stern} are exponentially sampled within this interval (see Fig.8(a)). The sampled v_{bow} and v_{stern} will be thus denser near zero and sparser as they approach $\pm 5[m/s]$. This approach assumes that Ymir RV's sway velocity does not exceed $\pm 5[m/s]$ and it follows an exponential distribution within this range. This assumption suggests that smaller sway velocities are much more common for Ymir RV than larger sway velocities. The corresponding (v_h, r) converted by the sampled (v_{bow}, v_{stern}) are shown in Fig. 8(b).

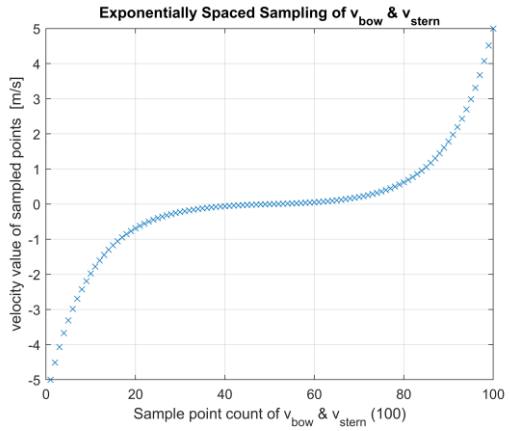

(a) The sampled values of v_{bow} and v_{stern}

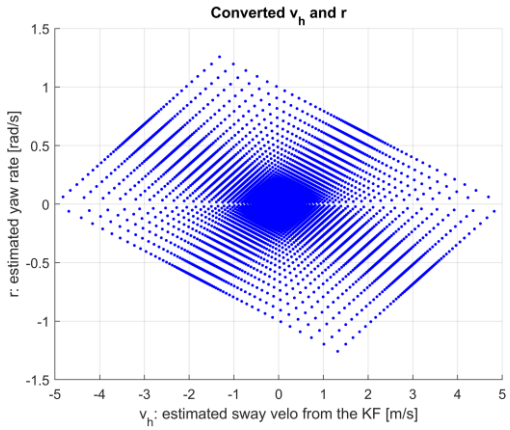

(b) the distribution of (v_h, r) calculated from the sampled v_{bow} and v_{stern}

Fig. 8. The generation of training data for the GPR model

Other initialized parameters for the GPR model are shown in Table 3. The algorithm for optimizing the hyperparameters is the Quasi-Newton method, which is particularly favored for dealing with large-scale optimization problems. This optimization algorithm aims to minimize the negative log-likelihood of the GPR model. The optimization process will terminate if the change in the negative log-likelihood between iterations is less than the threshold of 1×10^{-6}. The Gaussian white noise added to L_{PP} has a standard deviation of $0.1[m]$. When L_{PP} is considered to be at infinity, the value is artificially set to 1000[m]

Table. 3: Parameters in the ARD exponential kernel function

Para.	Definition	Value
N	number of the samples	10000
σ_f	signal standard deviation	1.5 [m]
σ_n	standard deviation of measurement noise	1.5 [m]
l_i	the characteristic length scale	$l_1 = 0.02$ [rad/s] $l_2 = 0.2$ [m/s]

5. Results and discussion

The experimental results are presented in this section. For each maneuver, the estimated states from the KF-based algorithm are presented first. These estimated states span the entire maneuvering period for each case. The second part presents the results of trajectory prediction. It is important to note that since there is no access to true vessel states in sea trial experiments, the estimated states from the KF-based algorithm are used as substitute true data for comparison with the predicted states.

5.1 Vessel state estimation

The estimated and measured positions of the two maneuvers are presented in Fig.9(a) and Fig.10(a). The vessel icon is presented approximately every 3 seconds during these maneuvers. For each maneuver, other vessel states u_h, v_h, ψ, and r are also presented. The calculated NIS for both maneuvers is presented in Fig.11 and Fig.12. The two-sided 95% chi-squared confidence interval of $(0.2158, 9.3484)$ is used for the consistency test, and the summary of the test is presented in Tab.4.

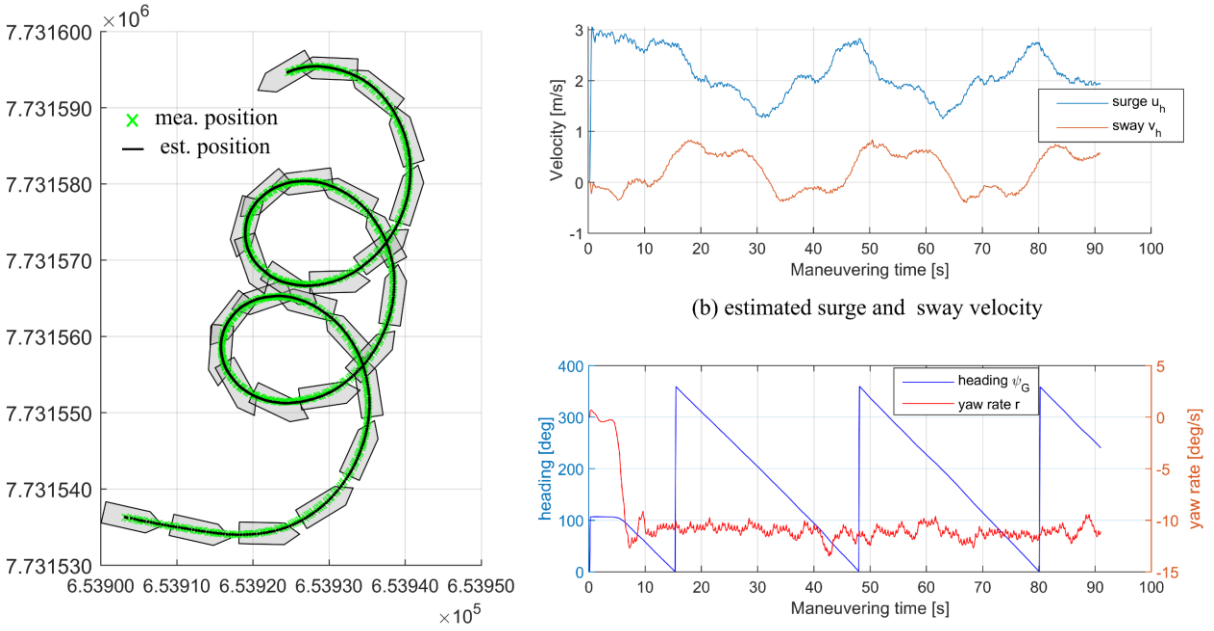

(a) estimated and measured position

(b) estimated surge and sway velocity

(c) estimated heading and yaw rate

Fig.9. Estimated vessel states from PT

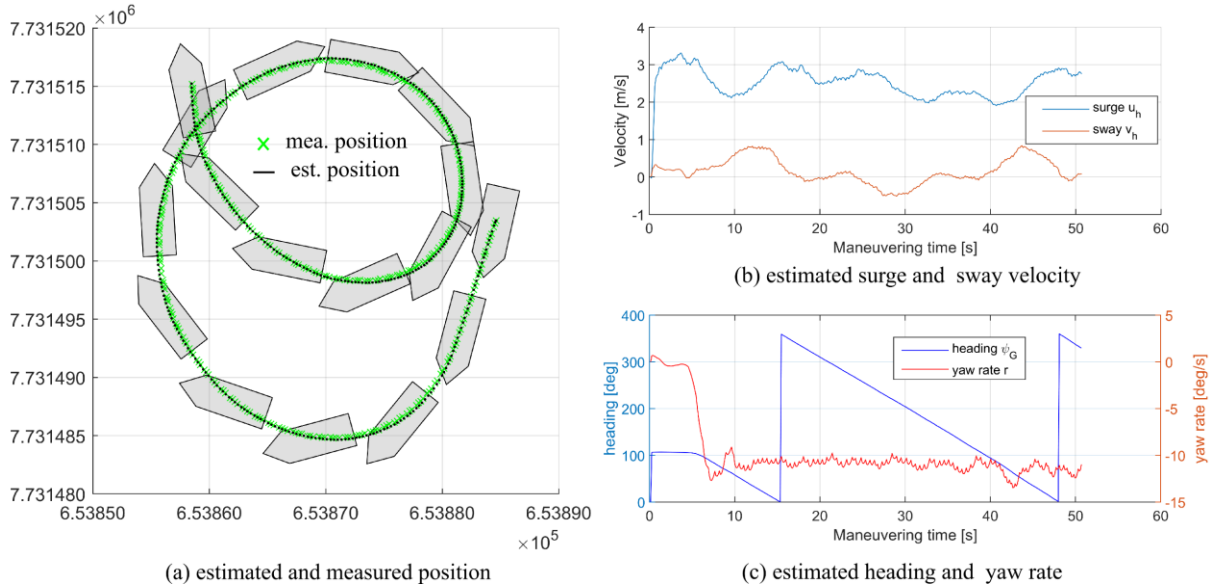

(a) estimated and measured position

(b) estimated surge and sway velocity

(c) estimated heading and yaw rate

Fig.10. Estimated vessel states from SBT.

For the PT maneuver, 91.79% of the calculated NIS from the 3D-PV lie within the bounded area, while 72.82% of the NIS from the CAA lie within this area. It indicates that the KF-based algorithms in both the 3D-PV and CAA models are consistent, thus ensuring precise and reliable state estimations. Moreover, almost no NIS exceeds the upper bound. This implies that the system noises $\boldsymbol{Q}$ values selected in both models are not underestimated, i.e. low model inaccuracies. Meanwhile, it can be also observed that the NIS at some steps is smaller than the lower bound. Taking a closer look at the NIS that fall below the lower bound, it is apparent that many of these occur at the beginning under the CAA model (see Fig.11(a)). Since the vessel starts with a straight-line maneuver, the initialized $\boldsymbol{Q}$ for the CAA is thus overestimated for the straight-line maneuver. In addition, it is noticeable that the overestimated steps in the 3D-PV are fewer than the CAA (see Fig.11(b)). The better consistency test in the 3D-PV suggests that the adaptive tuning mechanism for $\boldsymbol{Q}$ is effective. The results of the SBT maneuver are approximately similar to those of the PT maneuver, confirming the same discussions previously (see Fig.12(a) & (b)).

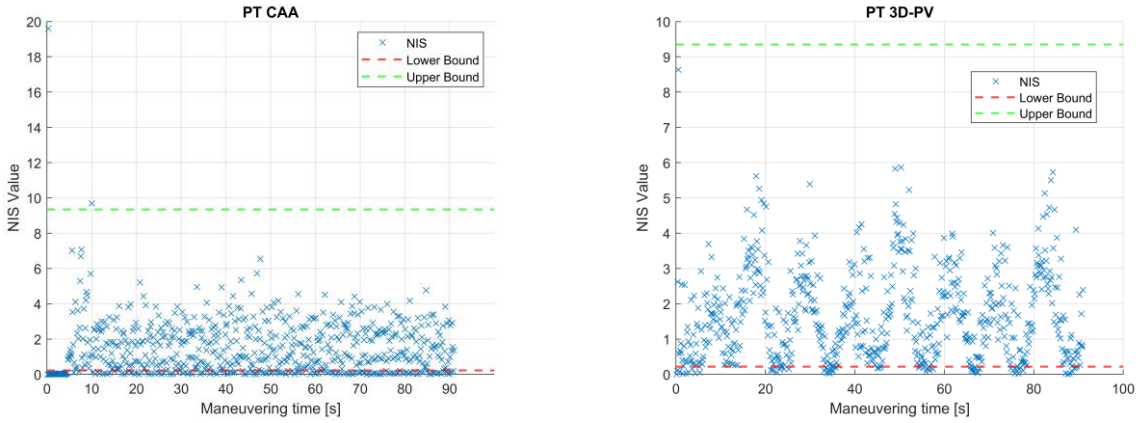

(a) (b)

Fig.11 Consistency test of CAA and 3D-PV in PT

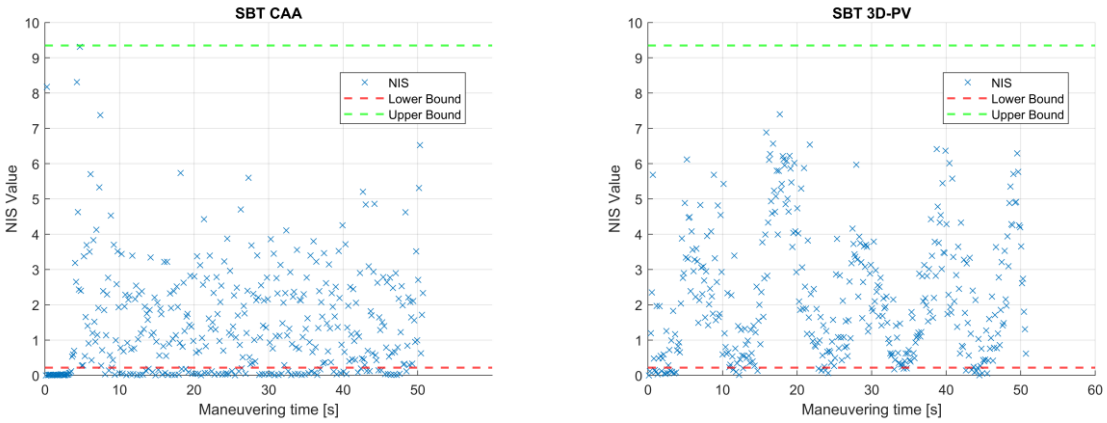

(a) (b)

Fig.12 Consistency test of CAA and 3D-PV in SBT

Table 4:

Percentage of NIS		within the bound	below the lower	above the upper
PT	CAA	74.57%	25.14%	0.29%
	3D-PV	91.29%	8.71%	0
SBT	CAA	72.82%	27.18%	0
	3D-PV	91.79%	8.21%	0

Although there are time steps where the NIS falls below the lower bound, it should be noted that, according to the KF algorithm, the overestimation of system noise implies a greater reliance on sensor measurements. With advancements in sensors performances and sensor fusion techniques, KF-based applications that slightly overestimate system noises can be less problematic.

5.2 Pivot point by GPR

The calculated PP of both maneuvers is shown in Fig.13. The mean value of L_{PP} is shown with blue lines, and the 95% confidence intervals are marked as the shadow areas.

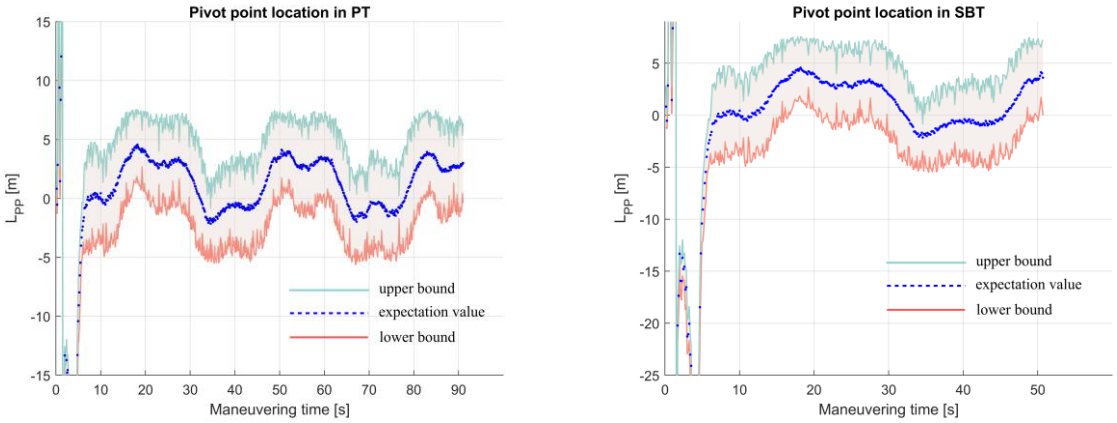

(a) Location of PP in PT (b) Location of PP in SBT

Fig.13 Calculation of PP based on the GPR model

Both maneuvers begin with a straight-line maneuver, where calculated L_{PP} exhibits vibrations. During the circular turning periods, L_{PP} has periodic fluctuations. It can also be observed that the 95% confidence intervals during the straight-line maneuvers are relatively narrow compared to those during the circular motion periods. This is due to the high sampling rate of sway velocity and yaw rate within the unit distance (see Fig.8). During the circular motion periods, the average values of the upper and lower bounds of the 95% confidence intervals are $\pm 2.30[m]$ and $\pm 3.34[m]$ for PT and SBT, respectively.

The fluctuations of L_{PP} in the circular turning periods can also be caused by sea currents, particularly given that Ymir RV has low weight. The influence of the sea current is clearly visible in the trajectory of the PT maneuver (see Fig.9(a)), as the vessel gradually moves in a northeastern direction during its circular motion. During the periods when the L_{PP} is increasing, such as between 10[s] and 20[s] in the PT maneuver and 15[s] to 20[s] in the SBT maneuver, Ymir RV turns while riding the current. In contrast, when the L_{PP} decreases, the vessel makes a turning while moving against the current.

It is also worth mentioning that the GPR model used in this study assumes that v_{bow} and v_{stern} follow an exponential distribution. As a result, a larger proportion of the training dataset is concentrated where both v_{bow} and v_{stern} are close to zero. However, the sea trial results show that when v_{bow} and v_{stern} are close to zero, the vessel performs the straight-line maneuvers. Consequently, the 95% confidence intervals are narrower during the straight-line maneuver periods compared to these during the turning periods. By increasing the samples of v_{bow} and v_{stern} values, the confidence intervals of L_{pp} during turning periods can be narrowed. However, since the computational cost increases exponentially with the sample size in GPR models, this approach is not economically recommended for a single model. A practical solution could involve designing multiple GPR models, each tailored to specific sway velocity ranges. For instance, during a turn with a sway velocity of 1 [m/s], the GPR model with the highest density of sample points near this value can be used to optimize the calculated L_{pp}.

5.3 PP-based trajectory prediction

In each maneuver, trajectory prediction begins at the selected time steps. Each prediction has the prediction horizon of 10 seconds. To illustrate the prediction performance, the estimates provided by the KF are used as the true values. The predicted position and heading are then compared with these true values.

For the PT maneuver, the turning begins 4[s] after the start. Predictions are initiated at the selected times: 5[s], 7[s], 15[s], and 30[s] after the start. It can be observed that there is a large error immediately after the vessel starts turning (see Fig.14(a)). However, significant improvements are noted when the prediction resumes just 2[s] later (see Fig.14(b)). Figures 14(c) and 14(d) show predictions during the steady turning period. These predictions reveal a slightly larger error between the predicted position and the actual position in the final prediction step; this is due to the fact that prediction accuracy will always decrease with the length of its prediction horizon.

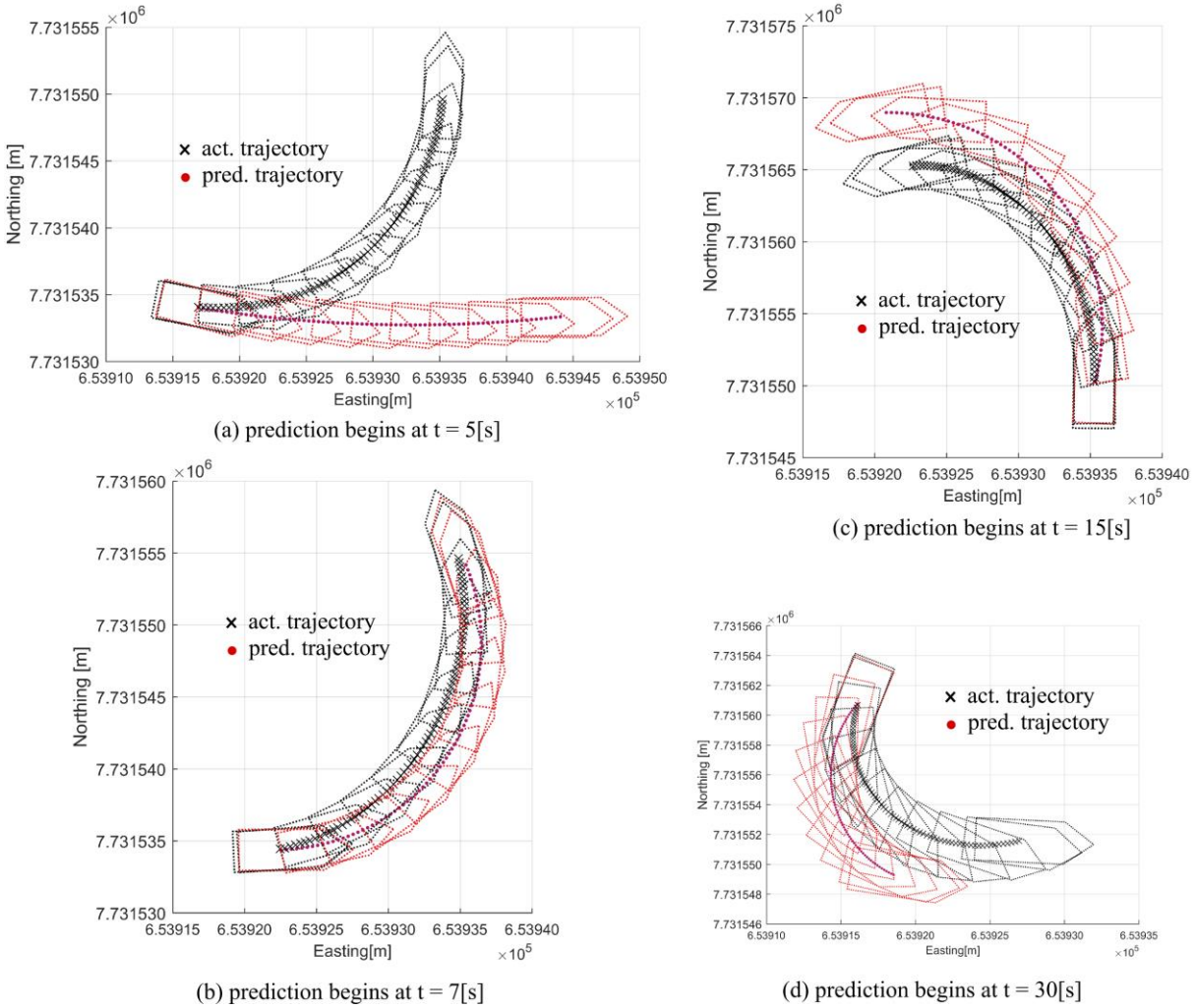

Fig.14 The comparison between actual and predicted positions and headings in PT. The ship icons are shown in ca. every 1 second.

For the SBT, the turning begins 3[s] after the start. The predictions are initiated at the selected times: 4[s], 6[s], 20[s], and 30[s] after the start (see Fig.15). The results show that predictions immediately following a new rudder order are less accurate, but the quality of predictions greatly improves after 2 seconds. During the steady turn phase, the influence of the sea current causes some discrepancies between the predicted results and the reference positions. However, in some instances, the predictions closely align with the actual values.

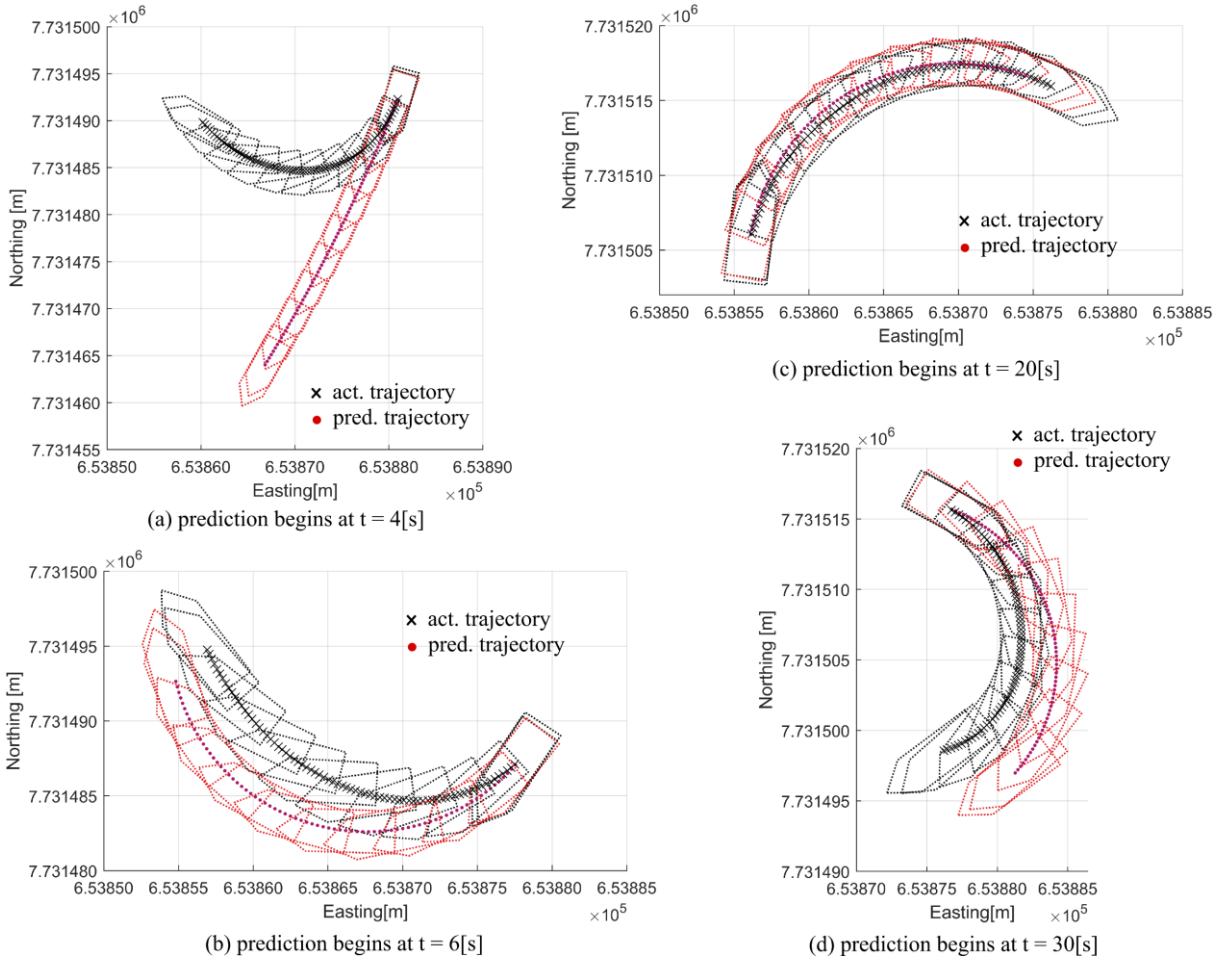

Fig.15 The comparison between actual and predicted positions and headings in SBT. The ship icons are shown in ca. every 1 second.

As mentioned in Section 5.2, the prediction algorithm assumes that L_{PP} is constant during the prediction horizon. However, due to the impact of the sea current, L_{PP} fluctuates during steady turning. This shift in the PP can result in relatively large prediction errors, particularly in position. Therefore, for ships like Ymir RV, which has relatively small weight, the influence of sea currents should be considered for local-scale trajectory prediction.

In addition, the calculated L_{PP} shown in Fig.13 indicates that the fluctuation of L_{PP} is related to the impact of sea currents. Therefore, if the magnitude and direction of sea currents are known or can be measured in advance, the prediction results could be improved by adjusting the L_{PP} accordingly. Conversely, for larger tonnage vessels, the designed prediction method may achieve better quality since they are less affected by ocean environmental conditions.

6. Conclusion

Two maneuvers executed by the UiT research vessel—Ymir RV—are used to validate the performances of the local-scale prediction which is one of the main functions in the ASP to support maritime SA to improve navigation safety. The local-scale prediction process is divided into three two stages. In the first stage, the KF-based algorithm and kinematic motion models (the 3D-PV and CAA) are employed to generate the required vessel navigation states. In the second stage, the estimated vessel navigation states are used to calculate the vessel PP through a GPR model in the second stage. The final stage involves the utilization of a PP-based algorithm to predict the vessel's trajectory over a specified prediction horizon. Meanwhile, a consistency check based on the NIS is conducted to assess the quality of the KF-based estimated states. These estimated states are then used as actual true values to evaluate the prediction.

The findings of this paper are presented in two parts. Firstly, the consistency test of the KF demonstrates that most of the calculated NIS from both the CAA and 3D-PV fall within the confidence interval. This confirms that the filter maintains consistency throughout most of the execution time. There are several instances where the NIS falls below the lower bound, indicating that the filter tends to rely more on the measurements at these steps. However, this reliance on measurements is considered reasonable in real-world applications. Secondly, the employed GPR model and the PP-based trajectory prediction method achieve good prediction results within a 10-second prediction horizon. For a low-tonnage vessel like Ymir RV, it is considered that a reliable 10-second prediction can significantly support the highest level of SA.

Regarding the previously mentioned limitations, as it is mentioned earlier that this study does not account for impacts from the sea environment, such as sea currents. To enhance prediction quality, it would be beneficial to incorporate relevant information from the sea environment into the prediction process. Additionally, the PP-based trajectory algorithm assumes that vessel navigation states remain constant throughout the prediction horizon. This assumption could be problematic in scenarios where these states change significantly after new rudder or engine orders. Finally, it should be noted that predictions should inherently be expressed in terms of probabilities rather than as definitive statements. Although the GPR model provides confidence intervals for the location of PP, this information is currently not utilized in the prediction process. Future work will aim to integrate the uncertainty from the GPR model to enhance the predictions with probabilistic information.

Acknowledgment
This work has been conducted under the Autonomous ship Program in UiT-The Arctic University of Norway, which aims to develop the digital helmsman as a part of the ship intelligence to operate future vessels supported by the MARKOM II project under the project title “Onshore Operation Center for Remotely Controlled Vessels (OOC 2023)" under the contract number PMK-2022-10014. An initial version of this study is presented at the 34th International Ocean and Polar Engineering Conference (ISOPE 2024), Rhodes, Greece, June 2024.

Reference

Artikis, A. and D. Zissis (2021). Guide to Maritime Informatics, Springer Nature Switzerland AG 2021**:** 10-11.
Capt. Cauvier, H. (2008). The pivot point. The Pilot, the United Kingdom Maritime Pilots' Association (UKMPA).
Clark, I. C. (2005). Ship dynamics for mariners. London, England, Nautical Institute.
EMSA (2024). EMSA Facts & Figures 2023, European Maritime Safety Agency.
Endsley, M. (1995). "Endsley, M.R.: Toward a Theory of Situation Awareness in Dynamic Systems. Human Factors Journal 37(1), 32-64." Human Factors: The Journal of the Human Factors and Ergonomics Society **37**: 32-64.
Endsley, M. (2000). "Situation awareness analysis and measurement, chapter theoretical underpinnings of situation awareness." A Critical Review: 3-33.
Endsley, M. and D. G. Jones (2004). Designing for Situation Awareness: An Approach to User-Centered Design, CRC Press.
Hover, F. and H. Chin (2009). Vehicle Internal Dynamics. Design Of Electromechanical Robotic Systems.
IMO. (2024). "Developing a MASS Code." Retrieved 5, June, 2024, from https://www.imo.org/en/MediaCentre/HotTopics/Pages/Autonomous-shipping.aspx.
Kawase, K. (2013). Concise Derivation of Extensive Coordinate Conversion Formulae in the Gauss-Krüger Projection.
Kim, T.-e., L. Perera, M.-P. Sollid, B.-M. Batalden and A. Sydnes (2022). "Safety challenges related to autonomous ships in mixed navigational environments." WMU Journal of Maritime Affairs **21**.
Kjerstad, N. (2021). Fagbokforlaget.
Kongsberg. (2023). "Autonomous ships equipment / products / systems - Kongsberg Maritime." Retrieved 28, May, 2024, from https://www.kongsberg.com/maritime/ship-types/autonomous-ships/.
Korotkin, A. I. (2008). Added masses of ship structures. New York, NY, Springer.
Kufoalor, D. K. M., E. F. Brekke and T. A. Johansen (2018). Proactive Collision Avoidance for ASVs using A Dynamic Reciprocal Velocity Obstacles Method. 2018 IEEE/RSJ International Conference on Intelligent Robots and Systems (IROS).
Li, X. R. and V. P. Jilkov (2003). "Survey of maneuvering target tracking. Part I. Dynamic models." IEEE Transactions on Aerospace and Electronic Systems **39**(4): 1333-1364.
MEGURI2040. (2022). "The Nippon Foundation MEGURI2040 Fully Autonomous Ship Program." Retrieved 28, May, 2024, from https://www.nippon-foundation.or.jp/en/what/projects/meguri2040.

Montella, C. (2011). "The Kalman Filter and Related Algorithms: A Literature Review."
Munim, Z. (2019). "Autonomous ships: a review, innovative applications and future maritime business models." Supply Chain Forum **20**: 266-279.
Murray, B. (2021). Machine Learning for Enhanced Maritime Situation Awareness. Doctoral, UiT The Arctic University of Norway.
Murray, B. and L. P. Perera (2021). "Proactive Collision Avoidance for Autonomous Ships: Leveraging Machine Learning to Emulate Situation Awareness." IFAC-PapersOnLine **54**(16): 16-23.
OpenStreetMap, c. (2024). Planet dump retrieved from https://planet.osm.org.
Perera, L. and C. Guedes Soares (2012). Detections of potential collision situations by relative motions of vessels under parameter uncertainties**:** 705-713.
Perera, L. and B. Murray (2019). Situation Awareness of Autonomous Ship Navigation in a Mixed Environment Under Advanced Ship Predictor. Proceedings of the 38th International Conference on Ocean, Offshore and Arctic Engineering (OMAE 2019). Glasgow, Scotland, UK.
Perera, L. P. (2017). "Navigation vector based ship maneuvering prediction." Ocean Engineering **138**: 151-160.
Perera, L. P. and B. M. Batalden (2019). Possible COLREGs Failures under Digital Helmsman of Autonomous Ships. OCEANS 2019 - Marseille.
Seo, S.-G. (2016). "Safer and More Efficient Ship Handling with the Pivot Point Concept." TransNav, the International Journal on Marine Navigation and Safety of Sea Transportation **10**: 605-612.
Tedaldi, D., A. Pretto and E. Menegatti (2014). A robust and easy to implement method for IMU calibration without external equipments. 2014 IEEE International Conference on Robotics and Automation (ICRA).
Thombre, S., Z. Zhao, H. Ramm-Schmidt, J. M. V. García, T. Malkamäki, S. Nikolskiy, T. Hammarberg, H. Nuortie, M. Z. H. Bhuiyan, S. Särkkä and V. V. Lehtola (2022). "Sensors and AI Techniques for Situational Awareness in Autonomous Ships: A Review." IEEE Transactions on Intelligent Transportation Systems **23**(1): 64-83.
Tzeng, C.-Y. (1998). "Analysis of The Pivot Point for a Turning Ship,." Journal of Marine Science and Technology **6**(1).
UiT. (2021). "UiT Autonomous Ship Program." Retrieved 28, May, 2024, from https://en.uit.no/prosjekter/prosjekt?p_document_id=668855.
UiT, A. M. S. O. (2023). "UiT Autonomous Test Vessel in Sea Trials." YouTube, Video. https://www.youtube.com/watch?v=mYZN-w7jCnQ&t=7s.
Wang, Y., L. P. Perera and B.-M. Batalden (2023). "Coordinate conversion and switching correction to reduce vessel heading related errors in high-latitude navigation." IFAC-PapersOnLine **56**(2): 11602-11607.
Wang, Y., L. P. Perera and B.-M. Batalden (2023). "Kinematic motion models based vessel state estimation to support advanced ship predictors." Ocean Engineering **286**: 115503.
Wang, Y., L. P. Perera and B.-M. Batalden (2024). "Localized advanced ship predictor for maritime situation awareness with ship close encounter." Ocean Engineering **306**: 117704.
Zinchenko, s., T. Oleh, P. Nosov, I. Popovych and K. Kyrychenko (2022). "Pivot Point position determination and its use for manoeuvring a vessel." Ships and Offshore Structures **18**: 1-7.